Photodissociation Dynamics of Atmospherically Relevant Alkyl Ketones and Methyl Nitrite by Velocity Map Imaging

Dissertation

zur Erlangung des Doktorgrades der
Mathematisch-Naturwissenschaftlichen Fakultät der
Christian-Albrechts-Universität zu Kiel

vorgelegt von

Siarhei Dziarzhytski

Kiel 2008

To my parents

Abstract

The photodissociation dynamics of *trans*-methyl nitrite and atmospherically relevant alkyl ketones in the near UV were studied by velocity map imaging.

The photolysis of *trans*-methyl nitrite excited to the S_1 state with 0 and 1 quanta of excitation in the N=O-stretching mode, has been investigated. The primarily NO fragments were probed by (1+1) REMPI in vibrational states $v'' = 0$ and 1, and a rotational excitation of $j'' = 33.5$. The results demonstrate two dissociation pathways: a vibrationally non-adiabatic predissociation, and an adiabatic channel *via* tunneling through a potential barrier on the S_1 potential energy surface. The O-NO bond dissociation energy was determined to be $D_0^0 = 13\ 560 \pm 200$ cm^{-1} and an S_1 excited state lifetime of $\tau \leq 350$ fs was found.

The photodissociation dynamics of acetone-$h6$ excited within the first absorption band ($\lambda_{pump} = 340 - 230$ nm) was investigated by detecting the nascent CH_3 fragments in their ground state ($v = 0$) by (2+1) REMPI through the $3p$ Rydberg state. The dissociation of acetone to CH_3 and CH_3CO fragments is not direct and proceeds *via* three pathways corresponding to three spectral regions of the excitation wavelengths. In region 1 (333.5 nm$\geq \lambda_{pump} \geq$ 305.3 nm), acetone is excited to the S_1 state followed by internal conversion to the S_0 state with unimolecular decay on it. Acetone excited in region 2 (305.3 nm$\geq \lambda_{pump} \geq$ 260 nm) dissociates over a small barrier on the T_1 surface ("tight" transition state). The height of the barrier was measured to be ≈ 4700 cm^{-1}. In region 3 ($\lambda_{pump} \leq 260$ nm), secondary dissociation reaction $CH_3CO^* \rightarrow CH_3+CO$ was observed. The α-C-C bond dissociation energy was measured to be $D_0^0 = 29\ 090 \pm 250$ cm^{-1}.

The same experiments were carried out on acetone-$d6$ by probing the CD_3 fragments. Isotopic substitution did neither demonstrate any noticable effect on the photodissociation dynamics nor on the α-C-C bond dissociation energy. This was interpreted as that the deuteration decreases the zero-point energy of acetone in the T_1 state and in the transition state. The rotational energy of the molecule itself and its internal rotors might lower the effective T_1 barrier height. The dissociation limit of acetyl-$d3$ was affected by the deuteration. The dissociation limit of acetyl-$d3$ was estimated to be $6\ 832 \pm 564$ cm^{-1}, that in acetyl-$h3$ is known to be 5 945 cm^{-1}. The increase upon deuteration may partially reflect the longer lifetime of the acetyl-$d3$ radical toward unimolecular dissociation.

The photolysis of methyl ethyl ketone *via* (a) $CH_3C(O)C_2H_5 + h\nu \longrightarrow CH_3+C_2H_5CO^*$ and (b) $CH_3C(O)C_2H_5 + h\nu \longrightarrow C_2H_5+CH_3CO^*$ channels was studied by probing CH_3 *via* (2+1) REMPI for reaction (a), and C_2H_5 by (1+1) REMPI through the $3s$ Rydberg state for reaction (b). The ion distribution was found to be independent of λ_{pump}. The present results do not provide enough data for a quantitative analysis. Further experimental and theoretical investigations would be of great interest.

Zusammenfassung

Die Photodissoziationsdynamik von *trans*-Methylnitrit und anderen, atmosphärisch relevanten Alkylketonen wurde mittels Photofragment-Geschwindigkeitskartographie untersucht.

Die Photolyse von *trans*-Methylnitrit wurde im S_1-Zustand verfolgt, wobei die N=O Streckschwingung 0 oder 1 Quant angeregt war. Die erzeugten NO-Fragmente wurden durch (1+1)-REMPI sowohl im Vibrationsgrundzustand als auch mit $v'' = 1$ und $j'' = 33.5$ detektiert. Zwei Dissoziationskanäle wurden beobachtet. 1) Es erfolgt eine schwingungsspezifische, nicht-adiabatische Prädissoziation oder 2) ein adiabatisches Tunneln durch eine Potentialbarriere im S_1-Zustand. Die O-NO Bindungsdissoziationsenergie wurde zu $D_0^0 = 13\,560 \pm 200$ cm^{-1} und die Lebensdauer des angeregten Zustand zu $\tau \leq 350$ fs bestimmt.

Die Photodissoziationsdynamik von Aceton-$h6$ wurde zwischen 340 und 230 nm unterzucht. Es wurden die bei der Photodissoziation entstandenen CH_3 Fragmente im Schwingungsgrundzustand durch ein (2+1)-REMPI über den 3p-Rydberg-Zustand nachgewiesen. Die Dissoziation von Aceton in CH_3 und CH_3CO erfolgte nicht direkt, sondern abhängig vom Anregebereich über drei verschiedene Kanäle. Im Bereich von 333.5 bis 305.3 nm kehrte das photoangeregte Aceton durch Interne Konversion in den S_0-Grundzustand zurück. Zwischen 305.3 und 260 nm erfolgte der Dissoziationschritt über einen Übergangszustand entlang einer kleinen Energiebarriere im T_1-Zustand ("tight" transition state), deren Höhe auf ≈ 4700 cm^{-1} extrapoliert wurde. Bei Anregewellenlängen $\lambda_{pump} \leq 260$ nm wurde ein zusätzlicher, sekundärer Weg beobachtet, der über die Reaktion $CH_3CO^* \rightarrow CH_3+CO$ verlief. Die α-C-C Bindungsdissoziationsenergie wurde zu $D_0^0 = 29\,090 \pm 250$ cm^{-1} bestimmt.

An Aceton-$d6$ wurden vergleichbare Experimente durchgeführt und das CD_3 Fragment detektiert. Es konnte kein Isotopeneffekt beobachtet werden, so dass angenommen wurde, dass die Deuterierung sowohl die Nullpunktsenergie des T_1-Zustand als auch die des Übergangszustands absenkt. Die Barrierenhöhe im T_1-Zustand könnte durch die Gesamtrotationsenergie des Moleküls und seine internen Rotatoren gemindert sein. Durch die Deuterierung wurde eine Verschiebung der Dissoziationsgrenze für Acetyl-$d3$ auf $6\,832 \pm 564$ cm^{-1} abgeschätzt, während die des Acetyl-$h3$ bei 5 945 cm^{-1} liegt. Diese Zunahme könnte der längeren Lebensdauer des Acetyl-$d3$ Radikals zugeschrieben werden.

In Methylethylketon liegen zwei Photolysekanäle vor: (a) $CH_3C(O)C_2H_5 + h\nu \longrightarrow CH_3+C_2H_5CO^*$ und (b) $CH_3C(O)C_2H_5 + h\nu \longrightarrow C_2H_5+CH_3CO^*$. Ersterer wurde anhand der entstandenen CH_3 Fragmente durch ein (2+1)-REMPI untersucht. Bei letzterem wurden C_2H_5 Fragmente durch ein (1+1)-REMPI über den 3s-Rydberg-Zustand detektiert. Es wurde keine Abhängigkeit von λ_{pump} gefunden. Die vorliegenden Daten erlaubten jedoch keine quantitative Analyse, hierzu wären weitere Experimente und theoretische Arbeiten notwendig.

Contents

List of Figures

List of Tables

1 Introduction

The study of the dynamics of photodissociation processes provides insights into one of the most basic chemical phenomena. The theory needed is extremely challenging and involves the most advanced theoretical and computational techniques. The great help for our understanding of primary photophysical and photochemical processes has been provided by the advancement of laser spectroscopy in combination with the supersonic molecular beams technique in the last decades. The continuously improving experimental techniques and equipment make it possible to excite molecules selectively and to study their time evolution, and to carry out state-specific detection of dissociation products. Beyond their fundamental importance, photodissociation processes play an important role in the Earth's atmosphere and atmospheres of other planets, and in the cooler regions of the stars [1, 2, 3, 4, 5, 6], and also in some biological processes [7, 8].

Optical excitation of molecules by absorption of one or more photons increases the amount of internal energy, which can be released in the form of heat or radiation (collisional or radiative decay) or can lead to chemical change (photodissociation, photoisomerization, or photoionization). The goal of understanding photodissociation processes is to fully describe the possible outcomes: The photoexcitation step and its influence on the photofragment formation, the molecular bond breaking process, the lifetimes of the intermediates, the nature of the primary and may be secondary photofragments, the energy partitioning among translational and internal degrees of freedom of the fragments, as well as the quantum state, in which fragments were formed during the photodissociation of the parent molecule.

Photodissociation can follow different pathways. Figure 1.1 schematically shows the most common of them for the dissociation of an ABC molecule. In Fig. 1.1 (a), the photon excites the molecule from the ground to a higher repulsive electronic state, from which it dissociates. The initial excitation is usually carried out with low intensity and narrow bandwidth, which can ensure that the photon creates a single upper electronic state. The dissociation is fast (10^{-12} s $\geq \tau_{S_1} \geq 10^{-14}$ s) and occurs within one rotational period of the molecule. In (b), the excited state is bound with respect to the reaction coordinate R but is coupled to the repulsive state (for example, by intersystem crossing, ISC), from which the excited molecule will decay. The rate of dissociation depends on the coupling between the two states. Figure 1.1 (c) demonstrate another type of indirect dissociation. The excited state potential energy surface has a well and a barrier, which prevent the excited molecule from instant dissociation. The barrier might be considered as the result of an avoided

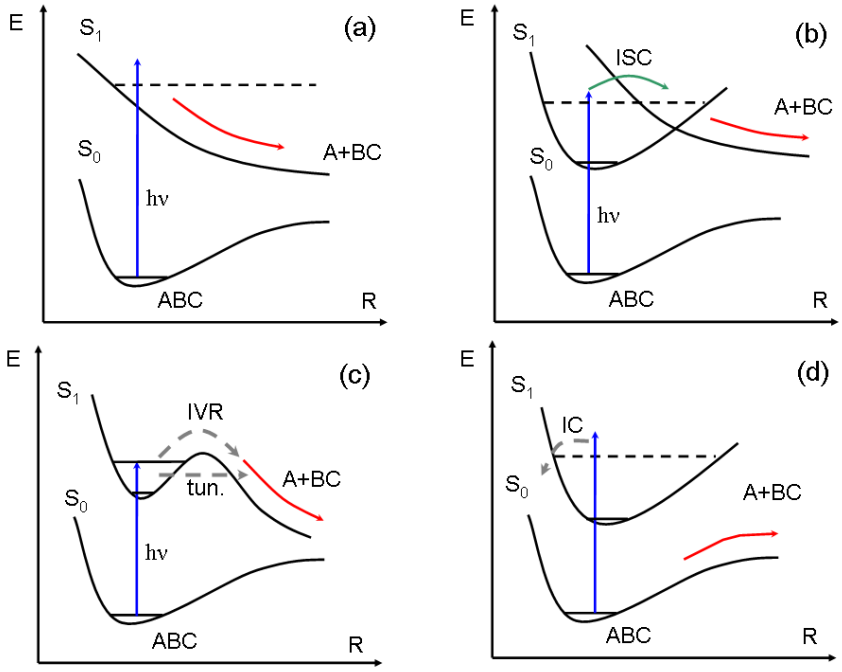

Figure 1.1: Schematic illustration of different types of photodissociation processes: (a) Direct photodissociation with a single photon, (b) indirect dissociation by electronic predissociation, (c) vibrational predissociation, and (d) unimolecular reaction. R is the dissociation coordinate.

crossing with a higher electronic state. The photon excites a quasi-stable state. The excited molecule can dissociate either by tunneling through the barrier or by internal vibrational energy redistribution (IVR) between the various vibrational degrees of freedom. The excited state lifetime depends on the tunneling rate or the IVR efficiency. Such a type of indirect photodissociation is called vibrational predissociation. The photodissociation of methyl nitrite (CH_3ONO) and some simple ketones studied in the present work (acetone ($(CH_3)_2CO$) and methyl ethyl ketone ($CH_3C(O)C_2H_5$)) follows just this mechanism. Additionally, there is another type of indirect photodissociation relevant to the present work as shown in Fig. 1.1 (d), where the photon first excites a bound electronic state, which subsequently decays following a transition to the lower electronic state. This dissociation pathway produces a highly excited vibrational-rotational quantum level above the dissociation threshold of the electronic ground state, which eventually breaks apart.

Many techniques for sample preparation and photodissociation have been developed over the last century. Introduction of molecular beam cooling technology let experimentalists prepare the molecules of interest in their lowest electronic and rovibrational states. Upon optical excitation of a sample, each photophysical process that can occur requires a proper detection technique. Laser spectroscopy provides an enormous choice of detection methods. Among them, velocity mapped ion imaging (VMI) in combination with resonance enhanced multi-photon ionization (REMPI)

is one technique that can provide such experimental data as internal state and kinetic energy distributions of all particles involved (neutral or ionic parent molecules and fragments), branching ratios between the possible dissociation channels, angular resolved distribution of all channels in space, lifetimes of the excited species, product alignments in space, and other vector correlations between fragment velocity, angular momentum and transition dipole moment [9].

This thesis deals with studies of the photodissociation dynamics of some simple ketones and VMI is an appropriate technique for a such purpose. The main focus of the work was on the photodissociation dynamics of simple ketones, such as acetone-$h6$, acetone$-d6$ and methyl ethyl ketone. Such a choice is conditionated by recent information on the role, which these molecules play in the Earth's troposphere [10, 11]. Additionally, the state selective photodissociation dynamics of the *trans*-methyl nitrite isomer was studied by velocity map imaging. This work was done to complete the investigations on *cis*-methyl nitrite which were done earlier in our research group and answer the question about the correct assignment of the origin of the $S_1 \leftarrow S_0$ transitions of the methyl nitrite isomers and, thus, the correct interpretation of the photodissociation mechanism. All studied species are shown in Fig. 1.2.

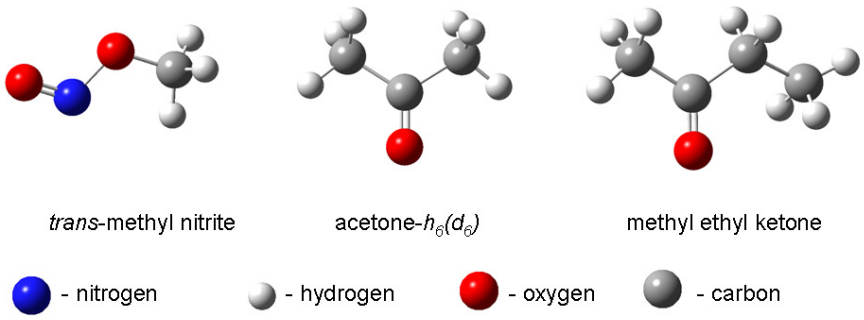

Figure 1.2: Chemical structure of the investigated molecules.

Methyl nitrite exists in two isomeric forms, the *cis*- and *trans*-isomers, with the former being thermodynamically more stable [12, 13]. The photodissociation of methyl nitrite induced by excitation into the first absorption band between $\lambda = 300 - 400$ nm has been studied intensively for many decades by many groups [14, 15, 16, 17, 18, 19, 20]. Of primary interest are the NO and CH_3O internal energy distributions and their dependences on the excitation energy and the initial vibrational state. Such information can provide insight into the dissociation dynamics and the multi-dimensional potential energy surface of the excited electronic state. The dissociation dynamics of methyl nitrite provides an interesting test for the theory of photodissociation. The question is to establish the correct pathway

for photodissociation, the determination of which strongly depends on the correct assignment of the UV absorption spectrum of methyl nitrite.

The UV/Vis absorption spectrum exhibits two absorption bands. The first band at $\lambda = 400 - 300$ nm is due to the $S_1 \leftarrow S_0$ transition and shows a progression of bands. This vibrational progression can be observed due to a shallow barrier on the S_1 excited state, which prevents instant dissociation after excitation to this state [21]. Tarte was the first who realized that the UV absorption spectrum consists of bands originating from *cis*- and *trans*-isomers and assigned the progression to the N-O stretching mode ν_3 in the parent molecule. The origin of the electronic transition of the *trans*-isomer was placed at $\lambda = 387$ nm and that of the *cis*-isomer at $\lambda = 381$ nm [22]. While the assignment of the vibrational progression to the N-O stretching mode is undebated, an alternative assignment of the origin of the electronic transition was given by Pfab, who based his assignment on the temperature dependence of the band intensities. Pfab's alternative assignment places the origin of the electronic transition of the *cis*-isomer at 365 nm and ascribes the red part of the UV absorption spectrum exclusively to the *trans*-isomer [23, 24].

Calculations demonstrated two different decay mechanisms of the photo-excited S_1 state of methyl nitrite. Accepting Tarte's assignment of the vibrational progression, these mechanisms are as follows: 1) The methyl nitrite molecule can decay *via* vibrational predissociation, *i.e.*, *via* a non-adiabatic transition, where the vibrational excitation of the N=O chromophore v^* converts into the vibrational energy of the NO fragment v'' with losing one vibrational quantum, so that $v'' = v^* - 1$; 2) Alternatively, dissociation can take place *via* a vibrationally adiabatic process, *i.e.*, with conservation of the vibrational excitation in the NO fragment ($v'' = v^*$) [25]. The first mechanisms would be different, if Pfab's assignments is choosen as the right one, namely, methyl nitrite would decay so that the vibrational excitation of the N=O chromophore v^* converts into the vibrational energy of the NO fragment v'' with one additional vibrational quantum, probably from the conversion of the electronic excitation, so that $v'' = v^*+1$. The second mechanism remains unalterated (dissociation *via* a vibrationally adiabatic process).

An enormous amount of researches were done on *cis*-methyl nitrite, but just a little is known about the photodissociation dynamics of its *trans*-isomer. The present work was invoked to complete the VMI studies done in [26] and elucidate the problem of the right assignment of the vibrational progression in the UV absorption spectrum.

Another and the main focus of this thesis is the study of the photodissociation dynamics of atmospherically relevant alkyl ketones in the near UV. Acetone and methyl ethyl ketone are typical molecules among a wide variety of aliphatic carbonyl compounds which are of great interest from a photochemical point of view. Beyond

their fundamental importance, these molecules were shown to play an important role in the Earth's atmosphere, as sources of OH and HO_2 radicals [10, 11, 27, 28].

The photodissociation of acetone and methyl ethyl ketone is the prototypical Norrish type-I reaction. Norrish and coworkers [29] realized that the photoexcitation of acetone to the first absorption band results in its dissociation by breaking of the α-C-C bond and yields such photofragments as ethane (C_2H_6), which was built by recombination of two methyl radicals (CH_3), and carbon monoxide (CO). The initial products proceed to form final products by a variety of secondary reactions [30]. Later, this reaction was called "Norrish type-I reaction", as a dedication to the correct interpretation of acetone photolysis and further intensive studies done by Norrish, who also pointed out the possibility that the acetone photolysis can be "stepwise" or "concerted". In the literature, the accepted definitions of the above mentioned reaction pathways are as follows. A *concerted* reaction is one that takes place in one kinetic step and needs not to be *synchronous*. A *synchronous* reaction proceeds simultaneously in one step with equal rates. A *stepwise* reaction takes place in several kinetically different steps *via* stable intermediates. Comprehensive experimental and theoretical investigations have clearly shown a "stepwise" dissociation mechanism of collision-free acetone molecules excited either to the S_1 or to the S_2 state resulting in methyl and acetyl photofragments [31, 32, 33, 34, 35, 36, 37].

A lot of data are available for the acetone photolysis reaction, leading to a detailed proposed mechanism. The photoexcitation of acetone within the first absorption band populates the S_1 state, which is efficiently coupled to the triplet T_1 state, and less efficiently to the S_0 state. After ISC, acetone molecules are placed on the triplet state, which possesses a low barrier, caused by an avoided crossing with the T_2 state. Once acetone molecule overcomes this barrier, it will dissociate.

Early work concentrated mainly on bulk samples, primarily in the gas phase. Data on the photodissociation of isolated acetone became available after the advent of modern techniques, such as supersonic jet cooling. The key processes both for the photodissociation of non-collisional samples $(1.1 - 1.2)$ and for acetone in the bulk gas phase $(1.1 - 1.7)$ are summarized below:

$$(CH_3)_2CO + h\nu \longrightarrow CH_3 + CH_3CO^* \tag{1.1}$$
$$CH_3CO^* \longrightarrow CH_3 + CO \tag{1.2}$$
$$2CH_3 \longrightarrow C_2H_6 \tag{1.3}$$
$$2CH_3CO \longrightarrow (CH_3CO)_2 \tag{1.4}$$
$$2CH_3CO \longrightarrow CH_2CO + CH_3CHO \tag{1.5}$$
$$CH_3 + CH_3CO \longrightarrow (CH_3)_2CO \tag{1.6}$$
$$CH_3 + CH_3CO \longrightarrow CH_4 + CH_2CO \tag{1.7}$$

In photochemical reactions carried out in bulk gas phase at $T = 298$ K, some nascent acetyl radicals are cooled by collisions and their concentration is high enough to

make the noticable contribution to the recombination and other reactions. Under collision-free conditions, hot nascent photoproducts will usually undergo secondary decomposition, if their energy exceeds the dissociation thresholds. Knowledge of the photolysis quantum yield of collision-free acetone and the internal energy distributions of the nascent fragments is very important, because such information dictates the unimolecular decay rate of acetyl in competition with the collisional deactivation with N_2 and the reaction with O_2 present in the Earth's atmosphere. N_2 is chemically inert, but O_2 reacts readily with many free radical species or can deactivate the vibrationally excited nascent photoproducts. In the troposphere, acetone is photolysed by the UV light of the Sun and yields methyl and acetyl radicals. The latter radical reacts with O_2 to produce peroxylacetyl radical in relative yields of $\sim$ 100% [38]. In its turn, peroxylacetyl reacts reversibly with NO_2 to produce peroxyacetylnitrate (PAN) [39]. All these species are important components of photochemical smog and air pollution [40]. Also, further reactions of the peroxyacetyl radical lead to production of OH radicals, which were shown to be main products of the $CH_3CO + O_2$ reaction [41, 42]. The hydroxyl radical is often referred to as the "detergent" of the troposphere, because it reacts with many pollutants, often acting as the first step in their removal [43]. Therefore, even a moderately large OH yield in the $CH_3CO + O_2$ reaction might give rise to significant effects for the Earth's atmosphere.

The present work sheds more light on the internal energy distribution of the nascent fragments of the photolysis of acetone and methyl ethyl ketone (MEK). The latter ketone does not have a symmetric α-C-C bond and can dissociate *via* two different channels:

$$CH_3C(O)C_2H_5 + h\nu \longrightarrow CH_3 + C_2H_5CO^* \tag{1.8}$$

$$CH_3C(O)C_2H_5 + h\nu \longrightarrow C_2H_5 + CH_3CO^* \tag{1.9}$$

The MEK photodissociation dynamics under this aspect is an interesting subject for the photochemical investigation and the results, obtained in the present work, are really surprising, compared to those of the acetone photolysis.

The present Thesis is organized in four chapters. The introduction is followed by an Experimental Chapter explaining the crucial technical aspects of the time-of-flight mass spectrometer and velocity map imaging apparatus used in the present work, as well as the procedure for the data analysis. Continuing, Chapter 3 ("Results and Discussion") is dividing into sections summarizing the current state of research for each molecule and presenting the measured results and their discussion. Chapter 4 ("Summary") underlines the conclusions drawn for the respective molecules.

2 Experimental

This Chapter describes the experimental setup which has been used in this work. It is divided into the five parts: Laser systems, supersonic molecular beam expansion, time-of-flight mass spectrometer, velocity map imaging apparatus, and a description of the experimental data analysis procedures.

2.1 Laser Systems

This section contains a description of the nanosecond pulsed laser systems used in the present experiments. All lasers were operated at a repetition frequency of 20 Hz. A variety of laser systems were available which allowed the production of nanosecond laser pulses over a wide range of wavelengths:

- A XeCl Excimer Laser EMG 201 (Lambda Physics), with a pulse length of 10 ns, and pulse energies of 220 - 450 mJ/pulse at a wavelength of 308 nm was used to pump the dye lasers (see below).
- A Nd:YAG Laser SpitLight 1200 (InnoLas). The fundamental of 1 064 nm (1 200 mJ/pulse) had a pulse length of 7 ns and horizontal polarization. The Q-switching was achieved by a Pockels cell and a polariser. The fundamental frequency could be doubled or tripled by a single type II KTP crystal or a combination of type II KTP and type I KDP crystals, respectively, to obtain pulses either at $\lambda = 532$ nm with a pulse energy of 600 mJ/pulse and vertical polarization or at $\lambda = 355$ nm with an energy of 300 mJ/pulse and horizontal polarization. The output power of the generated harmonics could be varied by the adjustment of the amplifier flash-lamp voltage and the Q-switch delay. Both wavelengths were used to pump the dye lasers. The laser was controlled by the software provided by InnoLas.
- Two dye lasers FL 3002E (Lambda Physics). The standard bandwidth of $0.2 - 0.4$ cm^{-1} could be improved up to 0.04 cm^{-1} by an intracavity Fabry-Perot etalon. The first dye laser was pumped with 355 nm (150 mJ/pulse) or 308 nm (220 mJ/pulse). The second dye laser was pumped at 532 nm (110 mJ/pulse). A variety of dyes and solvents were used to generate the specific wavelengths in the spectral region of interest. Additionally, the fundamental frequency of the dye laser output could be frequency doubled by using suitable second harmonic generation crystals. The output power of the dye lasers could be adjusted with a shutter, which partially blocked the energy of the pump

laser beam. The typical output power of the dye laser usually ranged from 10 to 30 % of the pump power, depending on the pump source and dye.

The polarization of the dye laser output beams was adjusted to vertical by a combination of $\lambda/2$ plates and Wollaston prisms, so that the polarization vectors lie in the plane of the MCP detector (see Fig. 2.1 and Fig. 2.7)

For the photolysis of CH_3I (CD_3I) excitation wavelengths of λ_{pump} between 333.5 and 286 nm and probe wavelengths of λ_{probe} =333.5 or 286 nm were used. The pump wavelengths were used for a molecule photolysis and the probe wavelengths were used in REMPI detection of the photofragments. The photolysis of CH_3ONO was studied using λ_{pump} = 388 - 374.5 nm and λ_{probe} = 224.7 or 234.5 nm. The photodissociation dynamics of acetone-*h*6, -*d*6 and methyl ethyl ketone was studied at excitation wavelengths of $\lambda_{pump} = 333.5 - 239$ nm and a probe wavelength of λ_{probe} = 333.5 (333.8) nm for the REMPI detection of the CH_3 (CD_3) fragments or λ_{probe} = 242 nm in the case of methyl ethyl ketone, where the C_2H_5 radical was probed.

In all cases, the pump laser beam was focused into the molecular beam with a quartz lens of 500 mm focal length and the probe beam was focused with a quartz lens of 300 mm focal length. The output wavelengths of the dye lasers were controlled by pulsed wavemeter (Burleigh WA5500, resolution $\Delta\nu = 0.3$ cm^{-1}).

2.2 Supersonic Molecular Beam Expansion

By using the molecular beam technique, not only collision-free conditions, but also drastically decreased translational, vibrational and rotational temperatures of sample molecules of interest in the molecular beam expansion could be achieved [44, 45].

The molecular beam setup has been described in detail in Ref. [46]. Briefly, the gas mixture consisting of the vapors of the substance of interest and a carrier gas (He or other inert gases), were expanded through a pulsed nozzle (General Valve, Series#9) into the entrance part of a differentially pumped vacuum setup (see Fig. 2.4), forming a molecular beam. The nozzle (diameter of 0.5 mm) was positioned axially $\approx 30 - 50$ mm in front of a nickel skimmer (Beam Dynamics, model 2; 0.5 mm aperture), connecting two vacuum chambers. The nozzle adjustment was performed by a xyz-translation stage. Therefore, only the homogeneous inner part of the molecular beam were carried into the second vacuum chamber, where the optical excitation was performed between the repeller and extractor plates of a Wiley-McLaren ion optics. The opening time of the nozzle was controlled by a power supply (General Valve, Iota One). The skimmed molecular beam passed centrally through a hole in the first electrode ("repeller") of the ion lens assembly. The valve nozzle, the skimmer, and the ion optics apertures formed a joint line (see the upper trace of Fig. 2.2) As illustrated in Fig. 2.2, the velocity distribution $P(v_z)$

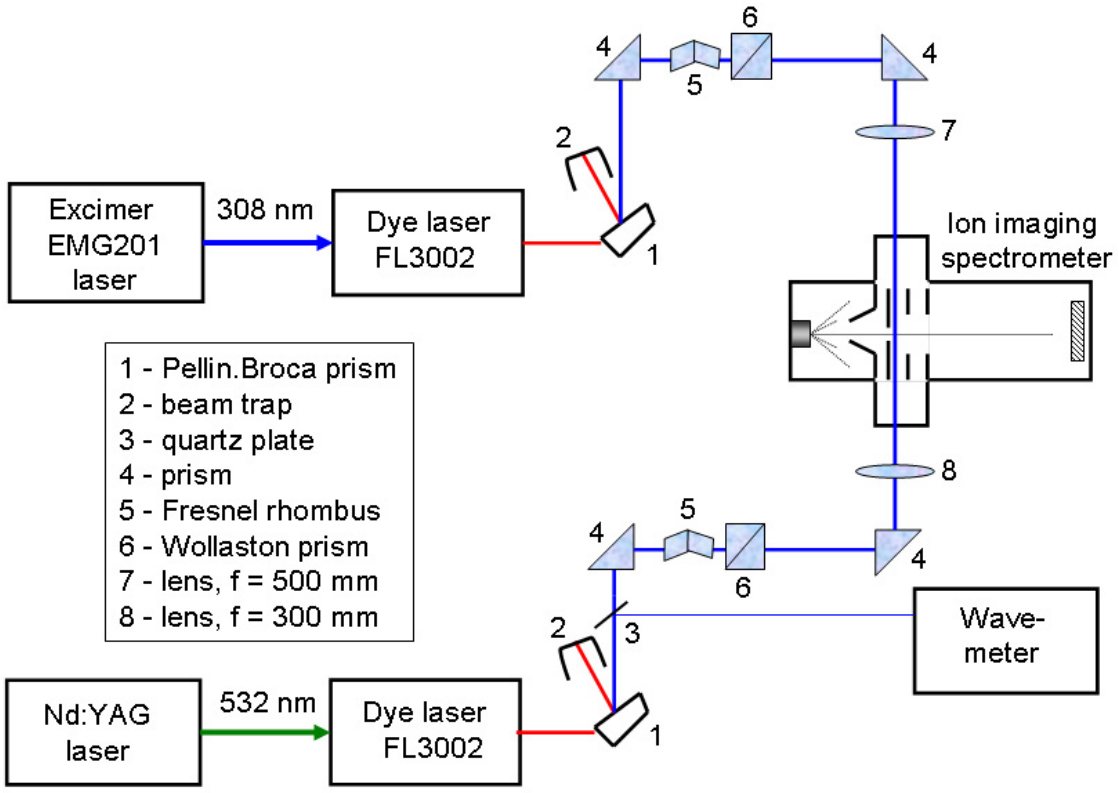

Figure 2.1: Laser systems and optical setup used in the present work.

of the molecules along the flight axis toward to the detector, is modified significantly in the case of the molecular beam expansion.

2.3 Time-of-Flight Mass Spectrometry (TOF-MS)

2.3.1 Basic Concepts

The time-of-flight (TOF) mass spectrometry is an essential part of the velocity map imaging technique. It has become a standard scientific and analytic procedure [47].

A simple TOF-MS setup consists of: an ion source, a field-free drift zone, and an ion sensitive detector (see Fig. 2.3). The generated ions are accelerated tpwards the detector by an electric field $\overrightarrow{E}$. Each ion travels through a field-free time-of-flight distance with a distinctive velocity, depending on the mass-to-charge ratio m/z, and therefore arrives at the detector after a defined flight-time. Since ions, which fragment in the drift zone, *i.e.*, after they have left the acceleration field, arrive at the same time-of-flight as their parent ions, simple TOF-MS setups cannot distinguish this sort of fragmentation.

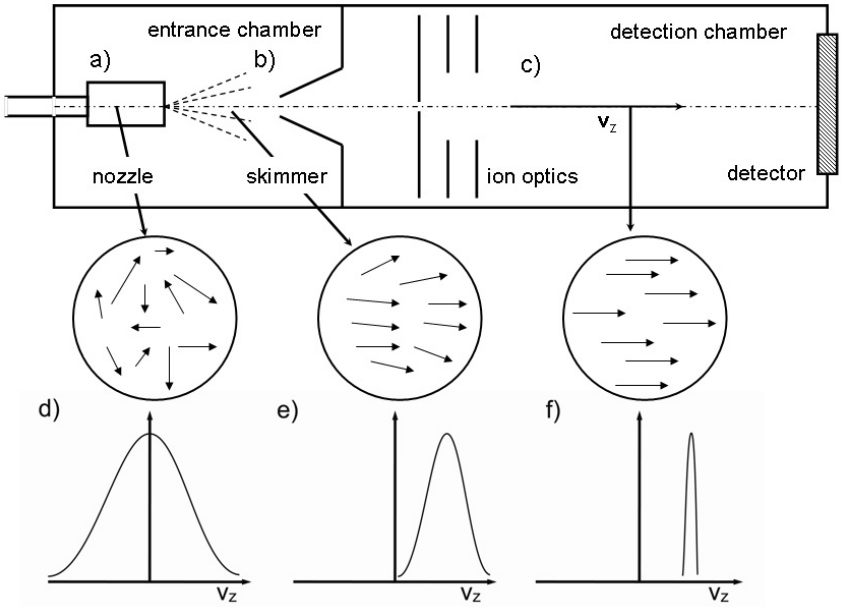

Figure 2.2: Molecular beam expansion in the velocity map imaging apparatus. The molecules are in thermal equilibrium initially (a and d). After expansion a modified distribution is formed (b and e). The skimmer cuts off all molecules, which velocities are not in z direction (c and f).

Inside the ion source, the ionization of the molecules, their acceleration and the focusing of the nascent ions onto the detector take place. This is achieved by so-called ion lenses (electrodes) set to different electric potentials, which create a specific electric field gradients (∇E) between them. The gradient depends not only on the supplied voltage but also on the geometry and the orientation of the electrodes. The resulting ∇E forms the forces which govern the ion trajectories, so that by manipulation of the electrode potentials, the way how the ions will be accelerated and focused can be controlled. While the first TOF-MS ion sources contained only one (∇E) and focusing was not possible there, more advanced ion sources consist of more than two electrodes, which solve the focusing problem by adjustment of the potentials (see Section 2.3.2.2). A sketch of the Wiley-McLaren ion optics used in the present work is shown in Fig. 2.5 in Section 2.3.2.2.

Ions of different masses are separated due to their differing velocities. This takes place in the field-free drift zone. The absence of the electric field in this zone is ensured by grounding of the time-of-flight tube.

To detect the incoming ions, multi-channel plates (MCPs) coupled to a phosphor screen with a coupled charge device (CCD) camera are commonly used. Higher impact velocity increases the sensitivity of the MCPs.

From the measurements of the intensity-time profile of the ions, the mass information can be calculated as follows: The force $\overrightarrow{F}$ affecting a charged particle in an electric

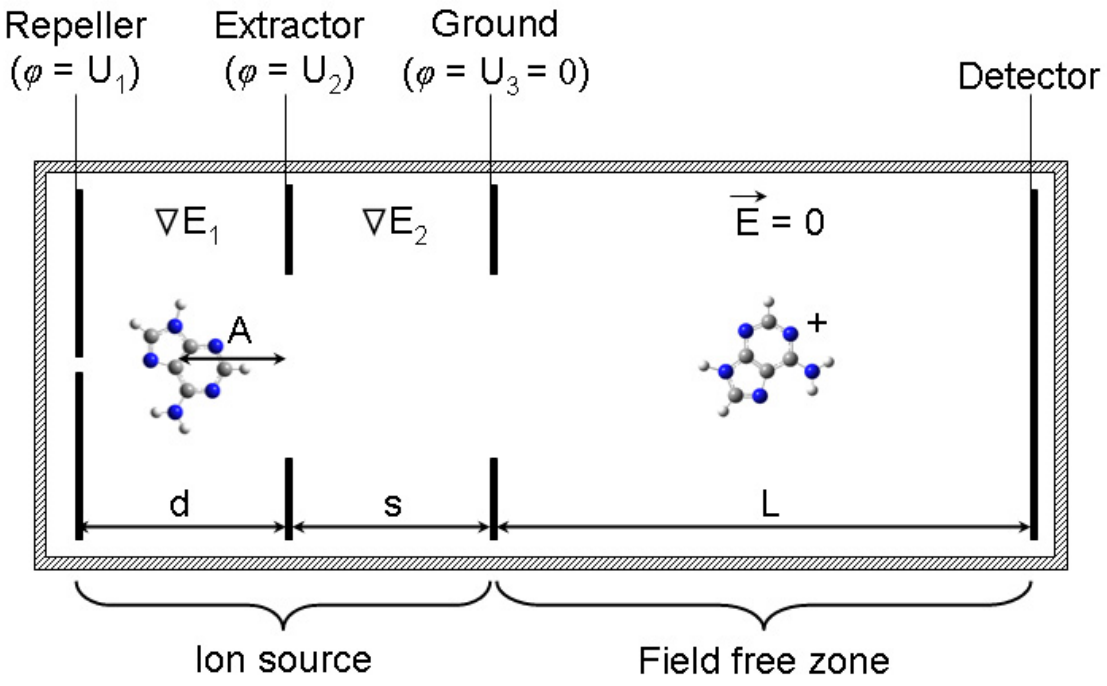

Figure 2.3: Sketch of a time-of-flight mass spectrometer. A is the point of ion formation. d and s are the distances between the repeller + extractor and the extractor and grounded electrodes, respectively. The field-free drift zone has a length L.

field $\overrightarrow{E}$ is given by

$$|\overrightarrow{F}| = ze|\overrightarrow{E}| = \frac{ze\Delta U}{d}, \tag{2.1}$$

where z is the charge number, e the elementary charge, and d the distance of the potential gradient ΔU. The particles are accelerated by the force $\overrightarrow{F}$ and leave the ion source with the kinetic energy

$$E_{kin} = \frac{mv^2}{2} = ze\Delta U = E_{pot}. \tag{2.2}$$

Equation 2.2 gives the mass-charge ratio as

$$\frac{m}{z} = \frac{2e\Delta U}{v^2} = \frac{2e\Delta U}{s^2} \cdot t^2, \tag{2.3}$$

From Eq. 2.3 it is obvious that m/z is proportional to the square of the time-of-flight, t^2. Thus, particles with the same charge, but different masses, are separated by their different arrival times at the detector. The factor $2e\Delta U/s^2$ depends only on the experimental settings and can be kept constant for all measurements.

2.3.1.1 Mass Resolution of a TOF-MS

The ratio between the full width at half maximum (FWHM) of the mass peak and its mass is the mass resolution $\Delta m/m$, which, in general, depends on five points:

1. The temporal separation, which can be increased by longer time-of-flight tubes. This follow directly from Eq. 2.3.
2. The temporal width of the starting ion packet. The shorter, the better is the resolution.
3. The size of the region, where the ions are formed. The smaller the region of ion formation, the less is the blurring of the resulting mass peaks. This can be reduced by the so-called space focusing, achieved by the ion optics (see Subsection 2.3.1.2).
4. The broadening of the ion kinetic energy distribution. This effect is commonly minimized by the energy focusing (see Subsection 2.3.1.3).
5. The rise time of the detector, which is limited by the quality of the MCP.

2.3.1.2 Spatial Resolution

The ionization point of the molecules in the ion source has a limited spatial extent and is usually much bigger than the size of the molecules and ions are formed with some initial spatial distribution, which decreases the mass resolution of the TOF-MS. Ions initially closer to the detector acquire less kinetic energy and are therefore eventually overtaken by ions which are initially further from the detector. A solution for this problem was suggested by Wiley and McLaren in 1955 [48], who developed a two-level gradient system with three electrodes: a repeller, an extractor and a grounded electrode, as shown in Fig. 2.3. Such a design allows molecules of the same mass to be detected simultaneously, independent from their place of formation by choosing optimal potential gradients between the repeller, extractor and ground electrodes.

The two-stage acceleration of the ions takes place between the three electrodes with the distances d and s. The potentials U_1, U_2 and U_3 at the electrodes create the homogeneous electric fields E_1 between repeller and exctracor and E_2 between extractor and grounded electrodes. The initial position of the ionization is A. The change in flight time, $\Delta T_{\Delta A}$, due to a small change ΔA in A about the center position between repeller and extractor, A_0, is given by

$$\Delta T_{\Delta A} = \sum_{n=1}^{2} \frac{1}{n!} \Big(\frac{d^n T(0,A)}{dA^n} \Big)_{A_0} (\Delta A)^n \tag{2.4}$$

where $d^n T(0,A)/dA^n(0,A)$ is the n^{th} derivative of T with respect to A, assuming that the initial ion energy is $E_0 = 0$ and the position is A, [48].

M_s, the measure of the space resolution, is the maximum value of m (a mass of an ion), for which $\Delta T_{\Delta A} \leq T_{m+1} - T_m$.

To find the length of the field free drift zone at which ions with initial value $A = A_0 \pm 0.5A$ pass each other (space focal plane), the following equation was obtained in [48]:

$$L = 2A_0 k_0^{3/2} \left[1 - \frac{s}{d} \frac{1}{k + \sqrt{k}}\right] \tag{2.5}$$

where

$$k = 1 + 2\frac{U_2}{U_1 - U_2}. \tag{2.6}$$

Eq. 2.5 and 2.6 allow to calculate the necessary voltages U_1 and U_2 to obtain spatial focusing for a given experimental setup (d, s and L).

2.3.1.3 Energy Resolution

The spatial focusing of the linear TOF-MS is further limited by the finite energy focusing. The approximation, of zero initial ion energy $E_0 = 0$, is not fulfilled in reality. This is due to the initial kinetic energy and the remaining angular distribution of molecules in the molecular beam, and because of the released part of the absorbed ionization energy as recoil kinetic energy.

For instance, consider ions of the same mass at position A having different velocity vectors v_+ and v_- with respect to the detector, with ions with v_- initially traveling opposite to the acceleration direction. These ions are slowed down first and then accelerated toward the detector. They need the turn-around time T_a to reach the initial starting point again, and the additional time T_a to catch up with those ions, which have started at A with v_+. The resolution limit of the TOF-MS is thus diminished, if $2 \times T_a > \Delta t$, where Δt is a time between adjacent mass peaks.

2.3.2 Experimental Setup for Time-of-Flight Mass Spectrometry

This section briefly reports on the experimental setup of the TOF mass spectrometer used in the present work.

2.3.2.1 Vacuum Equipment

The TOF-MS experiments were performed in an electro-polished stainless steel chamber, which is shown in Fig. 2.4) under ultrahigh vacuum (UHV) molecular beam conditions. The chamber was divided by a removable separating plate into two differentially pumped parts. Two water-cooled turbo molecular pumps (Pfeiffer, TPH 510 and LeyBold, Turbovac 151), which offer pumping speeds of 350 l/s and 210 l/s respectively, were used for evacuation.

The connection between the turbo pumps and the vacuum chamber could be individually sealed by two venting valves (VAT, 200 CF and 100 CF). The necessary

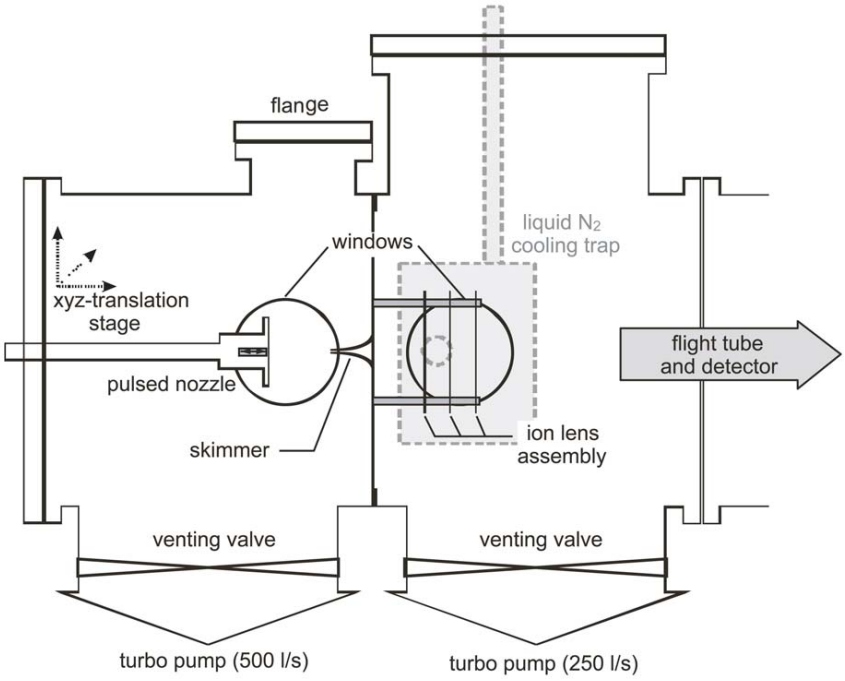

Figure 2.4: Sketch of the experimental setup of the TOF mass spectrometer. The entrance part of the vacuum chamber consisted of a pulsed nozzle, mounted on a xyz-translation stage, and a conical skimmer between the two differently pumped vacuum chambers. The ion lens assembly, the liquid nitrogen cooling trap, the flight tube and the detector are located in the detection part.

fore-vacuum was provided by two rotary vane pumps (Leybold, Trivac 253 and Pfeiffer, DUO10M) with a pumping capacity of 16 m^3/h and 12 m^3/h, respectively. To prevent oil exhalations in the chamber, molecular sieve (Leybold, Zeolith 13X) filled adsorption traps were inserted between the fore and the main pumps. Additionally, all devices were supplied by a power-guard, which turned off the electricity, if the pressure in the vacuum chamber exceeded $2 \cdot 10^{-5}$ mbar. The assembly provided a basic pressure of $1 \cdot 10^{-7}$ mbar in the entrance chamber and $2 \cdot 10^{-8}$ mbar in the detection chamber. Additionally, to decrease the background noise, a liquid nitrogen cooling trap surronded the ion optics. This improved the UHV pressure by one order of magnitude. The pressure was measured by gauges (Leybold, ITR100) at UHV pressure, and by two filament gauges (THERMOVAC Transmitters TTR 100) at higher pressure. The field free drift zone had a length of 1 m.

2.3.2.2 Ion Lens Assembly

The ion lens assembly used in the present work is shown schematically in Fig. 2.5. It consisted of three circular electro-polished stainless steel plates (Ø 70 mm, d = 0.5 mm), which were assembled at 15 mm distance on four threaded rods (M4, PVC). The repeller plate had a central hole of 2 mm diameter and the holes in the extractor and the ground plate were 20 mm.

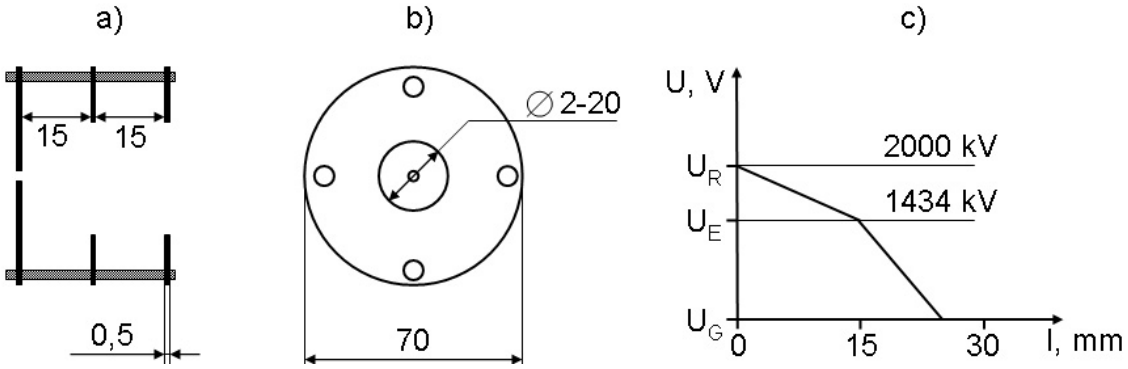

Figure 2.5: Sketch of the ion optics used in the present work (a and b). Supplied voltages and the corresponding potential field gradients are shown in (c). U_R, U_E and U_G denote the voltage on the repeller, extractor and grounded electrodes, respectively. All sizes are in mm.

The electrodes were fixed to the rods through insulating spacers between the plates, which have groove and tongue joints (for details see Fig. 2.5). Repeller and extractor were connected to two separate highly stable power supplies (FUG, HCE 35-6500), while the ground plate was conductively connected to the steel chamber. All cables were isolated on their whole length by glass tubes.

To improve the mass resolution of the TOF-MS, additionally a nickel mesh (Metal ThinParts, Transparancy 90%) covered the apertures of the electrodes (extractor and ground), only in the case of the acetone MS experiments, but not for the ion imaging experiments.

2.3.2.3 Sample Preparation

Helium carrier gas was passed through a glass reservoir, which contained the investigated sample. The concentration of the sample in the gas mixture was controlled by the carrier gas pressure and the temperature of the reservoir. In order to decrease the vapor pressure of the sample, the reservoir could be cooled down in a dewar with a mixture of ice, NaCl salt and water. The dwell time of the sample in front of the pulsed nozzle was minimized by drawing the waste by an additionally rotary vane pump (Alcatel, LS71) to decrease cluster formation. Tubes, joints and valves of HOKE GYROLOK type were used in the present work.

2.3.2.4 Detector and Data Acquisition

The detector consisted of two multi-channel plates assembled in chevron configuration (MCP; Hamamatsu F4294-07, Ø = 32.8 mm). The pore size was 10 μm, the channel bias was 12° to the perpendicular surface, and the distance between the channel centers was 12 μm. The gain over both MCPs at 2 kV was $0.289 \cdot 10^9$. The

MCPs were followed by a stainless steel hopper, which was connected directly to an oscilloscope (LeCroy, LT264).

For REMPI experiments the MCP output was connected to a fast gated integrator and boxcar averager (Stanford Research Systems). The boxcar integrator had a computer interface SR245, which was used for data transfer to a computer.

2.4 Velocity Map Imaging

Many experimental methods have been developed over the last decades for the study of molecular photodissociation dynamics. Among them is velocity map imaging (VMI), which was used in the present work. Since the first experiments performed on photolysis mapping by Solomon [49], the ion imaging technique has developed in a spectacular way [50], both from the side of preparation of the parent molecule as well as the detection methods.

In ion imaging, the total 2D projection of spatial distribution of the ionized photofragments is detected by means of a CCD camera. The resulting image comprises the kinetic energy distribution as well as the angular distribution. Both are extracted from the image using a reconstruction of the original 3D ion distribution from the 2D projection by reconstruction algorithms (see Section 2.4.4). The VMI method was originally developed by Eppink and Parker [9] and the basic principle will be briefly described here.

The dissociation of molecule AB by absorption of one or more photons can be regarded as the second half of a full reactive collision event:

$$AB + nh\nu \rightarrow (AB)^* \rightarrow A(\alpha) + B(\beta), \tag{2.7}$$

where $nh\nu$ is the energy of n photons with frequency ν, $(AB)^*$ represents the excited complex and the labels α and β specify the particular internal quantum states of the newborn products A and B, each of which can also be a molecule.

For a photodissociation process with one exit channel in which a parallel electronic excitation followed by a prompt axial dissociation, the product distributions lie on expanding Newton spheres in space as shown in Fig. 2.6, a so-called Newton diagram. The centre-of-mass (cm) velocity is determined by the thermal velocity of the parent molecule and, for the case of large kinetic energy release, can be neglected.

The probability for a one-photon absorption for an electric dipole moment transition is given by

$$P_{abs} \sim \cos^2(\Theta), \tag{2.8}$$

where Θ is the angle between transition dipole moment $\overrightarrow{\mu}$ and the polarization vector $\overrightarrow{E}$ of the photolysis laser. In the case of a prompt dissociation the photofragment angular distribution is entirely determined by the photo-excitation step and in

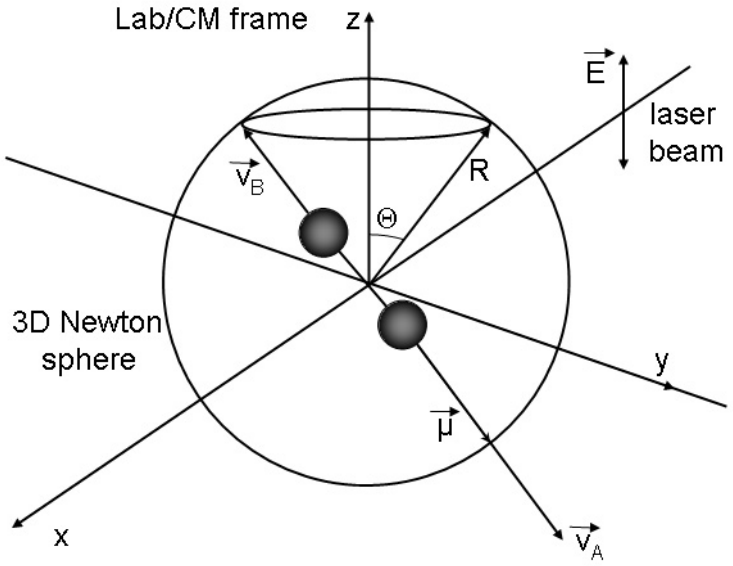

Figure 2.6: Newton sphere of a direct axial photodissociation process. The photofragments are distributed on expanding spheres (indicated for the B product). The spheres are cylindrically symmetric around the laser polarization $\overrightarrow{E}$.

case of a parallel transition, the recoil vector $\overrightarrow{v_B}$ lies parallel to the $\overrightarrow{E}$ vector. Using a linearly polarized photolysis laser, the resulting fragment distribution in space is anisotropic with respect to the angle Θ and cylindrically symmetric around the $\overrightarrow{E}$ vector of the excitation light.

2.4.1 Photofragment Speed Distributions

The conservation of energy and linear momentum yields the equations for the photofragment kinetic energy release in the reaction (2.7) [9]. The total kinetic energy release (TKER) of the reaction (2.7) can be calculated from the energy conservation law and is given by

$$T = T_A + T_B = E_{avail.} - E^A_{int} - E^B_{int} = nh\nu - D^0_0(AB) - E^A_{int} - E^B_{int}; \qquad (2.9)$$

where T_i is the kinetic energy of a fragment i ($i = A, B$), $nh\nu$ is the photon energy, $D^0_0(AB)$ is the A-B bond dissociation energy, $E_{avail.}$ is the available energy for the photofragments to be partitioned between their translational and internal degrees of freedom, and E^i_{int} is the fragment internal energy. Neglecting the thermal motion of the parent molecule AB, the conservation of momentum relates the velocity vectors of the fragments *via*

$$m_A \overrightarrow{v}_A + m_B \overrightarrow{v}_B = 0 \qquad (2.10)$$

The partitioning of the TKER among the fragments is, therefore, given by the fixed ratios

$$T_A = T \cdot \frac{m(B)}{M(parent)}, \tag{2.11}$$

and

$$T_B = T \cdot \frac{m(A)}{M(parent)}, \tag{2.12}$$

where M(parent) is the mass of the parent molecule, and $m(i)$ is the mass of fragment i.

Thus, by studying the kinetic energy (speed distribution) of either fragment, the TKER can be extracted, which allows to determine the bond dissociation energy and internal excitation of the fragment by Eq. (2.9). However, simultaneous determination of the internal energy distributions of both fragments is complicated because of the large amount of possible combinations. That is why the REMPI technique is widely used in VMI experiments, which allows a detection of one of the fragments in a specific quantum state and with specific internal energy. Then, the kinetic energy distribution of the detected fragment in that specific state reflects the correlated internal energy distribution of the co-fragment *via*

$$E^i_{int} = nh\nu - D^0_0(AB) - E^j_{int} - T, \tag{2.13}$$

with the internal energy of the co-fragment E^i_{int} and the internal energy of the detected fragment E^j_{int}.

2.4.2 Photofragment Angular Distributions

Details on the photo-excitation step, the following dynamical processes that lead to the bond cleavage and the ejection of photofragments can be extracted from the angular distribution of the nascent fragments [51]. If the parent molecule is excited through an electric dipole transition, the transition dipole moment $\overrightarrow{\mu}$ lies preferentially parallel to the electric vector $\overrightarrow{E}$ of the excitation light (see Eq. (2.8)), which leads to a preferential orientation of the excited parent molecules in space. Additionally, if the recoil time of the fragments is short compared to the rotational time of the parent molecule, like in the case of a direct dissociation, the fragments will have a $\cos^2\Theta$ distribution in case of a parallel transition and a $\sin^2\Theta$ distribution in case of perpendicular transition and the axial recoil of the diatomic molecule. For the electric transition of a mixed polarization or, if the transition dipole moment has a different angle to the molecular axis, or the dissociation is slow compared to the rotation of the parent molecule, the resulting angular distribution will be less anisotropic [9].

The general form of the photofragment distribution in a one-photon dissociation process was derived by Zare [51] and is given by

$$I(\Theta) = \frac{1}{4\pi}\left[1 + \beta\frac{1}{2}(3\cos^2\Theta - 1)\right], \tag{2.14}$$

where Θ is the angle between laser polarization axis and recoil velocity vector, and β is the anisotropy parameter. From Eq. (2.14) it follows that the angular distribution (and the subsequent vector correlation between $\overrightarrow{E}$ and $\overrightarrow{v}$) is characterized by only one parameter β, which ranges from -1 for a perpendicular transition to +2 for a parallel transition. If $\beta = 0$, the distribution is isotropic in space [9].

Generally, the anisotropy parameter is given by:

$$\beta = 2P_2(\cos\chi), \tag{2.15}$$

where $P_2(x)$ is the second-order Legendre polynomial [9] and χ is the angle between transition dipole moment and fragment velocity vector. The limiting values of β can only be obtained if the lifetime of the parent molecule in the excited state before dissociation (τ) is much shorter then the rotational period τ_{rot}. Otherwise, the anisotropy of the angular distribution reduces due to rotation according to

$$\beta = 2P_2(\cos\chi) \cdot \frac{\omega^2\tau^2 + 1}{4\omega^2\tau^2 + 1}, \tag{2.16}$$

where ω is the angular velocity of the parent molecule, τ its lifetime, and $(\omega\tau)$ is the average rotational angle. For very slow dissociation processes, when $\tau >> \tau_{rot}$, the anisotropy is therefore lowered by a factor of 4, but not completely to zero [9].

2.4.3 Experimental Setup for VMI experiments

The velocity map imaging apparatus is almost identical with the TOF-MS setup except: A shorter field free tube (length 351 mm) was used, non-meshed electrodes were used, and a different position sensitive MCP detector was inserted (see below). The schematic view of the VMI apparatus is shown in Fig. 2.7.

2.4.3.1 Position Sensitive Detector

The 2D position sensitive imaging detector consisted of a chevron double multi-channel plate phosphorescence screen assembly (Photek Limited, 40 mm) shown in Fig. 2.8. The pore size of the MCPs was 10 μm, the channel bias was 12°, and the distance between the channel centers was 12 μm. The gain over both MCPs at 1.6 kV was $\approx 1 \cdot 10^8$. The electron cascades from the MCP hitted a phosphorescence screen (visible diameter of 36 mm), which emitted light under electron collisions. These spots of light were monitored from the back through a quartz glass window by a coupled-charged device (CCD) camera (LaVision, 640x480 pixels of 6.34×4.75 μm^2, 12 bit). A standard P43 phosphor with an emission ranged from 370 to 680 nm and a maximum at 545 nm with luminescence decay period (intensity decreases down to 10 %) of $\approx$ 1 ms was used.

The MCPs and the phosphorescence screen could be attached at the end of the flight tube with a standard flange (NW100) as it is shown in Fig. 2.8. The power is

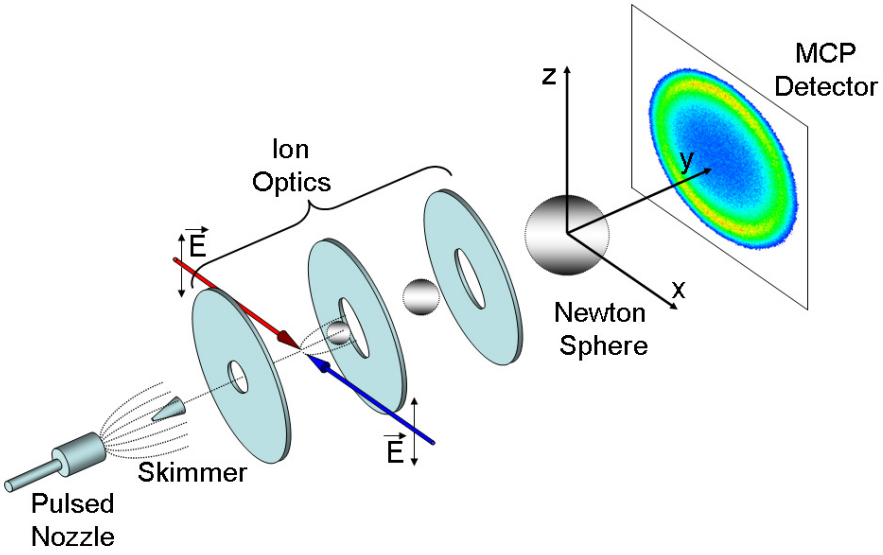

Figure 2.7: Schematic view of the velocity map imaging setup with coordinate system and MCP detector.

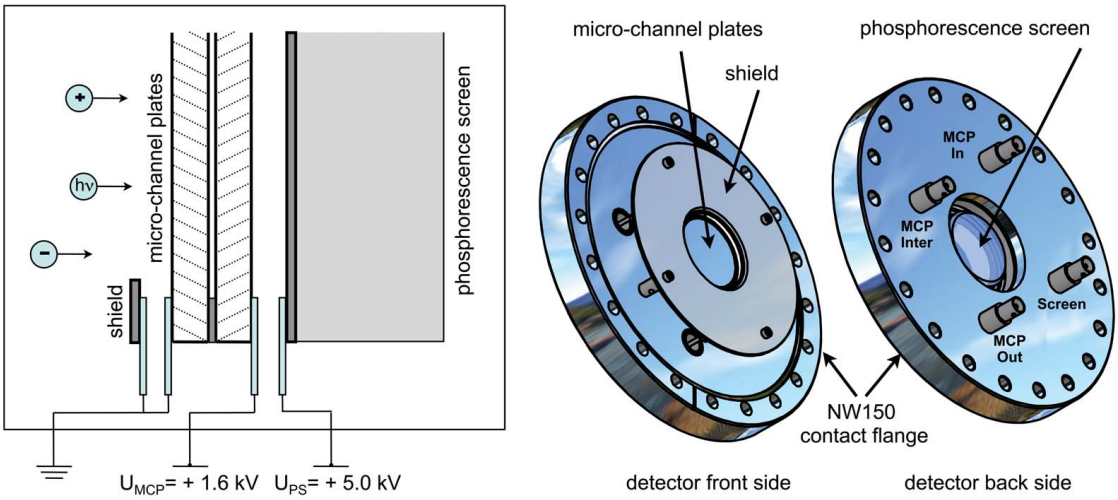

Figure 2.8: Sketch of the detector assembly consisting of two MCPs in chevron configuration followed by a phosphorescence screen. The assembly can be used for the position sensitive detection of electrons and ions.

supplied by two high voltage adapters (FUG, HCE 35-3500 and HCE 35-7000). To minimize the background signal from random photons and ions, the power supply of the MCPs was gated by a fast transistor switch (Behlke, HTS 31; minimum opening time of 30 ns).

The CCD camera was connected to the MCP assembly *via* a spacer of 160 mm length. The surface of the phosphorescence screen was imaged onto the CCD chip by a camera objective (1:8.4). The full frame rate of the camera was 30 (fps). The quantum efficiency reached 50 % at $\lambda = 545$ nm. The camera was controlled and readout *via* an A/D connection to PC. The camera control was performed by LaVision 3.1 software through a PCI-card (LaVision), and time synchronization of the MCP detector and the camera with the experiments was carried out by an external TTL puls, provided by a delay generator (Stanford Research System, DG535).

To improve the quality of the images, they were additionally processed with a centroiding and event counting algorithm provided with the commercial camera software DaVis (LaVision GmbH). Each event produces a light spot on the phosphor screen which corresponds to a typically 2-3 pixel wide spot seen by the camera, if the intensity of the spot was higher than the preset threshold. The algorithm analyses a 3×3 pixel area around each local maximum and calculates center of gravity, which is added as a single count at the appropriate pixel coordinate [52]. The complete image is obtained by accumulating such counts over 36 000 to 144 000 laser shots. In order to avoid multiple impacts onto the same position or blurring the image due to space charge effects, the pump and probe lasers were operated at low output powers (typically below 0.2 mJ/pulse, corresponding to a maximum of $10 - 40$ events per laser shot).

2.4.3.2 Reproduction Scale of the Camera System

The magnification factor of the CCD objective was determined by imaging a sheet of graph paper (1 mm grid) attached directly to the viewing window on the air side of the detector system. The paper was illuminated by a small photodiode. From this procedure, a common conversion factor for the vertical and horizontal directions for the camera of

$$1 \text{ pixel} \mathrel{\hat{=}} 84.5 \cdot 10^{-6} \text{ m},$$

was obtained. The spatial resolution of the velocity map images was determined by measuring the width of the detected ion peaks. The average peak width was 3.1 pixel ($\hat{=}$ 0.27 mm) at optimized space and energy focusing conditions.

2.4.3.3 Timing of the Components

Two delay generators (Stanford Research, DG535) controlled the timing of the experimental setup. Fig. 2.9 depicts the connections of all triggered components. The TTL pulses of the delay generator #2 operated at 20 Hz were used as master trigger. The triggered components were: The molecular valve, the Q-switch and flash lamp of the Nd:YAG laser, the excimer pump lasers, the fast transistor switch of the MCP detector and the PC readout the data from the CCD camera. The timing is shown schematically in Fig. 2.10.

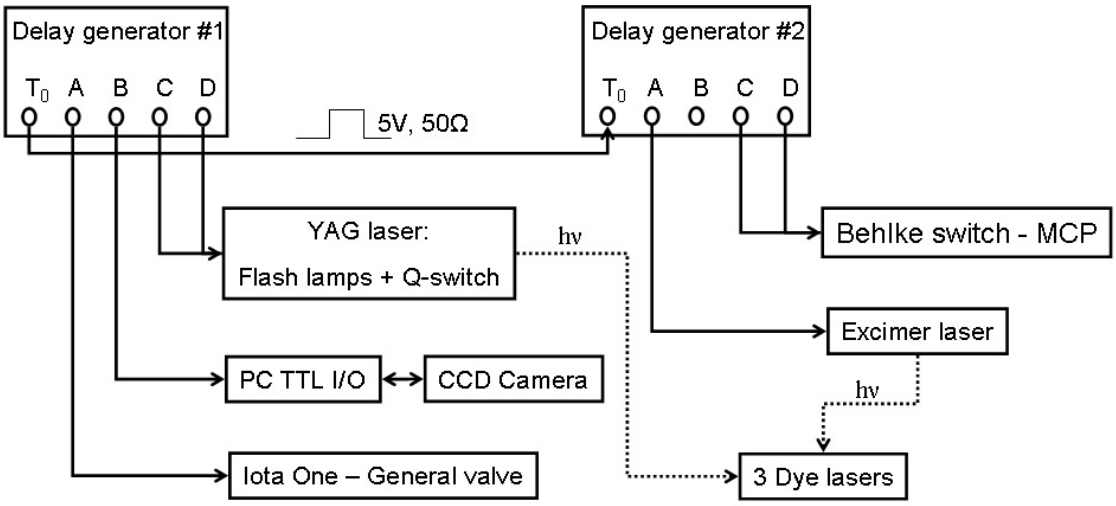

Figure 2.9: Control and timing of the velocity map imaging experiment by delay generators.

2.4.4 Data Analysis

The ion images collected in the VMI experiments are 2D projections of the 3D ion distributions formed in the photodissociation process. In order to analyse the 2D ion images quantitatively, the entire 3D velocity distribution has to be reconstructed Prior to processing, the experimental ion images have to be centered and in some cases also symmetrized with respect to the center line (2 fold symmetrization, [53])).

2.4.4.1 Abel Transformation

Traditionally, the so-called inverse Abel transformation has been used in ion imaging for reconstruction of the full 3D velocity distribution from its 2D projection on the detector. This algorithm uses the cylindrical symmetry of the image. The ion images possess cylindrical symmetry if the photodissociation processes is initiated and probed by vertically polarized pump and probe lasers, so that their electric vectors are parallel to each other and to the plane of the MCP detector (see Fig. 2.7). With the polarization axis along the z-axis (see Fig. 2.11)), the projection

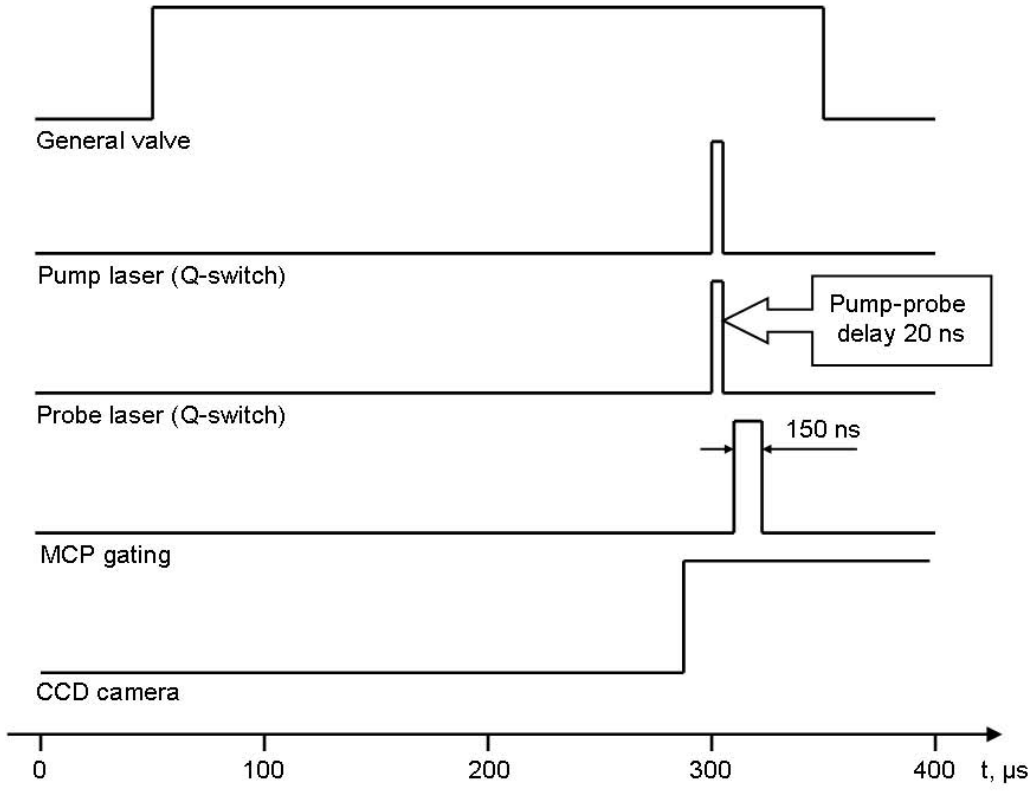

Figure 2.10: Schema depicting the connections between the triggered components of the velocity map imaging experiment and delay generators.

intensity $p(x, z)$ is related to the full 3D intensity $I(x, y, z)$ as follows:

$$p(x, z) = \int_{-\infty}^{+\infty} I(x, y, z)dy. \tag{2.17}$$

Considering only one row of the image along the x-axis with $z = z_0$ and $p(x, z_0) = p_{z_0}(x)$, and using the fact that the distribution is cylindrically symmetric around the z-axis, $p_{z_0}(x)$ is given by:

$$p_{z_0}(x) = 2 \int_0^{\infty} I(x, y, z_0)(\sqrt{x^2 + y^2})dy. \tag{2.18}$$

where $I(x, y, z_0)$ is a slice through the full distribution perpendicular to the symmetry axis z. Transformation of the integral (2.18) to polar coordinates by substituting $y = \sqrt{r^2 - x^2}$ gives:

$$p_{z_0}(x) = 2 \int_0^{\infty} \frac{I(r, z_0)r}{\sqrt{r^2 - x^2}} dr. \tag{2.19}$$

The Eq. 2.19 is called the Abel transformation of $I(r, z_0)$. The inverse Abel transformation, which can be used to reconstruct the original distribution $I(r, z_0)$ from $p_{z_0}(x)$ is given by:

$$I(r, z_0) = \frac{1}{\pi} \int_r^{\infty} \frac{\partial p_{z_0}(x)/\partial x}{\sqrt{r^2 - x^2}} dx. \tag{2.20}$$

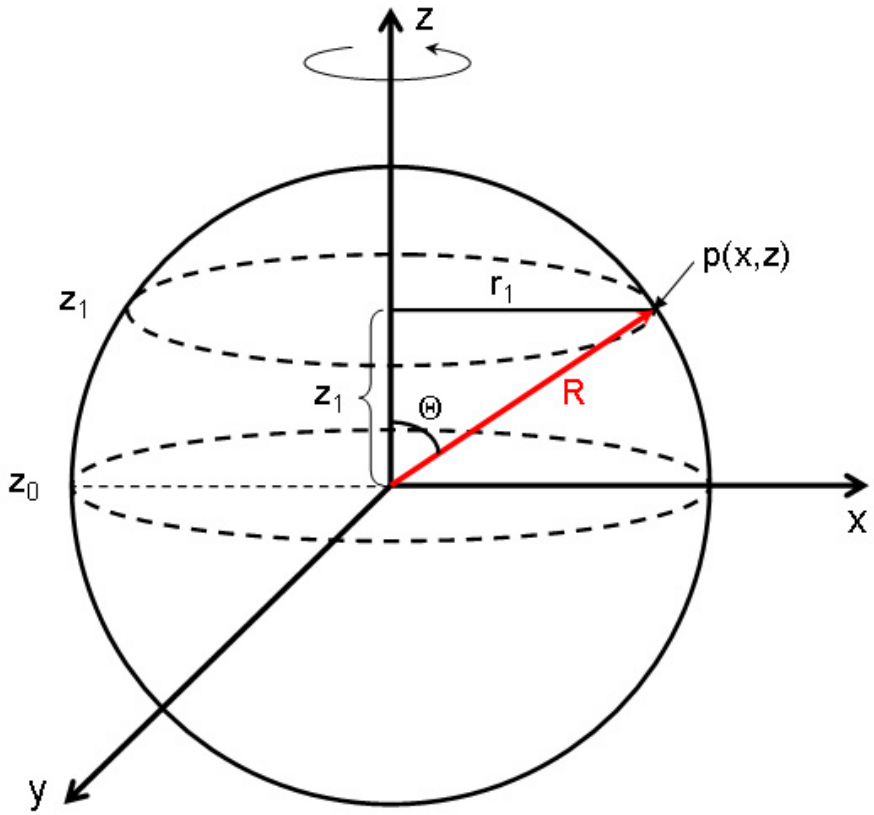

Figure 2.11: The coordinate system used for the derivation of the full 3D intensity distribution $I(x, y, z)$ and the angular distribution.

However, direct usage of Eq. 2.20 is problematic because of the singularity in the integral at the lower limit and because the derivative $\partial p_{z_0}(x)/\partial x$ tends to amplify the noise in the experimental data. Additionally, the intensities $p(x)$ are not available as a continuous function and usually consists of a discrete sample of points.

2.4.4.2 Iterative Regularization

A lot of procedures were suggested to avoid these difficulties and alternative algorithms were developed over the last decade. An overview of the different techniques is given in [46]. In the present work, the maximum likelihood inversion of velocity map ion images with iterative regularization, developed in our group [54], was used. This is a new technique for improved Abel inversion, which combines and extends the successful concepts already applied in forward convolution and basis set expansion [55, 56, 57]. The concept of this technique is as follows: The experimental image is modeled as a linear combination of a set of two-dimensional functions with known inverse Abel transformation in Cartesian coordinates. The Abel inversion is achieved by finding the unknown expansion coefficients of the resulting matrix equation and the subsequent reconstruction of meridional slices of the 3D distributions using these coefficients. Two iterative methods of regulariza-

tion of the problem, which both allow to take into account specific details of the imaging process and lead to constrained reconstructions, were proposed in [54]. The first variant is the Richardson-Lucy (RL) method [54], which provides a maximum likelihood reconstruction and incorporates prior knowledge about the non-negativity and the Poisson noise statistics of the image data. This method was used in the present work. The second variant is the projected Landweber (PL) algorithm [54], where direct constraints on the fitting coefficients are also input in the reconstruction process, but which does not take into account the noise statistics and non-negativity.

For both methods, the iteration count plays the role of a regularization parameter. To avoid the need for a subjective choice of the number of iterations, the image is partitioned into equivalent quarters and cross validation is employed. This provides a reliable criterion for stopping the iterative process to achieve optimal results. A detailed description of the method is given in [54].

2.4.5 VMI Apparatus Calibration

This section describes the calibration procedure of the VMI setup, which gives the magnification factor of the ion optics (see Section 2.3.2.2) and the resolution of the experimental set-up. After the calibration part, the TKER curve fitting procedure is described.

The calibration of the experimental VMI setup was performed by observing the photodissociation dynamics of the simple and very well studied molecule of methyl iodide (CH_3I), for which photophysical properties such as its potential energy surfaces and their correlations, dissociation energies and spin-orbit splittings are well known and can be used as reference values.

2.4.5.1 Introduction to the Photochemistry of Methyl Iodide

Most of the present knowledge of the methyl iodide photodynamics is reviewed in recent theoretical studies [58, 59, 60] and in the review article by Kinsey and co-workers [61]. Only the information essential for the calibration experiments will be highlighted here.

The absorption spectrum of the A-band of CH_3I is composed of three broad, optically allowed transitions from the $X(^1A_1)$ ground state to the dissociative states $^3Q_1$, $^3Q_0$, and $^1Q_1$, which lead to fragmentation into CH_3 and $I(^2P_{3/2})$ or CH_3 and $I^*(^2P_{1/2})$, respectively [62]. Figure 2.12 shows the potential energy surfaces involved into the methyl iodide (CH_3I) photochemistry.

The two weak perpendicular transitions to the $2E(^3Q_1)$ and $3E(^1Q_1)$ states lead to the dissociation of CH_3I to the CH_3 radical and I atom in the $^2P_{3/2}$ state (I channel). The strong parallel transition to the $^2A_1(^3Q_0)$ state leads to the methyl fragment and I atom in the $^2P_{1/2}$ state (I^* channel).

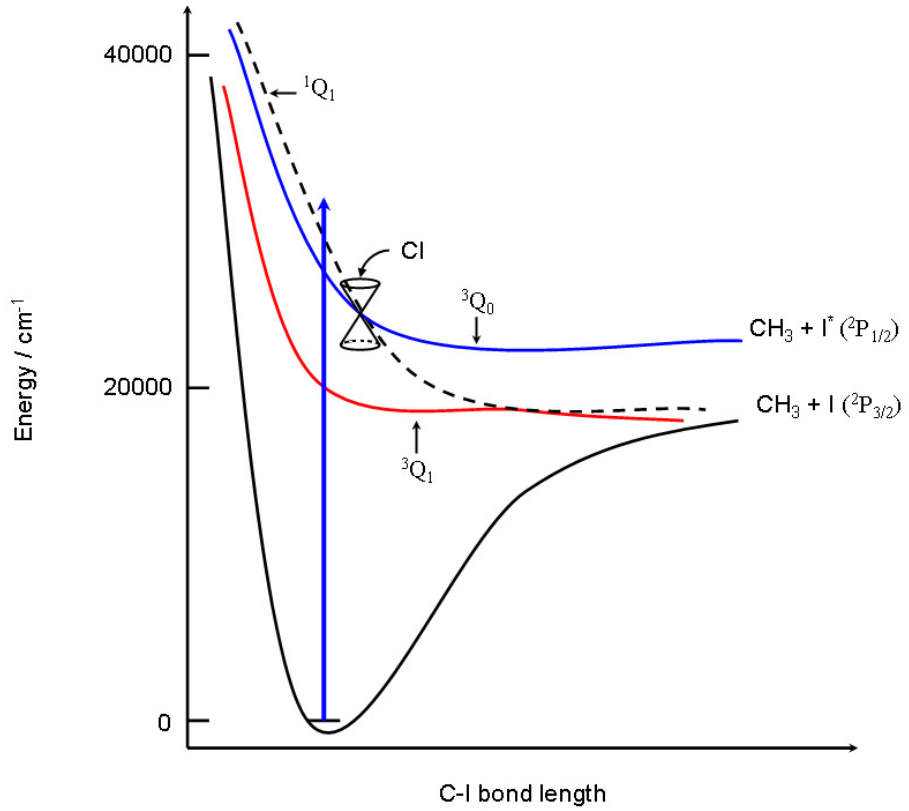

Figure 2.12: Schematic view of the potential energy surfaces involved in the methyl iodide A-band photodissociation [62].

The spin-orbit splitting between I and I* is 0.943 eV [63] and a C-I bond dissociation energy of 2.39 ± 0.03 eV has been determined by translational spectroscopy [64]. The photodissociation of CH_3I is direct (with a dissociation time of $\tau_{diss} \sim 0.065$ ps, and a much longer rotational time $\tau_{rot} \sim 1$ ps of the parent molecule [65]). It is therefore usually assumed to be an "axial recoil" case, for which the C_{3v} symmetry is maintained during the dissociation process. Theoretical studies [66] indicate, however, a slight CH_3–I bending ($\sim 5°$) during the dissociation, which breaks down the C_{3v} symmetry, and allows a ${}^3Q_0 - {}^1Q_1$ curve-crossing involving a nonadiabatic transition *via* a conical intersection, indicated by the double cone in Fig. 2.12. The experimentally observed large yield of I atoms with angular distributions characteristic of a parallel transition confirms this curve crossing. Thus, the excitation of CH_3I to the ${}^1Q_1$ state (dashed curve in Fig. 2.12) results in a dissociation of the parent molecule *via* both the I and I* channels. For both dissociation channels the corresponding methyl fragment can be produced in numerous rovibrational states [9].

2.4.5.2 Photodissociation of Methyl Iodide Studied by Velocity Map Imaging

The calibration was performed by two-color pump-probe experiments for excitation wavelengths of λ_{pump} = 333.5, 305.3, 300, 289 and 286.5 nm, all within the A-band of the absorption spectrum of methyl iodide. The methyl radical was probed in its ground vibrational state by the (2+1) REMPI technique *via* the 3*p* Rydberg state at λ_{probe} = 333.5 nm as described in Section 3.2.3. The schematic view of the experiment is shown in Fig. 2.7. The laser beams were counter-propagating, vertically polarized and crossed the molecular beam at right angles. The electric vectors of the pump and probe laser beams were orientated parallel to the plane of the MCP detector. An example of an ion image of the methyl fragments from CH_3I photolysis at 286.5 nm is depicted in Fig. 2.13.

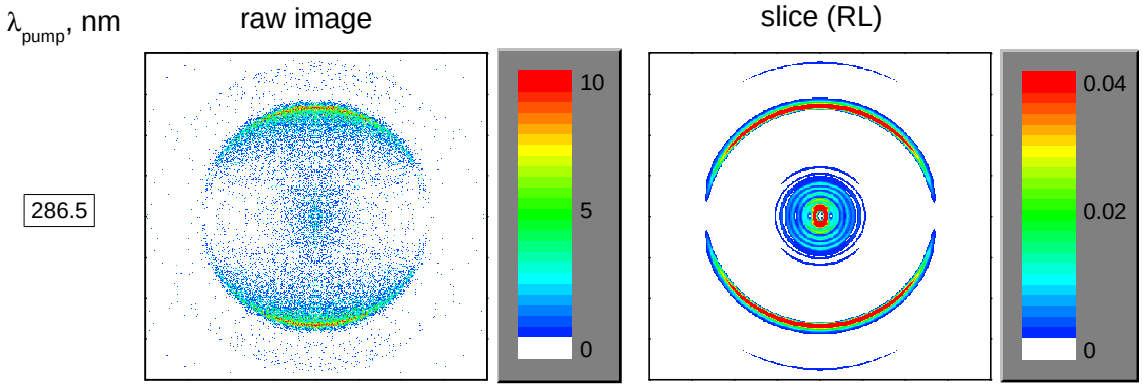

Figure 2.13: Two-color velocity map images of the methyl radical from the photolysis of methyl iodide at λ_{pump} = 286.5 nm. The left side shows the experimentally obtained ion image and the right side shows a meridional slice of the recovered 3D ion distribution. The intensity is RGB color scaled (color bar on the right side of the images), so that white corresponds to an intensity below 5% of the maximum intensity, green corresponds to a moderate intensity of ∼ 50% and red corresponds to the highest intensity of the ion image of 100%. The color bars on the right side of the images show the intensity in absolute units. The methyl radical was detected in its ground state ($v = 0$) by (2+1) REMPI *via* the 3*p* Rydberg state at λ_{probe} = 333.5 nm.

The ion image in Fig. 2.13 shows two ring-like features with the most intense parts at the top and bottom. This reflects the parallel character of the electronic transition preceding the dissociation of the parent molecule. The outer ring corresponds to ions with maximum kinetic energy. In accordance with the energy conservation law, the kinetic energies of these ions should not exceed the maximum available energy, assuming that $E_{avail.} = h\nu - D_0^0(CH_3\text{-}I)$ and the excitation took place from the ground state of the parent molecule. The inner ring is formed by methyl ions

with less kinetic energy, due to the fact that some fraction of the available energy contributes to the internal energy of the co-fragment (I atom). To perform a quantitative analysis of the energy distributions the following steps have to be performed:

1. Reconstruction of the 3D ion distribution from the experimental 2D projection by the Richardson-Lucy (RL) algorithm (see Section 2.4.4). This gives a meridional slice of the recovered 3D ion distribution with pixels as units.
2. By using the known magnification factor of the objective of the CCD camera (1 pixel = $84.5{\cdot}10^{-6}$ m, see Section 2.4.3.2), the ion distribution is transformed from the pixel domain to the metric system. This conversion gives the radii of the ion distribution in meters and in the units of velocity and energy. The velocity distribution can be obtained by simple division of the distribution radii by the time-of-flight of the probed fragment. The justification of this operation is provided by the fact that the longitudual kinetic energy acquired by the ions during the projection exceeds the kinetic energy released in the dissociation process by several hundreds times.
3. The MCP opening time was typically kept at 150 ns in velocity map imaging, which ensures that all projected ions of the mass of interest are detected by the CCD camera. However, such a wide gate does not provide an accurate time-of-flight value of the probed fragment. The shortest possible opening time is 30 ns, which only can provide an accuracy of $\pm$15 ns in the time-of-flight. In order to determine a correct time-of-flight, a simulation of the ions trajectories was performed with the SimIon 7.0 software [67], where all parameters of the VMI apparatus (ion optics assembly, acceleration voltages and the length of the drift zone) and of the ions (masses, energies, initial positions and flight orientations) were taken into account. The resulting calculated time-of-flight was used in the calculations of the velocity distributions.
4. The last step is to transform the ion distributions from the velocity to the kinetic energy domain, *via* the known equation:

$$T = \frac{1}{2}mv^2, \tag{2.21}$$

   with v is the velocity of the detected fragments and m their mass.

The resulting kinetic energy distributions of the detected fragment provide an information on the total kinetic energy release (TKER). The internal energy distribution of the co-fragment can be calculated as was described in Section 2.4.1 and the iterative regularization technique based on the RL algorithm provides information on the angular anisotropy (β) of the ion distribution for each radius in an ion image.

The calculated TKER profiles for all pump wavelengths give values of the dissociation energy and spin-orbit splitting which differ from the literature [9]. These discrepancies arise from the magnification factor of the ion optics. To determine this factor, the available energies ($E_{avail.} = h\nu - D_0^0$ for the I channel and

$E_{avail.} = h\nu - D_0^0 - E_{SO}$ for the I* channel) for each λ_{pump} were calculated and compared to the experimentally obtained values. The results are shown in Fig. 2.14.

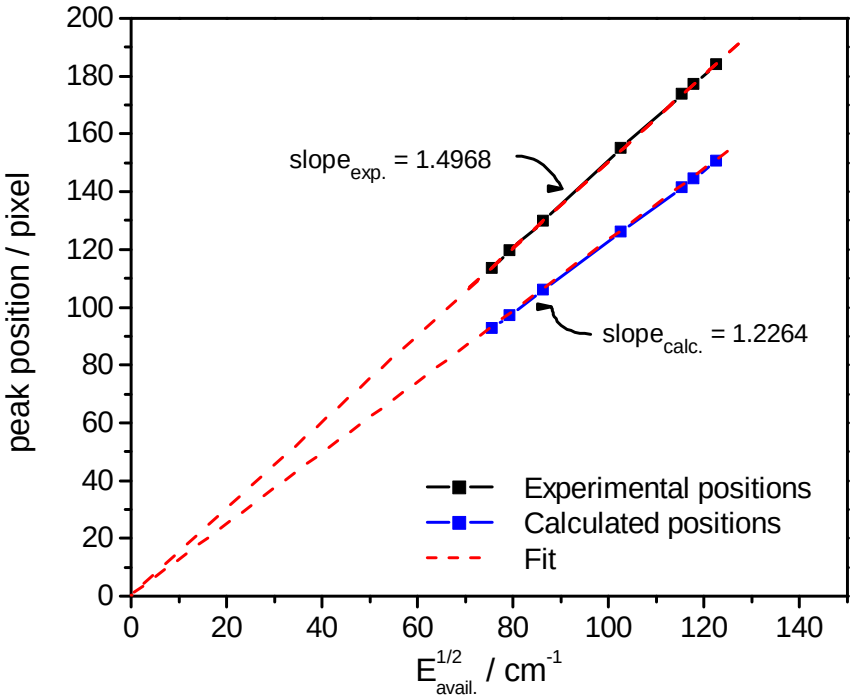

Figure 2.14: Experimental and calculated values of the peak positions of the ion distributions in the pixel domain as a function of the available energies for the photolysis of CH_3I at 333.5, 305.3, 300, 289 and 286.5 nm (see Text).

The correlation coefficient of the linear fit of the curves is 1 and both curves converge to coordinate 0. The magnification factor of the experimental setup, given by the ratio of the slopes of the experimental and calculated curves, equals N = 1.2204. Scaling of the experimental data with this factor results in a perfect agreement in dissociation energy and spin-orbit splitting (see Fig. 2.15) with literature [9]. This factor will be used in all following analyses of the VMI experiments. The scaled ion distributions and the resulting TKER profile is shown in Fig. 2.15.

The finite width of the peaks of the ion distribution is due to the apparatus function. The initial population of the ro-vibrational states of methyl iodide (hot molecules) is supposed to cool in the supersonic jet expansion (see Section 2.2), before the excitation step takes place. Except for a small vibrational excitation that may even be presented after adiabatic cooling. Figure 2.16 shows that experimental peaks of the CH_3 distributions can be perfectly described by assuming a Gaussian apparatus function and population of the vibrational states with 0, 1 and 2 quanta of excitation in the $\nu_3 = 560$ cm^{-1} mode. Since the apparatus function is radius-dependent, it has to be determined at different values of the image radius, which can be achieved by

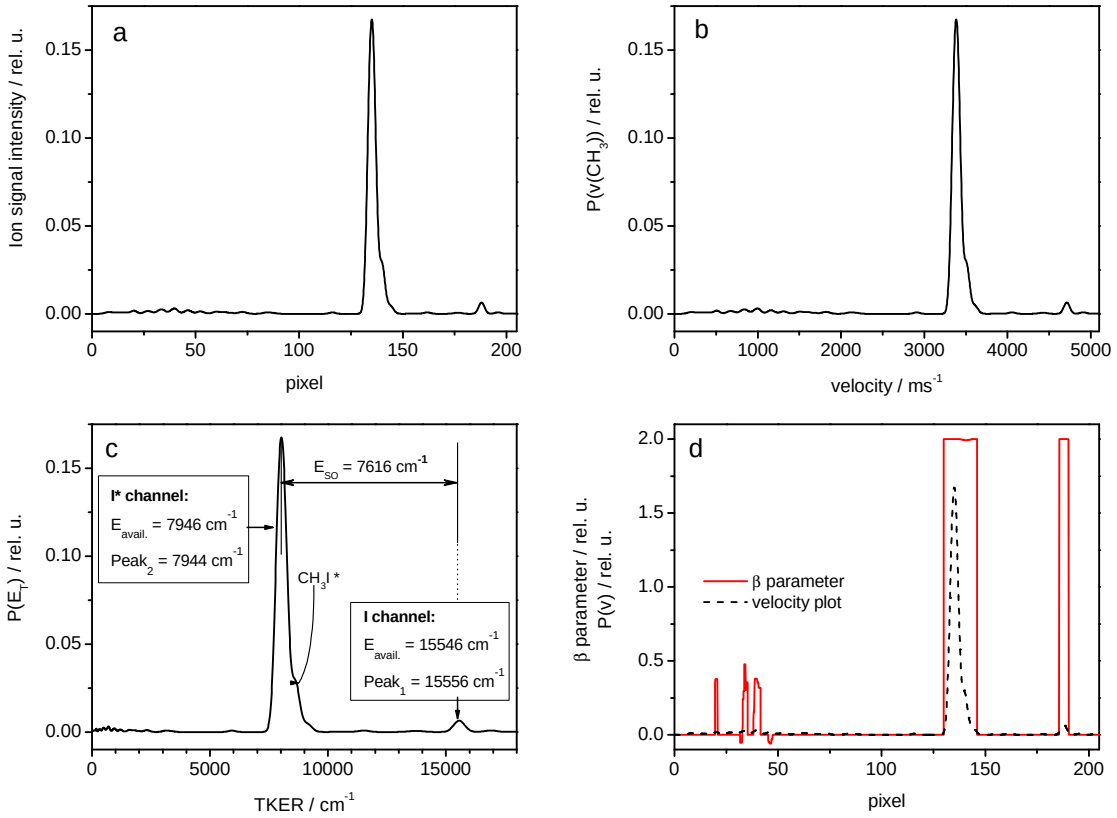

Figure 2.15: CH_3 ion distribution resulting from the CH_3I photolysis at 286.5 nm. (a) in the pixel (unscaled) and scaled with a factor N= 1.2204 in methyl velocity (b) and in energy domains (c). A small shoulder, denoted as CH_3I^*, corresponds to the dissociation of the vibrationally hot ($v_3 = 560$ cm^{-1}) methyl iodide molecules. Also, an angular anisotropy parameter β is shown at the bottom (d).

recording VMIs at different pump wavelengths. Excitation wavelenghts of $\lambda_{pump} =$ 333.5, 305.3, 300, 289, and 286.5 nm were used for this purpose.

From the ion images recorded at these different photolysis wavelengths, the peak positions and the corresponding full widths at half maximum (FWHM) were evaluated. The resolution ($\Delta E/E$) and a standard deviations σ were calculated for each peak in the TKER distribution and for each λ_{pump}. The results are presented in Fig. 2.17, and show that $\Delta E/E$ and σ are functions of the radius.

The fit of the data in Fig. 2.17 allows to determine the resolution and standard deviation of the VMI apparatus for the experimental ion images for arbitrary radii. The knowledge of the apparatus function allows to take the limited instrumental resolution into account. Since the detected ion distribution $D(r)$ is a convolution of the real distribution $R(r)$ with the apparatus function $A(r)$

$$D(r) = A(r) \otimes R(r), \tag{2.22}$$

where $\otimes$ denotes convolution, the instrumental resolution can be increased by deconvolution with the experimental instrument function (see Fig. 2.19). In the present

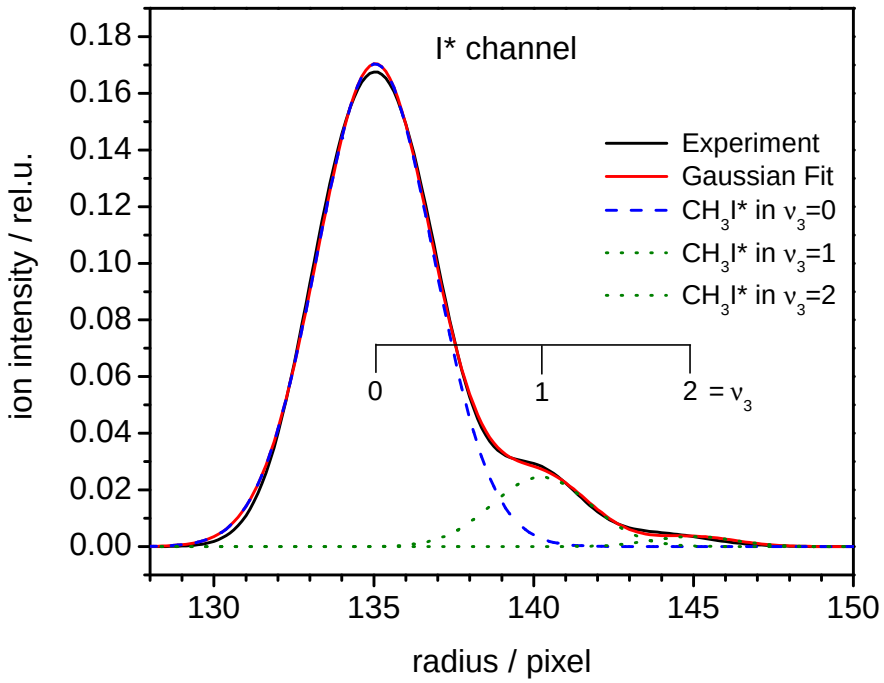

Figure 2.16: The apparatus function was determined from obtained fit of the experimental ion distribution. The best fitting results were obtained with three Gaussian functions, corresponding to the excitation of CH_3I from its ground ($v_3 = 0$), and vibrationally excited states (hot CH_3I molecules with $v_3 = 1$ and 2). The present ion distribution was detected after CH_3I photolysis at 286.5 nm.

work, deconvolution was performed by applying a forward convolution of suitable functions to describe the non-convolved distributions $R(r)$.

2.4.5.3 Distribution Fitting

A quantitative analysis of the ion distributions and corresponding energy release profiles with respect to the peak positions, maximal values of the TKER, the FWHM, and photofragment yields for the different dissociation pathways as well as the fractions of the photofragments which undergo a secondary dissociation can be achieved by fitting of the experimental data with an adequate mathematical model. The observed experimental data exhibit complex energy profiles and the choice of a suitable mathematical model is not trivial. Several parametric models based on Gaussian function (Eq. 2.23), Weibul function (Eq. 2.24), Gumbel function (Eq. 2.25) and an algebraic self-developed model (Eq. 2.26) have been tested.

$$y = \frac{1}{\sqrt{2\pi}x} \cdot \exp\left[-\frac{(x - x_0)^2}{2w^2} \right] \tag{2.23}$$

$$y = A \cdot B \cdot (C^{-B}) \cdot x^{B-1} \cdot \exp\left[-(\frac{x}{C})^B \right] \tag{2.24}$$

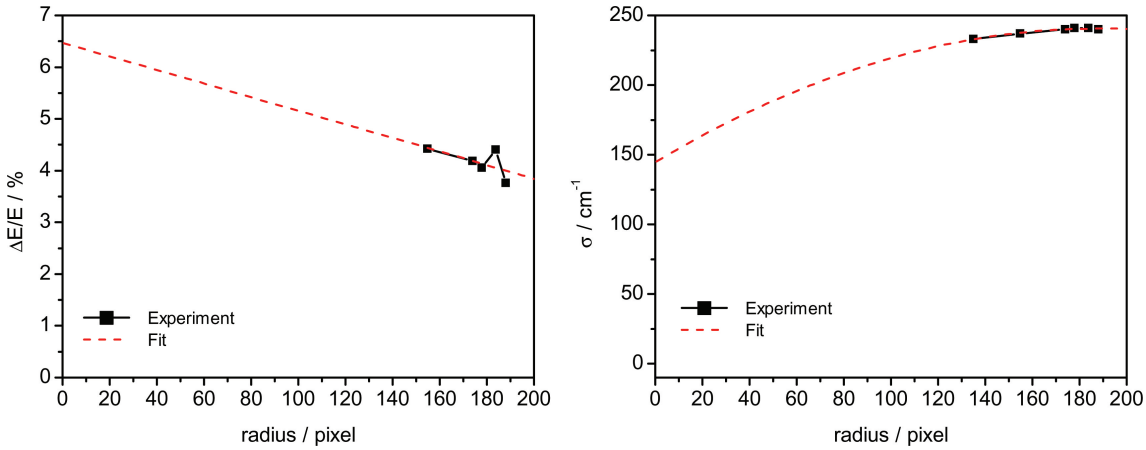

Figure 2.17: Apparatus resolution ($\Delta E/E$) (left side) and standard deviation (σ) (right side) as functions of the radius of the ion images recorded after CH_3I photolysis at 333.5, 305.3, 300, 289 and 286.5 nm. The experimental data (black lines) were fitted (red curves) to extrapolate the resolution function to the region of smaller radii.

$$y = A \cdot \frac{1}{B} \cdot \exp\left[\frac{x-C}{B} - \exp\frac{x-C}{B}\right] \tag{2.25}$$

$$y = A \cdot \left(\frac{x}{B}\right)^{C} \cdot \left(1 - \frac{x}{B}\right)^{D} \tag{2.26}$$

The results are presented and compared in Fig. 2.18.

As can be seen, the residuals over the peak are smallest for the Gaussian model (which is still far from perfect). In the following, the experimental ion distributions were nevertheless fitted using the Gaussian model functions.

The use of a Gaussian model for the description of the experimental ion distributions is further advantageous, since the convolution/deconvolution of the distributions with the instrument function (see previous Subsection) are particularly simple.

The broadening effect is illustrated in Fig. 2.19. The convolution of the apparatus function with the signal results in a ≈ 240 cm^{-1} broadening of the energy distribution profiles. This broadening must be taken into account especially for the determination of the maximum value of the TKER. As can be seen in Fig. 2.19, the deconvoluted distribution has a $\mathrm{TKER}_{max} \approx 240$ cm^{-1} smaller than the convoluted one.

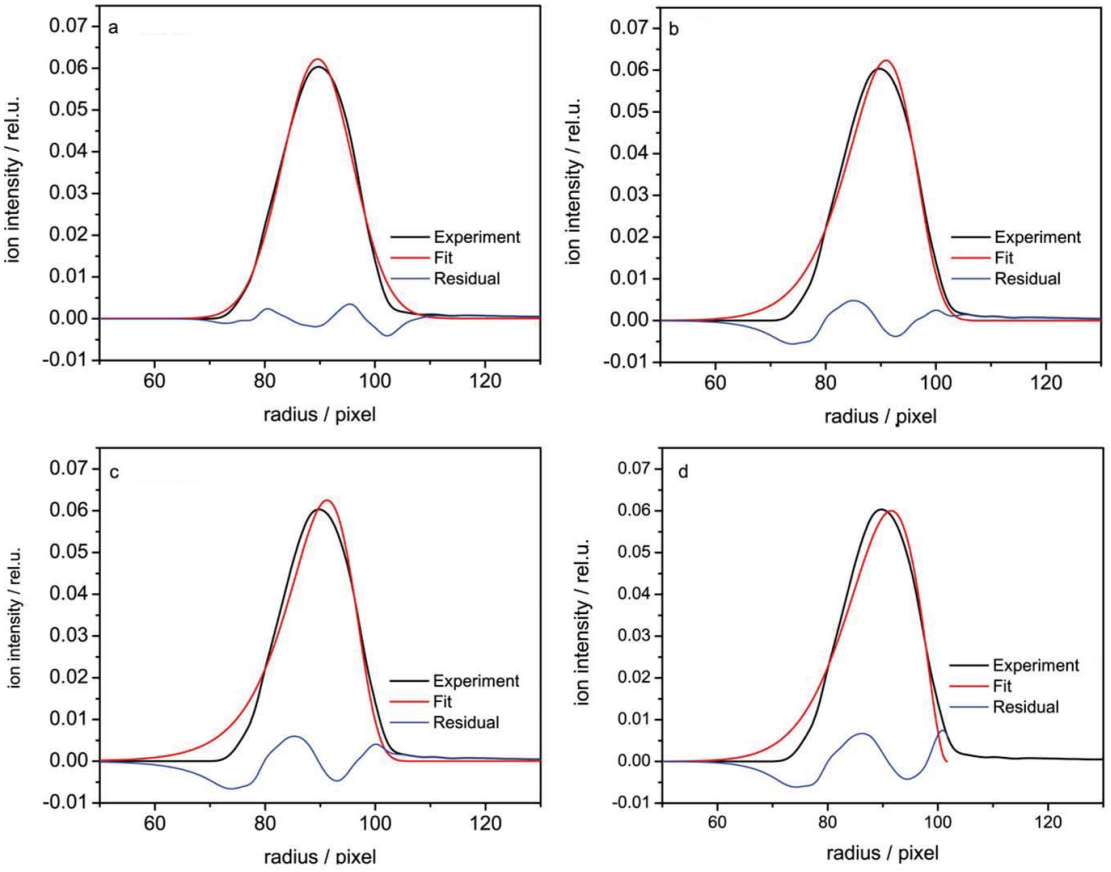

Figure 2.18: Test of different fitting functions used to find an optimum model to describe the experimental ion distribution. (a) shows the Gaussian model, (b) is the Weibul model, (c) shows the Gumbel distribution, (d) is the algebraic self-developed model. The data are taken from acetone-$h6$ photolysis at $\lambda_{pump} = 290$ nm.

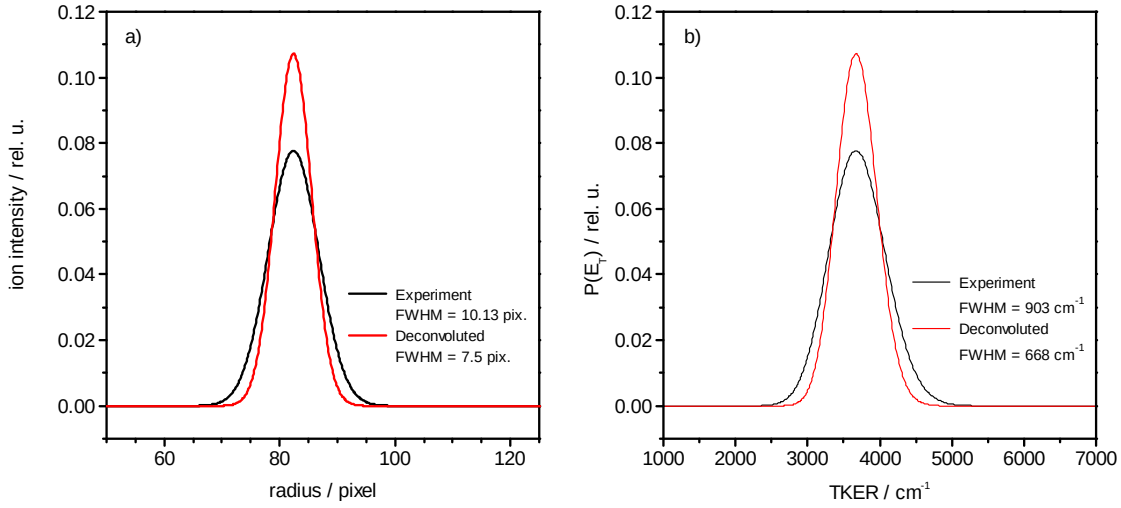

Figure 2.19: The deconvolution effect on the width of the ion distribution and TKER profile. The ion distribution and the corresponding TKER profile were taken from the acetone-$h6$ photolysis at 300 nm.

3 Results and Discussion

Chapter 3 reports on the experimental results of the present work. It is divided into four Sections.

Section 3.1 reports the results of a short series of VMI measurements on *trans*-methyl nitrite. This compound was studied mainly as test molecule to explore the differences of the dissociation dynamics and photofragment internal energy distributions of the *cis*- and *trans*-isomers of methyl nitrite.

Section 3.2 is concerned with ns time-resolved ToF-MS and VMI measurements on the photodissociation dynamics of acetone-$h6$ investigated over a wide range of excitation energies (333 nm $\geq \lambda_{pump} \geq$ 229 nm) of acetone, the simplest ketone molecule, which plays an important role in the Earth's troposphere.

Section 3.3 is concerned with the symmetrically deuterated acetone molecule, $(CD_3)_2CO$.

Section 3.4 reports the results for the photodissociation dynamics of methyl ethyl ketone as another ketone, which has asymmetric α-C-C bonds. Both acetone isotopomers and methyl ethyl ketone were studied in view of the recent interest in ketones as the sources of the alkyl and acyl radicals, which proved to be important in the forming of OH radicals in the atmosphere.

Each Section begins with an introduction, which lays out the motivation for our research work and summarizes previous results. This is followed by a brief experimental subsection that describes specific experimental details. The main subsections then report the detailed experimental results and the analysis of the data, followed by discussions of the new results, with the aim to derive comprehensive pictures of the photodissociation dynamics.

3.1 Photodissociation of *trans*-Methyl Nitrite

3.1.1 Introduction

Methyl nitrite exists in two isomeric forms, the *cis*- and *trans*-isomers. The former is thermodynamically more stable by 230 cm^{-1}, and can be converted to the *trans*-

isomer by internal rotation about the O-N single bond with a conversion barrier of about 3 500 cm^{-1} [12, 13] (see Fig. 3.1). The *cis/trans* ratio at room temperature is ~ 1.75.

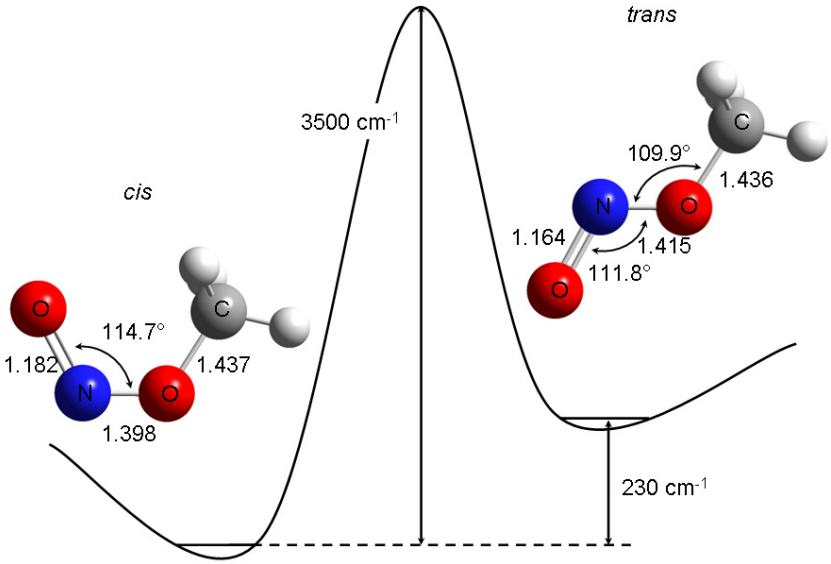

Figure 3.1: *Cis*- and *trans*-methyl nitrite isomers and corresponding geometrical and energetical parameters. Bond lengths are in Å.

The UV/Vis absorption spectrum shown in Fig. 3.2 exhibits two absorption bands. The first band at $\lambda = 400 - 300$ nm is due to the $S_1(n\pi^*) \leftarrow S_0$ transition and shows a progression of bands, separated by $\approx 1\ 000\ cm^{-1}$ and with a full width at half maximum (FWHM) between $500 - 800\ cm^{-1}$. This vibrational progression can be observed due to a shallow barrier on the S_1 excited state, which prevents instant dissociation after excitation to this state [21]. Tarte was the first who realized that the UV absorption spectrum consists of bands originating from *cis*- and *trans*-isomers and assigned the progression to the N-O stretching mode ν_3 in the parent molecule. The origin of the electronic transition of the *trans*-isomer is placed at $\lambda = 387$ nm and that of the *cis*-isomer at $\lambda = 381$ nm [22]. While the assignment of the vibrational progression to the N-O stretching mode is undebated, an alternative assignment of the origin of the electronic transition was given by Pfab, who based his assignment on the temperature dependence of the band intensities. Pfab's alternative assignment places the origin of the electronic transition of the *cis*-isomer at 365 nm and ascribes the red part of the UV absorption spectrum exclusively to the *trans*-isomer [23, 24]. The correct assignment has been rigorously debated because of its importance related to the photodissociation mechanism on the S_1 excited state.

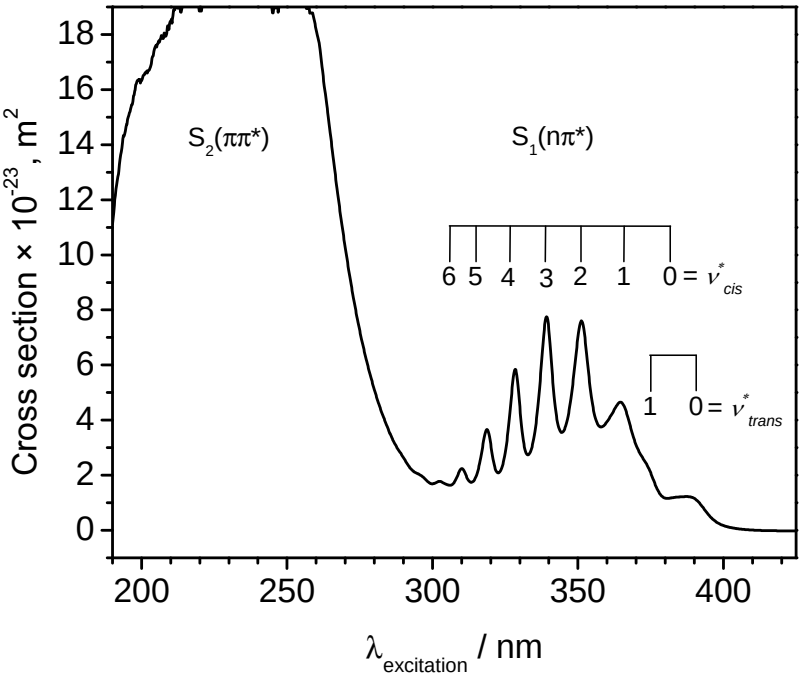

Figure 3.2: UV absorption spectrum of CH_3ONO recorded at room temperature. The vibrational progresion in the first (S_1) electronic band is due to the N-O (ν_3) stretching mode. The assignment is that of Tarte [22].

The second broad and unstructured absorption band is due to the purely repulsive S_2 state. Excitation of the methyl nitrite molecule to the S_2 state leads to an immediate dissociation and was studied in [68].

The photodissociation of methyl nitrite induced by excitation into the first absorption band between $\lambda = 300 - 400$ nm *via*

$$CH_3ONO + h\nu \longrightarrow CH_3ONO(S_1),$$
$$CH_3ONO(S_1) \longrightarrow CH_3O(\widetilde{X}\ ^2E) + NO(\widetilde{X}\ ^2\Pi_\Omega)$$

has been studied intensely for many decades by many groups [14, 15, 16, 17, 18, 19, 20]. Of primary interest are the NO and CH_3O internal energy distributions and their dependence on the excitation energy and the initial vibrational state. Such information can provide insight into the dissociation dynamics and the multidimensional potential energy surface of the excited electronic state.

Benoist-D'azy *et al.* have investigated the state-selective photodissociation dynamics of *cis*-CH_3ONO excited to the $S_1(n\pi^*)$ first excited singlet state with (1+1) REMPI detection of the NO fragment [14]. The results show a large amount of rotational excitation in this fragment which is independent of the excitation wavelength. The NO vibrational population depends on the vibrational level prepared in the excited

parent molecule and the fraction of the excess vibrational energy deposited in the N=O stretching mode of the excited methyl nitrite retained in the vibration of the free NO fragment [14].

Lahmani *et al.* have probed the alignment effect in rotationally highly excited NO ($X\ ^2\Pi,\ v'' = 1$) fragments generated from photodissociation of CH_3ONO ($n\pi^*$) at 355 nm [16]. The NO fragments were shown to be aligned preferentially along the transition moment of the parent molecule. The populations of the Λ doublets and spin components are not in equilibrium and exhibit a J-dependent ratio. Their results are consistent with the impulsive model of the dissociation with fragments recoiling close to the initial molecular plane.

The following notations of the NO stretching mode will be used: The N=O vibrational quanta of the parent methyl nitrite in the S_0 state are marked as v_3; those quanta in the S_1 state as v^*; and finally the vibrational excitation in the NO photofragment is marked as v''.

Schinke *et al.* studied the photodissociation dynamics of *cis*-methyl nitrite within the first absorption band quantum mechanically by taking into account only the O-N and N=O reaction coordinates [25] and extended their study to include the O-N-O bending angle as an additional reaction coordinate [69]. Their results reproduce the experimental absorption spectrum very well. It was shown that the absorption spectrum consists of two band progressions which can be associated with excitation of the O-N bond (vibrational quantum number $m = 0, 1$) and excitation of the N=O chromophor (vibrational quantum number $v^* = 0, 1, 2, ...$). The intensities of the $m = 1$ bands are negligibly small compared to those of the $m = 0$. The calculations demonstrated two different decay mechanisms associated with these two resonances ($m = 0,\ m = 1$). Assuming Tarte's assignment of the UV absorption spectrum, these two decay mechanism are as follows: For the $m = 0$ case, the methyl nitrite molecule decays primarily *via* vibrational predissociation, *i.e.*, *via* a non-adiabatic transition, where the vibrational excitation of the N=O chromophor v^* is converted into the vibrational energy of the NO fragment v'' with loss of one vibrational quantum, so that $v'' = v^* - 1$. The $m = 1$ resonance decays *via* a vibrationally adiabatic process, *i.e.*, with conservation of the vibrational excitation in the NO fragment ($v'' = v^*$). The calculated lifetime of the S_1 state was about 200 fs. A direct measurement of the methyl nitrite S_1 ($v^* = 2$) lifetime with a femtosecond pump-probe experiment gave a value of 125 ± 50 fs [69].

Very detailed studies of the photodissociation of *cis*-methyl nitrite on the S_1 and S_2 surfaces with excitation of ($v^* = 0, 1$ and 2) quanta in the NO stretching mode were performed by Kuzcmann [26] and Riedel [68] using velocity map imaging with a state selective probing of scalar and vector properties of the nascent NO product distribution. The resulting distributions of the total kinetic and the internal energy of the methoxy radical were consistent with a preferred vibrationally non-adiabatic predissociation with a loss of one quantum of the NO vibrational excitation in the

course of the dissociation and an additional adiabatic channel, where dissociation occurs by tunneling through a potential barrier on the S_1 potential energy surface. These conclusions were made on the base of Tarte's assignment. The dissociation energy of the O-NO bond was spectroscopically measured for the first time as $D_0^0 = 13\ 420 \pm 200\ \text{cm}^{-1}$ [26]. The observed angular anisotropies of the photofragment distributions led to a S_1 lifetime of $\tau \approx 280 \pm 80$ fs, which is in agreement with literature [69].

All mentioned studies were done on the *cis*-methyl nitrite isomer, which is the majority component in the gas phase, and have been interpreted as follows: Exciting an overtone of the N=O stretching mode (v^*) in the parent molecule leads to the NO fragments preferentially in the $v'' = v^* - 1$ state, but NO fragments with $v'' = v^*$ are also observable due to tunneling. This interpretation, however, relies on Tarte's assignment of the origin of the $S_1 \leftarrow S_0$ transition for *cis*-methyl nitrite. The interpretation would be different, and in favour of a direct dissociation on the S_1 state (*i.e.*, the NO fragment would be preferentially formed in the $v'' = v^*$ state and also, but less preferentially, in the $v'' = v^* + 1$ state) if one accepts Pfab's alternative assignment of the origin of the $S_1 \leftarrow S_0$ transition of *cis*-isomer. There is no doubt in the origin of the $S_1 \leftarrow S_0$ transition of *trans*-methyl nitrite. Both Tarte and Pfab have assigned a peak in the UV absorption spectrum at 387.7 nm to the origin of the $0 - 0$ transition of *trans*-isomer. Thus, no ambiguity in the interpretation of the photodissociation pathways of *trans*-methyl nitrite is expected.

In this chapter the results on the state selective photodissociation dynamics of the *trans*-methyl nitrite isomer studied by velocity map imaging are presented. This work was done to complete the investigations which were done earlier in our group and answer the question about the correct assignment of the origin of the $S_1 \leftarrow S_0$ transitions of the methyl nitrite isomers and, thus, the correct interpretation of the photodissociation mechanism of both isomers.

3.1.2 REMPI Spectra of the NO Photofragment

The photofragment translational and internal energy distributions after methyl nitrite photodissociation were studied by detecting the NO fragment in a specified quantum state with known internal energy. The energy distributions of the corresponding CH_3O fragments were calculated *via* energy and momentum conservation laws (see Section 2.4). The (1+1) REMPI spectra of the NO radical *via* $A^2\Sigma^+ \leftarrow X^2\Pi_\Omega$ were taken to determine the excitation wavelength for specified (v'', j'') NO quantum states (see Fig. 3.3).

These spectra reproduce previous experimental and calculated spectra in the literature [15, 26, 70]. The distribution of the rotational excitation of NO, marked as j'', was found to be skewed to the right, *i.e.*, to the region of the high j'', with a maximum around $30.5 < j'' < 34.5$. The dependence of the rotational distribution on the

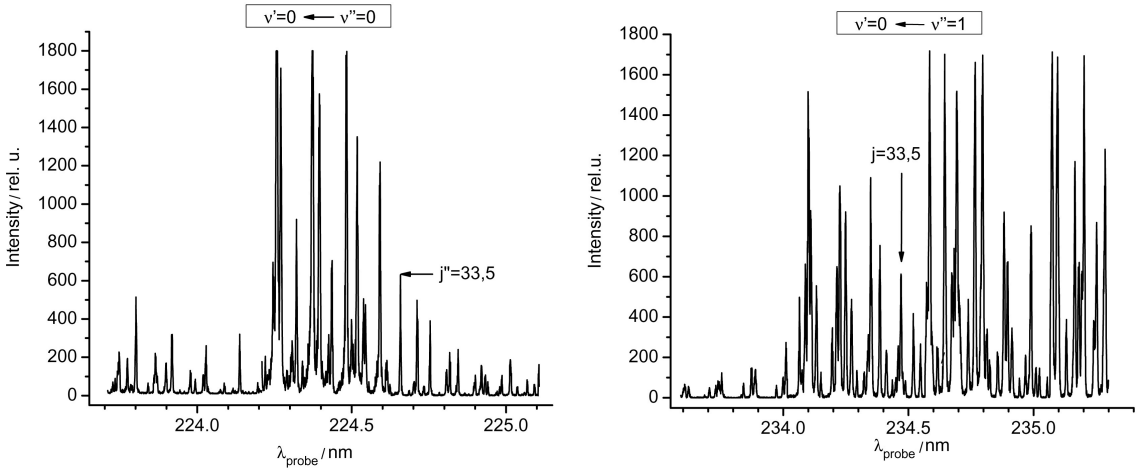

Figure 3.3: (1+1) REMPI spectra of the NO fragment probed in its vibrational ground ($v'' = 0$) (left) and excited ($v'' = 1$) (right) states *via* the $A^2\Sigma^+ \leftarrow X^2\Pi_\Omega$ transition. A photolysis wavelength of $\lambda_{pump} = 363.9$ nm was used.

photolysis wavelength ($\lambda_{pump} = 374.5,\ 363.9$ nm) was negligible. For the following velocity map imaging experiments, the NO radical was probed in its ground and first excited vibrational states at a rotational level of $j'' = 33.5$. The corresponding energies of NO are presented in Table 3.1.

Table 3.1: Rovibronic ($A^2\Sigma^+ \leftarrow X^2\Pi_\Omega$) transitions of NO used in the REMPI detection scheme and the corresponding internal energies of NO ($E_{int.}^{NO}$).

Rot. transition $\Delta jF'F''^a$	Vibr. transition $v' \leftarrow v''$	λ_{probe}, nm	$E_{int.}^{NO}$, cm^{-1} ^{b}
Q11 (j'' = 33.5)	$0 \leftarrow 0$	224.692	1922
Q11 (j'' = 33.5)	$0 \leftarrow 1$	234.475	3778

$^a F''$ denotes the spin-orbit components $^2\Pi_{1/2}$ ($F'' = 1$) and $^2\Pi_{3/2}$ ($F'' = 2$) in the electronic ground state ($L = 1,\ \Omega = L \pm S$), F' denotes the spin-orbit components in the electronic excited state ($L = 0,\ J = N \pm S$) and $F' = 1$ or 2 as for F''

^{b}Ref. [71].

3.1.3 Velocity Map Imaging Experiments

The photodissociation dynamics of *trans*-methyl nitrite was studied in the present work after excitation of the parent molecule either to the ground vibrational state ($v^* = 0$), at a pump wavelength of $\lambda_{pump} = 387.7$ nm or to the first vibrational state ($v^* = 1$) at $\lambda_{pump} = 374.5$ nm by monitoring the NO photofragment translation energy distributions using the velocity map imaging (VMI) technique. The vibrational peaks in the UV absorption spectrum of methyl nitrite, where the photolysis took

place are indicated by arrows in Fig. 3.4. In the following, Tarte's assignments will be used. In the VMI experiment, two laser beams were used, one for the photolysis and the second to probe the nascent NO fragment. The powers of the photolysis and probe laser beams were carefully controlled such that no ion signal could be detected produced by only one of the laser beams. The laser beams were polarized parallel to each other and to the plane of the MCP detector in all experiments.

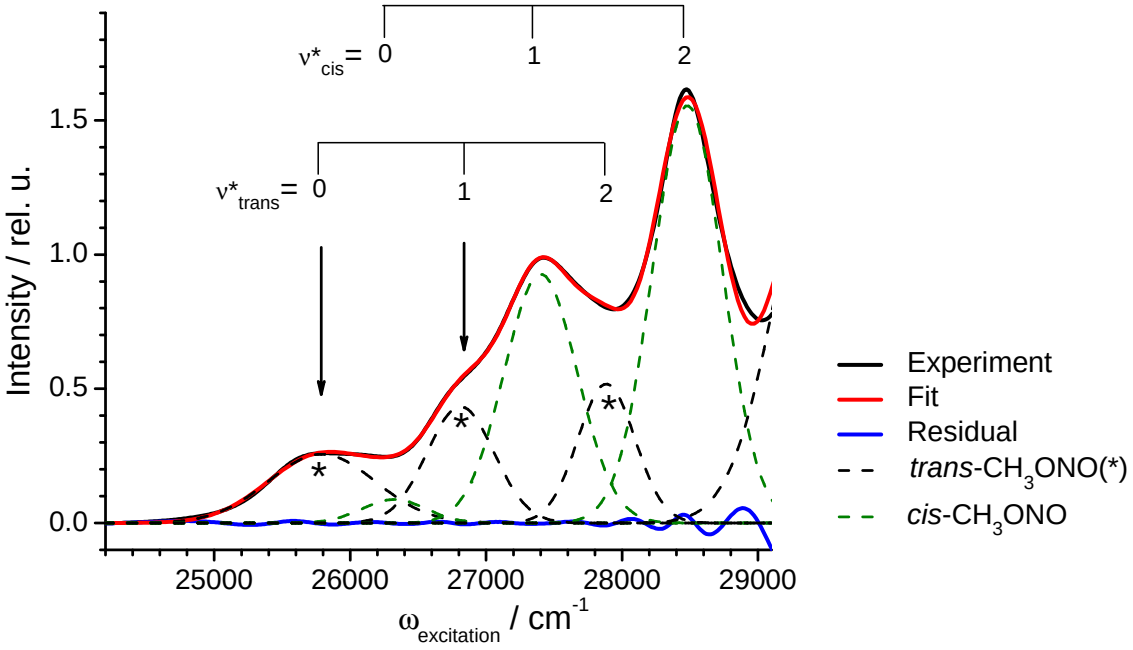

Figure 3.4: Enlarged view of the first band of the UV absorption spectrum of methyl nitrite. Peaks marked with an asterisk correspond to the vibrational progression of the N=O stretching mode in the *trans*-methyl nitrite. The arrows point out the excitation energies used for the photolysis.

Three experimental ion images of NO ($v'' = 0,\ 1$) from the photolysis of *trans*-methyl nitrite excited to ($v^* = 0,\ 1$) are presented in Fig. 3.5.

The intensities were RGB color coded as indicated by the color bars in Fig. 3.5. The NO radicals produced during photodissociation of methyl nitrite molecules were probed over the whole Doppler profile ($\sim$2 cm^{-1}) of a given REMPI transition. The experimental ion images and corresponding kinetic and internal energy distributions are organized as follows: The excited quanta of the N=O stretching mode (v^*) in the parent molecule increases from top to bottom; the vibrational excitation in the detected NO photofragment (v'') increases from left to right (see Fig. 3.5). Thus, the ion images on the diagonal of Figure 3.5 (a) and (c) show the velocity maps of the NO fragment formed in the adiabatic channels of the methyl nitrite dissociation, *i.e.*, when $v^* = v''$, and that one in the left bottom corner (Figure 3.5 (b)) shows the NO fragment spatial distribution formed in the non-adiabatic channel, when $v'' = v^* - 1$. A lot of efforts were taken to detect NO fragments with a vibrational

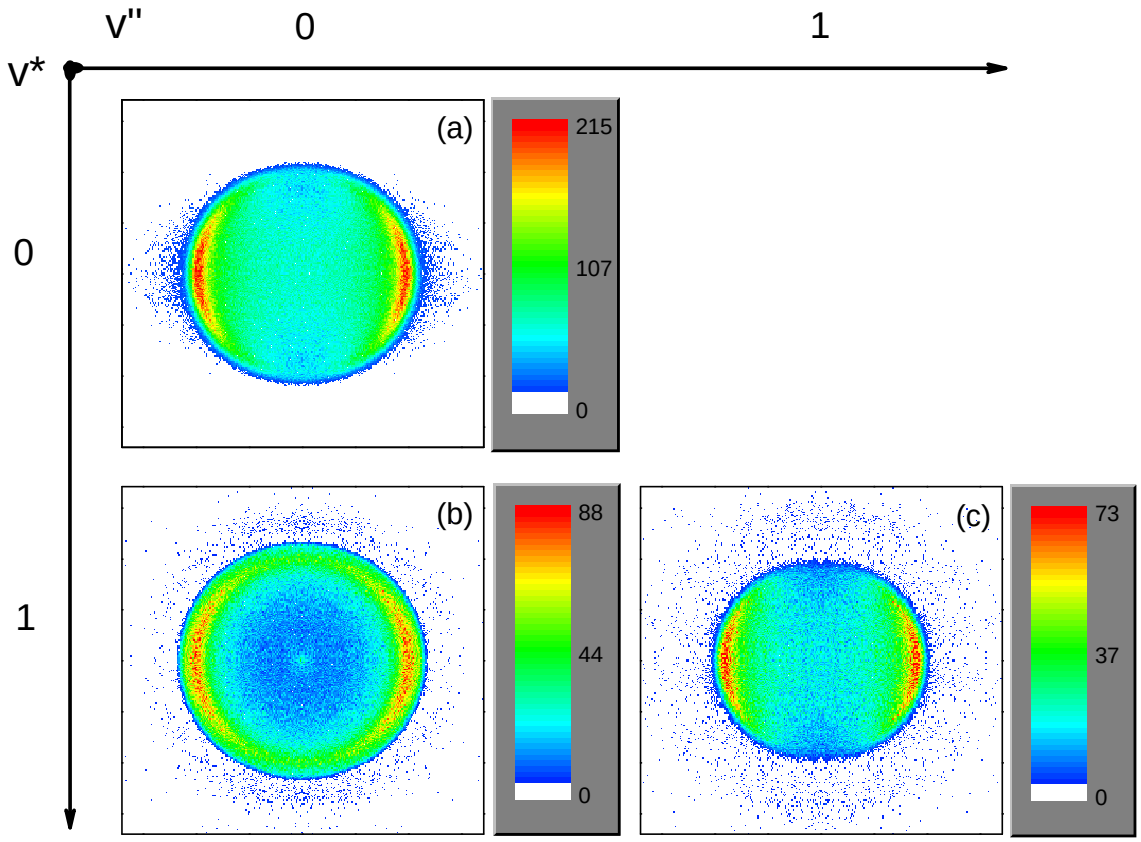

Figure 3.5: Velocity map images of NO ($j'' = 33.5$) from *trans*-methyl nitrite photodissociation at $\lambda_{pump} = 387.7$ nm (a,b) and $\lambda_{pump} = 374.5$ nm (c). v^* is the vibrational excitation of the NO chromophor in the parent molecule and increases from top to bottom; v'' is the vibrational excitation of the NO photofragment and increases from left to right. The intensity is RGB color scaled (color bar on the left side of the images), so that white corresponds to an intensity below 5% of the maximum intensity, green corresponds to a moderate intensity of $\sim$ 50% and red corresponds to the highest intensity of the ion image of 100%. The color bars on the right side of the images show the intensity in absolute units.

.

excitation of $v'' = v^* + 1$, but without success, *i.e.*, NO fragments with $v'' > v^*$ could not be observed.

The complete 3D ion distribution is required for a quantitative analysis of the ion energy profiles and angular anisotropy. This reconstruction was obtained *via* the iteratively regularized maximum likelihood inversion method [54]. The meridional slices through the reconstructed 3D ion distributions are presented in Fig. 3.6. 200 basis functions and about 1000 iterations were used for the reconstruction. All four quarters were tested for cross validation to optimize the iteration counts.

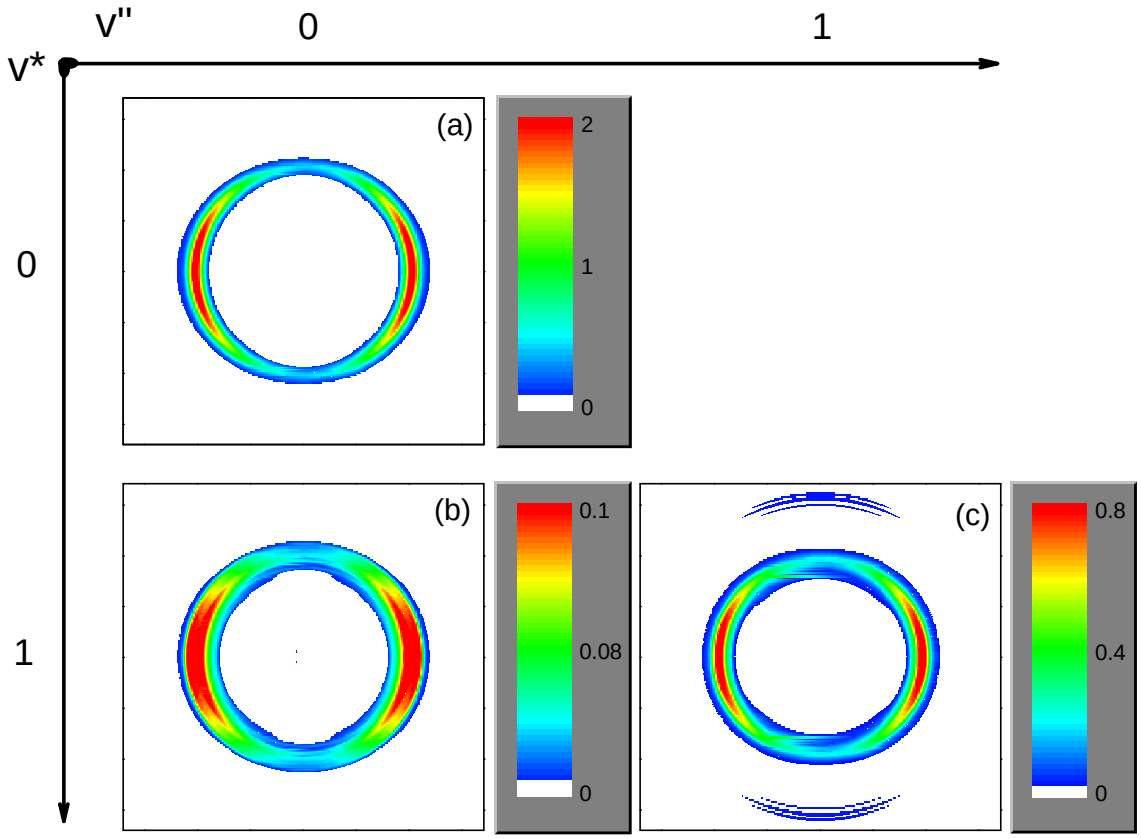

Figure 3.6: Meridional slices through the 3D NO distributions reconstructed from the 2D experimental ion images shown in Fig. 3.5. The notations and order of v^* and v'' are the same as in Fig. 3.5.

.

The slices demonstrate sharp, ring-like patterns with a lack of intensity at the center of the images which is an obvious sign that there are no "slow" NO fragments, which could originate from the dissociation of the methyl nitrite molecule in small clusters in the molecular beam. The non-adiabatic dissociation pathway of the methyl nitrite molecule results in a clear bimodal NO fragment distribution (see Fig. 3.6 (b)), whereas the adiabatic channels of the dissociation exhibit a simple monomodal ion distribution (see Fig. 3.6 (a) and (c)). Additionally, one can see a very weak outer ring in Fig. 3.6 (c), which is obviously formed *via* two photon absorption followed by methyl nitrite dissociation from the S_2 state, as it is suggested from the energy conservation.

All images demonstrate a strong angular anisotropy in the fragment distributions with anisotropy parameters β evaluated from the sliced images between -0.9 to -0.7. This is very close to the lower limiting value of -1 for a one-photon perpendicular dissociative transition in the axial recoil limit. The anisotropy parameter β did not show any significant dependence on the initially excited state in the parent molecule

or on the vibrational state of the probed NO fragment and thus can be averaged: $\langle\beta\rangle = -0.81 \pm 0.09$.

The angle-integrated photofragment distribution was obtained from the reconstructed 3D distribution and converted to the recoil kinetic energy distribution of the NO photofragment. Taking into account energy and momentum conservation laws, the total kinetic energy release (TKER) E_T could be calculated as were described in Section 2.4. The resulting TKER distributions calculated from the images above are shown in Fig. 3.7.

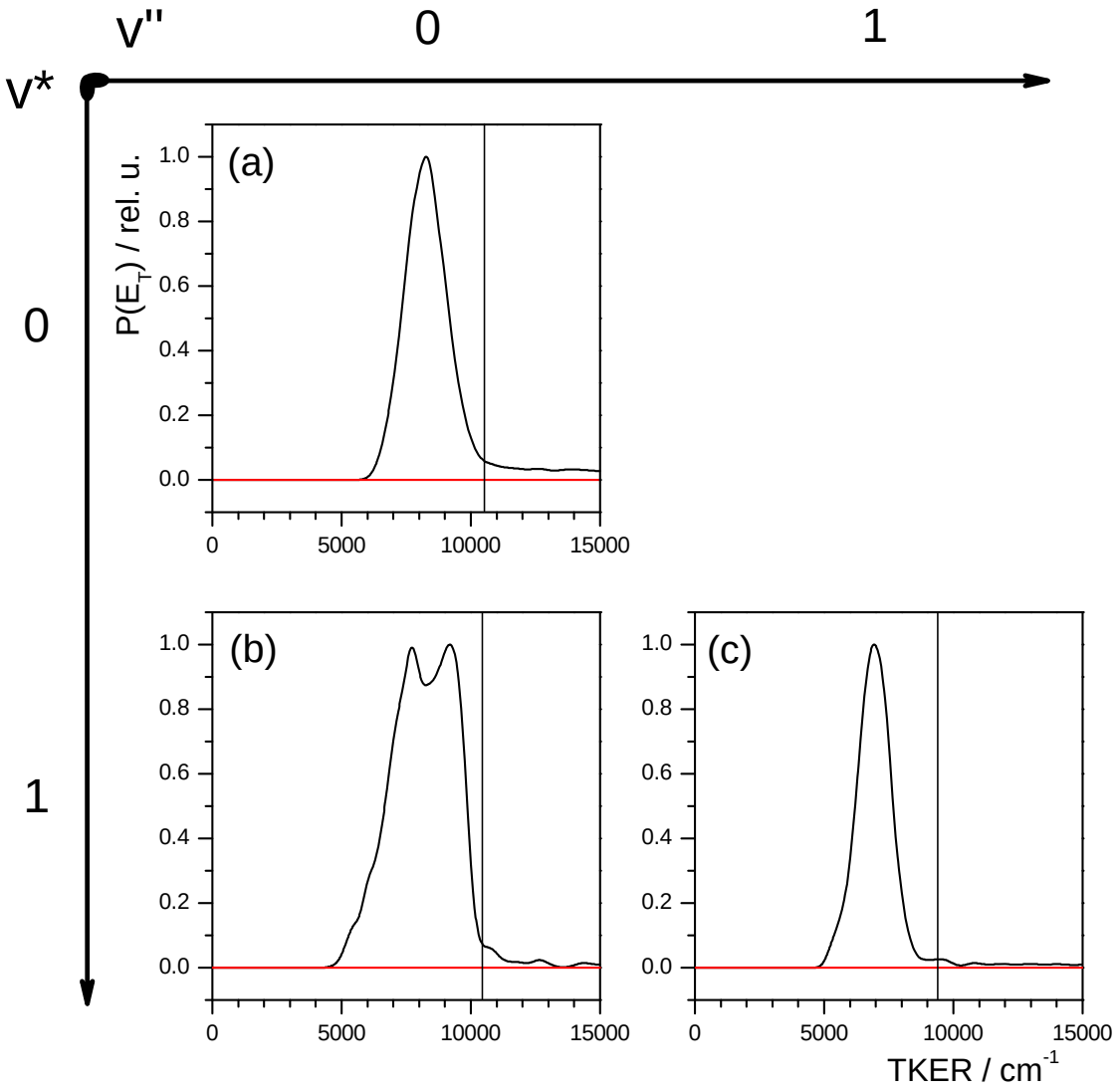

Figure 3.7: Total kinetic energy release distributions from *trans*-methyl nitrite photolysis at (a,b) $\lambda_{pump} = 387.7$ nm and (c) $\lambda_{pump} = 374.5$ nm. The black curves represent the experimental TKER profiles, red curves are the zero level and the vertical black lines indicate the available energies. The notations and order of v^* and v'' are the same as in Fig. 3.5.

.

The knowledge of the maximal TKER value, which corresponds to the minimum of the internal energy of the photofragments formed in the photodissociation, allows one to calculate the dissociation energy of the O-NO bond from the overall energy balance of the photochemical reaction as it was described in Section 2.4. The maximum of the total kinetic energy (E_T^{max}) was calculated in the following way: (1) The TKER curve was integrated to calculate the overall area under the curve and was accepted as 100%. (2) The E_T^{max} value is then defined as the upper limit for the integration, which would result in 99.99% of the overall area under the TKER profiles. The same approach was used in [26]. This approach is rather intuitive and has no real scientific background. On the other hand, it gives plausible values for the dissociation energies, which agree with literature. Averaging over the three TKER profiles gives the value of the dissociation energy of the O-NO bond of

$$D_0^0 = 13\ 560 \pm 200\ \text{cm}^{-1}.$$

The error arises from the apparatus resolution which was described in Section 2.4.

The non-adiabatic dissociation channel ($v^* = 1$ and $v'' = 0$) of methyl nitrite clearly demonstrates a bimodal distribution in the total kinetic energy release which, in principle, could have originated from the *cis*-isomer present in the molecular beam. It has to be considered that the overall intensity of the absorption peak at λ = 374.5 nm in the UV absorption spectrum is a sum of the absorptions due to the *trans*- and *cis*-isomers present in the molecular beam sample (see Fig. 3.4). The *cis/trans* ratio in the molecular beam can be assumed to be unaltered from the ratio in the bulk gas phase ($cis/trans \approx 1.75$ at room temperature). This is due to the rotational barrier of 3 500 cm^{-1} about the O-N single bond. In addition, FTIR measurements of the isomeric equilibrium of *cis/trans* methyl nitrite in the gas phase and in the matrixes have shown that the ratio of the *cis/trans* isomers in the sample at 180 K did not much differ from that at room temperature [72, 73]. It can be tested if the bimodality in the TKER profile is really originating from the *cis*-isomer by varying the excitation wavelength within the same vibrational band (λ = 374.5 nm) in order to increase or decrease the amount of photo-excited *cis*-CH_3ONO present in the sample. Therefore, if the bimodal distribution is due to a contribution from *cis*-CH_3ONO, one should observe the changes in the the peak amplitudes in the TKER profile by varing the excitation wavelength within the 1-0 vibrational band. Alternatively, one could increase the sample temperature before expansion into the vacuum to increase the amount of *trans*-CH_3ONO. The excitation wavelengths for the test procedure were λ_{pump} = 375.5 nm, 374.5 nm and 373.5 nm. Figure 3.8 depicts the resulting TKER profiles.

The ratio of the isomers in the sample mixture was estimated from their contributions to the amplitude of the absorption peak. In Fig. 3.9 the part of the fitted UV absorption spectrum of CH_3ONO, with accordance to Tarte's assignment, is

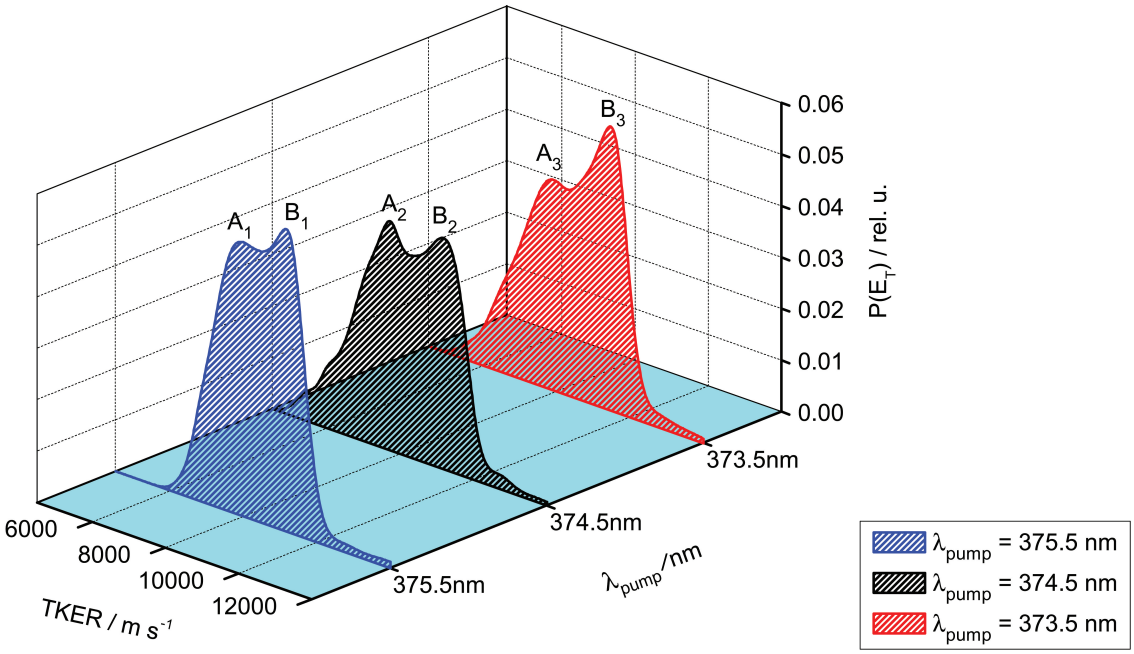

Figure 3.8: Total kinetic energy distributions resulting from CH_3ONO photolysis at λ_{pump} = 375.5 nm, 374.5 nm and 373.5 nm. Letters A and B with subindexes denote the peaks amplitudes for "*trans*" and "*cis*" isomers for a certain wavelength, respectively. For further elucidations see the text.

presented. The contributions from the isomers to the absorbance are denoted by indexes A_i, B_i and C_i for the *trans*-, *cis*- and overall intensities, respectively.

The calculated peak amplitude ratios from Figure 3.8 and corresponding amplitude ratios from Figure 3.9 are presented in Table 3.2.

Table 3.2: *cis/trans* ratios as a function of the different excitation wavelengths within the 1-0 vibration band of the UV absorption spectrum of *trans*-CH_3ONO and the peak amplitude ratios from Figure 3.8

λ_{pump}, nm	*cis* / *trans* (Fig. 3.9)	B_i / A_i (Fig. 3.8)
375.5	0.28:1	1.16:1
374.5	0.12:1	1:1.02
373.5	1:1	1.34:1

There is weak correlation between the peak ratios of the TKER profiles and the presence of the *cis*-CH_3ONO in the sample at the selected excitation wavelengths (see Table 3.2). However, no bimodal distribution was observed in the adiabatic channel ($v'' = v^*$) at the same photolysis wavelength (λ_{pump} = 374.5 nm). Thus, the presence of the *cis*-isomer in the sample cannot explain the bimodal distribution of

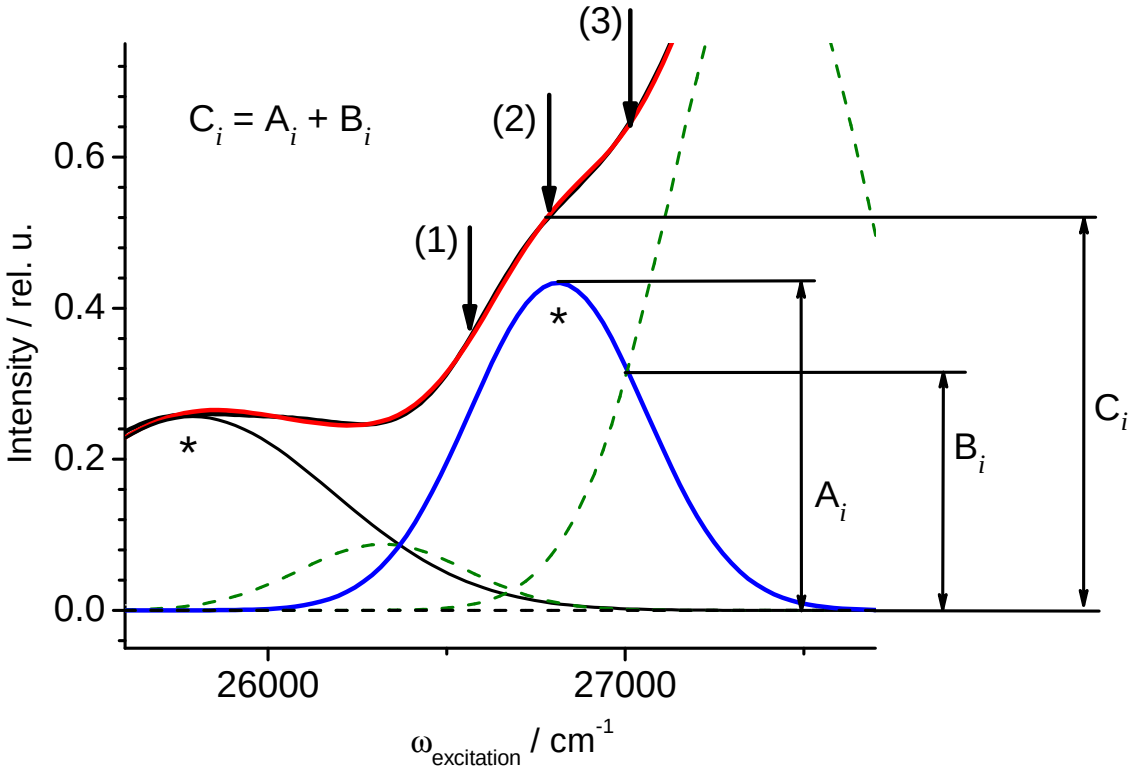

Figure 3.9: UV absorption spectrum of CH_3ONO with absorbance amplitudes for the *cis/trans* ratio estimation. The black solid curve represents the experimental absorption band, the red line is the fit result, the black dashed line is the $0-0$ transition of the *trans*-CH_3ONO, olive dashed lines are vibrational bands of the *cis*-CH_3ONO and the blue line is the vibrational band of the *trans*-CH_3ONO, which was chosen for the test of the possible influence of the *cis*-isomer.

the TKE observed for the non-adiabatic dissociation pathway of methyl nitrite. This isomer intermixture should be also observed for adiabatic channels, which is not the case. The bimodality of the TKE distribution cannot originate from the electronic excitation of the CH_3O molecule because the distance between two peaks (ΔE_{peak}) in the TKER profile is too small to be caused by the first excited state of the CH_3O: $\Delta E_{peak} = 1\ 159$ cm^{-1} at $\lambda_{pump} = 375.5$ nm, whereas intensive research has shown that the first electronic transition lies at $31\ 613.9 \pm 0.5$ cm^{-1} [74, 75, 76]. Another possible explanation might be vibrational excitation in the CH_3O co-fragment. It is well known that the methoxy radical has an electronically degenerate ground state ^2E in C_{3v} symmetry and is subject to Jahn-Teller (JT) distortion. The JT distortion lifts the electronic degeneracy occurring at the C_{3v} structure and leads to stationary points in C_s symmetry. A non-linear molecule in an orbitally degenerate state will spontaneously distort from a symmetric to an asymmetric configuration [77]. The symmetric modes do not provide the distortion necessary to remove the degeneracy and lower the energy, and thus only the asymmetric (e) vibrational modes can be Jahn-Teller active. The methoxy radical is known to exhibit a "dynamic" Jahn-

Teller effect, where the zero-point energies of the vibrations are much greater than the stabilization energy of the Jahn-Teller distortion [77]. Therefore the distortion is not large enough to provide a permanent change from C_{3v} to C_s symmetry and must be treated as a vibronic coupling problem where the asymmetric vibrational e modes couple to the degenerate E electronic states. Since CH_3O has an unpaired $p-$orbital electron primarily centered on the O atom, it has also large spin-orbit splitting of $\sim$64 cm^{-1} in the ground vibronic state. The theory of Jahn-Teller molecules with and without spin-orbit coupling has been reviewed by Barckholtz and Miller [77].

CH_3O with C_{3v} symmetry has six vibration modes: The symmetric C-H stretching ν_1, the CH_3 umbrella ν_2, and the C-O stretching ν_3 are totally symmetric A_1 modes, while the asymmetric C-H stretching ν_4, the CH_3 scissor mode ν_5, and the CH_3 rocking mode ν_6 are doubly degenerate E symmetry modes. Among these six fundamentals, only ν_2, ν_3, ν_4, ν_5 and ν_6 were assigned [77, 78, 79, 80]. The vibrational assignments remain uncertain for the C-H stretching mode ν_1. Table 3.3 lists experimental and calculated vibrational frequencies of the methoxy radical.

Table 3.3: Vibrational frequencies of the ground state of the CH_3O radical (all energies are given in wavenumbers)

Fundamental mode	Symmetry	Exp.[a]	Theory[b]	Theory[c]	
ν_1 symm. C-H stretch.	a_1	—	2907	2843[d]	2843[e]
ν_2 CH_3 umbrella	a_1	1359	1371	1416	1398
ν_3 C-O stretch.	a_1	1066[f]	1111	993	917
ν_4^+ asymm. C-H stretch.	e	2835	3030	2919	2915
ν_4^-		—	2987	2905	2857
ν_5^+ CH_3 scissors	e	1417	1517	1483	1473
ν_5^-		—	1360	1424	1241
ν_6^+ CH_3 rock.	e	—	961	1083	1078
ν_6^-		681	691	706	1018

[a] Ref. [77]
[b] This work: B3LYP/6-31^{++}G(d,p)
[c] Ref. [81].
[d] values in this column calculated at ROHF level
[e] values in this column calculated at CAS level
[f] Ref. [79]

Calculations on the vibrational frequencies of CH_3O in this work were done after geometry optimization of the methoxy radical in its ground electronic state *via* density functional theory (DFT) [82] using the unrestricted UB3LYP functional [83] with the 6-31^{++}G(d,p) basis set [84]. The calculations converged to the real minimum of the energy surface since no imaginary frequency was found. The vibrational frequencies were scaled with a factor of 0.9814 [85].

The distance between two peaks (ΔE_{peak}) in the TKER profile for the ($v^* = 1, v'' = 0$) case varies with the excitation wavelength: $\Delta E_{peak} = 1\,159$ cm^{-1} at $\lambda_{pump} = 375.5$ nm; $\Delta E_{peak} = 1\,473$ cm^{-1} at $\lambda_{pump} = 374.5$ nm and $\Delta E_{peak} = 1\,555$ cm^{-1} at $\lambda_{pump} = 373.5$ nm. Anisotropy parameter of $\beta = -0.8$ for all three excitation wavelengths. There are three vibrations, which have frequencies close to ΔE_{peak}: The umbrella mode of the CH_3 group ν_2, the stretching mode of the C-O bond ν_3, and the scissors like vibration in the CH_3 group ν_5 which is Jahn-Teller active due to its e symmetry. At the present time, vibrational excitation of one of these fundamentals in the CH_3O fragment seems to be the most feasible explanation for the bimodal distribution of the TKER after the methyl nitrite dissociation *via* the non-adiabatic channel. The internal energy distribution of the CH_3O radical can be calculated by known energy relations (see Section 2.4) and is shown in Fig. 3.10 for all three excitation cases.

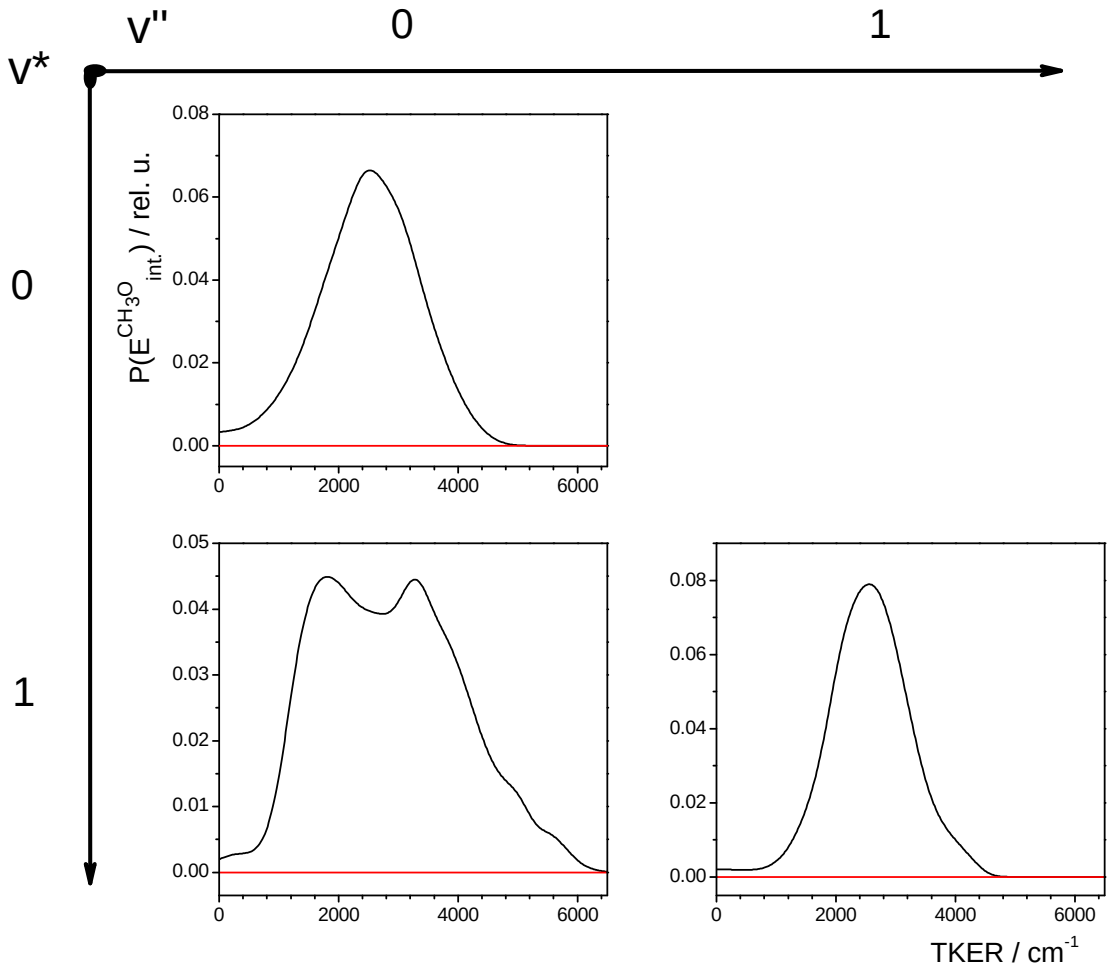

Figure 3.10: Internal energy distributions of the CH_3O radical from *trans*-methyl nitrite photolysis at: (a,b) $\lambda_{pump} = 387.7$ nm, (c) $\lambda_{pump} = 374.5$ nm. The notations and order of v^* and v'' are the same as in Fig. 3.5.

The internal energy distributions of the methoxy radical have complicated profiles which cannot be fitted with a simple Gaussian function and have considerable full widths at half maximum of up to 3 200 cm^{-1}.

All the relevant parameters characterizing the ion distributions, total kinetic energy release for all three excitation cases for the NO photofragments with rotational excitation $j'' = 33.5$ are collected in Table 3.4 (all energies are given in wavenumbers).

Table 3.4: Energetycal and angular parameters characterizing the observed photodissociation of CH_3ONO excited into $v^* = 0,\ 1$ by detecting NO fragment $(v'' = 0,\ 1)$ in $j'' = 33.5$ rotational state. All energies are given in cm^{-1}.

(v^*, v'')	ν_{pump}	$E_{int.}^{NO\,a}$	$E_T^{max\,b}$	$D_0^{0\,c}$	${E_{avl.}}^{d}$	E_T^{ave}	${\Delta E_T}^{f}$	$E_{int,av}^{CH_3O\,g}$	-β^h
(0,0)	25790	1922	10617	13251	12539	8238	1886	2379	0.8
(1,0)	26630	1922	10784	13724	12906	7995-9154	2658	2789-1830	0.7
(1,0)	26700	1922	11000	13778	12922	7723-9196	3200	3277-1804	0.8
(1,0)	26770	1922	11227	13621	13149	7916-9472	2921	3311-1755	0.8
(1,1)	26700	3778	9498	13424	13276	7043	1457	2556	0.9

[a] $E_{int.}^{NO}$ is the internal energy of the NO fragment
[b] E_T^{max} is the maximal total kinetic energy release
[c] D_0^0 is the CH_3O-NO bond dissociation energy
[d] $E_{avl.}$ is the available energy
[e] E_T^{av} is the average total kinetic energy release
[f] ΔE_T is the FWHM of the total kinetic energy release
[g] $E_{int,av}^{CH_3O}$ is the average internal energy of the methoxy radical
[h] -β is the angular anisotropy parameter.

The energetical parameters in Table 3.4 for the pump-probe scheme of $v^* = 1, v'' = 0$ are split into three rows since the bimodal distribution in the corresponding TKER profile in Fig. 3.8 was probed for three close-lying excitation wavelengths in the vicinity of the center of the $v^* = 1$ vibrational band. The FWHM and CH_3O internal energy values also correspond to those two peaks in Fig. 3.8. It is clear from Table 3.4 that a significant fraction of the available energy (about 65% on average) flows into the translation energy of the photofragments. This property is not strongly dependent on the excitation energy.

3.1.4 Discussion

The total kinetic energy release, the internal energy and the angular anisotropy measured in the present work provide further information about the photodissociation of *trans*-methyl nitrite and complement the previous data about the *cis*-isomer photodissociation dynamics which were obtained in our group [68, 26].

The assignment of the vibrational progressions of the UV absorption spectrum of methyl nitrite plays a crucial role in the understanding of the photodissociation dynamics of methyl nitrite. As it was mentioned above, two alternative assignments for *cis*-isomer were given by Tarte [22] and Pfab [23, 86]. It is commonly accepted in the literature to use Tarte's assignments due to different arguments (see introduction and Ref. [19]) and the same was done in the present work through the Section 3.1.3. Based on the temperature dependence of the low-energy tail of the UV absorption spectrum of methyl nitrite, Pfab and co-workers concluded that while the assignment for the *trans*-isomer remains undoubted, with the origin of the electronic transition around 387.7 nm, the correct assignment of the origin of the *cis*-isomer had to be revisited to 364.3 nm [86]. The weak feature in the vicinity of 381 nm, which was assigned originally to the origin of the $S_1 \leftarrow S_0$ transition of the *cis*-isomer by Tarte [22] was interpreted as a hot band of the *cis*-isomer and some impurity in the sample, most probably from traces of HONO. Additionally, in Ref. [86], the authors came to the conclusion that *cis*-methyl nitrite dissociates preferentially *via* a direct mechanism with conservation of the vibrational quanta in the NO fragment, *i.e.*, $v'' = v^*$ and not *via* a non-adiabatic coupling, *i.e.*, $v'' = v^* - 1$. This would mean that dissociation of both isomers follows two different pathways: (1) *trans*-methyl nitrite dissociates *via* both a non-adiabatic mechanism with loosing one vibrational quanta ($v'' = v^* - 1$) and an adiabatic channel ($v'' = v^*$), which is supported by the present results. In fact, it was impossible to detect the NO product with $v'' = v^*+1$, which agrees with the theory of the methyl nitrite dissociation elaborated by Schinke and co-workers [21, 25]. However, in [86], the authors claim that they observed about 10% of the NO fragment in the $v'' = v^* + 1$ state. (2) Previous work of Kuczmann [26] on the photodissociation of *cis*-methyl nitrite then would strongly support the direct dissociation of the parent molecule, where the released NO fragments are vibrationally excited to $v'' = v^* - 1$, $v'' = v^*$, and $v'' = v^* + 1$ states (see Ref. [26]). Thus, Pfab's assignment suggests that excitation of the 3_0^0 transition of *cis*-methyl nitrite results in NO fragments in $v'' = 0$ and $v'' = 1$ vibrational states, excitation of the 3_0^1 vibronic transition of the parent molecule results in NO fragments in $v'' = 0$, 1 and 2. Excitation of *cis*-methyl nitrite with the wavelength of $\lambda_{pump} = 380$ nm (which was atributed by Pfab to hot molecules and thus corrsponds to the 3_1^0) only results in NO fragments in $v'' = 0$ vibrational state. This is the first questionable point arising from the Pfab's assignments, because one and the same excited state ($v^* = 0$) of methyl nitrite results in such different vibrational population of NO fragments, *i.e.*, either in $v'' = 0$ and 1 vibrational states, for the case of 3_0^0 transition or only in $v'' = 0$ vibrational state, for the case of 3_1^0 transition. Also, it differs from the vibrational state population of NO fragments resulting from the photodissociation of *trans*-methyl nitrite. In both isomers, the vibrations of the N=O chromophor are excited and this energy is transfered to the dissociating ON-O bond. The structural difference of both isomers cannot explain such a difference in the final vibrational state population of NO fragments. On the

base of these arguments, the Pfab's assignment does not seem to be adequate. In the following, Tarte's assignment is accepted as the correct one.

The overall intensity of the ion signal observed in [26] has let the author to conclude that the non-adiabatic dissociation channel is more preferential for the *cis*-methyl nitrite isomer. In the present work, however, the overall intensities of the ion distributions for both channels are comparable.

3.1.4.1 Anisotropy

The observed NO photofragment angular distributions demonstrate high anisotropies with an anisotropy parameter β of about -0.8 which is close to the limiting case of -1 for a single-photon perpendicular dissociative transition in the axial recoil limit. The reduction of the β parameter from its limiting case could be caused by rotation of the parent molecule before it dissociates. Under this assumption, one can estimate the upper limit of the S_1 lifetime of $\tau \approx 350$ fs by using the model proposed in [87, 9] where the anisotropy parameter is given by Eq. 2.15.

Previous studies on the *cis*-isomer dissociation have clearly shown that the fragment trajectories lie in the plane of the parent molecule [16, 88]. Calculations done in the present work both at the CIS/6-311^{++}G(d,p) and TD-DFT/6-311^{++}G(d,p) levels of theory show that the transition dipole moment is almost perpendicular to the plane of the parent molecule. Assuming that the trajectories of the departing fragments of the *trans*-isomer also lie in the plane of the parent molecule, the angle Θ between the velocity vector of the departing photofragments $\vec{v}$ and transition dipole moment $\vec{\mu}$ is calculated as $\Theta = 89°$. The limiting values of β can only be obtained if the lifetime of the parent molecule in the excited state before it can dissociate (τ) is much shorter then the rotational period τ_{rot} since the anisotropy of the angular distribution reduces according to Eq. 2.16.

Approximating the methyl nitrite molecule by a pseudo-diatomic molecule, one can calculate the moment of inertia and estimate the angular velocity of the diatom ω of about $\sim 85 \cdot 10^{10}\ s^{-1}$. Solving Eq. 2.16 results in a lifetime of: $\tau \approx 350\ fs$.

The β parameter did not show any significant dependence on the photolysis wavelength and on the vibrational band of the NO fragment probed. Even though, in the present work only two photolysis wavelengths were probed, the results can be considered significant, since the values of the β parameter and the lifetime τ and their independence on the excitation energy are very close to the results obtained for the *cis*-methyl nitrite molecule [26]. Theoretical calculations on *cis*-methyl nitrite show that lifetime decreases monotonically from 250 fs ($v^* = 0$) down to 30 fs ($v^* = 8$) [89]. Most probably, the dependence of β and consequently the lifetime of the S_1 state within the experimental range investigated in the present work ($v^* = 0,\ 1$) is too weak to be observed. The average value of the β parameter for the *trans*-isomer

measured in the present work is slightly smaller than for the *cis*-isomer measured in [26], which means a longer lifetime of the parent molecule before it dissociates, compared to *cis*-methyl nitrite.

3.1.4.2 Dissociation energy

From the observed maximum kinetic energy release the dissociation energy of a chemical bond of interest can be determined *via* the energy conservation low. This gives a direct spectroscopic value of the bond dissociation energy. The present research demonstrates the independence of the dissociation energy of the O-NO bond of methyl nitrite on the vibrational excitation of NO chromophor of the parent molecule and the vibrational and rotational excitation of the detected NO fragment. The measured and averaged value of the dissociation energy is:

$$D_0^0 = 13\ 560\ \text{cm}^{-1} \pm 200\ \text{cm}^{-1}$$

This value of the O-NO dissociation energy of *trans*-methyl nitrite is the same as for the *cis*-isomer ($D_0^0 = 13\ 420\ \text{cm}^{-1} \pm 200\ \text{cm}^{-1}$ [26]) within the experimental error. The O-NO bond dissociation energy was calculated *via* Hess' law using the known enthalpies of formation at 0 K (ΔH_f^0) of the parent molecule (-65.44 ± 0.84 kJ/mol) [90, 91], the methoxy radical ($+17 \pm 4$ kJ/mol) [92, 93] and nitric oxide (+90.29 kJ/mol)[94]. This gives a value of $D_0^0 = 14\ 470\ \text{cm}^{-1}$, which is higher than the spectroscopically determined value due to discrepancies in the exact values of ΔH_f^0. Quantum chemical calculations of the dissociation energy made by Thuemmel within both the DFT level of theory with hybrid functional B3LYP and the multilevel G2 method [95] gave values of $D_0^0 = 13\ 595\ \text{cm}^{-1}$ [96]. It is well known that the G2 level typically gives results with ± 1.6 kcal/mol accuracy [97]. Thus, within the experimental and theoretical errors, our value of the dissociation energy and the Thuemmel's values coincide.

The internal energy distributions of the CH_3O fragments, shown in Fig. 3.10, demonstrate an offset of $\approx 500\ \text{cm}^{-1}$ for $v'' = v^* = 0$ and $v'' = v^* - 1 = 0$. For the case when $v'' = v^* = 1$, the offset is about $\approx 1\ 200\ \text{cm}^{-1}$. The average internal energies of the CH_3O fragments is even higher (see Fig. 3.10). These data point out that the assumption of the zero internal energy of CH_3O, which was made in the determination of the dissociation energy of methyl nitrite, is not completely reliable and results in the exaggerated value of the dissociation energy. Therefore, the dissociation energy determined here represents the upper limit value.

3.1.4.3 Energy Distributions

The observation of the kinetic energy distribution of the NO photofragment allows one to study the total kinetic energy release during the photolysis of methyl nitrite as

well as the internal energy distribution of the CH_3O co-fragment. The present results clearly show that 54% to 72% of the available energy flows into the translation energy and the rest (46% - 28%) flows into the internal energies of the photofragments (see Table 3.5). Some is in rotational energy of NO ($j'' = 33.5$).

Table 3.5: Partitioning of the available energy into the translational and internal energies of the NO and CH_3O photofragments in %.

$E_{avail.}$	$v^* - v''$	$\frac{TKER}{E_{avail.}}$	$\frac{E_T(NO)}{E_{avail.}}$	$\frac{E_{int}(NO)}{E_{avail.}}$	$\frac{E_T(CH_3O)}{E_{avail.}}$	$\frac{E_{int}(CH_3O)}{E_{avail.}}$
12539	(0 - 0)	67	34	0.15	33	19
12906	(1 - 0)	62 - 71	31 - 35	0.15	30 - 36	22-14
12922	(1 - 0)	60 - 71	30 - 36	0.15	30 - 35	25-14
13149	(1 - 0)	60 - 72	31 - 37	0.15	30 - 35	25-13
13276	(1 - 1)	54	27	0.28	27	19

In Table 3.5 the two values for the non-adiabatic dissociation channel of the methyl nitrite molecule correspond to the two peaks observed in the ion distribution (see Fig. 3.7 and 3.10 above).

The energy distibutions suggest that the excess energy in the photodissociation step initially stored in the vibrational excitation of the NO chromophor of the parent molecule preferentially flows directly into the dissociating bond and there is not enough time for the available energy to be redistributed among the other degrees of freedom of the parent molecule. The fraction of the available energy released as kinetic energy decreases with increasing vibrational excitation of the NO fragment.

Wilson *et al.* [98] have developed an impulsive model for the dissociation of a triatomic molecule, which was modified by Tuck [99] for polyatomic molecules. It was shown for the examples of C_2H_5ONO [99] and *cis*-CH_3ONO [14, 100] that this model gives reliable values of the fraction of the available energy which is shared between translational and internal energies of the NO fragment [14, 99], but no data are available for the CH_3O radical. The main idea of the impulsive model is that the photodissociation is rapid, occurring instantly as the result of the creation of a steep repulsive potential along the dissociation bond. It is assumed that the atoms of the dissociating bond recoil sharply and release the energy before the other atoms have time to respond. Other atoms are considered as spectators and the available energy $E_{avail.}$ is partitioned among the recoiling atoms according to the conservation of linear momentum. Such a model, because of the short lifetime of the photoexcited species, predicts a strongly anisotropic angular distribution of photofragments [99]. As discussed in section 3.1.4.1, the high anisotropy in the fragment distribution supports the main idea of the impulsive nature of the dissociation of methyl nitrite.

However, the model has to be used with care. The main reason is that not all assumptions are valid and work properly for all nitrites. Such assumptions that the atoms of the dissociating bond release the energy before the other atoms have time to respond and other atoms are just spectators, and additionally, the simplification of the molecule as pseudo-diatom, are questionable. The impulsive model does not work for the case of HONO molecule due to the non-rigidy of the OH bond (see [101]).

Within the impulsive model, the methyl nitrite molecule can be regarded as a planar molecule with the hydrogen atoms collapsed into the carbon atoms to which they are attached (Figure 3.11). This gives pseudo-diatoms with atomic masses 15, 16, 14 and 16 named by the Greek letters as α, β, γ and δ. The photodissociation of the $\alpha\beta - \gamma\delta$ molecule produces the fragments $\alpha\beta$ and $\gamma\delta$ with the masses of 31 and 30, respectively.

The following assumptions are made in the impulsive model: (1) All the available energy initially goes into translation of the atoms β and γ, which at the moment of dissociation are deemed to be independent of the rest of the atoms in the fragments. (2) The conservation of linear momentum is applied to the atoms recoiling from the impulsive dissociation, yielding their translational energies (E_T^β and E_T^γ). (3) The translational energy carried by those two atoms after the photolysis is shared among the translational, rotational and vibrational degrees of freedom of the fragments. (4) The fragment translational energies $E_T^{\alpha\beta}$ and $E_T^{\gamma\delta}$ are calculated by applying the conservation of momentum to each of the fragments as the recoiling atom in each is slowed by the remainder of the fragment. (5) The rotational energies of the fragments ($E_R^{\alpha\beta}$ and $E_R^{\gamma\delta}$) are calculated from the calculated angular momenta J_β and J_γ associated with the atoms recoiling with translational energies E_T^β and E_T^γ about the centres of mass of the fragments $\alpha\beta$ and $\gamma\delta$. (6) The vibrational excitation of the parent molecule is neglected. No assumptions are made about the stiffness of any of the vibrations, which means that no restrictions are placed on the amount of energy which may appear as fragment vibrational excitation. The following formulae result from the above assumptions:

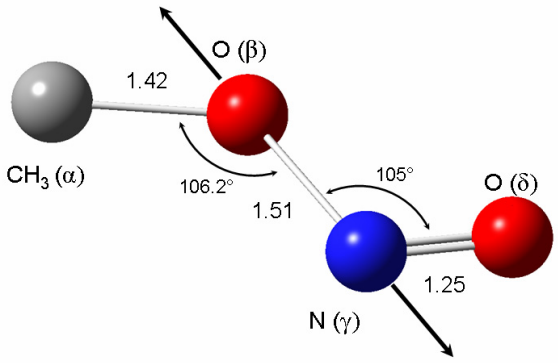

Figure 3.11: Impulsive model of the partitioning of the available energy among the photofragments.

$$E_T^\beta = E_{avail.} \cdot \left(\frac{m_\gamma}{m_\beta + m_\gamma} \right), \tag{3.1}$$

where E_T^β is the translation energy of the recoiling atom at the end of the dissociating bond, $E_{avail.}$ is the available energy from the dissociation step and m_i is the mass of the recoiling atom.

Application of the linear momentum conservation gives the relations for the translation energies of the fragment:

$$E_T^{\alpha\beta} = E_{avail.} \cdot \frac{m_{\gamma\delta}}{M} \cdot \frac{\mu_a}{\mu_f}, \tag{3.2}$$

where $E_T^{\alpha\beta}$ is the translation energy of the recoiling fragments, $m_{\gamma\delta}$ is the mass of the correlated fragment, M is the mass of the parent molecule, μ_a is the reduced mass of the recoiling atoms at the ends of the dissociating bond and μ_f is the reduced mass of the fragments.

Assuming that the angular momenta J_β and J_γ are conserved, the rotational energy of the fragment can be calculated from the following equation, using a $\alpha-\beta-\gamma$ bond angle χ of 106.2°, which was calculated for the transition state on the S_1 surface *via* the CASPT2 technique [102] in Ref. [103]:

$$E_R^{\alpha\beta} = E_{avail.} \cdot \mu_a \cdot \frac{r_\beta^2 \cdot sin^2\chi}{I_{\alpha\beta}}, \tag{3.3}$$

where $E_R^{\alpha\beta}$ is the rotational energy of the fragment, r_β^2 is the distance from the center of mass of the fragment to the recoiling atom of this fragment and $I_{\alpha\beta}$ is the principal moment of inertia of the fragment.

The fragment vibrational excitation may be calculated by applying the conservation of energy to the fragments. This gives:

$$E_V^{\alpha\beta} = E_T^\beta - E_T^{\alpha\beta} - E_R^{\alpha\beta}, \tag{3.4}$$

where $E_V^{\alpha\beta}$ is the vibrational energy of the fragment.

Taking into account that the NO radical has a certain internal energy because it was probed in a certain quantum state for each excitation scheme, the available energy must be corrected for this energy:

$$E_{avail.} = E_{h\nu} - D_0^0 - E_{int}^{NO}, \tag{3.5}$$

where $E_{avail.}$ is the available energy used in the impulsive model calculations, $E_{h\nu}$ is the photon energy, D_0^0 is the dissociation energy of the parent molecule and is equal to 13 560 cm^{-1} ± 200 cm^{-1} and E_{int}^{NO} is the internal energy of the NO fragment (E_{int}^{NO} = 1 922 cm^{-1} for $v''=0$ and E_{int}^{NO} = 3 778 cm^{-1} for $v''=1$).

The Table 3.6 presents the results of the energy partitioning between translational and internal (vibrational and rotational) degrees of freedom of the fragments calculated within the impulsive model approximation (Eq. 3.1-3.5). The geometrical parameters necessary for the estimation were taken from references [103, 104].

Table 3.6: Partitioning of the available energy between translational (E_T), vibrational (E_V) and rotational (E_R) degrees of freedom of the CH_3O photofragment calculated within the impulsive approximation compared with the experimental results. All energies are given in cm^{-1}.

$E_{avail.}$	$v^* - v''$	$E^{NO\,a}$	E_T^{imp}	E_T^{exp}	E_V^{imp}	E_R^{imp}	$E_{int}^{exper.}$
10617	0-0	5662	2558 (3908)[b]	4069	1350 (0)	1047	2379
11000	1-0	5867	2650 (4049)	3798	1399 (0)	1085	3277
9498	1-1	5066	2288 (3486)	3410	1208 (0)	937	2556

[a] $E^{NO} = E_T^{NO} + E_R^{NO} + E_V^{NO}$

[b] values in brackets correspond to stiff bond modification.

In Table 3.6 the estimated energies for the non-adiabatic channel ($v^* = 1, v'' = 0$) are only compared with the first peak in the bimodal distribution observed in the present experiment (see Fig. 3.7). The results of the impulsive model are not really in a good agreement with the experimental ones. The translational energies and the internal energies are underestimated for both adiabatic and non-adiabatic channels. These systematic discrepancies obviously arise from the assumptions made about the geometry and non-rigid bonds of the methoxy radical fragment. If, however, the C-O bond and the N-O bond are considered as infinitely stiff then there would be no vibrational excitation in the CH_3O fragment as well as in the NO and this fraction of energy would be transfered to the translational energies of the fragments (see values in brackets in Table 3.6). Such a modification results in a better agreement with the experimental values (the calculated values are very close to the experimental values of the translation energies within the experimental error of $\pm 200 cm^{-1}$). However, the situation with the internal energy, which is pure rotational energy for the case of the "stiff" modification, does not get better. In spite of all experimental hints for an impulsive nature of the dissociation of *trans*-CH_3ONO such as anisotropy parameter values and high fractions of the translation energies of the fragments, the impulsive model cannot be used for a correct analysis of the energy partitioning among the rotational and vibrational degrees of freedom of the CH_3O fragment. In the case of the non-adiabatic dissociation, the discrepancies are most pronounced, probably due to the non-impulsive character of the dissociation of the parent molecule in this case. The larger FWHM and the bimodality of the internal energy distribution of the CH_3O fragment strongly suggest a vibrational excitation of the methoxy radical, with a redistribution of the excitation energy among the vibrational degrees of freedom of the NO and CH_3O groups within the methyl nitrite molecule prior to the dissociation of the parent molecule. This violates the main assumptions of the impulsive model. The failure of the impulsive

model at least in the case of the non-adiabatic channel, is therefore not surprising.

Concerning the bimodal distribution, the most probable explanation is the vibrational excitation of the CH_3 umbrella mode ν_2, the C-O stretching mode ν_3 or the CH_3 scissor like vibration ν_5 in the CH_3O fragment. The ion distributions after photolysis of *cis*-CH_3ONO measured in [26] show a weak bimodal distribution in the case of $v^* = 1, v'' = 0$ for detection of the NO fragment with $j'' = 33.5$, but a much stronger bimodal distribution was observed for $v^* = 2, v'' = 1$ for NO with $j'' = 26.5$. A weak shoulder was also observed for $v^* = 1, v'' = 0$ with $j'' = 26.5$. The bimodal distribution was explained there as vibrational excitation in the methoxy radical and, interestingly, the possible vibrational modes were the same ν_2, ν_3 and ν_5. The different rotational numbers of the NO fragment at which the bimodal distribution in the non-adiabatic channel were observed for both isomers likely originate from the structural differences. The *cis*-CH_3ONO has a hydrogen bond between the CH_3 and NO parts of the molecule and the *trans*-isomer does not have such a bond which affects the rotational excitation of the NO fragment. The vibrational modes possibly responsible for the bimodal distribution in the non-adiabatic channel are not only energetically suitable but also geometrically. This follows from simple kinetic consideration of the dissociation process and the structure of the parent molecule just before dissociation on the S_1 surface [103] and the structures of the NO and CH_3O photofragments. The most pronounced structural changes are presented in Table 3.7, the values were taken from [103, 19, 105].

Table 3.7: Theoretical structural parameters of *trans*-CH_3ONO at the top of the S_1 barrier, and of the CH_3O and NO radicals. Angles are in degrees (°), distances are in Å

Species	R(O-N)[a]	(C-O)	N-O	∠ CON	∠ ONO	∠ OCH_1	∠ H_2COH_3[b]
CH_3ONO	1.503	1.42	1.293	106.2	105	102.6	118.9
CH_3O[c]		1.394				112.9	115.1
NO			1.151[d]				

[a] dissociating bond
[b] dihedral angle
[c] The CH_3O structure is given for the $^2A'$ (X^2A') state (Jahn-Teller splitting), which was predicted for the dissociation of *trans*-CH_3ONO on the S_1 surface [103]
[d] Ref. [106].

The changes in the structures make the assumption plausible of an excitation of the CH_3 umbrella mode ν_2, the C-O stretching mode ν_3 or the CH_3 scissor like vibration ν_5 in the CH_3O fragment.

3.1.5 Conclusions

The photodissociation of the *trans*-methyl nitrite molecule following excitation into the S_1 state with 0 and 1 quanta of excitation in the NO-stretching mode has been investigated using the method of velocity map imaging. State selective probing of the nascent NO fragments with (1+1) REMPI was performed for NO in the vibrational states $v'' = 0$ and 1, with a rotational excitation of $j'' = 33.5$.

The resulting distributions of the total kinetic energy release and the internal energy of the methoxy radical show both a vibrationally non-adiabatic predissociation with a loss of one quantum of the NO vibrational excitation in the course of the dissociation and an adiabatic channel, where the dissociation occurs by tunneling through a potential barrier on the S_1 potential energy surface. The overall intensity of the detected ion signal in both channels is comparable.

For the non-adiabatic channel, a highly asymmetric and bimodal ion distribution was found for a rotational excitation of $j'' = 33.5$. The ion distributions for the adiabatic channels were monomodal and less asymmetric. The results were interpreted in favour of a selective vibrational excitation in the CH_3O fragment *via* intramolecular vibrational relaxation preceding dissociation. The accepted assumption of the methoxy group being simply a spectator is therefore at least questionable in this specific case, and an overall dissociation mechanism with the methoxy group participating in the IVR has to be considered. This result supplement the results observed in the previous study of the *cis*-isomer.

From the maximum of the kinetic energy release, the O-NO bond dissociation energy could be determined spectroscopically as $D_0^0 = 13\ 560 \pm 200\ \mathrm{cm}^{-1}$. This value is an upper limit, because some of the available energy is conserved as the rotational energy by CH_3O fragments, as it follows from the experimental results. The observed anisotropies of the photofragment angular distributions lead to an S_1 excited state lifetime of $\tau \approx 350$ fs.

3.2 Photolysis of Acetone-$h6$

3.2.1 Introduction

The photodissociation of acetone is the prototypical Norrish type-I reaction, a class of reaction that has been a subject of an enormous amount of photochemical investigations. Norrish and coworkers [29] investigated the fluorescence and photodissociation of acetone in bulk gas experiments and came to the conclusion that the main photolysis products of acetone after α-C-C bond cleavage are ethane (C_2H_6), formed by recombination of two methyl radicals (CH_3) and carbon monoxide (CO) (so-called Norrish Type I reaction). The exact mechanism of this reaction was intensively studied in the literature [107, 108, 109, 110, 111, 112].

The emission properties of acetone and acetone-$d6$ in different solvents and at different temperatures ($77-300$ K) have been studied by measuring the phosphorescence spectra to investigate the mechanism for relaxation of electronic excitation in [113]. The fluorescence as well as phosphorescence spectra of acetone and acetone-$d6$ were found to be identical under all conditions. The lifetime of the lowest (n,π^*) singlet state of acetone ($\tau_s = 2.5 \times 10^{-8}$ sec) was found to be primarily determined by intersystem crossing to the lower-lying excited triplet state. The quantum yield of acetone fluorescence at room temperature was found to be $\Phi_F = 0.01 \pm 0.003$. No deuterium effect on Φ_F was observed and therefore it was concluded that internal conversion was much slower than intersystem crossing which was not affected by deuteration [113].

Breuer and Lee have measured the fluorescence lifetime of acetone in the gas phase by using a single-photon time correlation technique at excitation wavelengths in the range from $313-260$ nm [114]. It was found that the quantum yield of the $S_1 \rightarrow T_1$ intersystem crossing was close to unity. The fluorescence lifetime was found to vary from 2.7 ns at $\lambda_{pump} = 313$ nm to less than 1.6 ns at $\lambda_{pump} = 260$ nm.

All experimental results obtained before 1985 can be summarized as follows:

1. The fluorescence lifetime of acetone is practically the same in the gas phase as it is in many solvents (a value of 2 ± 1 ns is almost universal).
2. This value is approximately the same for other small ketones.
3. There is a small isotope effect, that is, the decay time of acetone-$h6$ is shorter than that of acetone-$d6$.
4. There is a small wavelength dependence for acetone, *i.e.*, the lifetime decreases somewhat as the excitation wavelength is decreased.

The processes governing the decay of the S_1 state are fluorescence, intersystem crossing (ISC) to the T_1 state, and internal conversion (IC) to the S_0 state. Intersystem crossing from the initially excited $^1n\pi^*(S_1)$ state to the triplet state $^3n\pi^*(T_1)$, although symmetry forbidden [115] does in fact take place, due to some degree of mixing of $^3\pi\pi^*$ character into the singlet state. The $^3n\pi^*$ state is the only triplet state

energetically accessible near the low-lying vibrational levels of the S_1 state. That the radiationless transition takes place is evident from the fact that phosphorescence is observed in the gas phase and in condensed phases [114, 116, 117, 118, 113]. Triplet-triplet absorption was observed by flash spectroscopy following optical excitation of acetone (Ref. 37 in [111]).

Since supersonic jet cooling became available, Baba and Hanazaki have measured fluorescence excitation spectra of the S_1 state of acetone and acetone-*d*6 [116]. Active vibrational modes were determined as those of the CH_3 torsion and the CO out-of-plane wagging. The barriers to internal rotation of acetone-*h*6 and -*d*6 in the S_1 state have been estimated to be 740 ± 90 and 720 ± 60 cm^{-1}, respectively. The origin of the $0-0$ $S_1 - S_0$ electronic transition was measured to be 30 431 cm^{-1} and 30 435 cm^{-1} for acetone-*h*6 and -*d*6, respectively [116].

Comprehensive studies of the fluorescence properties of acetone in a molecular beam excited to the S_1 state were later done by Haas and co-workers [119, 120, 121] and summarized in the recent review [111]. The fluorescence decay time was measured to be ~ 800 ns for acetone and ~ 3300 ns for acetone-*d*6. The abrupt fluorescence decay and a spike-like signal profile overlapped with a long-lived component were detected for both isotopomers at an excess excitation energy above the $0-0$ origin of 800 for acetone-*h*6 and 1800 cm^{-1} for acetone-*d*6. This behavior was interpreted as an effective $S_1 - T_1$ coupling. The excess excitation energy of 2250 ± 50 cm^{-1} for acetone and 2500 ± 50 cm^{-1} for acetone-*d*6 leads to complete quenching of the long component in the fluorescence decay profile, which was attributed to a quenching of the signal due to the dissociation of acetone over a barrier on the T_1 state. The triplet dissociation barrier was estimated to be ~ 13.4 kcal/mol [120, 121, 111].

The first photodissociation experiments on gaseous acetone and formaldehyde were performed by photolysis mapping by Solomon *et al.* [109]. The samples were kept at very low pressure to prevent collisions. They observed an anisotropic angular distribution of the photofragments and interpreted their results as the carbonyl compounds becoming nonplanar in the excited state [109]. The first really collision-free photodissociation experiments on acetone were performed by Trentelman and co-workers [31]. The photofragment internal and translational energy distributions resulting from the 193 nm photolysis of acetone were measured. They found that the energy partitioning between the fragments could be well described by a simple impulsive model [98]. The obtained results might be characteristic for a stepwise dissociation reaction. Waits *et al.* have studied the photolysis of acetone excited to the S_1 state in a molecular beam. The following results were obtained: Excitation of a molecular beam of acetone at 266 nm leads to methyl photofragments that have been examined by REMPI and TOF-MS spectrometry. Analysis of the arrival time profile of CH_3 reveals a broad translational energy distribution for vibrationless (0_0) methyl photofragments, with mean energy $E = 45.8 \pm 4.0$ kJ/mol. The CH_3 0_0 photofragments are ejected isotropically in space, which contradicts early results

of Solomon [109]. Actually, all later researches on the acetone photodissociation have shown isotropic angular distributions of the fragments. The fragmentation was suggested to follow a stepwise mechanism [32]. It is necessary to mention, that for a symmetric ketone with two methyl groups which have equal probability for removal, the question arises whether the photolysis of acetone proceeds in a *concerted* or a *stepwise* manner. Additionally, if it does *via* a *concerted* mechanism, then whether it is *synchronous* or not. Comprehensive investigations of several work groups [31, 32, 33, 34, 35] have clearly shown a stepwise dissociation mechanism of collision-free acetone molecules excited either to the S_1 or to the S_2 state resulting in methyl and acetyl photofragments. Theoretical calculations also confirmed a stepwise mechanism [122, 37, 112].

The photodissociation dynamics of acetone excited to the S_1 and S_n (primary Rydberg) states was the subject of an enormous amount of femtosecond researches [123, 124, 125, 35, 126, 127, 112, 128, 129]. Owrutsky and Baronavski [125, 35, 127] and Zhong *et al.* [126] have suggested that excitation with 260 nm fs pulses induces decomposition on the S_1 state in less than 200 fs to form long-lived acetyl radicals, whereas Shibata *et al.* [130] and Diau *et al.* [112] argue that decomposition is preceded by a ratedetermining intersystem crossing from S_1 to T_1 and that decomposition to form long-lived acetyl radicals takes place from this state. With regard to the higher-lying excited states, there is computational evidence for the existence of an effectively repulsive surface that is reached though a series of conical intersections with resulting ultrafast decomposition of the Rydberg excited species [131, 128]. All of the pump–probe experiments with femtosecond resolution on gaseous acetone have been carried out with ionizing probe and time-of-flight detection [126, 131, 127, 128] or ion-photoelectron imaging [130, 129] techniques. The recent time-resolved photoelectron spectroscopy and mass spectrometry experiments in the spectral range of the excitation wavelengths of $288 - 253$ nm, performed by Rusteika and co-workers, have shown that the photodissociation dynamics of acetone that is induced by a one-photon excitation is governed by motion out of the Franck–Condon region on the S_1 surface to the relaxed geometry in less than 30 fs. The relaxed S_1 species does not decay in 100 ps and actual C-C bond breakage must take place on a longer time scale [129].

Acetone also plays an important role in the photochemistry of the Earth's troposphere [10]. Particular interest arises in the yield of acetyl (CH_3CO) radicals and its internal energy distribution as a function of photolysis wavelength, because the reaction $CH_3CO + O_2$ has recently been identified as a new source for tropospheric OH radicals. Corresponding experiments were done using pulsed photolytic generation of the radical and its detection by transient absorption spectroscopy at 216.4 nm. Experiments were carried out at room temperature (298 ± 3 K) and at pressures between 5 and 1500 Torr N_2. Quantum yields for CH_3 formation were derived relative to CH_3I photolysis at the same wavelength in back-to-back experiments [132, 133]. In this sense, the measurements on the photodissociation dynamics of bulk gaseous

acetone performed for a variety of pressures and sample temperature are of a special interest.

The photochemistry of acetone under tropospheric conditions was studied using a diode array spectrometer by Gierczak *et al.* [134]. The quantum yield for the photodissociation of acetone was measured as a function of pressure and wavelengths ($337 - 248$ nm) over the temperature range of 235 to 298 K. At wavelengths of $\lambda_{pump} > 270$ nm, the quantum yields were found to decrease with increasing pressure. The zero pressure quantum yield was found to increase as the wavelength decreased and reached a value of unity near 290 nm. The quantum yields at 308 nm were found to be nearly independent of temperature between 298 and 195 K. An expression for the variation of the acetone photodissociation quantum yield with pressure and wavelength was derived. The calculated atmospheric photolysis lifetime of acetone shows the photolysis to be the main loss process for acetone in the upper troposphere, while reaction with OH radicals dominates its loss rate near the Earth's surface [134].

Somnitz and co-workers measured the pressure dependent CO quantum yield (Φ_{CO}) of the acetone photolysis at 248 nm and 298 K [135]. The pressure was varied between $20 - 900$ mbar (N_2). It was found that the quantum yield of CO shows a significant dependence on total pressure with Φ_{CO} decreasing with increasing backing gas pressure. The CO production was shown to result from prompt secondary fragmentation of the internally excited primary acetyl photolysis with an excess energy of approximately 62.8 kJ/mol. A concerted acetone dissociation mechanism was considered to be unimportant [135].

Photolysis of several ketones over the wavelength range $330 - 248$ nm, the temperature range $218 - 298$ K, and the pressure range $0.3 - 400$ Torr was studied in [136]. The acetyl yield was determined relative to that at 248 nm by conversion to OH by reaction with O_2 [42]. Linear and non-linear Stern-Volmer (SV) plots ($1/[OH]$ *vs.* $[M]$) were interpreted as evidence for dissociation from two excited states of acetone: from the S_1 state, when SV plots are linear and both from S_1 and T_1, when SV plots are nonlinear. A model for acetone photolysis was proposed that can adequately describe the experimental data. The pressure quenching was observed to become more efficient with increasing wavelength. The simulations done by Blitz *et al.* show that acetone photolysis occurs more slowly at the top of the troposphere [136].

The reaction $CH_3CO + O_2 \rightarrow OH +$ products, proposed in [42] as a detection scheme, was studied experimentally in isothermal discharge flow reactor with LIF monitoring of OH [132] and theoretically [137] due to the important role, which this reaction plays itself in the Earth's atmosphere. OH formation was found to be the dominant reaction channel for the aforementioned reaction, which shows the characteristics of a chemically activated system. The rate constant of the overall

reaction has been found to be pressure dependent. The OH yield decreases rapidly with increasing pressure [132].

The unimolecular decomposition of the acetyl radical, formed *via* acetone photolysis, competes with the reaction of CH_3CO and O_2 in the Earth's troposphere. The knowledge about the photolysis quantum yield of collision-free acetone and the internal energy distributions of the nascent fragments is very important, because such information dictates the unimolecular decay rate of acetyl in competition with the collisional reaction with N_2 and O_2, present in the Earth's atmosphere. The main role in the photolysis of acetone in the Earth's atmosphere is determined by UV-B (280 nm $\leq \lambda \leq$ 315 nm) and UV-A (315 nm $\leq \lambda \leq$ 400 nm) radiation, since radiation shorter than 200 nm (UV-C) is mostly blocked by oxygen in the upper layers of the atmosphere.

The investigation of the internal energy distribution among the photofragments with respect to certain dissociation pathways was the subject of the present research. The present work focuses on investigations of the acetone dissociation dynamics following photoexcitation of the S_1 state (220 nm $\leq \lambda \leq$ 333.5 nm). The CH_3 fragment has been monitored from the photodissociation of acetone following $S_1 \leftarrow S_0$ excitation at wavelengths between 333.5 and 230 nm using velocity map imaging.

The UV absorption spectrum of acetone in the gas phase (p = 18.2 mbar and T = 298 K) recorded in the wavelength range from 400 nm to 190 nm is shown in Fig. 3.12. It demonstrates two absorption bands, a weak, unstructured and broad one in the region from 340 to 220 nm with its maximum around 280 nm and a strong band with a weak vibrational progression peaking at 193.7 nm.

The first weak band corresponds to the transition from the ground singlet state (S_0) to the first electronically excited singlet S_1 state. An enlarged view is shown in the inset in Fig. 3.12. Acetone in its ground electronic state belongs to the C_{2v} point group, thus direct photoexcitation of acetone to the first excited singlet state $^1A_2 \leftarrow {}^1A_1$ is symmetry forbidden. Typical absorption cross sections found are of the order of 10^{-20} cm^2 [134].

The electronic transition between the states ϕ_e'' (lower state) and ϕ_e' (upper state) is allowed, if the electric dipole moment selection rule is fulfilled:

$$\begin{aligned} \Gamma(\phi_e') \otimes \Gamma(T_x) \otimes \Gamma(\phi_e'') &\supset A_1 \\ \text{and/or } \Gamma(\phi_e') \otimes \Gamma(T_y) \otimes \Gamma(\phi_e'') &\supset A_1 \\ \text{and/or } \Gamma(\phi_e') \otimes \Gamma(T_z) \otimes \Gamma(\phi_e'') &\supset A_1 \end{aligned}$$

From these expressions, it follows that the $^1A_1 \rightarrow {}^1A_2$ transition is forbidden. However for acetone the selection rule is lowered by vibronic coupling of the $^1A_2$ state

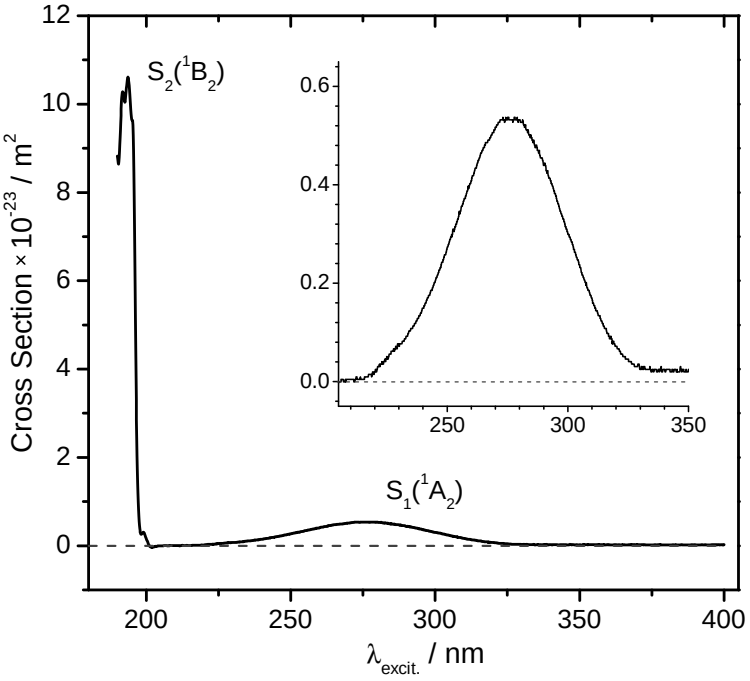

Figure 3.12: UV absorption spectrum of acetone in the gas phase. The inset shows the scaled-up absorbance peak assigned to the $S_0 \rightarrow S_1$ ($n\pi^*$) transition.

to the energetically higher $^1B_2$, 2^1A_1, and $^1B_1$ states *via* the Herzberg-Teller mechanism, which makes the $^1A_2 \leftarrow {}^1A_1$ transition visible in the absorption spectrum by intensity borrowing.

The second $^1B_2$ band in the UV absorption spectrum of acetone occurs due to a relative strong (σ $\sim 10^{-22}$ m^2) electronic excitation to the second excited singlet $S_2(^1B_2)$ state, which has Rydberg-(3s) character.

Electronic excitation of the S_1 state proceeds *via* promotion of the non-bonding electron to an antibonding orbital in the carbonyl group (CO), so the first electronic transition has ($n\pi^*$) orbital character. The broad unstructured shape of the first absorbtion band originates from significant changes in geometry. The optimized acetone geometry in its ground and first excited singlet states are shown in Fig. 3.13. The calculations were performed using the Gaussian 03, Revision C.02, suite of programmes [138].

The ground state geometry of acetone was optimized at MP2 level of theory with the 6-311^{++}(3df,p) basis set of functions. The calculations show that the C-C(O)-C atomic frame is planar. These results are in a good agreement with those of Liao *et al.* [36] calculated at the B3LYP/6-311G** level.

The excitation energy of the S_1 state and its optimized geometry were calculated at CIS level with the same basis set. As was mentioned above, the S_1 state has

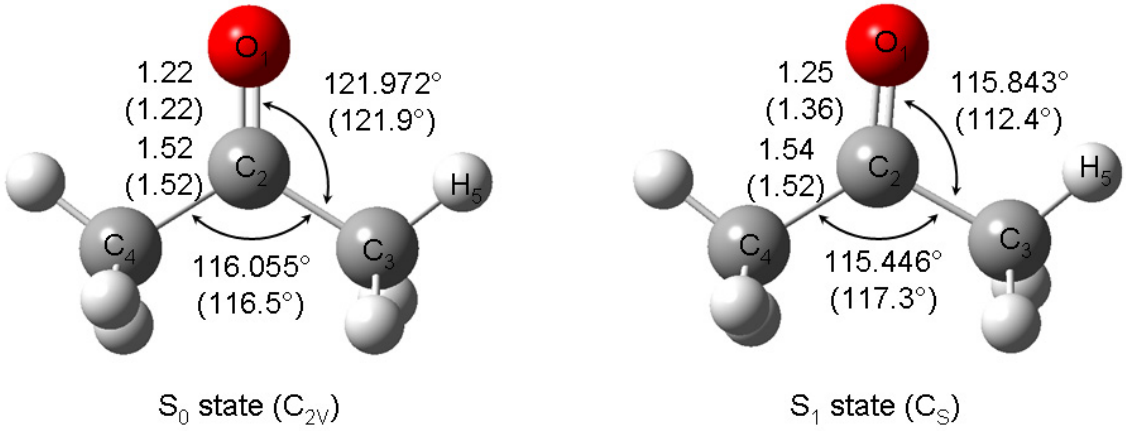

Figure 3.13: Geometries of acetone in its S_0 and excited S_1 states calculated at the MP2 level of theory with 6-311^{++}(3df,p) basis set (this work). For comparison, values in parentheses for the ground and excited states are taken from reference [36].

$n\pi^*$ molecular orbital character which results in a weaker and longer C=O bond (1.25 Å in the excited state state instead of 1.22 Å in the ground state) due to the π^* electron. The C-C bonds do not change significantly. Another geometry change occurred to the plane angle formed by C-C(O)-C atoms. The oxygen atom lies far out of the plane formed by the three carbon atoms and forms 140.1° angle. The C-C-O angles change strongly as well and the difference in their values in the ground and excited states is about $\approx 10^0$. Liao *et al.* [36] calculated the $n\pi^*$ transition in acetone by the CASSCF approach with an active space formed by 10 electrons distributed among 11 orbitals approximated by the 6-311** basis set. Their results show little difference in the excited state geometry (see values in parentheses in Fig. 3.13) compared with the calculations in the present work. The C=O bond elongation effect was calculated to be $\Delta r = 0.135$Å, which is more than calculated at the CIS level. The C-C(O)-C plane angle is slightly less but equal to 132.4°. Similar changes occur with the C-C-O angles. It is well-known that the CIS method is not a good technique to calculate excited state energies because of the strong exaggerations, but it can be used for geometry optimizations of low-lying excited states. The geometry parameters evaluated at the CIS level do not differ drastically from the more advanced CASSCF approach. As it was shown above, upon excitation of acetone molecule to the first excited singlet ($^1n\pi^*$) state, a pyramidalization of the carbon atoms and a stretching of the C=O bond occurs. Thus S_1 acetone in its equilibrium geometry belongs to the C_S point group and the optimized excited state is described by the $^1A''$ symmetry species rather than $^1A_2$.

Irradiation of ketones in the gas phase with wavelengths corresponding to the absorption of the carbonyl group is known to result in their decomposition [139]. Comprehensive investigations of several groups [31, 32, 33, 34] have clearly shown a stepwise dissociation mechanism of collision-free acetone molecules excited either to the S_1

or to the S_2 states resulting in methyl and acetyl products with a successive decomposition of the acetyl fragment to a secondary methyl radical and carbon monoxide, if the internal energy of the acetyl fragment exceeds the dissociation barrier of $\sim$ 17 kcal/mol [140], *e.g.*:

$$(CH_3)_2CO + h\nu \xrightarrow{k_1} CH_3 + CH_3CO^*$$
$$CH_3CO^* \xrightarrow{k_2} CH_3 + CO$$

The dissociation energy necessary for these two types of photoreactions can be estimated from the standard enthalpies of formation at 0 K, taken from Ref. [141, 142]:

$$\begin{aligned}\Delta_f H^o((CH_3)_2CO) &= -202 \pm 0.6 \text{ kJ} \cdot \text{mol}^{-1}\\ \Delta_f H^o(CH_3CO) &= -3.6 \pm 1.8 \text{ kJ} \cdot \text{mol}^{-1}\\ \Delta_f H^o(CH_3) &= 150.3 \pm 0.4 \text{ kJ} \cdot \text{mol}^{-1}\\ \Delta_f H^o(CO) &= -113.8 \pm 0.8\text{kJ} \cdot \text{mol}^{-1}\end{aligned}$$

Using Hess' law: $D(AB) = \Delta_f H^o(A) + \Delta_f H^o(B) - \Delta_f H^o(AB)$, we obtain

$$D_0((CH_3)_2CO \rightarrow CH_3 + CH_3CO) = 348.9 \text{ kJ/mol} = 29166 \pm 135\text{cm}^{-1} \quad (3.6)$$
$$D_0((CH_3)_2CO \rightarrow 2CH_3 + CO) = 388.8 \text{ kJ/mol} = 32518 \pm 184\text{cm}^{-1} \quad (3.7)$$

Intensive theoretical investigations [122, 37, 112] have shown that the S_1 state is bound with respect to the C-C reaction coordinate and the direct dissociation which can result in CH_3 and CH_3CO fragments in their ground states ($^2A''$) and ($^2A'$), respectively, is not possible from the S_1 state, *i.e.*, the S_1 state of acetone does not correlate with the ground states of methyl and acetyl. Indeed, several groups have recorded fluorescence excitation spectra from acetone following the excitation to the S_1 state [29, 116, 119]. The fact that acetone exhibits strong and long-lived ($\sim 4\times10^{-4}$ s) phosphorescence decisively points out the existence of an effective intersystem crossing process between the initially populated singlet S_1 state and a low-lying triplet ($^3n\pi^*$) state (T_1) [113]. The phototofragment translation and internal energy distributions data on acetone dissociation, gathered by several groups [31, 32], were interpreted as follows: The dissociation of acetone molecule occurs on the triplet $T_1(^3n\pi^*)$ state, which has a dissociation barrier caused by an avoiding crossing with the $T_2(^3\pi\pi^*)$ state. The height of the barrier was estimated by Zuckerman and coworkers and postulated to be 13.4 kcal/mol [120]. Thus, it is obvious that acetone photolysis involves one or several radiationless transitions which can result in different final internal energy distributions of CH_3 and CH_3CO photofragments. Potential energy surfaces (PESs) involved in the photochemistry of acetone are shown in Fig. 3.14.ted as follows: The dissociation of acetone molecule occurs on the triplet $T_1(^3n\pi^*)$ state, which has a dissociation barrier caused by an avoiding crossing with the $T_2(^3\pi\pi^*)$ state. The height of the barrier was estimated by Zuckerman and coworkers and postulated to be 13.4 kcal/mol [120]. Thus, it is obvious

that acetone photolysis involves one or several radiationless transitions which can result in different final internal energy distributions of CH_3 and CH_3CO photofragments. Potential energy surfaces (PESs) involved in the photochemistry of acetone are shown in Fig. 3.14.

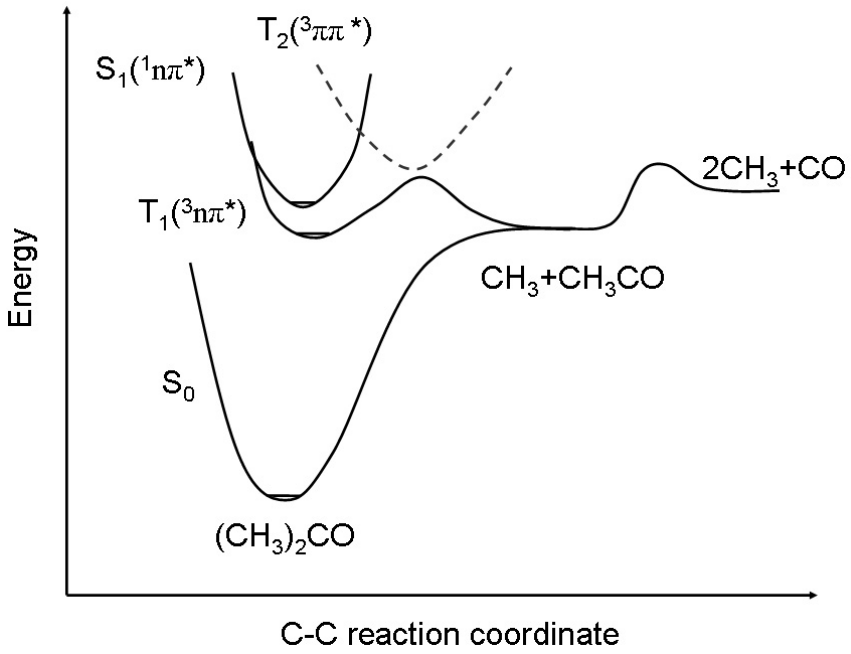

Figure 3.14: Schematic view of potential energy surfaces of acetone.

3.2.2 Time-of-Flight Mass Spectrometry of Acetone

The time-of-flight mass spectrum of acetone in Fig. 3.15 was taken at a photolysis and ionization wavelength of $\lambda = 286.3$ nm at moderate laser powers ($\sim$ 0.37 μJ/pulse). Ion signals due to the parent ($(CH_3)_2CO$ = 58 Da) and photolysis reaction intermediates, corresponding to the acetyl (CH_3CO = 43 Da) and methyl (CH_3) radical can be clearly identified in the TOF mass spectrum. There are also other fragments (mass peak intensity less then 10% of the normalized intensity) which increase in intensity with increasing photolysis laser power.

The TOF mass spectrum also exhibits an undesired mass peak corresponding to $(acetone)_2$ clusters. Clusters of higher order were not detected. The presence of clusters in the molecular beam negatively influenced the results of transient measurements. Therefore, different experimental conditions were tested to optimize the conditions to avoid clusterization in the molecular beam, but it was impossible to eliminate it completely. The best set of experimental parameters minimizing acetone clusterization were found as following: liquid acetone reservoir temperature $T = 233$ K, helium carrier gas pressure $p = 1013$ hPa, molecular valve opening

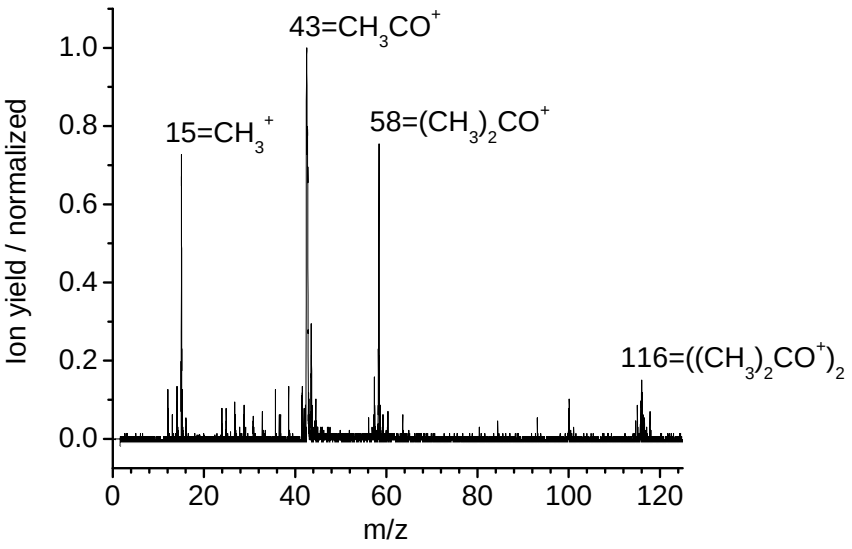

Figure 3.15: Acetone one-color time-of-flight mass spectrum recorded at 286.3 nm

time of $\Delta t = 200$ μs. The time delay between valve and photolysis laser was synchronized so that the laser crossed the molecular beam at the early part of the molecular beam. Short molecular pulse durations combined with the detection of molecules only at the front region of the molecular beam negatively affected the cooling efficiency, but reduced the amount of clusters drastically (see Section 2.2).

3.2.3 REMPI Detection of the Methyl Radical

After photoexcitation of acetone, its dissociation dynamics were studied by detecting the methyl photofragment distribution in the present work. The methyl radicals were probed by resonance enhanced multi-photon ionization (REMPI). Firstly, for calibration and line identification purposes, different electronic transitions of methyl, produced by photolysis of methyl iodide (CH_3I) at $\lambda = 286$ nm were probed (see Fig. 3.16). The recorded REMPI spectra are in a good agreement with the literature [143, 144]. They exhibit a well pronounced peak, which corresponds to the ionization of methyl radicals in their vibrational ground state ($v = 0$) *via* the Q-branch of the electronic transition either to the $3p^2A_2''$ or the $4p^2A_2''$ states (Figures 3.16 a) and b), respectively). The (2+1) REMPI spectra of the methyl radicals produced by photolysis of acetone at 286 nm are shown in Fig. 3.17. The detection scheme of the methyl radicals *via* the Q-branch of the $3p^2A_2''$ electronic transition ($\lambda_{probe} = 333.5$ nm) (see Fig. 3.17 (a)) was chosen as the better one compared to the (2+1) REMPI *via* the $4p^2A_2''$ state ($\lambda_{probe} = 286.3$ nm) (see Fig. 3.17 (b)) for several reasons: (i) The intensity of the REMPI signal *via* the $3p^2$ Rydberg state is much stronger than *via* the $4p^2$ Rydberg state. (ii) The ionization of methyl *via* the $3p^2$ state demands

laser pulses of wavelength $\lambda_{pump} = 333.5$ nm, which is lower in energy than the first absorption band of acetone (see Fig. 3.12). This fact is very helpful for two-color experiments, where the pump laser beam is adjusted over a broad spectral region scanning the first absorption band.

Probing methyl radical fragments using the Q-branch gives an additional advantage. The Q-branch is formed by rotational transitions with $\Delta J = 0$, thus all possible J states of the fragments within a given electronic transition can be probed simultaneously. The width of the Q-branch base is ~ 8 cm^{-1}, dictating the minimal necessary spectral region to be scanned over for the methyl detection in velocity map imaging experiments.

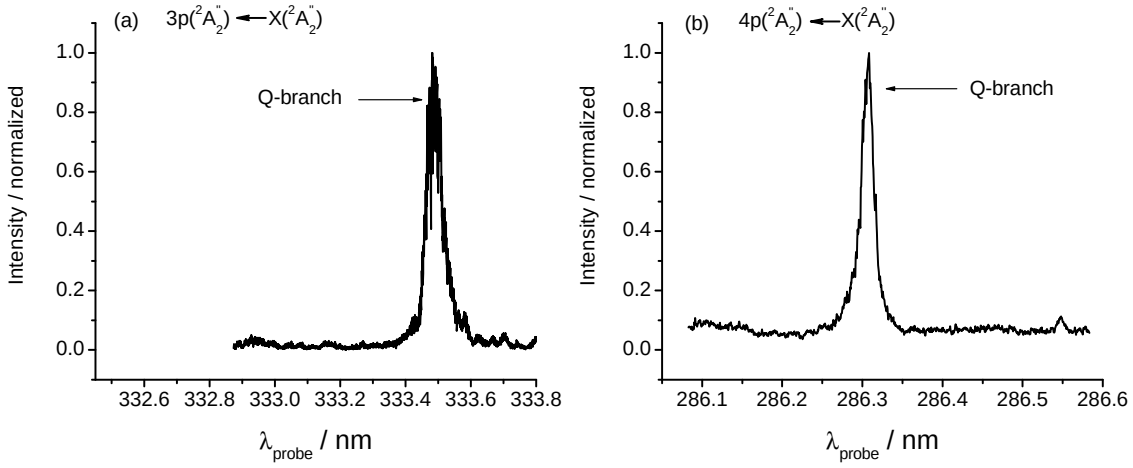

Figure 3.16: (2+1) REMPI spectra of CH_3 ($v = 0$) *via* the $3p^2A_2''$ state (a) and *via* the $4p^2A_2''$ state (b) from methyl iodide photolysis at $\lambda_{pump} = 286$ nm.

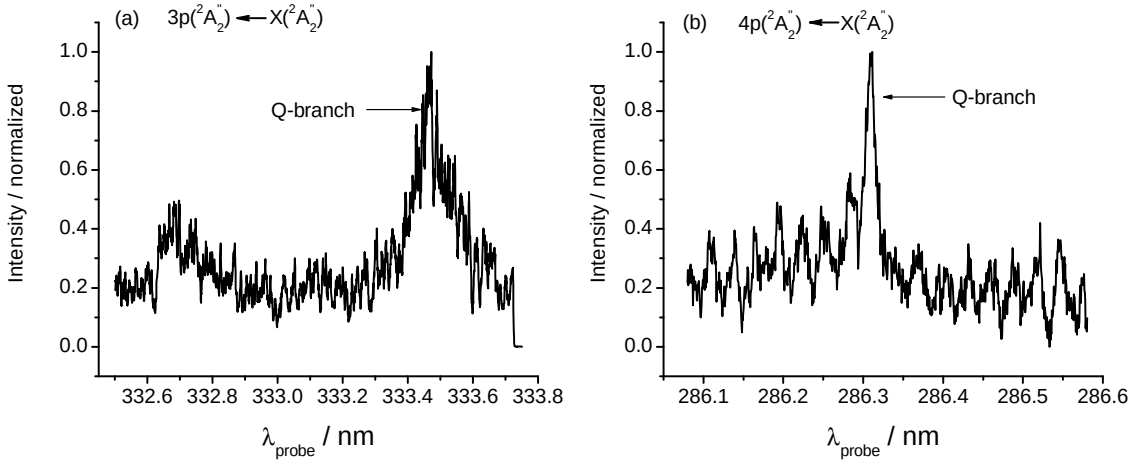

Figure 3.17: (2+1) REMPI spectra of CH_3 ($v = 0$) *via* the $3p^2A_2''$ state (a) and *via* the $4p^2A_2''$ state (b) from acetone photolysis at $\lambda_{pump} = 286$ nm.

The powers of the photolysis and probe laser beams were decreased until no ion signal produced by one-color only was detected. As can be seen on the lower trace of Figure 3.18 (a), no photodissociation of acetone was caused by the probe beam alone and no methyl radical ionization was observed by the photolysis laser beam. The intensity of the mass peak at 15 Da, and accordingly the REMPI signal as well, depend on the time delay between the photolysis (pump) and probe laser beams. This dependence was carefully checked for the range of time delays from 0 ns to 100 ns (Figure 3.18 (b). It stands to reason that the most intense mass peak was detected at 20 ns time delay between pump and probe laser, so this time delay was used for all following experiments.

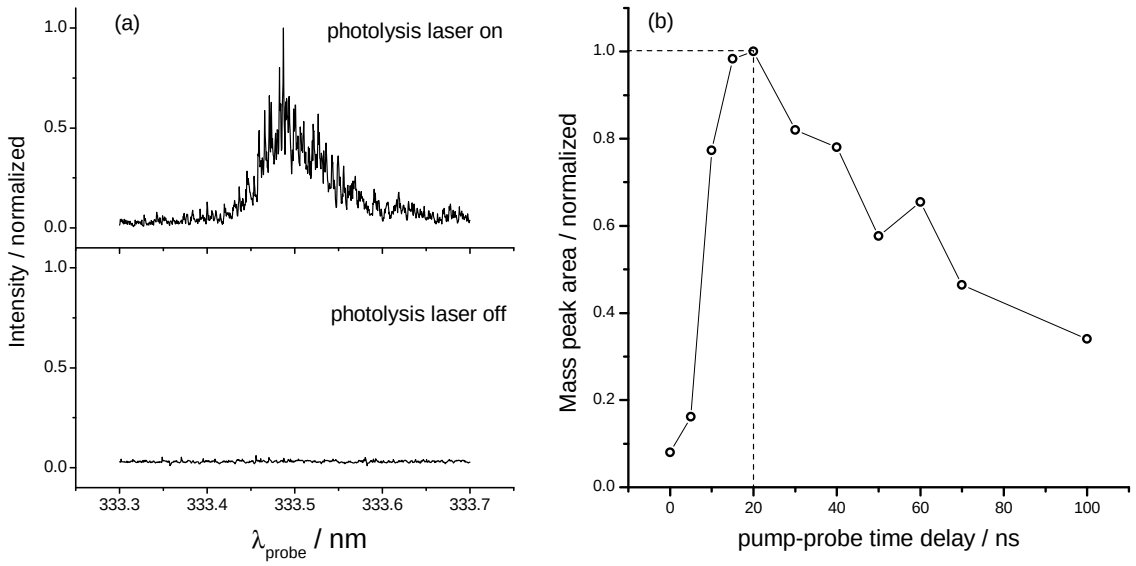

Figure 3.18: Dependence of the CH_3 REMPI signal on the photolysis laser (a) and dependence of the intensity of the mass peak at 15 Da on the time delay between the pump and probe laser pulses. ($\lambda_{pump} = 286$ nm; $\lambda_{probe} = 333.5$ nm).

The dependence of the REMPI signal on the time delay was also investigated. The most representative REMPI spectra are shown in Fig. 3.19. The REMPI signal showed several characteristic features. The overall signal intensity decreased with increasing time delays from 20 ns to 100 ns. The shape of the Q-branch changed, as well its widths became smaller, and at a delay of 100 ns the Q-branch was hardly recognizable. There are several reasons for such an evolution of the REMPI signal: (i) A decrease of the overall intensity of the ion signal was caused by removal of methyl photofragments from the ionization volume due to their high translation energy which they acquired during the dissociation act. (ii) The change of the Q-branch shape and its width can be explained by relaxation of the population of the rotational states of the methyl radical so that the occupation number of the rotational states with higher J decreased.

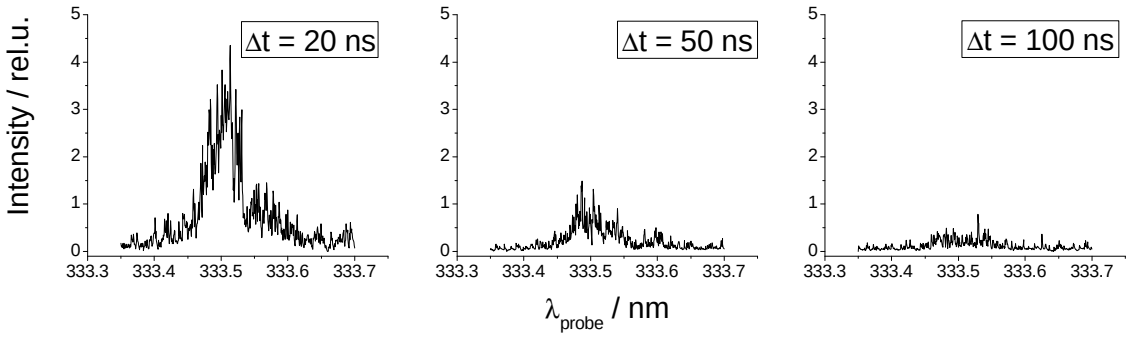

Figure 3.19: (2+1) REMPI of methyl radical recorded at different time delays between pump and probe laser pulses. ($\lambda_{pump} = 286$ nm; $\lambda_{probe} = 333.5$ nm)

3.2.4 Velocity Map Imaging of the Photodissociation Dynamics of Acetone

The acetone dissociation dynamics following $S_1 \leftarrow S_0$ photoexcitation were studied by monitoring the methyl photofragment translation energy distributions using the velocity map imaging (VMI) technique. Velocity images of methyl radicals were taken for the spectral region corresponding to the first absorption band of acetone (333.5 nm to 229.7 nm). The results provide clear evidence for three distinct photodissociation pathways corresponding to the three spectral regions of the excitation wavelengths:

$$\text{Region 1: } 333.5 \text{ nm} > \lambda_{pump} > 305.3 \text{ nm}$$
$$\text{Region 2: } 305.3 \text{ nm} > \lambda_{pump} > 261 \text{ nm}$$
$$\text{Region 3: } 260.9 \text{ nm} > \lambda_{pump} > 230 \text{ nm}$$

(1) The photodissociation dynamics of acetone in Region 1 were probed at 5 different discrete photolysis wavelengths. Three representative ion images are shown in Fig. 3.20, where the left column presents the photolysis wavelength, the column in the middle contains experimental raw two dimensional (2D) ion distributions, and the right column demonstrates corresponding meridional slices of the recovered three dimensional (3D) fragment distributions. The intensities were scaled in RGB color code (32 bit). The methyl radicals produced during photodissociation of acetone were probed over the whole Doppler profile (~ 9 cm^{-1}) for a given REMPI transition. The polarization axis of the photolysis and the probe laser beam were held collinear to each other and parallel to the plane of the MCP detector. The laser power was turned down to get the real two-color signal as was described above. Velocity map images of the methyl photofragment were summed over 72 000 laser shots for $\lambda_{pump} = 305.3$ nm, and over 144 000 shots for $\lambda_{pump} = 333.5$ nm and 305.8 nm. Inversion of the experimental 2D projections and meridional slices of the reconstructed 3D ion distributions were obtained *via* the Richardson-Lucy (RL) algorithm as described in Section 2.4.4. 294 basis functions and about 1000 iterations

were needed for the reconstruction. The reconstruction was repeated for each cross correlation quarter to optimize the iteration count and the respective results were averaged.

All velocity map images in this spectral region of the photolysis wavelengths demonstrate a very broad, structureless and isotropic ion distributions with intense central spots. However, the photolysis of jet-cooled acetone molecules at $\lambda_{pump} = 305.3$ nm exhibits one additional feature, namely a ring-like ion distribution, strongly overlapped with diffused distributions. This feature is very weakly seen also at $\lambda_{pump} = 305.8$ nm, but was absent at all longer wavelengths.

The photofragment distribution is detected in the "pixel domain" of the CCD camera, originally, and the velocity distributions need to be extracted by knowing the time-of-flight (TOF) of the fragments. For the methyl radical, the TOF was 2.742 μs for the drift zone with 351 cm length. In order to describe the observed distributions quantitatively, efforts were done to find an optimum model and function that could satisfactory describe the experimental distribution. Gaussian functions was finally chosen, but albeit they were the best, they are not perfect (see Fig. 2.18).

The area under the experimental curve was normalized to unity. The parameters of the fitted Gaussian functions were used for the quantitative analysis in the following. The experimental and fitted velocity distributions were converted to the energy domain by Eq. 2.21.

The recording of the velocity distribution or the kinetic energy release of one of the possible photofragments gives the total kinetic energy release (TKER) for the photodissociation process due to the laws of momentum and energy conservation (see Eq. 2.11 and 2.12 in Section 2.4.1). TKER distributions resulting from acetone photolysis at this spectral region are shown in Fig. 3.21.

The intense central spot, in the ion images corresponds to slow methyl fragments. Methyl photofragments with low kinetic energy originate from two dissociation pathways: (i) cluster dissociation,*i.e.*, acetone$_2$ and (ii) unimolecular decay of acetone excited to high vibrational levels of the ground S_0 state *via* internal conversion (IC) processes $S_1 \rightarrow S_0$. The latter process competes with two-photon absorption, which is described latter. The intensity of the central spot was strongly depending on the sample temperature. With rising temperature it became more intense as Fig. 3.22 clearly demonstrates. This indicates, that the intense central spot is mostly due to clusters dissociation.

The dependence of the dimer cluster fraction in the molecular beam on the sample temperature, pressure, nozzle diameter and configuration was qualitatively described in [145] and is proportional to P_0, $T_0^{-2.4}$ and to d_0^{-1}, where index "0" stands for the relevant sample parameters before expansion. In the present experiment $P_0(He) = 1$ bar and $D_0 = 0.5$ mm were used to suppress cluster formation. As a result, the increase of the intensity of the central spot with rising

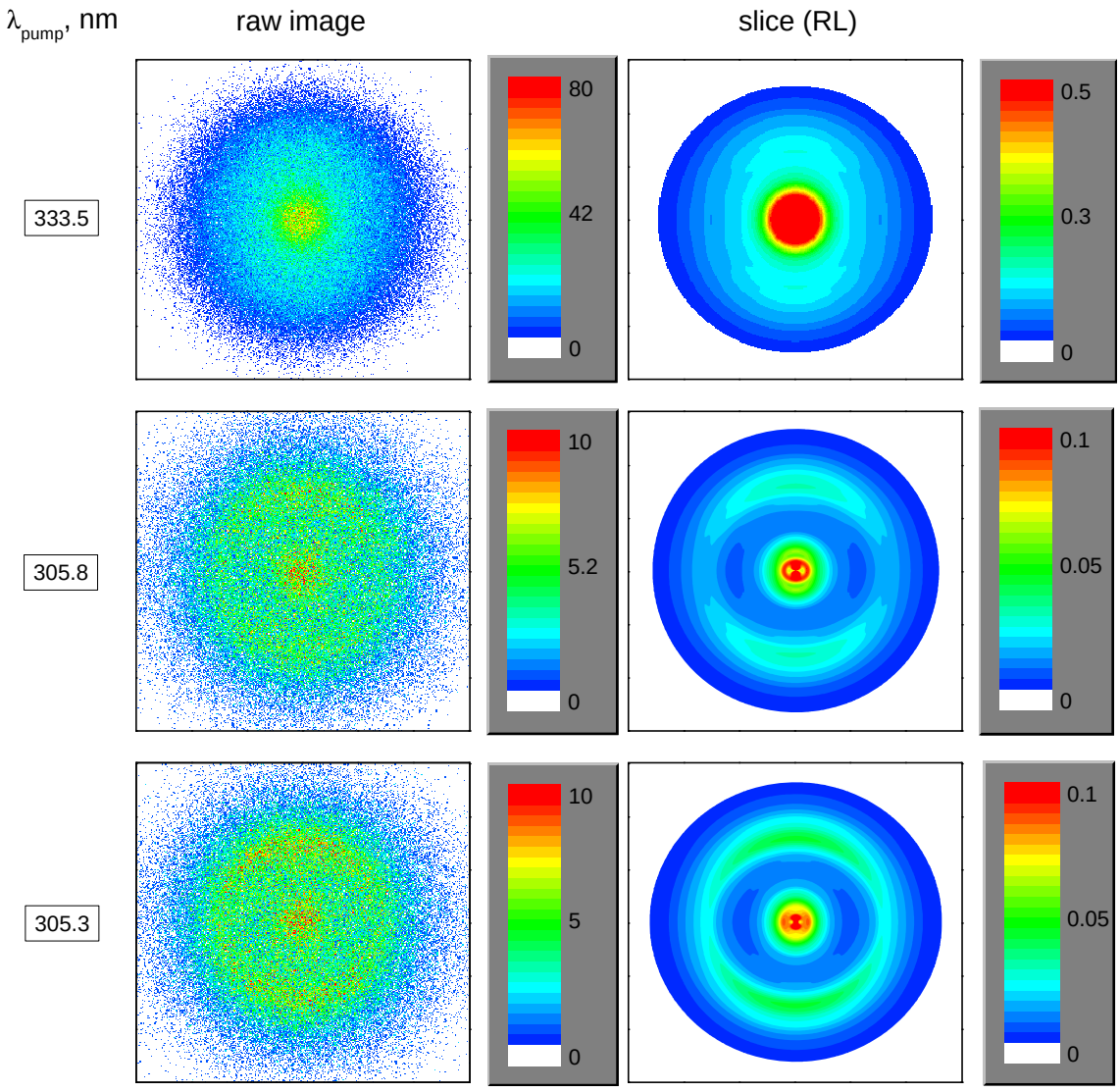

Figure 3.20: Two-color velocity map images of the methyl radical from acetone photolysis in Region 1 (left column). The middle column presents experimentally obtained ion images and the right column presents meridional slices from the recovered 3D ion distributions. The methyl radical was detected by the (2+1) REMPI technique *via* the 3*p* Rydberg state at 333.5 nm. Color code is the same as in Fig. 2.13

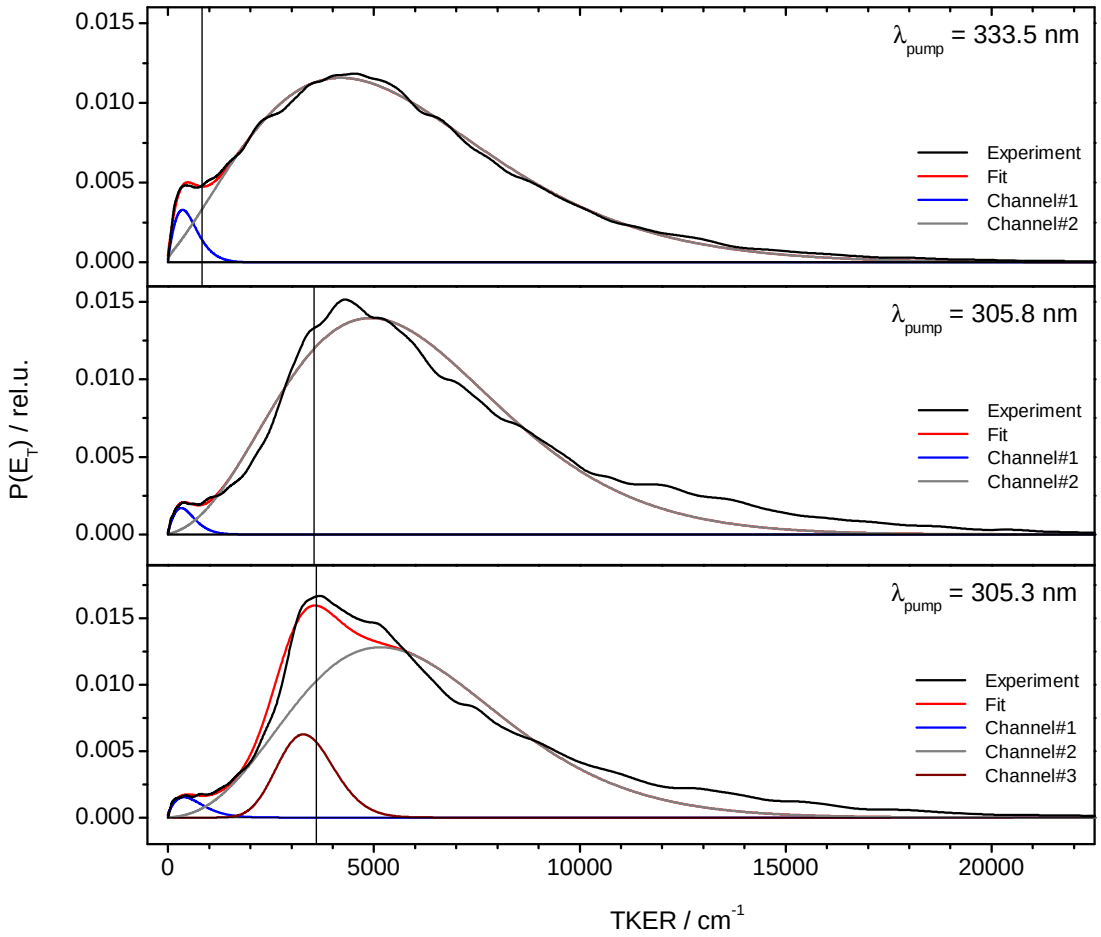

Figure 3.21: TKER distributions for $\lambda_{pump} = 333.5$ nm (top), 305.8 nm (middle), and 305.3 nm (bottom). Vertical solid lines in the TKER distribution graphs present the corresponding available energy ($E_{avail.}$) for one-photon dissociation assuming that D_0(acetone) = 29166 cm^{-1}. See the text for further elucidations.

reservoir temperature T_0, shown in Fig. 3.22, can be assigned to the increased amount of the "hot" molecules (which were not effectively cooled down) or clusters (acetone)$_2$. If we assume, that the central spot in the ion images is due to the "hot" molecules, this would lead to a conclusion that these molecules are excited to the S_1 state and pass an internal conversion (IC), emerging on high vibrational levels of the ground electronic state followed by a successive unimolecular decay. The coupling mechanism for the IC process becomes more efficient for "hot" molecules excited to the first singlet excited state, which should be quite unlikely, because of worse Frank-Condon factors for the excitation processes. On the other hand, the formation of complexes requires three body collisions (Z_3), while the cooling of the beam requires only two body collisions (Z_2) and the ratio of Z_3/Z_2 is proportional to n_0 (the density of molecules). The temperature in the molecular beam is a

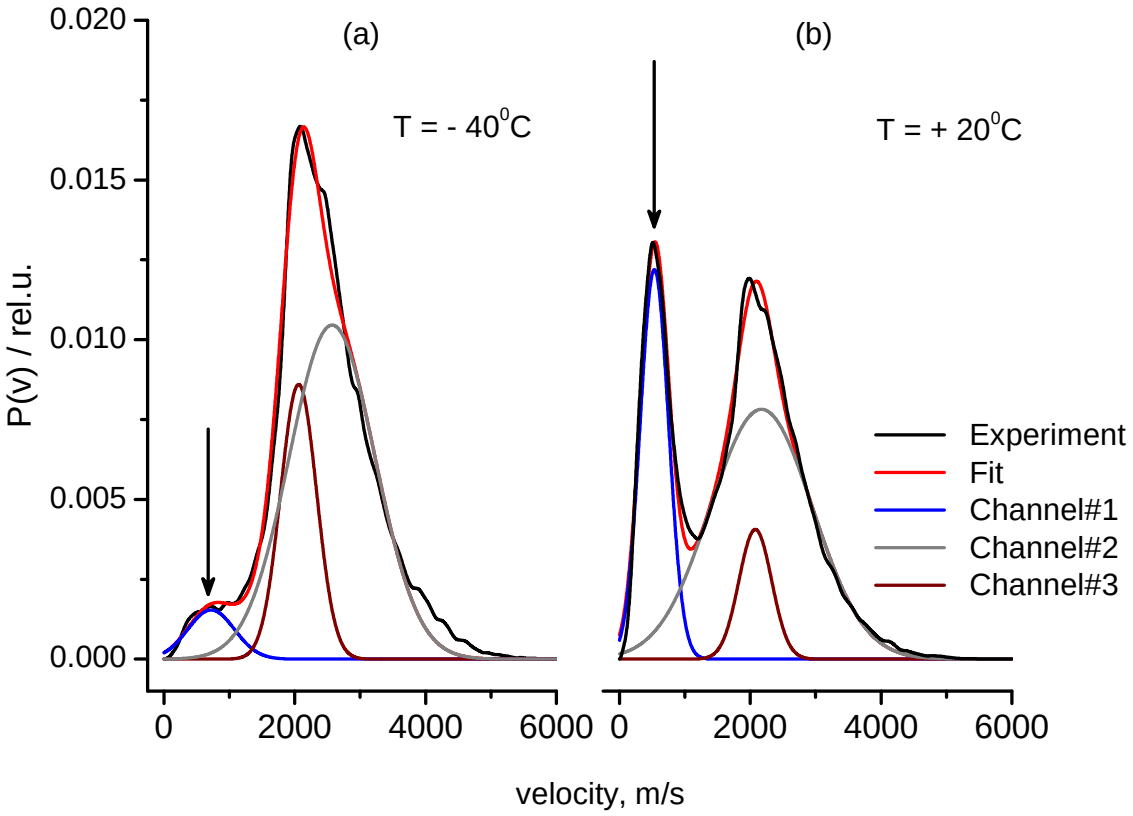

Figure 3.22: Effect of the acetone reservoir temperature on the photofragment velocity distributions (λ_{pump}). Acetone was kept at -40°C (a) and at room temperature $+20$°C (b). The pressure of the carrier gas He was lowered down to 1 bar. The area under the curves is normalised to unity.

function of $n_0 \times d$, where d is the nozzle diameter [45], therefore at a given terminal temperature the cluster amount can be minimized by decreasing n_0 and increasing d, keeping $n_0 \times d$ constant. In the present example (see Fig. 3.22), since the nozzle diameter d was fixed, the reservoir temperature T_0 only affected the n_0 and thus, the amount of clusters in the molecular beam. Therefore, "channel #1" in the TKER profiles in Fig. 3.21 was assigned to the methyl radicals arising from $(\text{acetone})_2$ clusters decomposition.

The maximal available energy $E_{avail.}$ calculated by

$$E_{avail.} = h\nu - D_0^0, \tag{3.8}$$

where $h\nu$ is the photon energy and D_0^0 is the parent molecule dissociation energy, can be distributed among internal and translation degrees of freedom of the photofragments. Obviously, TKER has a maximum if no internal energy is kept in the fragment. Considering the first TKER profile at $\lambda_{pump} = 333.5$ nm, the maximum TKER value for the one-photon absorption process calculated from Eq. 3.8 is 820 cm^{-1},

represented by the solid vertical line in Fig. 3.21, which is tens times smaller than that one determined from Figure 3.21, where $TKER_{max} > 25\ 000$ cm^{-1}. The only reasonable explanation for such a discrepancy is a two-photon absorption followed by dissociation. Acetone, being initially excited to the S_1 state, has a lifetime which is long enough to let it absorb a second photon with successive dissociation from the two-photon excited state. Another way would be that acetone relaxes from the S_1 state down to high vibrationally excited levels of the ground electronic state *via* internal conversion. Again, molecules on the high vibrational levels do not undergo an instant dissociation, but rather dissociate slowly and dictated by unimolecular rate theory [146]. The time the molecules need to dissociate is long enough to absorb the second photon with successive dissociation from the corresponding higher states. The low intensity of the fluorescence signal of acetone excited to the S_1 state within this first spectral region suggests a presence a radiationless transition $S_1 \rightarrow S_0$ which efficiently and quickly quenches the fluorescence. The IC process is one of the possible processes which can be responsible for the radiationless decay of the S_1 state. Another S_1 decay pathway is intersystem crossing (ISC) to the triplet T_1 state, from which acetone can also absorb a second photon with successive dissociation. The LIF spectra recorded by Zuckermann *et al.* exhibit a weak signal with a diffusive character at excitation wavelength shorter than 320 nm, this signal abruptly disappears at $\lambda_{pump} = 305.8$ nm. Such a behavior was assigned to quenching of the fluorescence by both IC and ISC processes, but the latter one does not play a significant role at the excitation wavelength longer than 305.8 nm [121]. Therefore, the TKE curve marked as channel #2 in Fig. 3.21 is assigned to the absorption of a second photon by acetone regardless from which electronic state it occurs.

The TKER distribution resulting from the photolysis of acetone at $\lambda_{pump} = 305.3$ nm exhibits a profile, which cannot be fitted with only two Gaussian functions (Figure 3.21 lower row). The use of three Gaussian functions clearly points at the opening of some additional dissociation channel. The meridional slice over the inverted 3D ion distribution at 305.8 nm photolysis wavelength also demonstrates a weak ring-like feature, but the intensity is so low that it is impossible to resolve something on the TKER profile. The photolysis wavelength of 305.3 nm corresponds to an excess energy of 2 323 cm^{-1} above the origin of the $S_1 - S_0$ transition which was determined in [116] and lies at 30 431 cm^{-1}. The photolysis wavelength of 305.8 nm would correspond to an excess energy of 2 250 cm^{-1}. Considering that the additional ring-like feature in the ion distribution images appears between 305.8 nm and 305.3 nm of excitation wavelength one can estimate the excess energy of 2 285 $\pm$ 40 cm^{-1} for the origin of the dissociation channel. Zuckermann *et al.* have observed a sharp increase in the decay rate at an excitation energy of about 32 700 cm^{-1} which corresponds to 2 250 cm^{-1} excess energy above the $0-0$ transition and a concomitant sharp decrease in the emission intensity. It was suggested that these changes were due to the onset of the homolytic dissociation of acetone on the triplet

T_1 state to methyl and acetyl radicals [120]. This value and the one determined for the ion image are in excellent agreement. The coincidence of the excess energy, at which the changes happen both to the ion distributions resulting from the acetone photolysis and the fluorescence decay suggests that the same process is taking place in acetone excited at this energy. Previous researches have assigned this process to the dissociation of acetone in the T_1 PES, which is populated *via* intersystem crossing. Thus, the T_1 state has a shallow dissociation barrier of $\sim$2 250 $\pm$ 50 cm^{-1} with respect to the origin of the $S_1 - S_0$ transition. The ISC process becomes more efficient when the initially prepared rovibrational state of the S_1 state couples with many rovibrational states of the triplet T_1 state. As the density of the rovibrational states also increases with increasing excitation energy, the ISC process becomes even more efficient and thus easily detectable. Therefore, the dissociation pathway marked as "channel #3" is assigned to the dissociation of acetone from the T_1 state.

The angular distributions of the photofragments are isotropic (anisotropy parameter $\beta < 0.2$) calculated by Eq. 2.14, does not exceed values of 0.3 for all excitation wavelengths.

The majority of the experimental researchers [32, 33], except the work of Solomon *et al.* [109], demonstrate that the isotropic photofragment distributions suggesting a relative long ($\sim$1 ns) lifetime of acetone excited to the S_1 state. This is in agreement with the calculated geometry of the PES, the S_1 state has a double well shaped and is coupled to the T_1 state which has a small barrier which prevents it from an instant dissociation. Owrutsky *et al.* however, measured in their femtosecond research on the acetone dissociation a subpicosecond lifetime of the S_1 state for excitations below 268 nm [35]. The isotropic fragment distribution was interpreted by them as a result of the isotropic transition dipole moment originating from the excitation to the mixed singlet-triplet $\{S_1,\ T_1\}$ state [35].

(2) Photolysis of acetone in Region 2 (305.3 nm$> \lambda_{pump} >$ 261 nm) proceeds essentially *via* one dissociation channel, which takes place on the T_1 PES and is marked here as "channel #3". The importance of this dissociation pathway is clearly demonstrated by Fig. 3.23 and the corresponding TKER profiles in Fig. 3.24, which were measured at excitation wavelengths lying in the vicinity of the dissociation barrier on the T_1 state.

The amplitude of the curve corresponding to channel #3 increases drastically and at the same time the amplitudes of channels #1 and #2 decreases, indicating that the efficiency of the former dissociation channel becomes higher and rivals with the latter ones. This agrees well with the theory of ISC because the higher the initially prepared rovibrational state on the S_1 surface is, the more efficient the coupling with rovibrational states of the triplet T_1 PES becomes by the high density of the triplet states. The available energy represented as a solid vertical line in Fig. 3.24 is smaller than the maximal kinetic energy release after acetone dissociation, which is

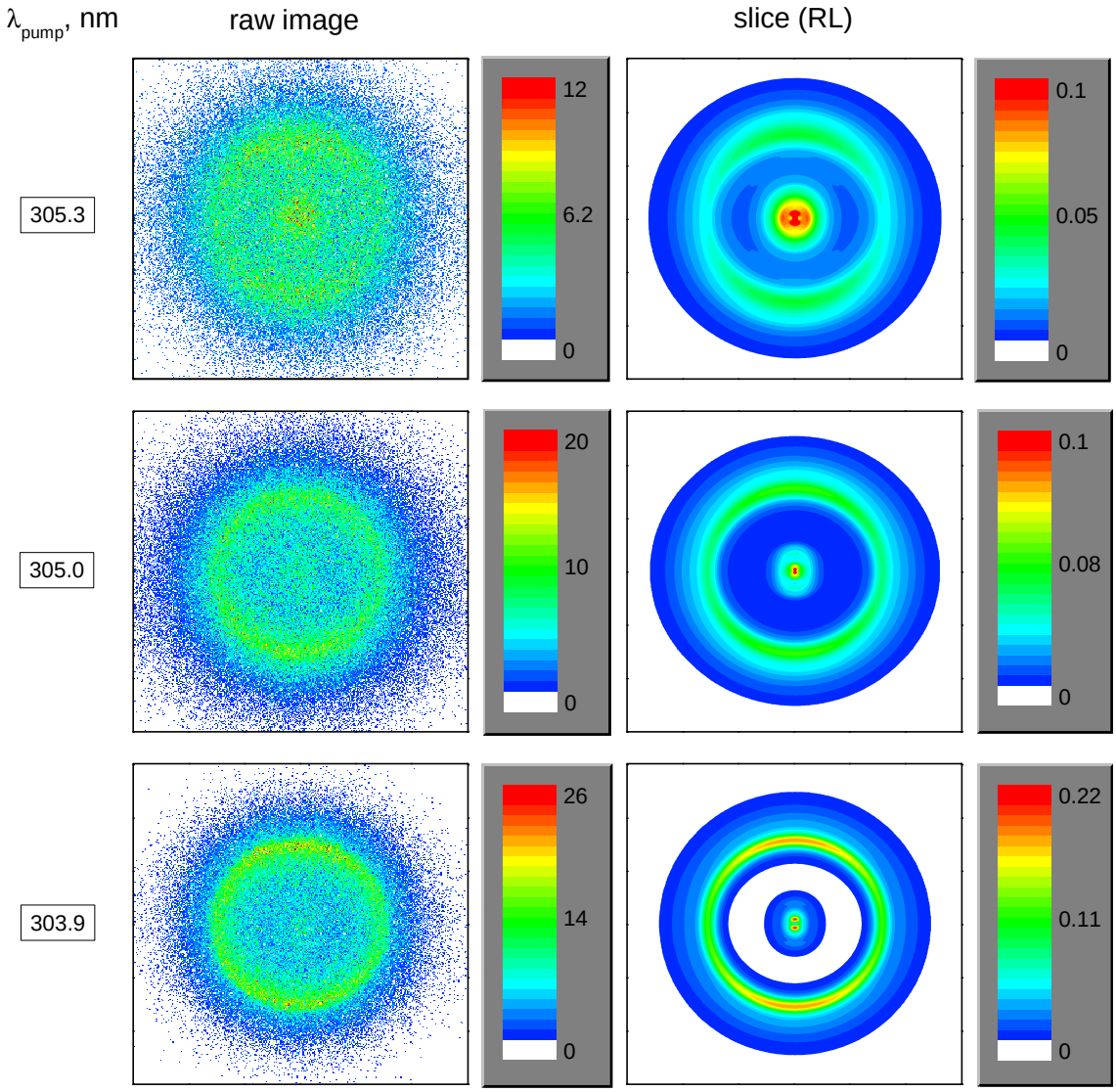

Figure 3.23: Two-color velocity map images of methyl from acetone photolysis at certain excitation wavelength in region 2 (left column). The notations and detection scheme are as in Fig. 2.13.

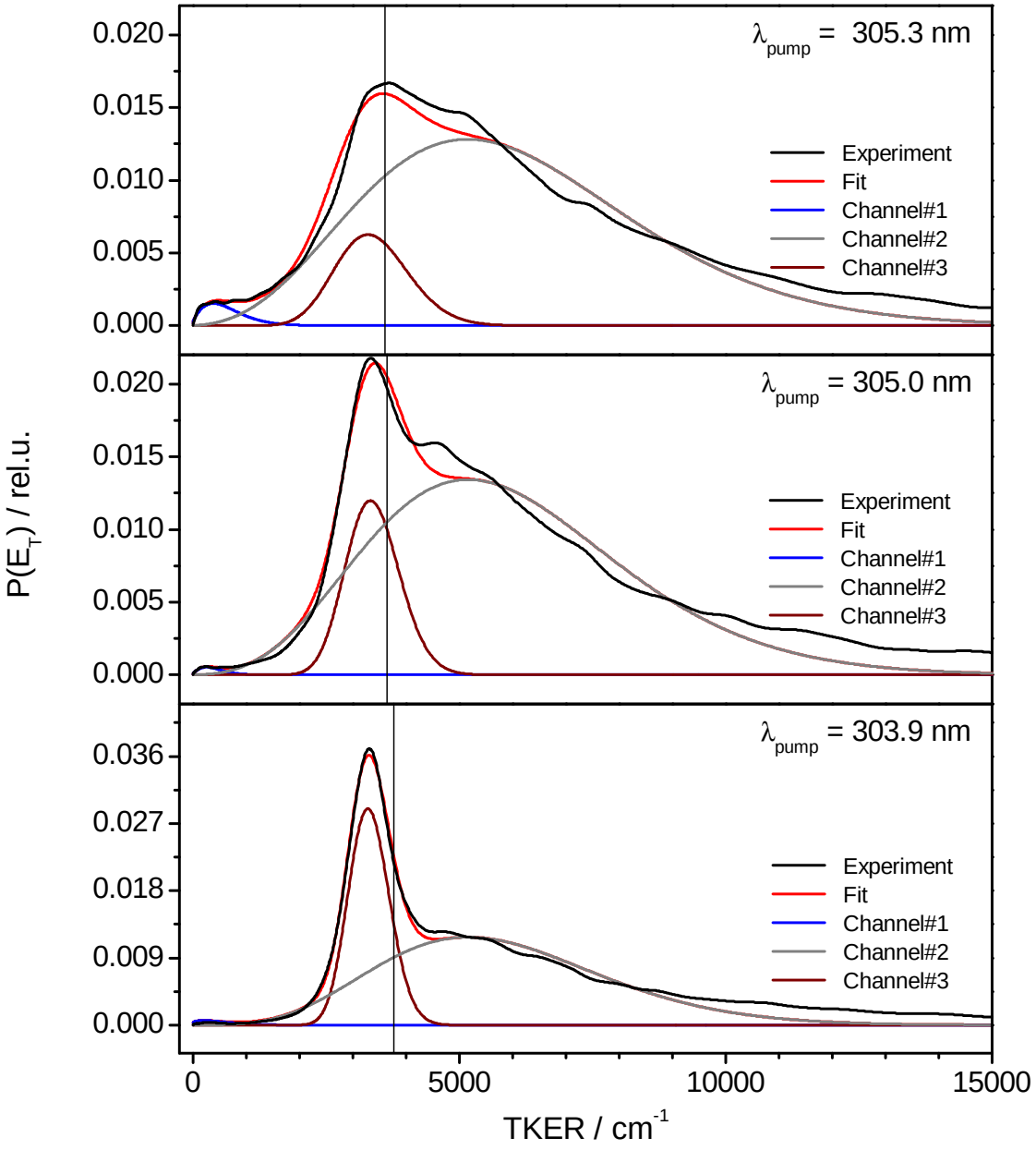

Figure 3.24: TKER profiles for acetone photodissociation in the vicinity of the triplet T_1 dissociation barrier. Vertical solid lines represent corresponding $E_{avail.}$.

not feasible from the energy conservation law. This discrepancy cannot arise from a "wrong" estimation of the dissociation energy value *via* the Hess's law. If these curves are correct, then the dissociation energy calculated from the maximal total kinetic energy values would vary strongly from 27 175 cm^{-1} for $\lambda_{pump} = 305.3$ nm to 28 105 cm^{-1} for $\lambda_{pump} = 303.9$ nm, which is outside the error limit and does not make sense. Instead, this effect is due to a broadening effect of the fitted Gaussian curves by the strong overlapping of channels #2 and #3. Another reason is the instru-

ment resolution (250 cm^{-1}). Convolution of the instrument function and the true physical signal and additionally fitting problems make the curve corresponding to channel #3 broader. Additionally, the dissociation of "hot" acetone molecules in the molecular beam must be taken into account. Under the expansion conditions used to suppress acetone cluster formation, vibrational relaxation of the molecules in the molecular beam cannot be expected to be complete. At threshold, the ion imaging experiment detects vibrationally "hot" molecules more efficiently than vibrationally cold molecules. All these effects make the fitting procedure quite complicated, but the fact that the peak of the Gaussian functions do not exceed the maximal available energy preserve the fitting from a fatal error. Indeed, the dissociation of acetone molecule proceeds from a tight transition state and is just above the dissociation barrier on the T_1 state, resulting in high fraction of the translation energy presented in the photofragments compare to their internal energy. Hence, at this point, acetone dissociation can be approximated by a model where low or almost no internal energy is presented in the fragments after the bond breaking. Rather, the available energy flows directly to the translation degrees of freedom. At this region the mechanism of acetone dissociation is very close to a two-atom molecule dissociation and a simple impulsive model can be applied to estimate the relative energy fractions. Therefore, the translation energy from the two-atom molecule dissociation must be close to the maximal available energy. About 90% of the whole available energy is transformed to translational energy of the acetyl and methyl radicals in the present case.

The dissociation of a molecule with constant energy *via* a certain reaction coordinate can be regarded as a reaction flux in phase space, which is fully described by its spatial coordinates and conjugated momenta. Furthermore, for constant energy, the molecule is limited to a surface for which the Hamiltonian is $H = E$ [147]. If $E > E_0$, where E_0 is the height of the dissociation barrier (transition state TS), the molecule can dissociate. There are many ways for the dissociation reaction to pass through the transition state region, and these ways differ in how the available energy ($E_{avail.} = E - E_0$, the energy above the barrier) participates between the internal energy of the TS and the kinetic energy associated with the momentum in the reaction coordinate. The dissociation of acetone caused by photolysis wavelengths within this spectral region occurs just above the triplet barrier with only a small excess energy ($\approx$75 cm^{-1} for $\lambda_{pump} = 305.3$ nm and 225 cm^{-1} for $\lambda_{pump} = 303.9$ nm), which is lower than low frequency vibrations of the TS of T_1 acetone molecule. The peak values of the TKE distributions lie very close to the available energies and form about $\sim$ 90% of it. The rest of the available energy flows into rotational modes of the fragments. The fact that all TKE profiles corresponding to channel #3 do not peak at zero energy but rather have an "onset" of about $\sim$2 100 cm^{-1} shows unambiguous that the acetone dissociation at these excitation energies proceeds over a tight transition state (TS). This result is thus in good agreement with theoretical predictions for the PES.

The anisotropy parameter β does not exceed values above 0.2, thus, the methyl fragment angular distributions stay practically isotropic in this excitation region as well.

Velocity map images of the methyl radical formed by the acetone photolysis at shorter wavelengths are shown in Fig. 3.25. The corresponding TKER profiles are shown in Fig. 3.26. The average TKER values of channel #3 have a tendency to shift to higher energies starting from 3 290 cm^{-1} at 305.271 nm, where the kinetic energy forms about 90% of the whole available energy, and increases up to 5 030 cm^{-1} at $\lambda_{pump} = 269.5$ nm, which corresponds to only 60% of the available energy (see Table 3.8). This behaviour can be understood as follows: The more energy is deposited in the molecule by a photon, the more available energy above the dissociation barrier can be distributed to internal degrees of freedom of the photofragments. The decrease of the translational-to-available energy ratio ($\langle E_T \rangle / E_{avail.}$) with increasing excitation energy is caused by the fact that acetone initially promoted to higher rovibrational levels of the S_1 state after internal vibrational relaxation (IVR) and ISC processes is still positioned high above the dissociation barrier of the T_1 state, but the redistribution of the available energy has than a more statistical character. The available energy partitioning process is highly affected by the presence of the barrier, and even at high excess energies the translation energy is the bigger fraction of the available energy. The FWHM (ΔE) of the TKE distribution of the acetone photodissociation *via* channel #3 is broadened with increasing excess energy above the triplet dissociation barrier. The TKER distribution is a direct reflection of the photofragment internal energy distribution and the tendecy of ΔE to get broader has the same reason as the decrease of the $\langle E_T \rangle / E_{avail.}$ ratio, *i.e.*, the available energy partitioning becomes more statistical.

The TKE profile calculated for the acetone photolysis at $\lambda_{pump} = 286$ nm has a bimodal shape although the experimental ion distribution does not seem to have any features like this. Nevertheless, this $P(E_T)$ curve was firstly fitted with two Gaussian functions with $\langle E_T^1 \rangle = 4\ 085$ cm^{-1}, $\Delta E^1 = 1\ 083$ cm^{-1} and $\langle E_T^2 \rangle = 4\ 940$ cm^{-1}, $\Delta E^2 = 1\ 150$ cm^{-1} for the first and second peaks respectively. These kinetic energies correspond to the acetyl fragment internal energies of 1 714 cm^{-1} and 859 cm^{-1} and the difference between them is equal to 855 cm^{-1}, which is very close to the energy of the acetyl C-C stretching mode (884 cm^{-1}) [148]. On the other hand, the methyl fragment distributions from acetone photolysis at $\lambda_{pump} = 290$ nm and at 270 nm do not result in such "vibrational progressions" of the correlated acetyl fragment. At these energies, the number of modes in the acetyl and methyl fragments is too high to resolve any structure. It is also possible, however, that the bimodal shape of the TKE profile at 286 nm is artificial, splitting caused by the inversion procedure, so called "ringing" effect [54]. The angular distribution is essentially isotropic ($0 < \beta < 0.3$).

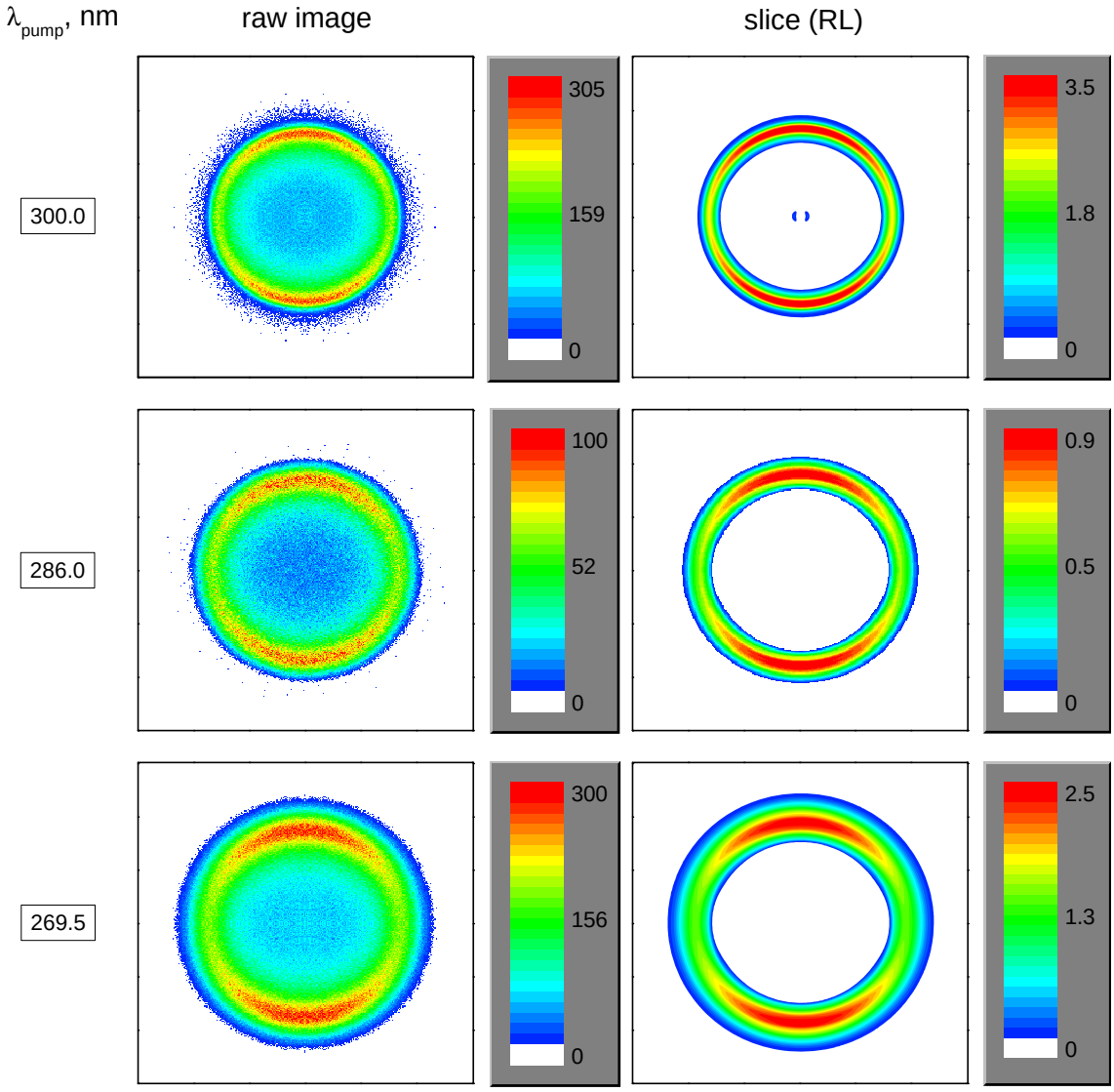

Figure 3.25: Two-color velocity map images of methyl radical from acetone photolysis at certain excitation wavelength (left column). The notations and detection scheme are as in Fig. 2.13.

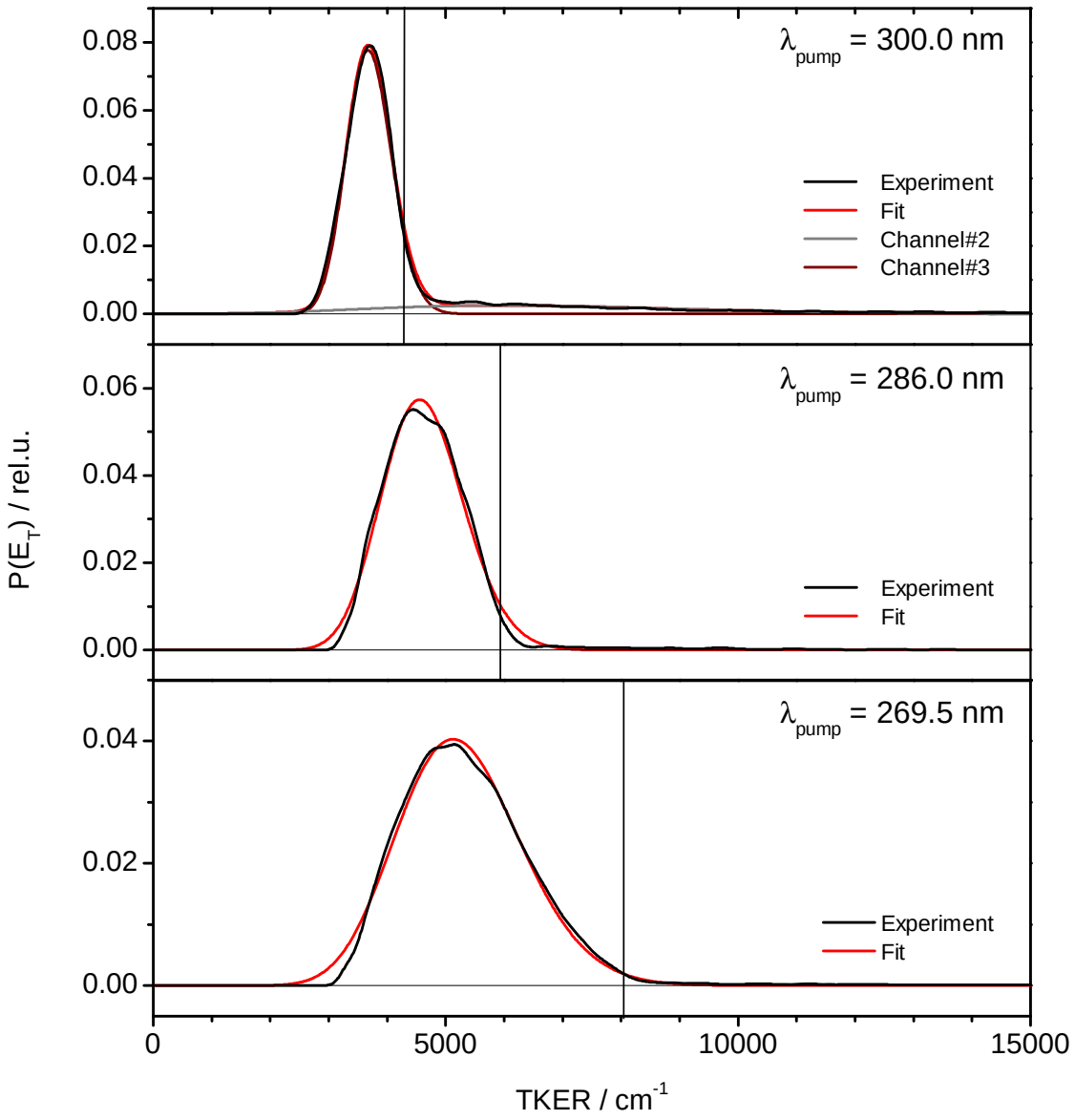

Figure 3.26: TKER profiles for acetone photodissociation appreciably above the triplet T_1 dissociation barrier. Vertical solid lines represent corresponding $E_{avail.}$.

The TKE distribution curve of channel #3 in this spectral region of the excitation wavelength is the most prominent one and, in fact, all other channels are hardly noticeable. Thus, it is obvious that the acetone photodynamics initiated by wavelengths in this region (305.3 nm> λ_{pump} > 261 nm) is dominated by ISC to the T_1 state, followed by dissociation over the small barrier on the T_1 PES along the C-C stretching reaction coordinate. This is an applicable region to estimate the dissociation energy of the acetone molecule, as the influence of all other channels is negligible and so the error should be small. The dissociation energy is calculated *via* Eq. 3.8, where $E_{avail.}$ corresponds to the maximal total kinetic energy release,

which can be estimated from the TKER profile as was described in Section 3.1.3. This gives the following result:

$$D_0(CH_3CO - CH_3) = 29\ 090 \pm 250\ \text{cm}^{-1}. \tag{3.9}$$

This value is in good agreement with that estimated from the standard enthalpies of formation taken from [141, 142] calculated *via* Hess' law:

$$D_0(CH_3CO - CH_3) = 29\ 166 \pm 135\ \text{cm}^{-1}.$$

(3) In excitation Region 3, acetone was probed at 261 nm $> \lambda_{pump} >$ 220 nm. The ion images taken in this region exhibit a clear bimodal product distribution. The new additional channel corresponds to the formation of slow methyl radicals and is marked as "channel #4" (see Fig. 3.27 and 3.28).

Photolysis of acetone molecule at λ_{pump} = 261 nm releases a total kinetic energy, which on average forms about 54% of the whole available energy for the third dissociation channel ($\langle E_T \rangle$ = 4 950 cm^{-1}, ΔE = 3 100 cm^{-1}, $E_{avail.}$ = 9 220 cm^{-1}), indicating that the internal energy of acetyl increased. The average value of the TKE distribution corresponding to the formation of slow methyl fragments is increasing as the photolysis wavelength is shortened (1 634 cm^{-1} at λ_{pump} = 261 nm up to 1 900 cm^{-1} at λ_{pump} = 229.7 nm). There are two possible sources of slow methyl radicals:

1. Direct dissociation of acetone from the first singlet excited state. However, the S_1 state correlates adiabatically only with fragments in the excited state, CH_3CO in $^2A''$ and CH_3 in $^2A_2''$, which is not the case for the present experiment. Beyond, theoretical calculations predict that the dissociation barrier of the S_1 state is lying about ∼27.5 kcal/mol above the origin, which was not excessible for excitation at 261 nm [37]. On the other hand, Zewail *et al.* proposed an excistance of a conical intersection (CI) of the S_1 and S_0 states. The fraction of the wave packet, which moves from the singlet S_1 state to the triplet T_1 state *via* ISC, is responsible for formation of fast CH_3 fragments. Another fraction of the wave packet, which is not effectively coupled with the T_1 state flows to the CI and results in the slow CH_3 channel [112]. Taking this into account, the present experimental data can be interpreted such that ISC is getting less efficient at higher excitation energies. For more arguments against the assignment of slow methyl radicals as arising due to the CI mechanism see Section 3.2.5.
2. The second possible source of the slow methyl radical, is the successive dissociation of the internally excited acetyl photofragment.

The acetyl fragment receives enough internal energy during the photolysis of acetone to overcome the dissociation barrier on its ground $S_0(^2A')$ state and thus can result in the slow CH_3 and CO fragments. Indeed, several groups have measured the acetyl dissociation barrier to be ∼17 kcal/mol [140, 148]. These results were also proved

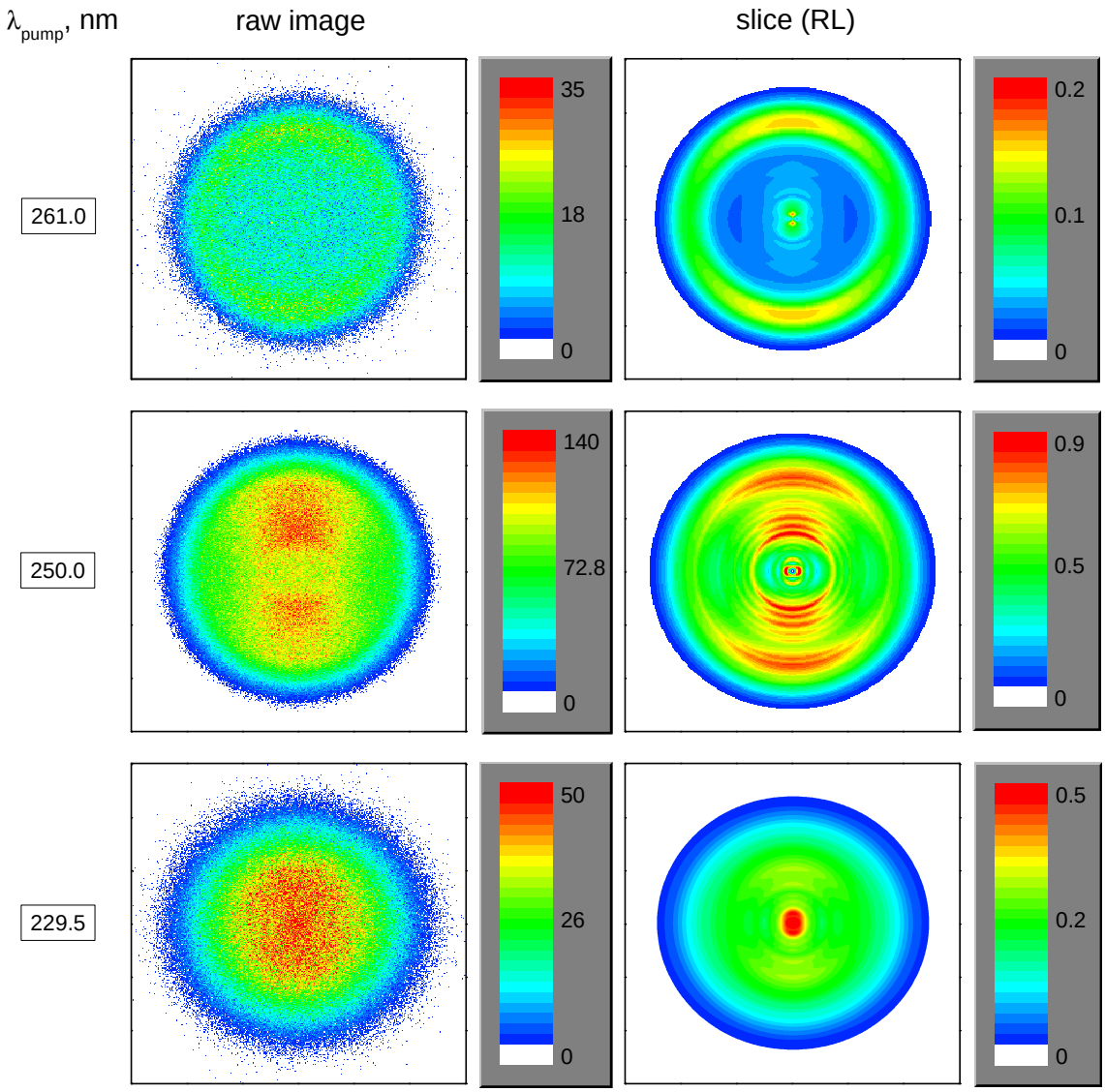

Figure 3.27: Two-color velocity map images of methyl radical from acetone photolysis at certain excitation wavelength (left column). The notations and detection scheme as in Fig. 2.13.

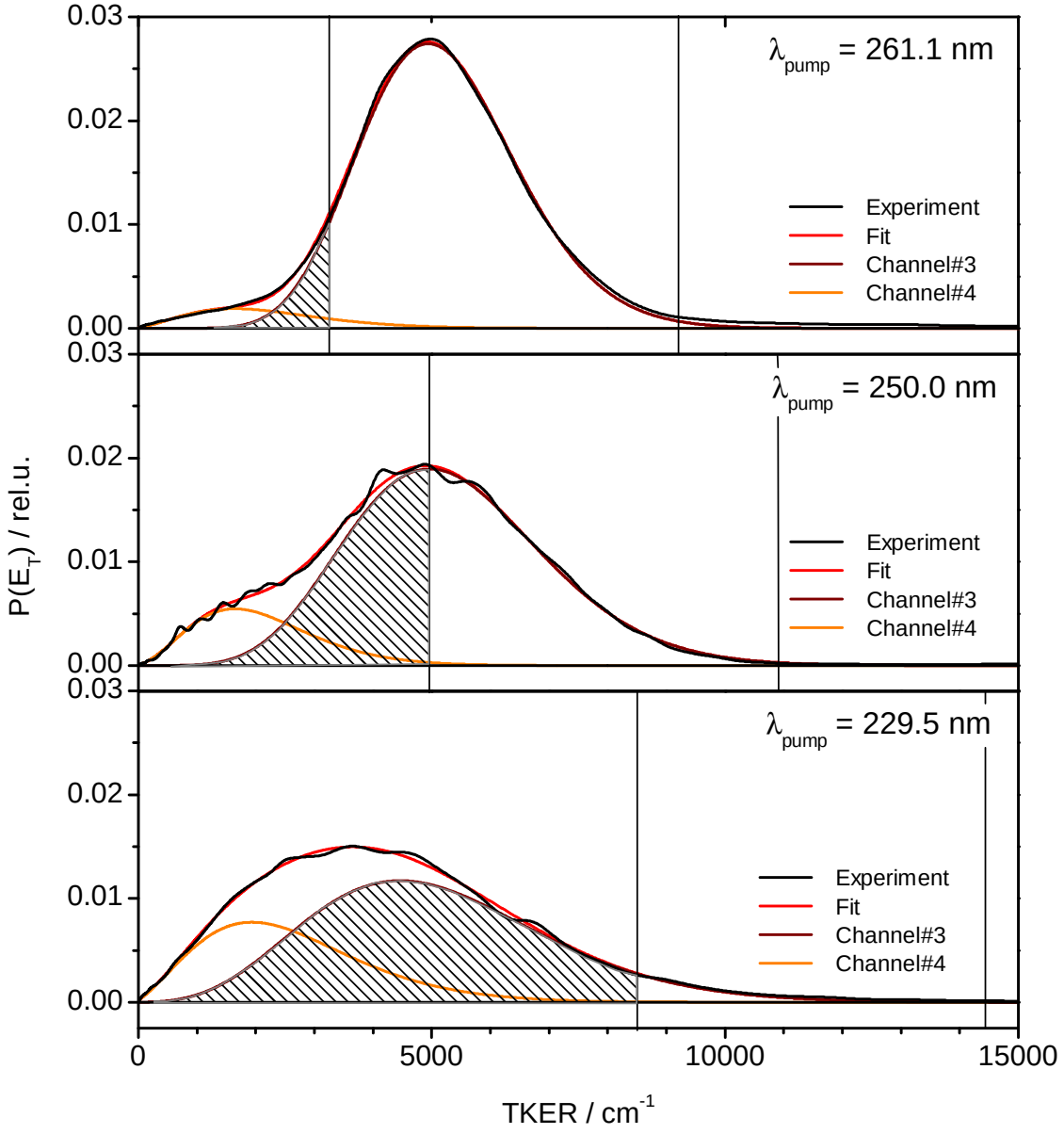

Figure 3.28: TKER profiles for acetone photodissociation with the secondary dissociation channel of the acetyl fragment. Vertical solid lines correspond to $E_{avail.}$ for channel #3 and #4. The shaded area under the curves exhibits the fraction of the acetyl fragments which have enough internal energy to undergo secondary dissociation yielding secondary methyl radical and carbon monoxide fragments (see the text).

theoretically [148, 149]. From the energy conservation law, it follows that acetyl, produced by photolysis at $\lambda_{pump} = 261$ nm can undergo a secondary dissociation, if the maximal TKE value, released in the acetone dissociation step, does not exceed the limit of 3 258 cm^{-1}, *i.e.*

$E_{avail.} = h\nu - D_0(\mathrm{CH_3CO\text{-}CH_3}) = E_{int.}(\mathrm{CH_3}) + E_{int.}(\mathrm{CH_3CO}) + E_T$,

$E_{int.}(\mathrm{CH_3CO})$ must exceed the threshold value of 5945 cm^{-1} to let acetyl undergo secondary dissociation and assuming that $E_{int.}(\mathrm{CH_3}) = 0$, the limit TKER value can be evaluated from the following condition:

$E_T^{limit} = E_{avail.} - E_{int.}(\mathrm{CH_3CO}) = E_{avail.} - 5495$ cm^{-1}.

Using this simple condition, it is possible to estimate the amount of acetyl molecules produced in the first step of dissociation, which can undergo successive decay and produces CH_3 and CO fragments. The amount of the "potentially hot" acetyl fragments is marked as the shaded region in Fig. 3.28. If that slow methyl fragment comes from acetyl fission, then the area under the corresponding TKE profile (channel #4) should be equal or less than the shaded area under the curve corresponding to channel #3. In fact, the area under the TKE curve of channel #4 ($\sim$ 5.1) is almost equal to the shaded part of the TKE profile of channel #3 ($\sim$ 5.2). This shaded area forms $\sim$ 6% of the total area of the TKER distribution of channel #3 at $\lambda_{pump} = 261$ nm. Because of all these aspects, the slow methyl radical channel detected in the present work was assigned to the acetyl radical secondary dissociation. However, at shorter photolysis wavelengths there is not such one-to-one correspondance of the respective areas. The shaded area under the TKE curve of the 3rd channel rises faster than the area under the TKER profile of the 4th dissociation channel. The fraction of the acetyl radicals which undergo secondary dissociation forms only 40% of the whole "potentially hot" acetyl fragments fraction for excitation at 250 nm. This discrepancy is caused by the assumption made above for the estimation of the truncated total kinetic energy. The approximation of the $E_{int.}(CH_3) = 0$ obviously does not really work at higher excess energies. Indeed, in the present experiment, CH_3 was probed only in its ground vibrational state ($v = 0$, all J), so the truncated E_T^{limit} value determined from that condition was somewhat exaggerated. Additionally, the fraction of the available energy saved in $E_{int.}(CH_3CO)$ after the primary acetone dissociation does not flow completely to the C-C acetyl bond rather redistributes among rotational and vibrational degrees of freedom of the acetyl radical resulting in the broad and structureless TKER distribution for the slow methyl radical (channel #4). Some internal energy of the nascent radicals CO(v, J) and $\mathrm{CH_3}(v = 0,\ J)$ could be expected. The CH_3 fragment most probably possess some vibrational excitation at least in the umbrella vibrational mode after dissociation of the acetyl radical, because of the dissociation impact direction. Trentelman *et al.* have observed internally excited carbon monoxide and methyl fragments in the first vibrational state ($v = 1$) after acetone photolysis at 193 nm [31].

The fraction of the TKE profiles marked as the shaded area is increasing from $\sim$ 6% at 261 nm to $\sim$ 90% at 229.7 nm. The respective fraction of the acetyl radicals, which undergo secondary decomposition, is also increasing from $\sim$ 6% at λ_{pump} = 261 nm up to $\sim$ 45% at λ_{pump} = 229.7 nm (see Table 3.8). The maximal TKE values corresponding to channel #4 are equal to the truncated TKE values calculated from the TKE profiles of channel #3 (maximal TKE value of the shaded area in Fig. 3.28).

The fact that the ion distribution is isotropic and has only very weak parallel character ($\beta < 0.3$) points at the relatively long lifetime, which is enough to let the acetone molecule have several rotational periods prior to its dissociation. Given the $\sim$1 ns lifetime of the $\{S_1, T_1\}$ excited states [150, 114], rotation prior to dissociation is a plausible explanation for the isotropic angular distribution.

Table 3.8: Fractions of the available energy appearing as the translation energy with respect to the photolysis wavelength in channel #3 of the acetone dissociation and the ratio of the acetyl fragments which undergo the secondary decomposition (all energies are given in wavenumbers) and the angular anisotropy parameter β.

λ_{pump}, nm	$E_{avail.}$ [a]	$\langle E_T \rangle$ [b]	ΔE_T [c]	$\langle E_T \rangle / E_{avail.}$	E_T^{limit} [d]	Acetyl [e]	β [f]
305.3	3 667	3 290	1 620	0.89	—	—	0.23
305.0	3 697	3 331	1 189	0.90	—	—	0.21
303.9	3 816	3 290	900	0.86	—	—	0.17
300.0	4 243	3 669	915	0.86	—	—	0.20
286.0	5 875	4 552	1 560	0.77	—	—	0.20
269.5	8 016	5 030	2 463	0.63	—	—	0.18
261.0	9 224	4 940	3 112	0.54	3 279	6	0.21
250.0	10 910	4 966	3 900	0.46	4 965	40	0.12
229.5	14 483	4 466	4 690	0.31	8 518	45	0.11

[a] $E_{avail.} = h\nu - D_0^0 = h\nu - 29\,090$ cm^{-1}
[b] $\langle E_T \rangle$ is the average value of the total kinetic energy release
[c] ΔE is full width at half maximum value of the TKE profile
[d] E_T^{max} is the maximal TKER value at which the acetyl fragment possess enough internal energy to overcome the dissociation barrier (5945 cm^{-1}) and produce secondary methyl radicals
[e] $Acetyl = \frac{A_{Ch.\#4}}{A_{shaded}}$ is the fraction of the acetyl fragments which undergo successive dissociation (in percent)
[f] β is angular anisotropy parameter.

The final internal energy distributions of the acetyl fragments $P(E_{int.}(CH_3CO))$ resulting from the acetone photolysis are presented in Fig. 3.29. These $P(E_{int.})$ distributions were calculated from the TKER profiles with an assumption that $E_{int.}(CH_3) = 0$, see Eq. 3.10, which gives the upper limit for the internal energy of

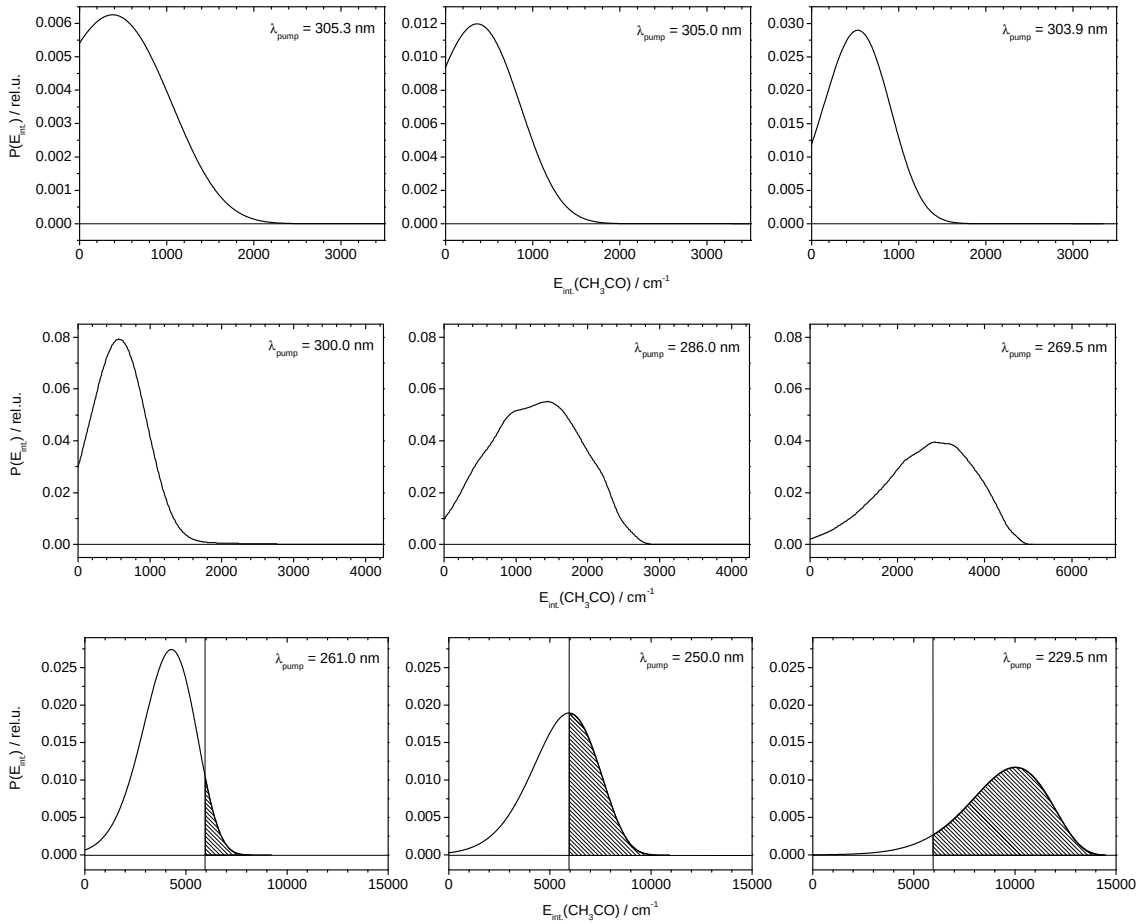

Figure 3.29: Acetyl internal energy distributions resulting from the acetone photolysis at different excitation wavelengths within the first absorption band (340 nm - 230 nm) of the acetone molecule. Vertical solid lines on the lower row demonstrate the dissociation barrier height of the acetyl fragment: $D_0^0 = 5945$ cm^{-1} [33]. The shaded area under the curves exhibits the fraction of the acetyl fragments which have enough internal energy to undergo secondary dissociation yielding slow secondary methyl radical and carbon monoxide.

the acetyl radical.

$$E_{int.}(CH_3CO) = h\nu - D_0^0 - E_T, \tag{3.10}$$

The same assumption was used to calculate the internal energy distribution of the carbon monoxide fragments. The total kinetic energy release for the secondary acetyl dissociation (E_T^{II}) was calculated from the detected kinetic energy of the slow methyl radical with the following mass ratio:

$$E_T^{II} = E_k(CH_3^{IV}) \cdot \frac{M(CH_3CO)}{m(CO)}, \tag{3.11}$$

and

$$E_{int.}(CO) = E_{int.}(CH_3CO) - D_0^0(CH_3CO) - E_T^{II}, \tag{3.12}$$

where $E_k(CH_3^{IV})$ is the kinetic energy of the slow methyl fragment, formed *via* dissociation channel #4, $D_0^0(CH_3CO)$ is the dissociation energy of the acetyl radical, for which the value of 5 945 cm^{-1} was taken from [33]. The results are shown in Fig. 3.30.

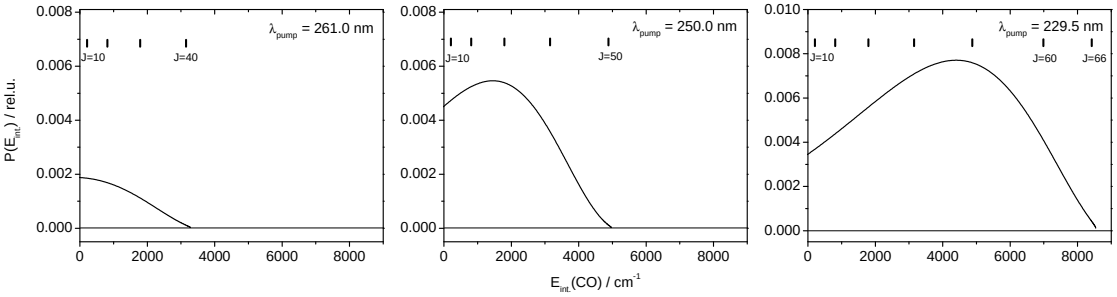

Figure 3.30: Carbon monoxide internal energy distributions resulting from the acetyl secondary dissociation. The vertical bold hatches exhibit rotational levels of the CO molecule calculated for the non-rigid rotator with rotational constant $B = 1.93$ cm^{-1} and centrifugal distortion parameter $D = 6 \cdot 10^{-6}$ cm^{-1}, taken from [71].

The internal energy distributions of the carbon monoxide fragments exhibit smooth and monomodal curves. The rotational energy distribution was analysed for the zero vibrational level ($v'' = 0$). The rotational energy of the CO fragment gradually rises with increasing excitation energy. At excitation close to the threshold for the secondary acetyl decomposition ($\lambda_{pump} = 261$ nm) pathway the carbon monoxide fragments populate up to $J'' > 40$ rotational levels but peaking at $J'' = 0$. On the other hand, acetone photolysis at $\lambda_{pump} = 229.5$ nm wavelength results in very high rotational excitation of the CO ($J''_{max} > 66$; $J''_{peak} \approx 47$). Such high rotational excitation is caused by a strong torque, imparted to the CH_3CO fragment after the parent acetone molecule has decomposed and pushed acetyl out of the linear configuration resulting in high rotational energy of CO. Note, that these curves (see Fig. 3.30) represent the upper limit of the internal energy of CO because of the assumption that $E_{int}(CH_3) = 0$ and CO possess no vibrational energy, accepted in the present estimation. However, acetyl is formed in its ground electronic state [111], where it has a bended geometry (the O-C-C angle is about 123°) [37]. The acetyl dissociation on the ground state PES proceeds *via* a transition state [149], where the O-C-C angle is even smaller (about 118°) [37]. Such a geometry of the transition state of the acetyl radical and simple kinetic consideration of the dissociation as a half collision process point out that CO must possess some vibrational excitation as well.

3.2.5 Discussion and Conclusions

The experimental results clearly demonstrate that three distinct dissociation pathways exist corresponding to three different spectral regions of acetone excitation. The following discussion is subdivided into three parts, each discussing a certain excitation region.

Region 1: 333.5 nm$> \lambda_{pump} >$ 305.3 nm

Acetone photolysis ($(CH_3)_2CO \rightarrow CH_3 + CH_3CO$) at this excitation region essentially proceeds *via* two-photon absorption of the high vibrational states of the S_0 state followed by methyl radical detachment. Another dissociation pathway is a slow unimolecular decomposition on the S_0 PES.

Acetone, excited to the S_1 state, can leave the potential surface and populate both the T_1 state and high vibrational states of the S_0 state *via* ISC and IC, respectively. The intersystem crossing does not play a significant role in acetone photodynamics for excitation wavelengths longer than 305.3 nm. An efficient $S_1 \rightarrow T_1$ coupling starts at wavelengths shorter than 320 nm, but the T_1 surface has a dissociation barrier lying at 2 285 $\pm$ 40 cm^{-1} above the $0-0$ origin of the $S_1 \leftarrow S_0$ transition. This barrier preserves acetone from direct decomposition. Dissociation of acetone *via* tunneling does not seem to be feasible, because of the heavy mass of the methyl radical and the width of the barrier [110]. Indirect dissociation pathways, which provide enough time for energy to be redistributed among many vibrational degrees of freedom, result in isotropic and statistical photofragment distributions (see Fig. 3.20 and 3.21).

Region 2: 305.3 nm$> \lambda_{pump} >$ 261 nm

An excess of 2 285 $\pm$ 40 cm^{-1} above the $0-0$ origin of the $S_1 \leftarrow S_0$ corresponds to the dissociation barrier height on the T_1 potential energy surface of $\approx$ 4 700 cm^{-1}. Acetone molecules placed above this barrier undergo a relatively fast dissociation, compared to that in the first spectral region, resulting in the fast methyl fragments and slower acetyl radicals (see Fig. 3.31).

The kinetic energy ratio between the photofragments is governed by the corresponding mass ratio. The dissociation of acetone over a barrier on the T_1 state is marked as channel #3 on the TKER graphs and this channel becomes the most prominent among all others, when the excitation energy is high enough above the dissociation barrier (see Fig. 3.24 and 3.26). Further, simultaneous dissociation through channels #1 and #2, corresponding to acetone dissociation *via* high vibrational states on the S_0 state and two-photon absorption followed by dissociation from the higher states, respectively, almost completely loses significance, when $\lambda_{pump} <$ 302.5 nm. This is an obligate result following from the theory of intersystem crossing.

The coupling of the $\{S_1 - T_1\}$ potential energy surfaces of acetone becomes more efficient at higher excitation energies. This was explained in great details in [121,

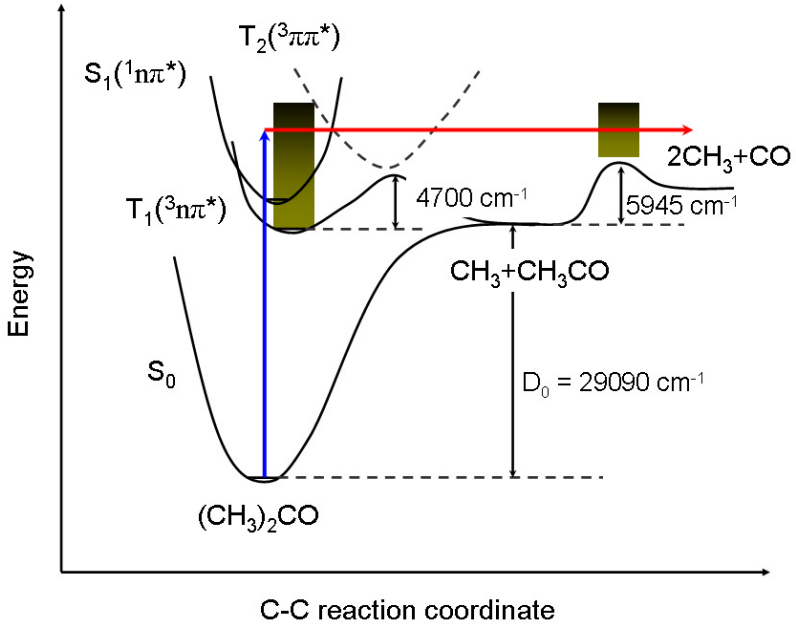

Figure 3.31: Potential energy surfaces involved in acetone dissociation dynamics.

151]. Briefly, three states are involved in the acetone photochemistry: The ground electronic state S_0, the first excited singlet S_1, and the first triplet T_1. A schematic energy level diagram is shown in Fig. 3.32, similar to that discussed in Ref. [151].

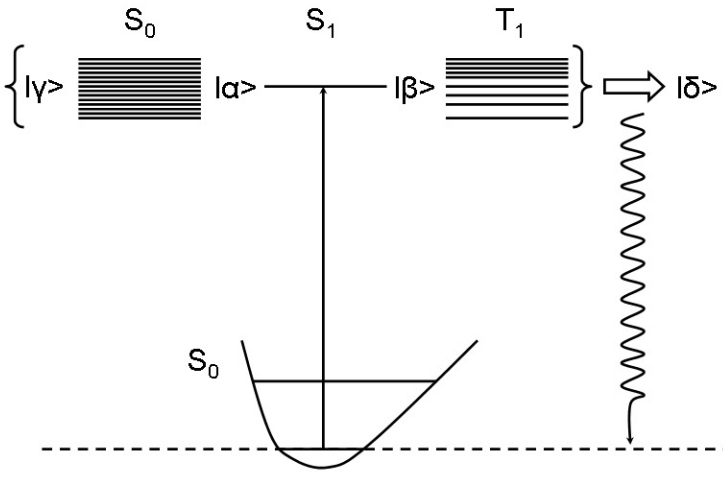

Figure 3.32: Schematic energy level diagram for the acetone molecule. For further elucidations see the text.

Initial excitation places acetone onto a rovibrational state $|\alpha\rangle$ of the S_1 surface (see Fig. 3.32). The $|\alpha\rangle$ state is coupled to a set of rovibrational states ($|\beta\rangle$) in the T_1 surface and also to a set of states $|\gamma\rangle$ of the S_0. Thus the molecular eigenstate is a superposition of all these states and is denoted as $|\delta\rangle$ in the following equation 3.13

$$|\delta >= c_{\alpha\delta} \cdot |\alpha\rangle + \sum c_{\beta\delta} \cdot |\beta\rangle + \sum c_{\gamma\delta} \cdot |\gamma\rangle \tag{3.13}$$

where the summation are over all T_1 and S_0 states within the coherence width of the excitation source ($\Delta\nu_{coh} \sim 1/(2\Delta t)$) that are coupled to the initial rovibrational state $|\alpha\rangle$.

The time evolution of this eigenstate depends on the number of coupled states and the coupling constants. The density of states for a set of s classical, harmonic oscillators of frequency ν_i with the total energy equal or less than some certain value E is determined by Whitten-Rabinovitch equation [152, 153]:

$$\rho(E) = \frac{(E + aE_z)^{s-1}}{(s-1)! \prod h\nu_i} \left[1 - \beta \frac{d\omega}{d\epsilon}\right], \tag{3.14}$$

where E_z is the zero-point energy, a is a molecule-dependent function of the internal energy, $\omega = (1 - a)/\beta$, and β is given by

$$\beta = \frac{s-1}{s} \frac{\langle\nu^2\rangle}{\langle\nu\rangle^2}. \tag{3.15}$$

Equation 3.14 demonstrates that the density of states is a rapidly increasing function of the energy E. However, despite the enormously large density of states of S_0 in the vicinity of the S_1 state ($\sim 10^{10}$ $states/\mathrm{cm}^{-1}$), the coupling is weak and only the high-frequency vibrational modes related to the C-H bond stretching and some other promotional vibrations are expected to be involved in the IC process [121]. The depopulation of the initial $|\alpha\rangle$ state back to the S_0 state is described by the radiative (fluorescence) Γ_R and non-radiative (conversion) $\Gamma_{S_0S_1}$ dissipative decay constants. Additionally, the $|\alpha\rangle$ state is coupled with the rovibrational states of the T_1 state, which in turn can be depopulated *via* phosphorescence, dissociation and coupling to the S_0 state as described by Γ_{T_1}. The density of rovibrational states of T_1 in the vicinity of the $S_1 \leftarrow S_0$ origin is much smaller than that of the S_0 state and is about $\rho_{vib.} = 80$ $states/\mathrm{cm}^{-1}$ rising up to $\rho_{vib.} = 800$ $states/\mathrm{cm}^{-1}$ at an excess energy of 1 000 cm^{-1} [121], but the coupling constant for the T_1 state is stronger than that of the S_1 state. Thus, the decay of the $|\delta\rangle$ state is proportional to:

$$\epsilon_{\gamma\gamma} = \frac{(\Gamma_R) + \Gamma_{S_0S_1}}{N} + \frac{(\Gamma_{T_1}) \times N}{(N-1)}, \tag{3.16}$$

where $\epsilon_{\gamma\gamma}$ is the damping matrix and N is the number of the T_1 rovibrational states effectively coupled to the initial $|\alpha\rangle$ state [151].

From above, it is obvious that the ISC process becomes the most important one in the acetone photodissociation with increasing excitation energy and the IC process almost completely loses its significance at $\lambda_{pump} < 302.5$ nm. The release of the total kinetic energy after the dissociation act has a certain offset value and forms the largest fraction of the whole available energy. The average value of the TKE and the FWHM of the kinetic energy profiles gradually shift to the region of higher values with increasing excitation energy and do not peak at zero values (see Table 3.8). Such a distribution of the available energy among the translational and internal degrees of freedom of the photofragments is not a typical simple bond rupture *via* a loose transition state [147]. Incomplete randomization of the available energy could result in a greater than statistical fraction in the reaction coordinate, but it is not a feasible explanation for the present case, because of the amount of available energy for $\lambda_{pump} > 261$ nm, which counts up to 9 224 cm^{-1} and the measured lifetime of 1 ns at excitation wavelength of 260 nm [114]. The impulsive model predicting the partitioning of the available energy between the translational and internal energy reservoirs of the photofragments for triatomic molecules first has been developed by Busch and Wilson [98] and was then generalized for polyatomic molecules by Tuck [99]. The impulsive approach assumes that all of the available energy flows to the reaction coordinate, which is repulsive along the bond between the two atoms. The other atoms in the molecule are considered as spectators and the redistribution of the available energy proceeds in accordance with the remaining bond angles and masses. The impulsive model predicts that 54% of the available energy should appear as fragment translation and this fraction is invariant with respect to the excitation energy since the available energy partitioning in the impulsive model depends solely on the mass ratios. In the present experiments the fraction of the available energy appearing as translation is decreasing from 90% at $\lambda_{pump} = 305$ nm down to 54% at $\lambda_{pump} = 261$ nm.

The excited state lifetime of ~ 1 ns implies that intramolecular vibrational redistribution (IVR) occurs prior to dissociation and the translational energy release will be dominated by the repulsive forces acting beyond the transition state rather than the magnitude of the available energy. Dissociation will occur when sufficient energy, which is statistically redistributed among the vibrational modes of the parent molecule, flows into the reaction coordinate to overcome the barrier on the T_1 potential energy surface. Photofragment translation, therefore, increases with available energy in proportion to the probability of finding the excess energy in the reaction coordinate. This dependence is moderate as it follows from the experimental results, and mostly affects the width of the kinetic energy distribution (see Fig. 3.34). The insensitivity of the photofragment translation to the excitation energy suggests that the dissociation dynamics are mediated by the exit barrier on the potential energy surface, which is consistent with the theoretical findings. The presence of an exit barrier on the potential surface of the reaction state makes the resulting product energy distribution generally irreproducible by statistical models for chemical reac-

tions even if the excited complex persists for many vibrational periods. The observed behavior in the present work cannot be well described neither by the statistical or impulsive model. There are many theories predicting the product state distributions for nonstatistical unimolecular dissociation over a barrier. The statistical adiabatic channel model (SACM) is generally used in the vicinity to the threshold but for loose transition state [147], North *et al.* have developed a barrier-impulsive model, which was used to interpret the low degree of vibrational excitation among the photoproducts [33]. Neumark *et al.* [154] suggested a statistical adiabatic impulsive model and there are many others. The common concept of all these theories [147, 33, 154] is that the available energy is regarded to be partitioned between two reservoirs: the barrier height relatively to the exit valley and the second one, the available energy above the barrier (see Fig. 3.33). The way how these reservoirs are treated, depends on the respective theories. The work of North *et al.* demonstrates a good agreement between experimental results and those calculated in the assumptions of the barrier-impulsive model.

Region 3: 261 nm$> \lambda_{pump} >$ 229 nm

The maximal TKE values corresponding to channel #4 are equal to the truncated TKE values calculated from the TKE profiles of channel #3 (maximal TKE value of the shaded area in Fig. 3.28). Increasing the excitation energy makes the total available energy greater, which results in higher translation and internal energies of the photofragments. Obviously, at a certain excess energy over the T_1 acetone dissociation barrier, the acetyl fragment can receive enough internal energy to release the secondary methyl radical and carbon monoxide. Thus, the flow of the available energy into the acetyl fragment competes with the flow of energy to the primary α-C-C bond cleavage in the parent acetone molecule. After the preparation of the initial state on the S_1 surface of the acetone molecule, IVR splits the wave packet in two unequal fractions, but this inequality becomes less and less with increasing excess energy, and, in some sense, the secondary dissociation loses its meaning as "second step". That means that the acetone dissociation dynamics move to the concerted limit rather to the stepwise. The average TKE values appearing in both channels (#3 and #4) become more close to each other (Figure 3.34). This can be viewed as the first methyl radical detaches from the already decaying acetyl fragment at sufficiently high excitation energy of this spectral region. High rotational excitation of the CO fragment is a sign for a relatively strong torque, imparted to the CH_3CO fragment after the parent acetone molecule has decomposed, which immediately pushes acetyl out of the linear configuration with the result that the CO rotates quickly.

However, Zewail *et al.* have calculated that the S_1 state of the acetone molecule possess a barrier of about 18 kcal/mol along the single α-C-C bond coordinate, which leads together with the C-C-O bending to the S_0/S_1 conical intersection (CI) [112]. The geometry of the acetyl radical at the CI point is almost linear, which is con-

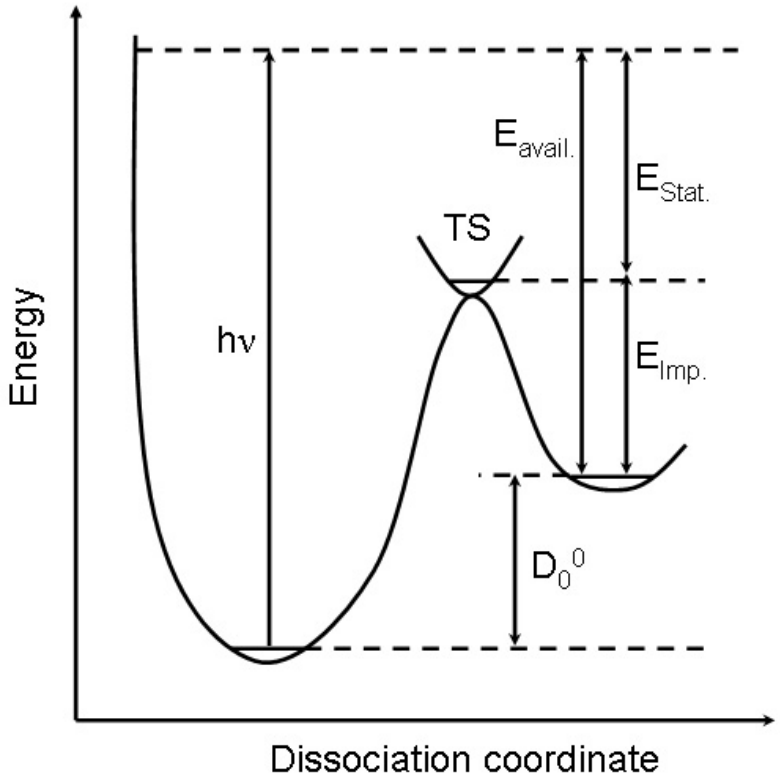

Figure 3.33: SAI model of the partitioning of the energy available into two independent energy reservoirs: The statistical reservoir ($E_{Stat.} = E_{avail.} - E_{TS}$) and the impulsive "sudden" reservoir ($E_{Imp.} = E_{TS}$) [154].

.

sistent with previous findings characterizing the potential energy surfaces involved in the acetone photodynamics [110]. After passing the CI funnel, acetone dissociates to methyl and acetyl radicals. Additionally, in the present work, λ_{pump} was scanned from 286 nm to 261 nm near this "barrier to CI" and the slow component corresponding to channel #4 appeared at $\lambda_{pump} = 261$ nm. This excitation energy corresponds to 22.5 kcal/mol and differs from the value calculated by Zewail *et al.* by ∼4 kcal/mol, but considering the calculation accuracy, it is possible that the new feature in the TKER distribution belongs to CH_3 fragment originating from acetone dissociation after passing through the CI between the S_0 and S_1 potential energy surface. A shift of the peak position and the FWHM of this new TKE profile of the slow CH_3 fragments and simultaneous decrease of the peak and FWHM values of the fast channel #3 (see Fig. 3.34) would than mean that the higher excess energy makes the coupling of the S_1/S_0 surfaces *via* CI more favorable in expense of the ISC coupling. In principle, the initially prepared wave packet on the S_1 state then

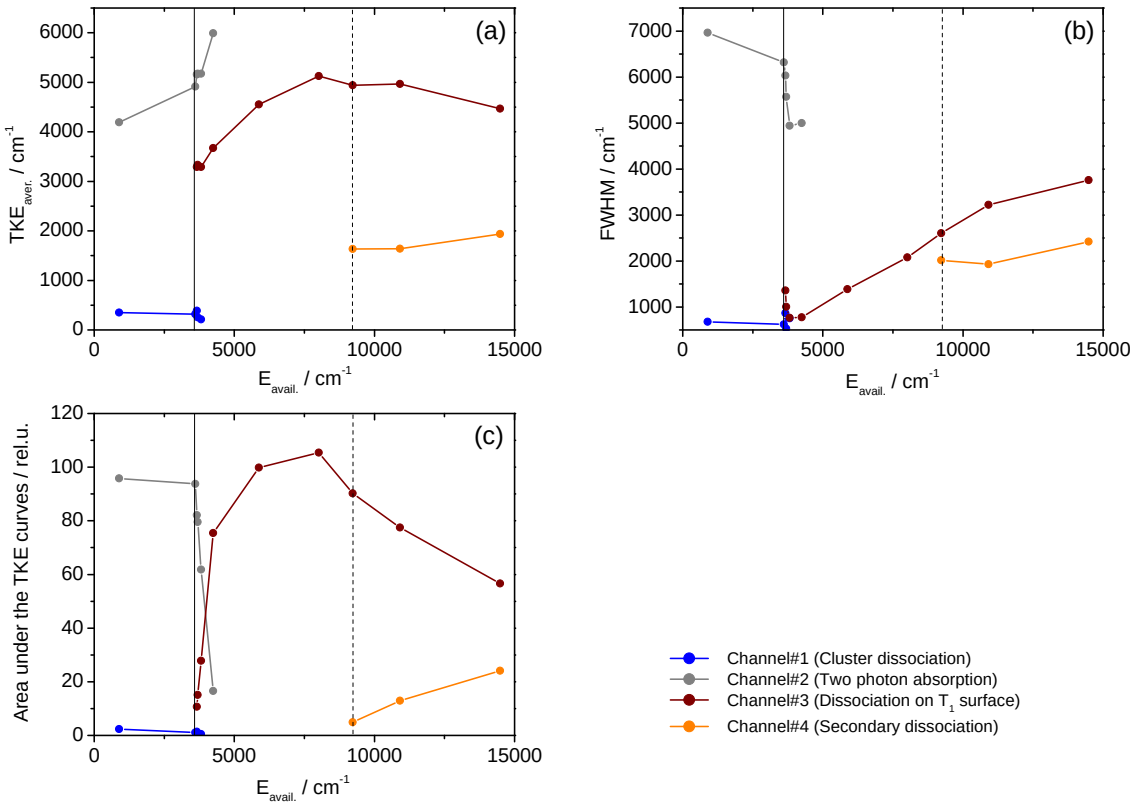

Figure 3.34: Diagrams of average TKER value (a), FWHM (b) and area under the curves (c) of the TKER profiles resulting from the acetone dissociation as functions of the available energy $E_{avail.}$. Vertical black solid and dashed lines represent the minimum $E_{avail.}$ values, which are enough to open dissociation channels #3 ($E_{avail.}$ = 3 638 cm^{-1}) and #4 ($E_{avail.}$ = 9 224 cm^{-1}), respectively.

slides down to the minimum of the S_1 surface, which results in pyramidalization of the acetone molecule and linearization of the acetyl moiety. The movement of the wavepacket from the Franck-Condon region is very fast (< 200 fs) and was measured by several groups investigating acetone dissociation with femtosecond time resolution [124, 35, 112]. The last measurements, done by Rusteika *et al.*, show that this wavepacket motion out of the Franck-Condon region is even faster, shorter then 30 fs [129]. The S_0 and S_1 potential energy surfaces at such linear pyramidalized geometry are degenerate and population of the S_0 state *via* CI is possible. The IVR process could redistribute the vibrational energy in a such way that one quantum in the C-C stretching mode and C-C-O bending angle is presented making it possible to drive the wave packet to the CI funnel on the PES. This could result in a low kinetic energy release and high internal (rotational and necessarily vibrational) energy of the methyl and carbon monoxide photofragments. In fact, the detected CO fragment, which is conjugated to the detected vibrationless CH_3 fragment, did not exhibit any vibrational progression in the internal energy distribution

(see Fig. 3.30), but vibrational excitation can take place for C-C-O bending mode, C-C stretching as well as CH_3 rotation and after dissociation they would result in fragment translation and rotation energy rather than in vibration excitation. Additionally, CH_3 radicals must be probed in its vibrationally excited states, which can be associated with dissociation impulse along the C-C bond of the acetyl fragment to get a full picture of the slow methyl component on the TKE curves. On the other hand, from calculations of Zewail *et al.*, it follows that acetone molecules which went through the CI between the S_0 and S_1 states, could go back to the S_0 surface rather than dissociate. It is unlikely that unimolecular decomposition in this case would be faster than that one observed in the present work at $\lambda_{pump} > 306$ nm, therefore the hot acetone molecules on the S_0 surface should have, before they dissociate, a possibility to absorb the second photon and dissociate from the upper states resulting in a broad TKE distribution with maximal values exceeding the total available energy from the one-photon absorption process (as it was observed in Region 1). In fact, no such broad tail was observed in the present work suggesting that either the amount of hot acetone molecules on the S_0 surface is negligibly small compared to the acetone molecules, which undergo dissociation directly after passing through the CI and the signal is indistinguishable from the noise or the CI process does not play a significant role and the slow methyl fragments detected at $\lambda_{pump} < 261$ nm originate from secondary decomposition of the acetyl fragments. The last argument against the CI mechanism is that such dissociation pathway would only result in methyl and acetyl radicals, but Somnitz *et al.* have detected carbon monoxide as a photoproduct of acetone photolysis at 248 nm excitation wavelength [135]. On the other hand, the acetyl radical can dissociate later, thus one can observe CO as well. The slower timescale of the secondary dissociation of acetyl can confute the argument concerning the CO yield.

Summarizing all arguments above, the most plausible assignment of channel #4 is secondary decomposition of the acetyl fragment on its S_0 potential energy surface. This acetyl decay is responsible for the slow secondary methyl radical marked as channel #4 in Fig. 3.28.

3.3 Photolysis of Acetone-*d*6

3.3.1 Introduction

The photodissociation of the deuterated acetone-*d*6 molecule was investigated in the present work to understand the influence of the peripheral isotope substitution effect on the dissociation process, barriers height, and available energy partitioning between the photofragment translation and internal degrees of freedom.

Haas *et al.* investigated the fluorescence properties of both acetone-*h*6 and -*d*6 excited to the S_1 state *via* LIF spectroscopy and observed biexponential decay of the fluorescence signal at an excitation energy excess of 800 - 1 800 cm^{-1} above the $0-0$ transition [120, 121]. The fast component was ascribed to the efficient coupling of the S_1 state to the T_1 state *via* ISC due to the higher density of the states. The long-lived component of the fluorescence signal was associated with internal conversion of the initially prepared S_1 state to the ground S_0 state and intersystem crossing of the T_1 to the S_0 state. This long-lived component completely disappears at an excess energy of 2 250 cm^{-1} for acetone-*h*6 and 2 500 cm^{-1} for acetone-*d*6. Such behavior was interpreted as the opening of the dissociation channel on the triplet state once the parent molecule possess enough energy to overcome a small dissociation barrier on the T_1 surface. Differences in the excess energies for both isotomers were interpreted as the lowering of the zero-point energy of the vibrations participating in the dissociation process caused by the deuteration of the methyl groups of the parent molecule [121].

Isotope effects on the ultrafast photodissociation dynamics of acetone excited to the 3*s* Rydberg state was also studied in the literature [155, 35, 156]. The decomposition of the acetone-*d*6 molecule to 2 CD_3 + CO was observed to be stepwise, intermediated by a fast internal conversion $S_2 \rightarrow S_1$. There are two alternative possibilities considered in the literature about the further fate of the acetone molecule. It has been commonly assumed that a subsequent intersystem crossing $S_1 \rightarrow T_1$ followed by dissociation over the T_1 barrier happens after $S_2 \rightarrow S_1$ IC [157, 31, 124]. An alternative dissociation pathway taking place directly on the S_1 state was regarded theoretically [112, 131] and proved experimentally [128, 158]. A huge influence of the deuterium substitution on the decay rate constant of the transient mass signals was observed for the every step of the photoreaction. The initial decay from S_2 to S_1 slows down by a factor of three, the subsequent adiabatic dissociation on the S_1 surface slows down by a factor of four, and the secondary decomposition slows down by a factor of two [35, 156]. It is important to mention that acetone excited to the 3*s* Rydberg state converts back to the S_1 state within $\sim$ 4 ps with a large amount of vibrational energy ($\sim$ 250 kJ/mol) and dissociates to CH_3 (CD_3) radicals in their ground state and CH_3CO (CD_3CO) fragments in the electronically excited state which differs from the dissociation on the T_1 surface, where acetyl fragment is produced in its ground state. Electronically excited acetyl then converts to its

ground state ($\sim$ 100 fs) producing a hot acetyl radical on the ground state which undergoes secondary dissociation, resulting in the second methyl radical and carbon monoxide [159, 160].

In the following, the experimental results observed in the present work are presented and discussed in comparison with those from acetone-*h*6 and previous research on acetone-*d*6.

3.3.2 UV Absorption Spectrum of Acetone-*d*6

Isotopic substitution changes the nuclear spin, decreases the zero-point energy of the molecule and changes the moments of inertia of the molecule which affects the absorption spectrum, dissociation energy and fragments energy distributions. There is neither influence on the symmetry of the electronic states nor on the geometry of the molecule caused by isotopic substitution. Therefore, as in the case of acetone-*h*6, the same symmetry notation of the electronic states involved in the photodissociation dynamics of acetone-*d*6 can be used. Acetone-*d*6 in its ground state $S_0(^1A_1)$ belongs to the C_{2v} point group, thus the direct photoexcitation to the $S_1(^1A_2)$ state is symmetry forbidden, but vibronic coupling with the higher $S_2(^1B_2)$ state makes the electronic transition $^1A_1 \rightarrow ^1A_2$ observable in the absorption spectrum just like in the case of acetone-*h*6. The photoexcitation proceeds *via* promotion of a non-bonding n electron of the oxygen atom to the antibonding π^* orbital. The excited singlet S_1 state is coupled to the S_0 and $T_1(^3n\pi^*)$ state *via* IC and ISC, respectively.

The UV absorption spectrum of gaseous acetone-*d*6 is presented in Fig. 3.35 together with that of acetone-*h*6. The spectrum was recorded at 298 K and 18 mbar. It exhibits the first absorption band of both isotopomers.

The peak position of the absorption band for acetone-*d*6 is shifted by $\sim$320 cm^{-1} to the red relative to the acetone-*h*6 absorption maximum. Baba *et al.* have detected LIF spectra of acetone-*h*6, and -*d*6 in molecular beams and determined the origin of the $S_1 \leftarrow S_0$ transition to be 30 431 cm^{-1} and 30 435 cm^{-1}, respectively [161]. Obviously, the deuteration of the methyl rotors in the acetone molecule does not have a large influence on the electronic states.

The broad and unstructured shape of the absorption band of acetone-*d*6 is essentially like for acetone-*h*6 due to strong changes in the geometry of the molecule, such as lengthening of the C=O bond, change in the C-C-O angle, and pyramidalization of the molecular C-C(O)-C frame.

In the present work, the photolysis of the acetone-*d*6 excited in the first absorption band was studied.

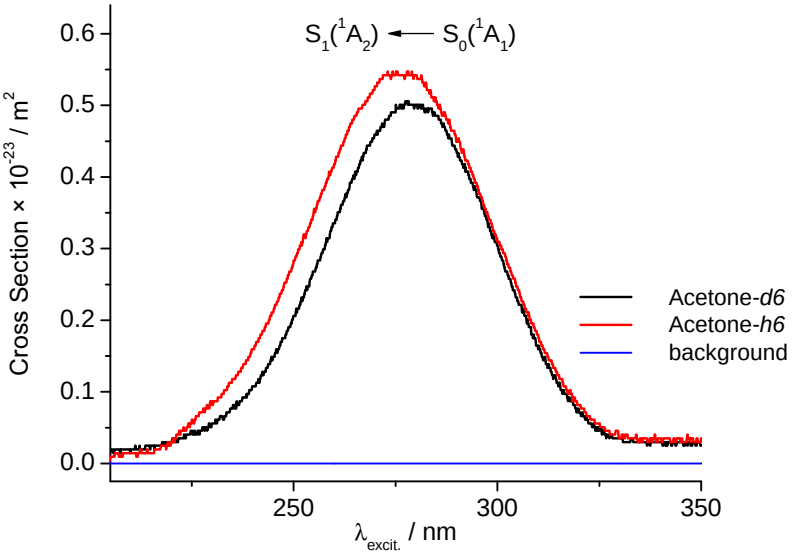

Figure 3.35: Bulk gas phase UV absorption spectrum of the first band $S_0 \rightarrow S_1$ ($n\pi^*$) of acetone-*d*6, and -*h*6.

3.3.3 REMPI Detection of the CD_3 Radical

Acetone-*d*6 excited to the first absorption band in the UV absorption spectrum (S_1 state) dissociates to CD_3 and CD_3CO. The photodissociation dynamics was studied in the present work *via* observing velocity and angle distributions of the CD_3 fragment as a function of the photolysis wavelength. The CD_3 radicals were detected by the REMPI technique *via* the same resonance as CH_3 radical in the acetone-*h*6 experiments. That is, CD_3 radical in its ground vibrational state ($v = 0$) was probed *via* the Q-branch of the electronic rotational transitions to the $3p^2A_2''$ state, which corresponds to $\lambda_{probe} = 333.85$ cm^{-1}. Line identification was done by a comparison of the REMPI spectra of CD_3 from acetone-*d*6 with those from CD_3I, both photolysed at 286 nm. The experiments were done with care to ensure that only the two-color signal contributed by ions. The results are presented in Fig. 3.36.

The REMPI spectra are in a good agreement with the literature [143, 162] and exhibit a well pronounced peak corresponding to the ionization of CD_3 in its ground vibrational state ($v = 0$) *via* the Q-branch of the electronic rotational transitions to $3p^2A_2''$. The width of the Q-branch in the base is ∼9 cm^{-1}. The REMPI spectra of the CD_3 radical do not differ in shape from those of CH_3, except that the origin of the electronic transition lies around 333.85 nm for CD_3 and around 333.5 nm for CH_3. The time delay between the pump and probe laser beams was optimized to be 20 ns, which repeats the result for the case of acetone-*h*6.

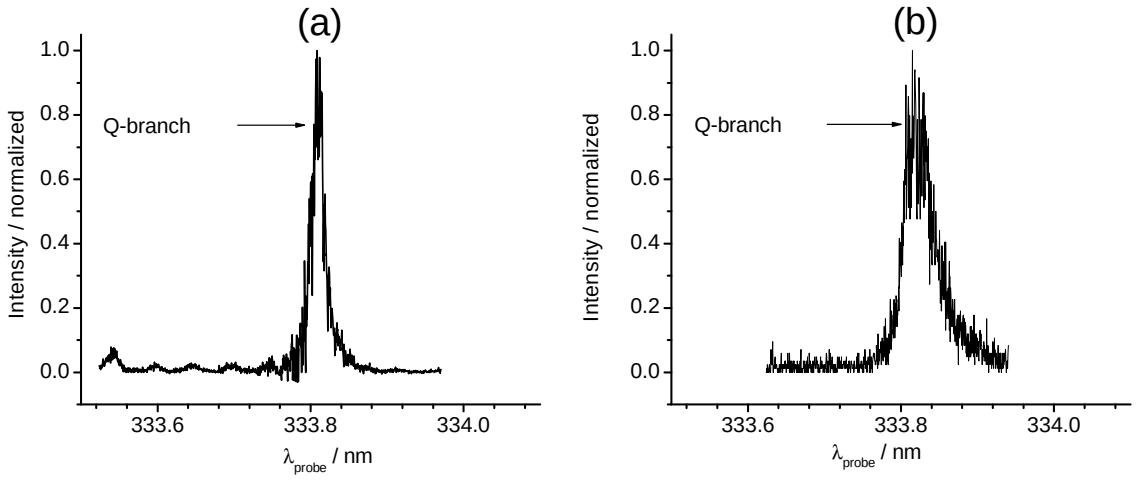

Figure 3.36: (2+1) REMPI spectrum of CD_3 ($v = 0$) *via* $3p^2A_2'' \leftarrow X(^2A_2'')$ resonance transition from CD_3I (a) and from acetone-*d*6 (b), both photolysed at $\lambda_{pump} = 286$ nm wavelength.

3.3.4 Velocity Map Imaging of the Acetone-*d*6 Photodissociation Dynamics

The photodissociation dynamics of acetone-*d*6 excited at different wavelengths within the first absorption band was studied by detecting the vibrationless CD_3 fragments using velocity map imaging. The photolysis of the deuterated acetone proceeds essentially like that of acetone-*h*6 and the distinct spectral regions where the excitation takes place corresponding to certain dissociation pathways can be defined here as well. The following results Section is subdivided in three spectral regions:

$$\text{Region 1: } 333 \text{ nm} > \lambda_{pump} > 305 \text{ nm}$$
$$\text{Region 2: } 305 \text{ nm} > \lambda_{pump} > 260 \text{ nm}$$
$$\text{Region 3: } 230 \text{ nm} < \lambda_{pump} < 260 \text{ nm}$$

In the VMI experiments, the polarization of the laser beams (pump and probe) was held parallel to each other and to the surface of the MCP detector. The probe laser was scanned over the Doppler width ($\sim$9 cm^{-1}) of the detected CD_3 photofragment.

(1) The CD_3 ion images recorded at excitation wavelengths within Region 1 exhibit diffusive, structureless and isotropic fragment distributions with an intense central spot. The ion images recorded from the acetone-*d*6 photolysis at $\lambda_{pump} = 306$ nm and $\lambda_{pump} = 305$ nm are presented in Fig. 3.37.

It is clearly seen from Figure 3.37 that already excitation of acetone-*d*6 with $\lambda_{pump} =$ 305 nm results in a specific CD_3 fragment distribution. There is a ring-like structure suggesting a very different dissociation pathway of the parent molecule than one at

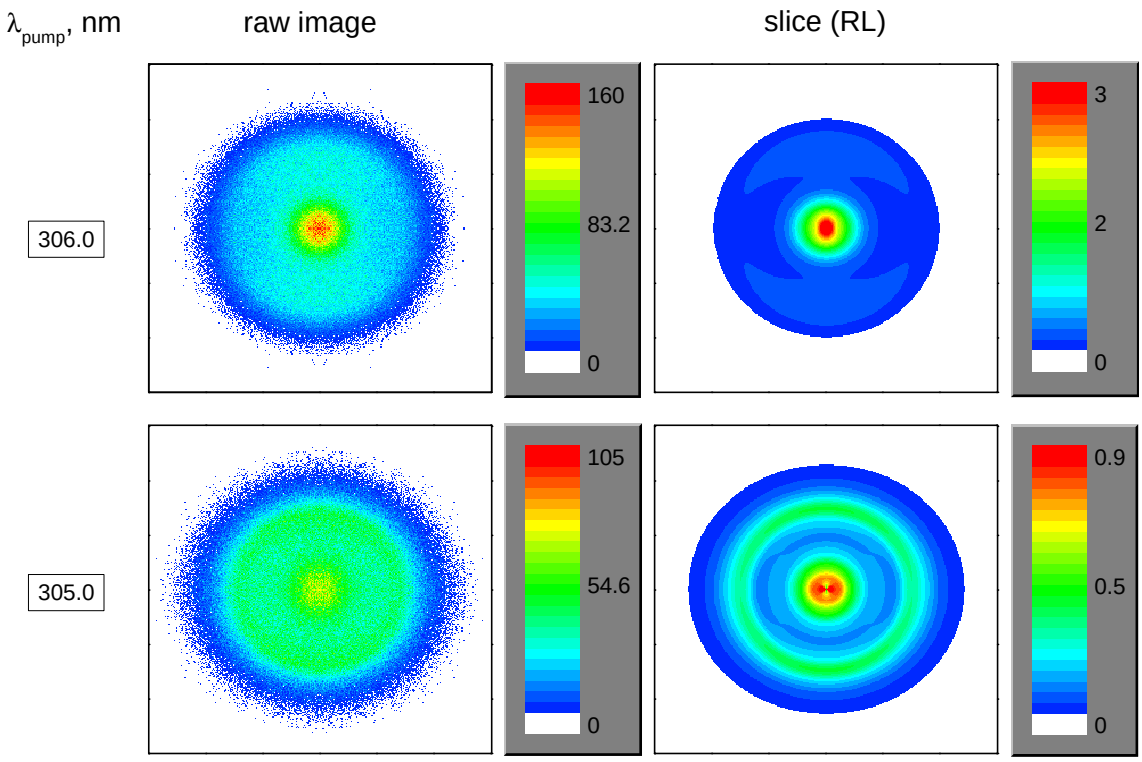

Figure 3.37: Two-color velocity map images of CD_3 from acetone-*d*6 photolysis at certain excitation wavelengths (left column). Notations and color code are the same as in Fig. 2.13.

longer excitation wavelengths. The same tendency in the dependence of the ion distribution on λ_{pump} for this spectral region was observed for acetone-*h*6.

Corresponding TKER distributions were calculated as was described previously in Sections 2.4.4 and 2.4.5 for the CD_3 fragment time-of-flight of 3.009 μs and are shown in Fig. 3.38.

Gaussian functions were used to fit the experimental distributions in the velocity domain followed by the conversion to the energy domain. The area under the experimental curve was normalized to unity. The TKER distribution resulting from the acetone-*d*6 photolysis at $\lambda_{pump} = 306$ nm demonstrates a broad bimodal profile with the maximum kinetic energy value up to $E_T^{max} \sim 30\,000$ cm^{-1} (not shown in Fig.). The bimodal distribution of the photofragments suggests an existing of two different dissociation pathways, marked as channel #1 and #2 in Fig. 3.38. The deuteration of acetone did not cause any significant changes in the excitation spectrum. Additionally, the molecular geometries in the S_0 and in the S_1 state of both isotopomers are very similar to each other. It is assumed here for the moment, based on these facts, that the dissociation energy of acetone-*d*6 does not differ from that of acetone-

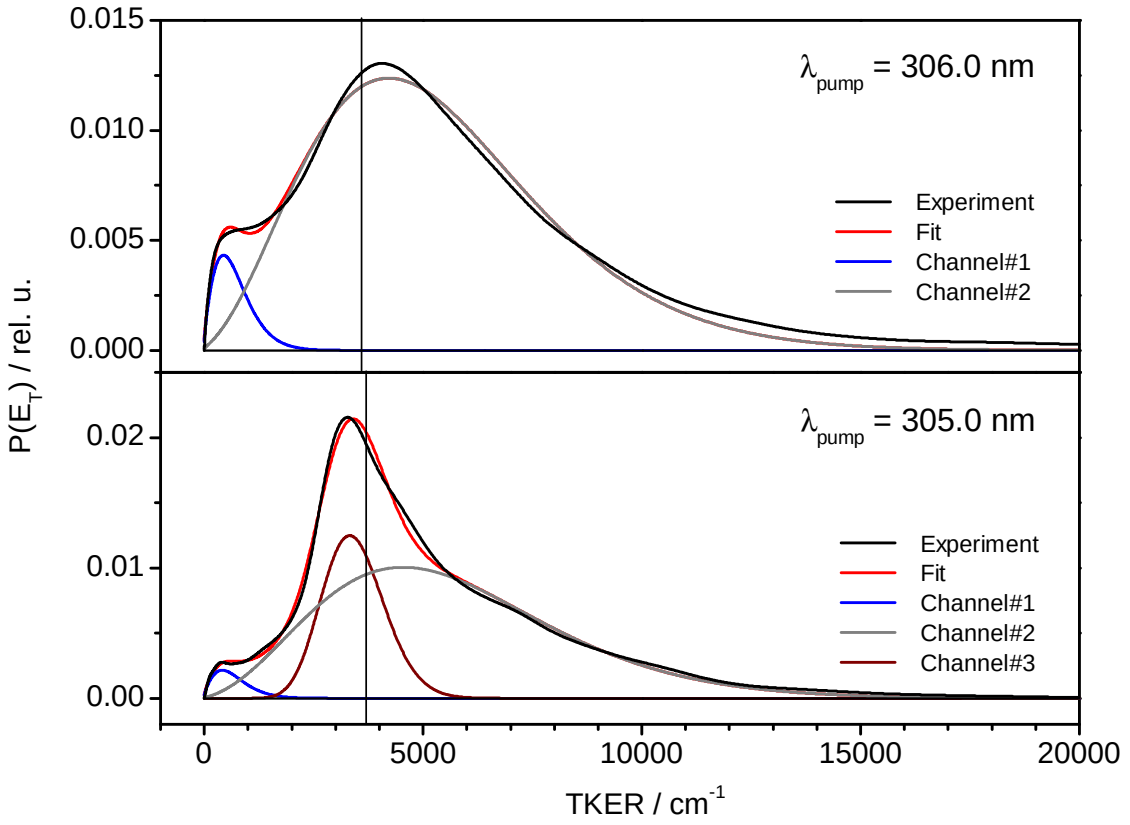

Figure 3.38: TKER distributions for $\lambda_{pump} = 306$ nm (upper trace) and $\lambda_{pump} = 305$ nm (lower trace). Vertical black solid lines on the TKER distribution graphs present corresponding available energies ($E_{avail.}$) for one-photon dissociation assuming that D_0(acetone-$d6$) = 29 090 cm^{-1}. See the text for further elucidations.

$h6$ and is temporarily accepted as $D_0^0 = 29\ 090$ cm^{-1}. This assumption results in the maximum available energy $E_{avail.}^{max} = 3\ 590$ cm^{-1}. From $E_{avail.}^{max}$ and E_T^{max} values, it is immediately seen that such broad TKER distribution is only possible from the two-photon absorption process. In the following, channel #2 is always associated with the two-photon absorption followed by dissociation of acetone-$d6$ from higher states. The maximum energy value of the curve in Fig. 3.38 marked as channel #1 does not exceed $E_{avail.}^{max}$ and is affected by the sample pressure and temperature in the same way as in the case of acetone-$h6$. By analogy with acetone-$h6$, it was concluded that this narrow distribution peaking at the zero TKER value arises due to clusters dissociation and due to the slow CD_3 fragments coming from unimolecular decay of acetone-$d6$ from the high vibration levels of the S_0 state populated *via* internal conversion.

The increase of the excitation energy to $2\ 350 \pm 60$ cm^{-1} above the $0-0$ origin of the $S_1 \leftarrow S_0$ transition (30 435 cm^{-1}) opens an additional dissociation pathway for acetone-$d6$, which is observable as an additional ring-like feature in the ion

distribution (see Fig. 3.37). The corresponding curve in the TKER distribution is denoted as channel #3 in Fig. 3.38. This curve peaks at 3 329 cm^{-1} has a full width at half maximum ΔE_T of 1 667 cm^{-1}, and a maximum energy $E_T^{max} \sim 5\,795$ cm^{-1}. The reasons why E_T^{max} of channel #3 exceeds the $E_{avail.}^{max}$ for 2 205 cm^{-1} could be the following: (i) The strong overlapping of the ions coming from this channel with the ions produced in the channels #1 and #2. This causes a big error in the fitting procedure. (ii) The presence of the vibrationally hot molecules in the molecular beam. This, however, should not account much for the broadening because the vibrational temperature of acetone measured at room temperature is ~ 600 cm^{-1} [163] and most of this excitation involves low frequency modes such as skeletal bends and methyl rotations, which are expected to undergo at least partial relaxation in the supersonic expansion. (iii) The convolution of the signal with the resolution function of the apparatus (250 cm^{-1}). This effect is described in the Section 2.4.5.3.

Symmetric isotopic substitution affects the zero-point energy of the vibrations and rotations and decreases their frequencies, but has no influence on the shape of the potential energy surface [63]. This fact suggests that the same potential surfaces with the same topology are involved in the photodynamics of the isotopomers. The only difference appears in the barriers height, coupling constants and the density of states. Assuming a similarity of the potential surfaces of acetone-*h*6, and -*d*6, it is accepted here that the ring observed in the ion distribution at $\lambda_{pump} = 305$ nm comes from fast CD_3 fragments after acetone-*d*6 photolysis over the dissociation barrier on the T_1 state which is populated by wavepacket transfer from the S_1 state *via* ISC. The excess energy at which channel #3 opens up ($2\,350 \pm 60$ cm^{-1}), is only slightly higher and actually can be regarded as equal to the excess energy detected in the present work for acetone-*h*6 ($2\,285 \pm 40$ cm^{-1}) within the experimental error. At the first look, the present results suggest that there is no a significant influence of the methyl rotors deuteration on the dissociation barrier height of the T_1 state. However, Zuckermann *et al.* have observed that the measured fluorescence decay rate increases rather abruptly at about 2 500 cm^{-1} for acetone-*d*6 and at 2 250 cm^{-1} for acetone-*h*6 [121]. These results were interpreted with the isotopic substitution effect on the ZPE level, *i.e.*, deuteration of the methyl groups of the acetone molecule decreases the ZPE levels, resulting in the increased dissociation energy [121]. Additionally, deuteration causes the decrease of the vibrational and rotational frequencies thus increasing the density of ro-vibrational states and improving the efficiency of ISC which was also observed in this group [121]. Interestingly, the dissociation barrier on the T_1 surface in the present experiment appears with approximately the same height for the deuterated acetone as for the protonated one. The difference of the present results and those from the work of Zuckermann [121] is puzzling and will be discussed in Section 3.3.5.

Fast CD_3 fragments observed from acetone-*d*6 photolysis at $\lambda_{pump} = 305$ nm exhibit an isotropic angular distribution with $\beta = 0.19$. Such a low value of the angular anisotropy parameter suggests a long lifetime of the parent molecule in the excited

state relative to the rotational period of the molecule. Additionally, internal vibrational redistribution together with intersystem crossing reduce β even stronger.

(2) Photodissociation of acetone-*d*6 in Region 2 (306 nm $> \lambda_{pump} >$ 260 nm) makes the dissociation of the parent molecule going principally *via* channel #3, *i.e.*, the parent molecule excited to the S_1 state undergoes ISC and appears on the T_1 surface, where acetone-*d*6 still has enough energy to overcome the dissociation barrier formed by an avoided crossing with the T_2 state. This is clearly seen on the ion distributions images where the ring-like feature becomes the most pronounced one (Figure 3.39) and the corresponding curve on the TKER distribution forms the biggest fraction of the overall ion signal (see Fig. 3.40).

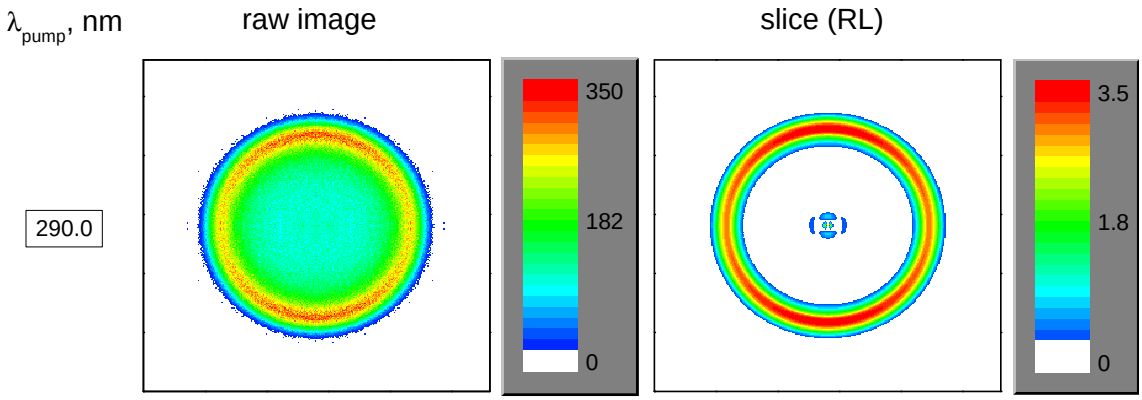

Figure 3.39: Two-color velocity map images of CD_3 from acetone-*d*6 photolysis. Notations and color code are the same as in Fig. 2.13.

Acetone-*d*6 excited to the S_1 state in this spectral region possesses enough rovibrational energy to make the coupling with the T_1 state highly efficient due to increased density of rotational and vibrational states of the corresponding electronic surfaces. ISC followed by the parent molecule dissociation on the T_1 state becomes essentially the only dissociation pathway, making the influence of other channels negligible. The same behavior was observed in the case of acetone-*h*6. This advantage was used here to determine the maximum kinetic energy release E_T^{max} in order to estimate the dissociation energy of the C-C bond of acetone-*d*6. The average total kinetic energy $\langle E_T \rangle$ released *via* channel #3 is 3 816 cm^{-1}; FWHM is $\Delta E_T =$ 1 363 cm^{-1} and $E_T^{max} =$ 5 496 cm^{-1}. This results in a dissociation energy of

$$D_0^0 = 28\ 987\ \text{cm}^{-1} \pm 250\ \text{cm}^{-1}$$

This value is slightly lower than the dissociation energy of acetone-*h*6 measured in the present work but is the same as for acetone-*h*6 within the experimental error.

The ion angular distribution stays essentially isotropic ($\beta = 0.11$).

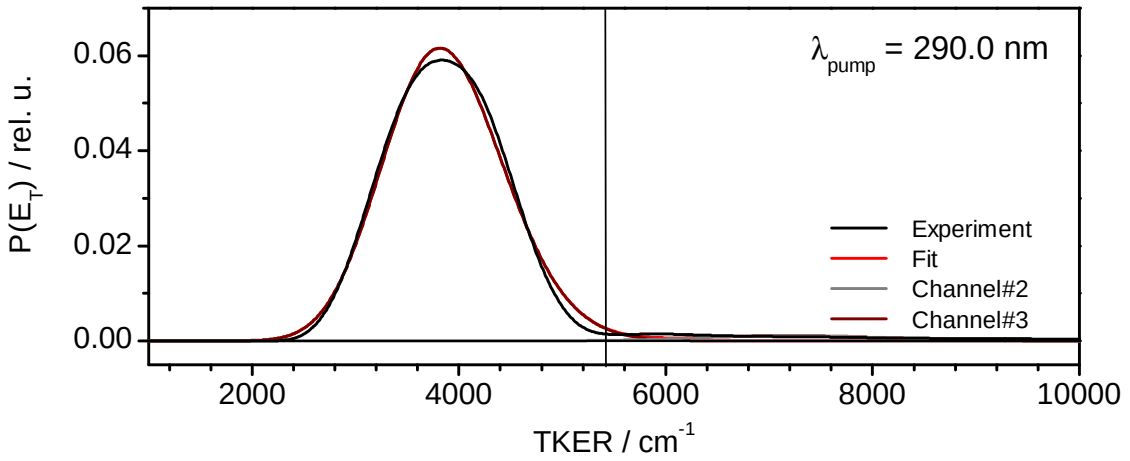

Figure 3.40: TKER distributions for $\lambda_{pump} = 290$ nm. Notation is as before (see Fig. 3.38).

(3) In order to complete the comparison of the dissociation dynamics of the acetone-*h*6, and -*d*6 molecules, the photolysis wavelengths were varied in the Region 3 (230 nm $< \lambda_{pump} <$ 260 nm). Acetone-*h*6 photolysis in this region exhibits bimodal CH_3 fragments distributions, where the nature of this behavior was interpreted as secondary decomposition of the highly internally excited acetyl photofragments CH_3CO. The ion distributions from the photolysis of acetone-*d*6 in this excitation region are presented in Fig. 3.41.

A new pattern is observed in the ion distributions, that arises from slow CD_3 photofragments with a high intensity at the center of the images. The quantitative description of the new feature on the velocity map images is possible *via* analysis of the TKER profiles in Fig. 3.42. The new slow CD_3 fragments are characterized by a curve denoted as channel #4 on the TKER distribution graphs.

Channel #3 exhibits the following tendency with increasing the photolysis wavelength: The average value of the total kinetic energy release decreases from 4 941 cm^{-1} down to 4 570 cm^{-1}, but FWHM suffers opposite changes, *i.e.*, it increases from 2 958 cm^{-1} up to 3 331 cm^{-1}. Additionally, the area under the curve of channel #3, which is a measure of the fraction of CD_3 fragments formed *via* the triplet state dissociation of the parent molecule, decreases as well. At the same time channel #4 evolves differently with varying λ_{pump}, *i.e.*, the area under the curve increases drastically. The area under the channel #4 curve accounts for only $\sim 4\%$ of the overall area at $\lambda_{pump} = 260$ nm, but it is already about 24% after acetone-*d*6 photolysis at $\lambda_{pump} = 250$ nm. The FWHM also increases from 2 192 cm^{-1} up to 2 536 cm^{-1} and the average TKER of channel #4 ($\langle E_T \rangle$) demonstrates a slight increase from 1 370 cm^{-1} at $\lambda_{pump} = 260$ nm to 1 373 cm^{-1} at 250 nm, but this

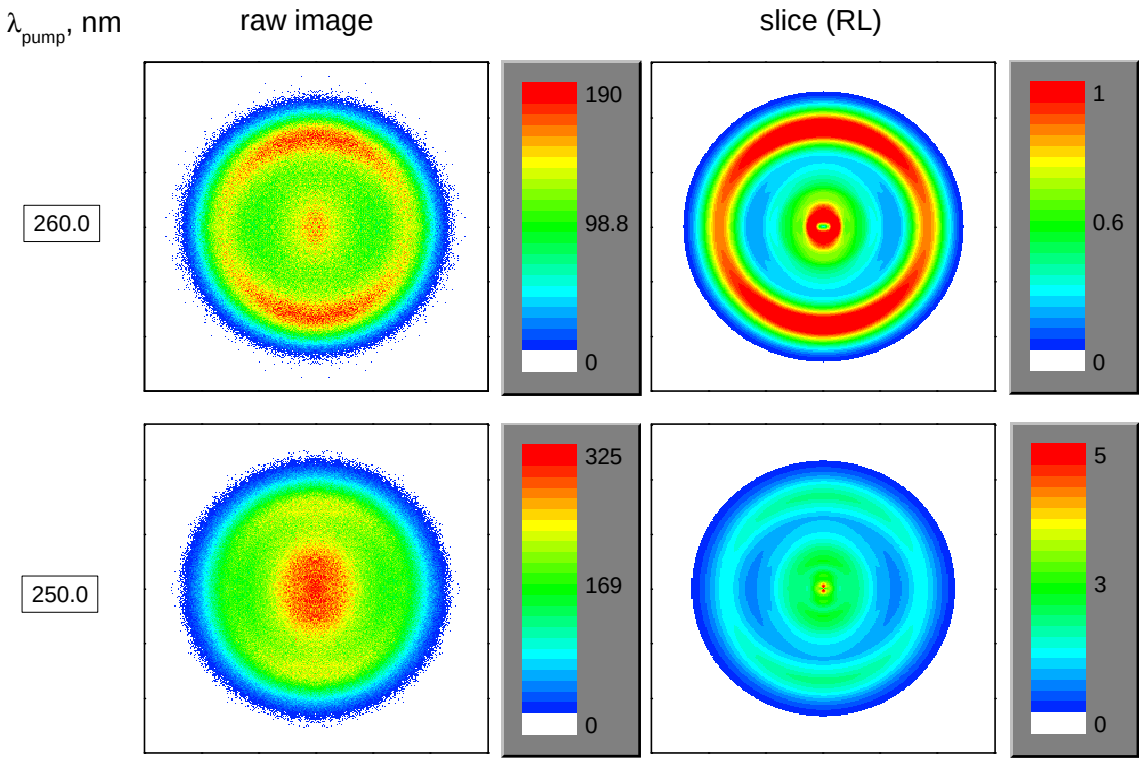

Figure 3.41: Two-color velocity map images of CD_3 from acetone-*d*6 photolysis. Notations and color code are the same as in Fig. 2.13.

is within the experimental and fitting error and cannot be regarded as a reliable change. The same changes in the kinetic energy distributions and correlations between them for the dissociation channels #3 and #4 were observed in the acetone-*h*6 photolysis at $\lambda_{pump} < 261$ nm.

The results of the CD_3 ion imaging experiments on the photodissociation dynamics of acetone-*d*6 repeat the main and crucial features observed in the CH_3 ion distributions from the photolysis of acetone-*h*6 for the whole spectral region corresponding to the first absorption band in the UV absorption spectrum. Such tendency in the results suggests that the same photochemical processes are responsible for the bimodal ion distributions observed in the third excitation region of acetone-*d*6 as for acetone-*h*6 photolysis in this spectral region, *i.e.*, secondary dissociation of the highly internally excited acetyl radical. The CD_3CO radical must possess enough internal energy to overcome the dissociation barrier on the ground state potential energy surface of the radical. Several groups have measured the acetyl dissociation barrier and its height varied around $11.1 - 21.7$ kcal/mol [164, 165, 166, 167], but the relative new values were measured to be ∼17 kcal/mol [140, 148]. These results were also obtained theoretically [149, 148]. The height of the dissociation barrier of CD_3CO can be

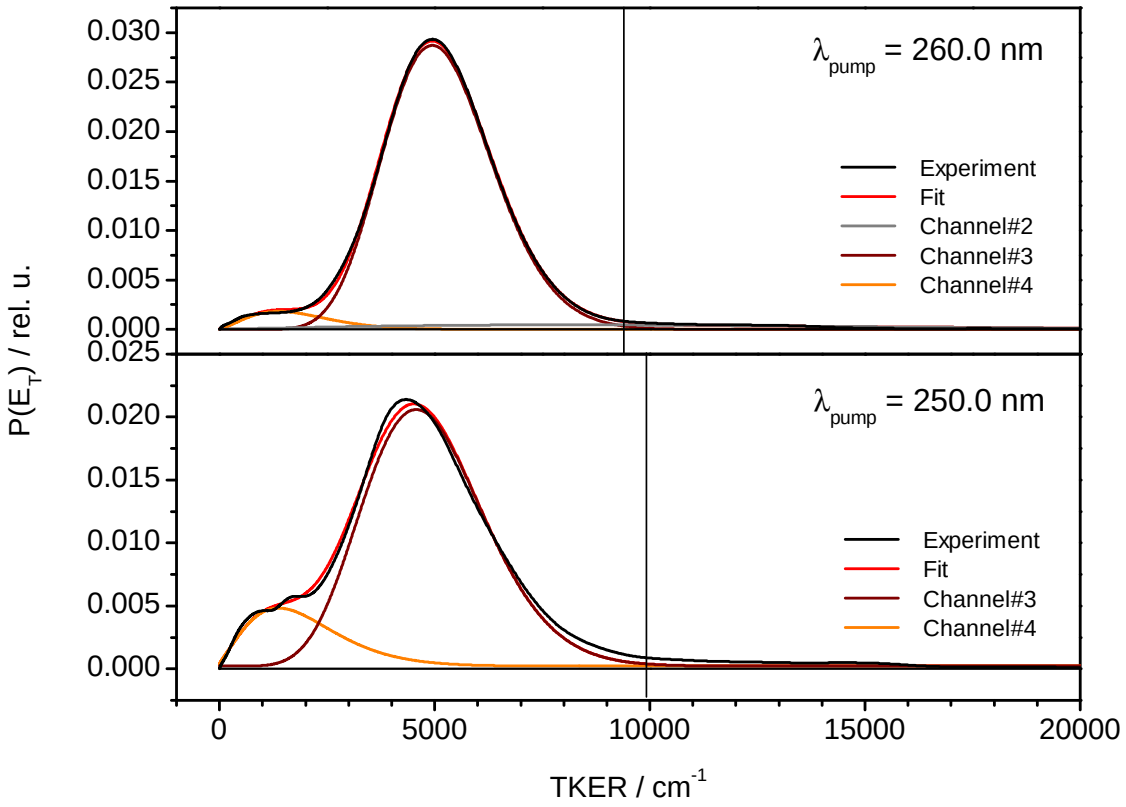

Figure 3.42: TKER distributions for $\lambda_{pump} = 260$ nm (upper trace) and $\lambda_{pump} = 250$ nm (lower trace). Notations are as before (see Fig. 3.38).

estimated from the present results by considering the slow CD_3 radical distributions. The internal energy distributions of CD_3CO and the dissociation barrier height are considered below in Section 3.3.4.1.

CD_3 ions formed *via* both channel #3 and #4 exhibit an isotropic angular distribution with $\beta_{Ch.\#3} = 0.14$ and $\beta_{Ch.\#4} = 0.1$.

The results of the total kinetic energy distributions as functions of the excitation energies and the angular anisotropy parameters are collected in Table 3.9.

The ratio $\langle E_T \rangle / E_{avail.}$ decreases rapidly with the excitation energy due to the increase of the saved available energy after acetone-*d*6 dissociation in the internal energy of the fragments. In the present work, the CD_3 fragment was probed in its ground state, so one can estimate the internal energy distributions in the CD_3CO fragments which correlate only with the CD_3 radical in the ground $\widetilde{X}\ ^2A_2''$ state.

Table 3.9: Parameters of the total kinetic energy distributions in the dissociation channel #3 for the corresponding photolysis energy of acetone-*d*6 (in cm^{-1}) and the angular anisotropy parameter β

λ_{pump}, nm	$E_{avail.}{}^a$	$E_T^{max\,b}$	$\langle E_T \rangle^c$	$\Delta E_T{}^d$	$\frac{\langle E_T \rangle}{E_{avail.}}$, %	β^e
305.0	3 799	5 795	3 329	1 667	88	0.19
290.0	5 496	5 496	3 816	1 363	69	0.11
260.0	9 474	9 458	4 941	2 958	52	0.14
250.0	11 013	10 996	4 570	3 331	41	0.1

[a] $E_{avail.} = h\nu - D_0^0 = h\nu - 28987$ cm^{-1}
[b] E_T^{max} is the maximum translation energy
[c] E_T is the average value of the total kinetic energy release
[d] ΔE is full width at half maximum value of the TKE profile
[e] β is the angular anisotropy parameter.

3.3.4.1 Internal Energy Distribution of CD_3CO and CO Photofragments

The momentum and energy conversation laws let one determine the kinetic and internal energy distributions of the CD_3CO co-fragment from the known energy distributions of the detected CD_3 fragments. The results are presented in Fig. 3.43.

The CD_3CO fragments exhibit relative high internal excitation with the maximum internal energy $E_{int}^{CD_3CO}$ increasing from 2 451 cm^{-1} at λ_{pump} = 305 nm up to 10 121 cm^{-1} at λ_{pump} = 250 nm; the average internal energy $\langle E_{int}^{CD_3CO} \rangle$ and FWHM $\Delta E_{int}^{CD_3CO}$ are also increasing from 471 cm^{-1} to 6 442 cm^{-1} and from 1 254 cm^{-1} to 3 331 cm^{-1} respectively. Such tendency in the internal energy distribution of the deuterated acetyl radical is obvious, if one takes a look at the potential energy surfaces of the S_1 and T_1 states (see Fig. 3.31). Excitation of the acetone-*d*6 molecule places it on the S_1 state which is coupled very efficiently with the T_1 state and less efficiently with the ground state S_0. The higher the excitation energy the better coupling with the T_1 state. The acetone-*d*6 molecule appears on the T_1 surface with more internal energy, a part of which is spent to overcome the dissociation barrier of about 2300 cm^{-1}, another part flows into translation energy of the fragments and the last part is kept by the fragments as their internal energy. Thus, increasing the excitation energy rises up the translational and internal energies of the CD_3 and CD_3CO radicals. If the internal energy of the CD_3CO radicals is high enough to overcome the dissociation barrier on the ground state, it will dissociate to CO and secondary CD_3 fragments which will possess lower translational energy than the primary CD_3 fragment formed in the first step of the dissociation of the parent molecule. Channel #4 in Fig. 3.42 describes this slow CD_3 fragment distribution. The maximum kinetic energy released in this channel corresponds to the minimum of the internal energy of the CO radical, *i.e.*, $E_{int}^{CO} = 0$. Taking into account the fact

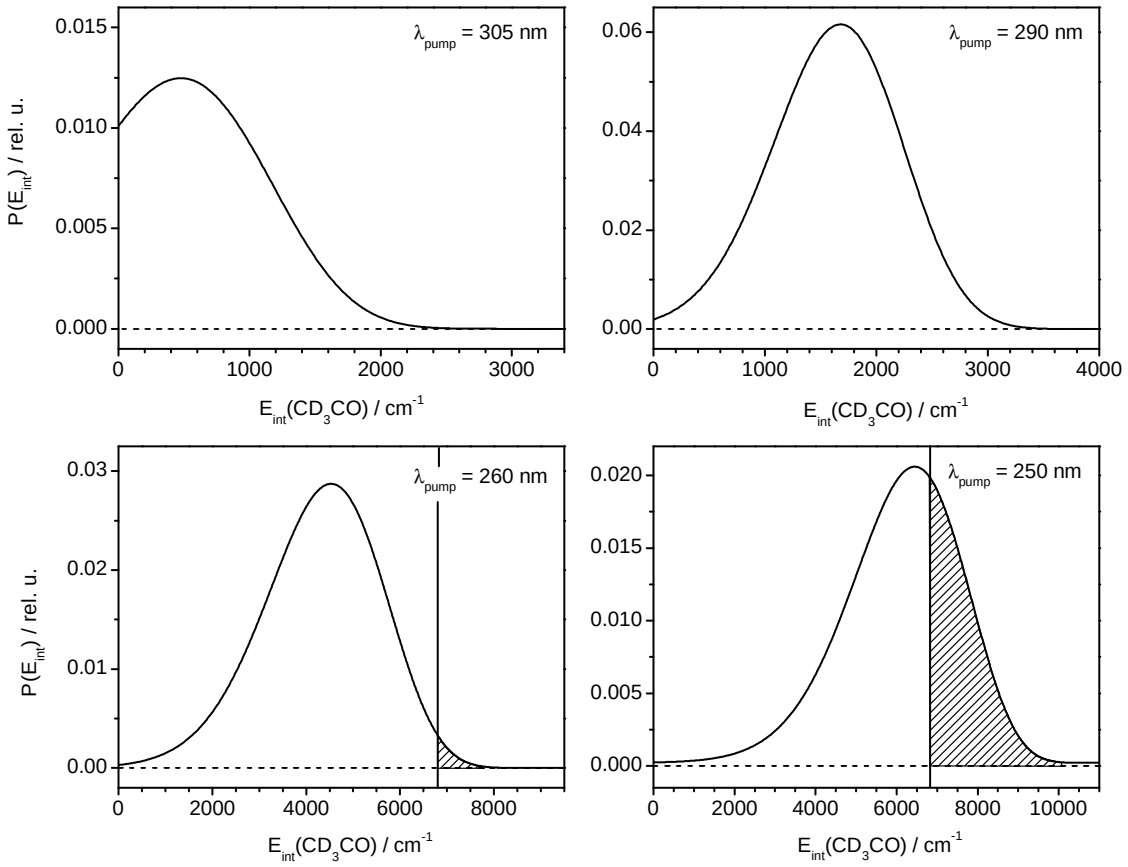

Figure 3.43: Internal energy distributions of the CD_3CO photofragments resulting from the photodissociation of acetone-*d*6 at different photolysis wavelengths within the first absorption band (340 nm - 230 nm). Shaded areas under the curves denote the fraction of the acetyl-*d*3 molecules possessing enough internal energy to undergo secondary dissociation *via* $CD_3CO^* \rightarrow CD_3 + CO$, assuming the dissociation energy of CD_3CO is 6 832 cm^{-1} (see text).

that the CD_3 products were probed in their ground electronic and vibrational state, *i.e.*, assuming that the methyl radical does not posses any internal energy, makes it possible to estimate the threshold for the height of the dissociation barrier of the CD_3CO radical. This approximations give a value of

$$D_0^0(CD_3CO) = (6\ 832 \pm 564)\ \mathrm{cm}^{-1}.$$

The effect of the deuteration of the methyl group on the zero-point energy (ZPE) of the acetyl radical calculated in the present work within the G3 level of theory, showed some lowering of the zero-point corrected electronic energy of 6.3 kcal/mol ± 1.5 kcal/mol. This lowering of the ZPE could result in the higher dissociation energy

of the molecule which is observed for the case of acetyl-$d3$, but not for the acetone-$d6$ molecule (see Section 3.3.4). This value must be considered as upper limit due to the assumption made that $E_{int}^{CO} = 0$. Additionally, the lifetime of acetyl-$d3$ could be longer than that of acetyl-$h3$, because in this case the dissociation of deuterated acetyl occurs later and the detection of the CD_3 fragments is less efficient. If this channel does arise from the secondary decomposition of the acetyl-$d3$ fragments, then the area of the shaded regions in Fig. 3.43 should be equal or more than the area under the curve corresponding to channel #4. Indeed, in the case of $\lambda_{pump} = 260$ nm, the area of the shaded region is 3.8% and the area under the curve of corresponding channel #4 is 4%, which is the same within the fitting error. In the case of $\lambda_{pump} = 250$ nm, the shaded area is 24% and the corresponding area under the curve of channel #4 is 13%. The discrepancy arises from the fitting errors and assumptions made about the internal energy of the CO radical. Additionally, the high internal energy of the CD_3CO radical reserved in the first step of the parent molecule dissociation does not necessary flow immediately and completely to the C-C reaction coordinate which means that actually one can observe the CO and CD_3 fragments with vibrational and rotational excitation. Trentelman *et al.* have observed internally excited carbon monoxide and methyl radical fragments in the first vibrational state ($v = 1$) from acetone-$h6$ photolysis at 193 nm [31]. The same situation can be expected for acetone-$d6$. Thus, the area under the curve of channel #4 exhibits the fraction of CD_3CO molecules which undergoes secondary dissociation and the shaded area exhibits the fraction of the acetyl-$d3$ molecules which can dissociate to CO and CD_3 fragments.

Table 3.10 exhibits the parameters of the internal energy distributions in the CD_3CO fragments after acetone-$d6$ photolysis.

Table 3.10: Parameters of the internal energy distributions of the CD_3CO fragments resulting from acetone-$d6$ photolysis *via* channel #3 (all energies are in cm^{-1})

λ_{pump}, nm	$E_{avail.}$	E_{int}^{max} [a]	$\langle E_{int} \rangle$ [b]	ΔE_{int} [c]	$\frac{\langle E_{int} \rangle}{E_{avail.}}$, %	Acetyl [d]
305.0	3 799	2 551	471	1 254	12	—
290.0	5 496	3 578	1 680	1 363	31	—
260.0	9 474	8 250	4 546	2 958	48	1
250.0	11 013	10 121	6 442	3 331	58	0.54

[a] E_{int}^{max} is the maximum internal energy
[b] $\langle E_{int} \rangle$ is the average value of the internal energy
[c] ΔE_{int} is full width at half maximum value of the E_{int} profile
[d] Acetyl = $\frac{A_{Ch.\#4}}{A_{shaded}}$ is the fraction of the acetyl fragments which does undergo successive dissociation.

The knowledge of the internal energy distribution of the CD_3CO radical together with energy and momentum conversation laws let one estimate the internal energy distribution in the CO radical corresponding to the CD_3 fragment in its ground state. The procedure to calculate the internal energy of the CO fragment is the same as described in Section 3.2.4. This gives the following results shown in Fig. 3.44.

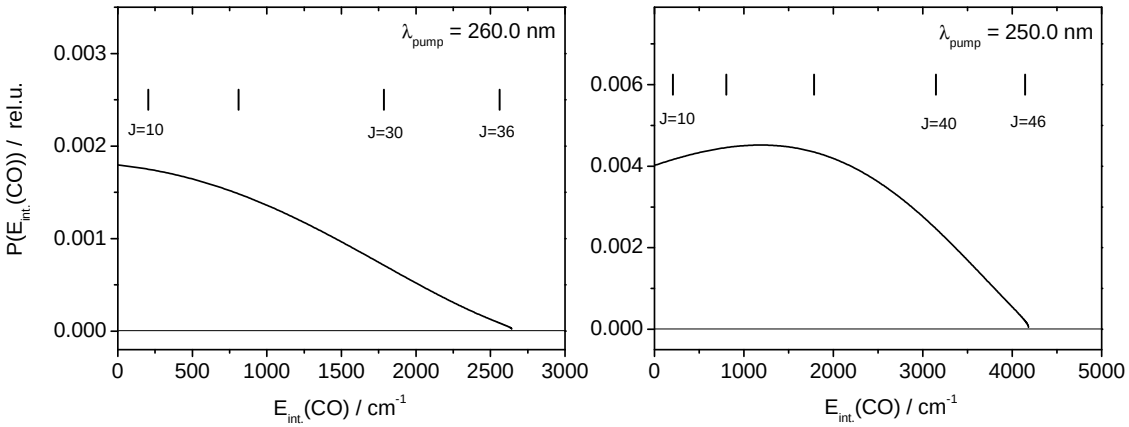

Figure 3.44: CO internal energy distributions resulting from the acetyl-*d*3 secondary dissociation. The vertical bold hatches exhibit rotational levels of the CO molecule calculated for the non-rigid top with $B = 1.93$ cm^{-1} and $D = 6 \cdot 10^{-6}$ cm^{-1} [71]; the dissociation energy of CD_3CO was accepted to be 6 832 cm^{-1} (see text).

The internal energy distributions of the CO radical after acetyl-*d*3 decomposition are very similar to those calculated for acetyl-*h*3 (see Section 3.2.4). The internal energy profiles exhibit a smooth and monomodal shape. The rotational excitation gradually rises with increasing internal energy saved in the acetyl-*d*3 fragment after the primary dissociation of the parent $(CD_3)_2CO$ molecule. In the vicinity of the acetyl-*d*3 dissociation barrier ($\lambda_{pump} = 260$ nm), the rotational levels of the CO are populated up to $J = 36$, but the peak of the population is at $J = 0$. The photolysis of acetone-*d*6 at ($\lambda_{pump} = 250$ nm) results in the highly rotationally excited CO fragments, the peak of the rotational level population is at $J = 24$ and the maximal rotational excitation extends up to $J = 46$. Exactly the same tendency in the rotational excitation of the CO photofragment was observed in the case of acetone-*h*6 photolysis. The highest populated rotational level of the CO radical in the case of acetone-*d*6 photolysis is slightly lower then in the case of acetone-*h*6, which probably originates from the overestimation of the CD_3CO dissociation energy. It was assumed that no internal energy is presented in the CD_3 radical. High rotational excitation can be explained by a strong torque, imparted to CD_3CO

fragment after the parent acetone-*d*6 molecule has decomposed and pushed acetyl-*d*3 out of the linear configuration resulting in high rotational energy of CO.

3.3.5 Discussion and Conclusions

The photodissociation dynamics of the acetone-*d*6 molecule excited to the first singlet electronic state was investigated *via* velocity map imaging. The observed results repeat those for acetone-*h*6, *i.e.*, the experimental results clearly demonstrate three distinct dissociation pathways of the acetone molecule corresponding to three different spectral regions of the excitation wavelengths.

(1) Photolysis of acetone-*d*6 in Region 1 proceeds *via* unimolecular decay on the ground state. The high vibrational levels of the S_0 state are populated *via* internal conversion from the initially populated S_1 state. Such a dissociation pathway results in slow photofragments. The translational energy distributions peak at zero values. This is rather an assumption about the fate of the acetone-*d*6 molecule excited in this spectral region of the UV absorption spectrum because in the present work it was impossible to distinguish CD_3 fragments formed *via* this pathway from those resulting from clusters decomposition. Additionally, the dissociation lifetime of acetone-*d*6 is long enough to let a second photon be absorbed by the molecule which is followed by dissociation from higher energy levels. The same photodissociation dynamics was observed for acetone-*h*6.

(2) Excitation of the acetone-*d*6 molecule within Region 2 results in a sharp CD_3 fragment distribution with the average translational energy peaking above the zero value. It was well established by many research groups that the dissociation of acetone-*h*6 excited to the S_1 state proceeds on the T_1 PES to which the ro-vibrational states of the S_1 state couple *via* ISC ([111] and references therein). The fact that the observed TKER distributions after $(CD_3)_2CO$ photolysis peaking above the zero value shows the presence of a dissociation barrier and a relative tight transition state on the T_1 surface. This means inapplicability of the pure statistical or pure impulsive models in the description of the acetone molecule dissociation.

The results observed in the present work did not demonstrate any significant isotopic effect on the dissociation barrier height of the triplet T_1 state. The excess excitation energy above the origin of the $S_1 \leftarrow S_0$ electronic transition at which the fast CD_3 fragments (channel #3) are already observed has been measured in the present work to be $2\,350 \pm 60$ cm^{-1}. In comparison, channel #3 in the case of acetone-*h*6 appears at the excess energy of $2\,285 \pm 40$ cm^{-1}. The origin of the $S_1 \leftarrow S_0$ electronic transition also did not exhibit any effect of the deuteration of the methyl groups in the acetone molecule. The energy difference in the origin of the $0 - 0$ transition is only 4 cm^{-1} for the *h*6- and *d*6-isotopomers [161]. On the other hand, Zuckermann *et al.* investigated the fluorescence decay characteristics of the supersonically cooled acetone-*h*6 and -*d*6 molecules upon excitation of the $S_1(^1A_2)$ state and found an

abrupt decrease of the fluorescence lifetime at the excess energy of 2 250 ± 50 cm^{-1} and 2 500 ± 50 cm^{-1}, respectively [121]. The fluorescence decay was observed to be biexponential with a fast "spike" and a slow component. This sudden decrease of the decay times (spike) at a certain excess excitation energy (800 cm^{-1} for *d*6- and 1 800 cm^{-1} for acetone-*h*6) was interpreted by the authors as effective coupling of the S_1 and T_1 states. Another excess excitation energy of 2 250±50 cm^{-1} for acetone-*h*6 and 2 500 ± 50 cm^{-1} for acetone-*d*6 results in the rapid vanishing of the long-lived component of the fluorescence decay signal. This phenomenon was ascribed to the onset of the dissociation on the T_1 surface over a barrier of 93.5 kcal/mol (above the ground state minimum of acetone-*h*6). The present results contradict with the results observed in [121]. In the present work, the dissociation of the parent acetone-*d*6 molecule was observed directly *via* the detection of the CD_3 photofragments; by contrast, the conclusions about the dissociation of acetone-*d*6 in [121] were made on the grounds of the fluorescence signal decay only. On the other hand, there is an excellent agreement between the results observed in the present work for acetone-*h*6 with those from the same experimental group (see Section 3.2.4).

A possible explanation for this discrepancy could be an inefficient dissociation on the T_1 surface so that the fluorescence decay of the acetone-*d*6 molecule is insensitive to this leak of the population (the intensity of channel #3 is very weak in the vicinity of the triplet dissociation barrier), and only when it becomes comparable to the ISC ($T_1 - S_0$) and radiative decay of the T_1 the decrease of the long-lived component become noticeable. The increase of the efficiency of the intersystem crossing of the T_1 and S_0 states cannot explain it, because the density of states in $(CD_3)_2CO$ is higher than in $(CH_3)_2CO$ and coupling should be more efficient in the deuterated molecule. The deuteration of the methyl groups of the parent acetone molecule did not cause any significant influence on the photodissociation dynamics. The fact that the T_1 barrier height was found to have the same height within the experimental resolution as for acetone-*h*6 can be interpreted as an internal rotational effect on the effective barrier height, *i.e.*, acetone dissociation *via* α-C-C bond does not go through only one reaction coordinate (C-C bond stretching) rather an elongation of this bond is accompanied by the rotation of the methyl groups or skeletal hidden rotors and the rotation of the molecule itself also affect the barrier, so that the height of the dissociation barrier on the triplet potential surface is a sum of the potential barriers corresponding to C-C stretching and rotational energy of the overall molecule and internal CD_3 groups. The isotopic substitution of the CH_3 groups renders a double effect: On the one hand, it decreases the ZPE level of the vibrations of the molecule and thus the dissociation barrier should get higher, but on the other hand, the ZPE of the transition state on the T_1 PES will also decrease, thus compensating the first effect. Additionally, the rotational excitation of the internal rotors of acetone can decrease the height of the T_1 barrier due to the heavier masses and thus the frequency of the rotating methyl groups in the transition state. The last argument is quite speculative and needs further investigations.

For reactions with "tight" transition states (TS) and reverse activation energies, the rotational energy in the TS may be larger or smaller than the rotational energy in the molecule, which depends on the rotational constants of the TS. For reactions with no reverse activation energy in the $J = 0$ PES ("loose" TS), rotational energy gives rise to a centrifugal barrier along the reaction path. This barrier tends to be smaller than the molecule's rotational energy because it is determined by moments of inertia at a large internuclear separation. If the transition state has a real barrier and is described solely in terms of vibrational oscillator (plus one or two internal rotors), that is, a vibrational transition state and angular momentum conservation results in a larger rotational barrier, than a centrifugal barrier. The effect of rotations on the activation energy can be determined only if the geometry of the transition state is known [147]. Figure 3.45 shows the effect of rotational energy on the activation barrier.

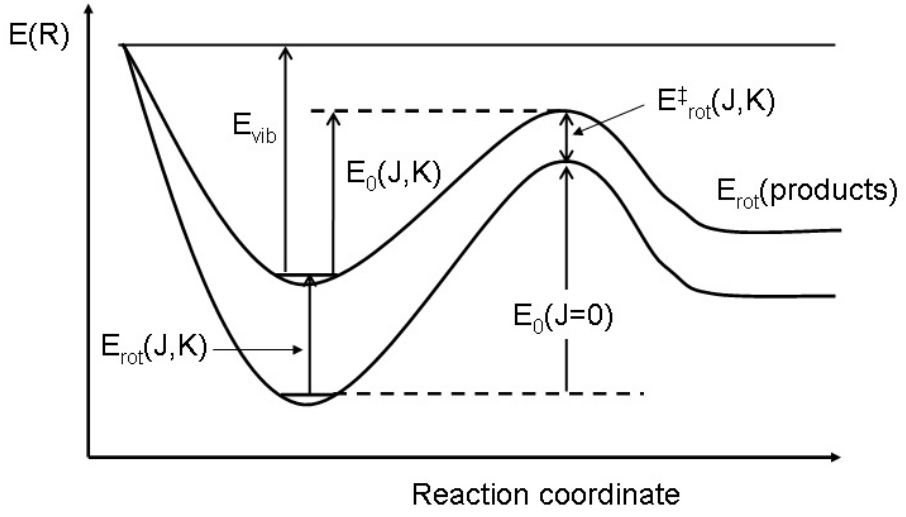

Figure 3.45: The potential energy diagram for a reaction with a saddle point and a "tight" transition state. E_{vib} is the vibrational energy, $E_{rot}(J, K)$ is a rotational energy of the molecule, $E_0(J = 0)$ is the activation energy at $J = 0$, $E_0(J, K)$ is the activation energy with rotational energy in the molecule, $E^{\ddagger}_{rot}(J, K)$ is the rotational energy of the TS, and E_{rot}(products) is the rotational energy of the products. Note, that rotational energy in the TS is not equal to that in molecule [147]

The rotational constants of acetone in the T_1 transition state were calculated here from the known structure of the TS of acetone taken from [37]. Acetone in the TS has slightly lower rotational constants ($A \approx 10$ GHz, $B \approx 9$ GHz and $C \approx 4$ GHz for acetone in the minimum of the T_1 state and $A^{\ddagger} \approx 13$ GHz, $B^{\ddagger} \approx 5$ GHz and $C^{\ddagger} \approx 4$ GHz for acetone at the TS), which imply that the rotational effect on the $E^{\ddagger}_{rot}(J, K)$ energy of the TS would be slightly smaller than that on the $E_{rot}(J, K)$ energy of the molecule. The REMPI spectrum of CD_3 from acetone-$d6$ photolysis at $\lambda_{pump} = 286$

nm (see Fig. 3.36) demonstrates rotational excitation of the methyl fragments, which is a consequence of the parent molecule rotation prior to dissociation and the dissociation torque itself. The same was observed for the CH_3 fragment (see Fig. 3.17). The rotational constants of acetone-*d*6 are lower than those of acetone-*h*6 and, therefore, the rotational energy associated with internal or hidden rotors of the parent molecule and its effect on the activation energy must be lower than for acetone-*h*6. Thus, the rotational excitation of the molecule and internal rotors and its effect on the PES can also be a reason of the negligible isotopic substitution effect on the height of the T_1 barrier.

(3) Further increase of the excitation energy, which correspond to excitation of acetone-*d*6 in Region 3 results once again in the primary dissociation of acetone-*d*6 and also provides enough internal energy for the CD_3CO fragments to overcome the dissociation barrier of $6\,832 \pm 564$ cm^{-1}. This process becomes more efficient with increasing excitation energy as it follows from the correlated changes of the average total kinetic energy and FWHM of the TKER profiles in channels #3 and #4. The $\langle E_T \rangle_{ch.\#3}$ decreases and $\langle E_T \rangle_{ch.\#4}$ increases with energy once λ_{pump} becomes shorter than 260 nm. ΔE_T increases, which points out the available energy redistribution prior to dissociation of the parent molecule. The excitation energy threshold for the secondary dissociation (channel #4) was observed at the same level as for acetone-*h*6, thus the deuteration of the methyl groups did not make any noticible influence on this dissociation pathway denoted as channel #4. The dissociation barrier of the acetyl-*d*3 radical, however, was found to be slightly higher than in the case of the protonated acetyl radical; thus the isotopic substitution in the acetyl molecule causes a normal isotopic effect due to the lowering of the ZPE levels of the respective vibrations, most probably C-C stretching and C-C-O bending. The increase upon deuteration may partially reflect the longer lifetime of the acetyl-*d*3 radical toward unimolecular dissociation.

The dissociation energy of acetone-*d*6 was measured to be $D_0^0 = (28\,987 \pm 250)$ cm^{-1}. This is slightly lower than the dissociation energy of acetone-*h*6, but is within the experimental error. No substantial effect of deuteration was observed. On the other hand, the dissociation energy of acetyl-*d*3 was estimated to be $D_0^0(CD_3CO) = (6\,832 \pm 564)$ cm^{-1}, which is higher than for the acetyl-*h*3 molecule. In the case of acetyl, a normal isotopic effect was observed.

The fragment distributions for the probed range of λ_{pump} within the first UV absorption band are essentially isotropic, which is not surprising, if one takes into account the fact that several processes such as internal conversion, internal vibrational redistribution, intersystem crossing and parent molecule rotation occur prior to the dissociation of acetone-*d*6 as well as acetone-*h*6.

3.4 Photolysis of Methyl Ethyl Ketone

3.4.1 Introduction

Another ketone, for which the photodissociation dynamics were studied in the present work, was methyl ethyl ketone (MEK) or 2-Butanone. Recent researches have shown that OH radicals, which play a central role in the oxidation of hydrocarbons in the troposphere, originate from a variety of sources and not just from the ozone photolysis [43]. Ketones have been shown to play an important role in the upper atmosphere as a source of OH radicals [11]. Their relatively long lifetimes with respect to the dissociation process allow ketones to reach the upper troposphere, where they are photolysed by UV sun light yielding alkyl radicals, which in the presence of NO can generate OH radicals. The acetone photolysis with high excitation energy results in 2 CH_3 and CO radicals. MEK is not a symmetric molecule and its photolysis by analogy with acetone would result in CH_3, C_2H_5 and CO radicals, when the photolysis energy is high enough. At moderate excitation energies, the MEK photodissociation will result in the formation of only one alkyl (CH_3 or C_2H_5) and the associated acyl radicals (C_2H_5CO or CH_3CO) [168, 11]:

$$CH_3C(O)C_2H_5 + h\nu \longrightarrow CH_3 + C_2H_5CO^*$$
$$CH_3C(O)C_2H_5 + h\nu \longrightarrow C_2H_5 + CH_3CO^*$$

The present work was focused on the study of the internal energy distributions of the products of MEK photolysis. Further, the photodissociation dynamics of 2-butanone and acetone as the two most simple ketones were compared.

A previous study of the infrared spectrum of the methyl ethyl ketone has shown that this molecule has two isomers in the gas and liquid phases as a result of restricted internal rotation about the C-C axis adjacent to the C=O bond. One isomer is by 2.0 (1.1) kcal/mol more stable in the gas(liquid) phase, and only the more stable isomer remains in the solid phase [169]. Figure 3.46 shows the geometries of the existing MEK isomers.

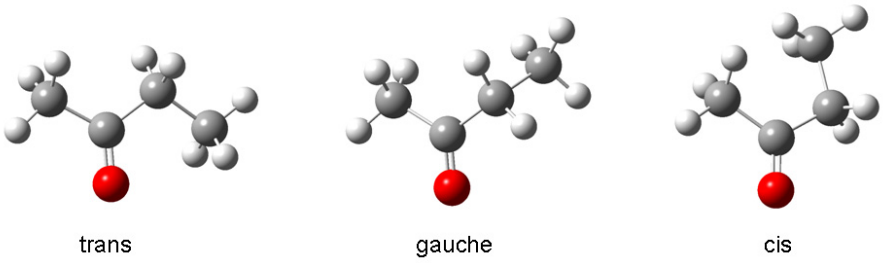

Figure 3.46: Methyl ethyl ketone isomers.

This molecule has also been studied by gas electron diffraction in the gas phase [170]. The more stable isomer has *trans* conformation with regard to the end of the C(O)-CH_2 bonds. The ratio between this isomer and the less stable one (possibly gauche

conformation) are $(95 \pm 3)\% : (5 \pm 3)\%$ at room temperature [170]. This corresponds to a difference in free energy of $\Delta G = 2.1 \pm 0.4$ kcal/mol, in good agreement with the ΔH of 2.02 ± 1 kcal/mol obtained by infrared spectroscopy [169, 170].

The ground state geometry of *trans*-MEK as the most stable one was optimized in the present work at the MP2 level of theory [171, 172] with the 6-311^{++}G(d,p) basis set using the Gaussian 03, Revision C.02, suite of programs [138]. The calculations show that MEK, like acetone, is planar in its ground state (see Fig. 3.46).

Like other aliphatic ketones, methyl ethyl ketone has the first absorption band between $\lambda = 210$ nm and $\lambda = 340$ nm, corresponding to an $n\pi^*$ transition from the ground (S_0) to the first excited state (S_1). One has to keep in mind that only the MEK molecule in its ground and first excited S_1 states belongs to the C_s point group and the first electronic transition is a $a' \leftarrow a''$. The UV absorption spectrum recorded at 298 K and 18 mbar is shown in Fig. 3.47.

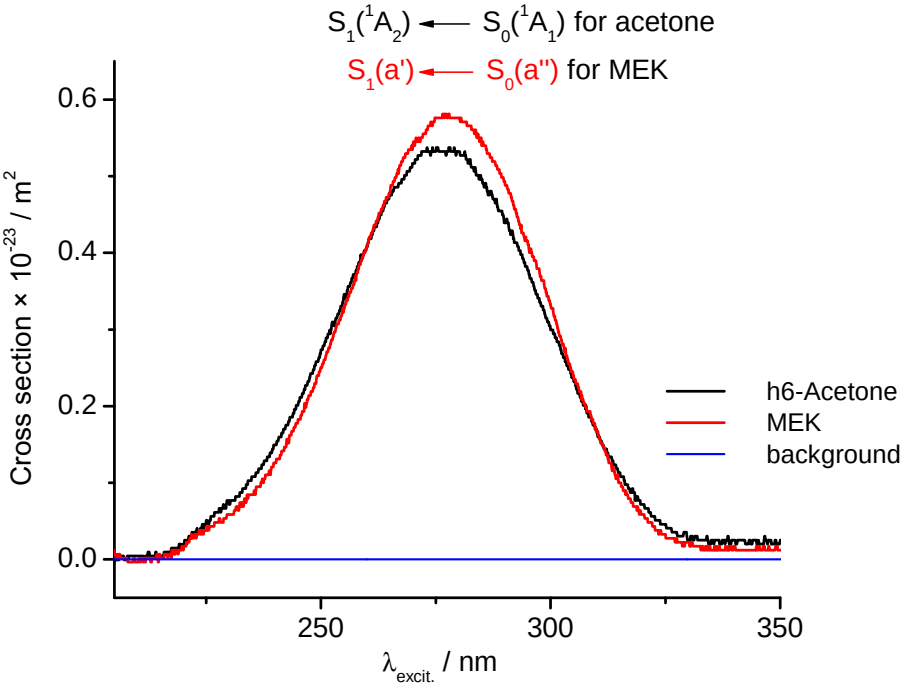

Figure 3.47: UV absorption spectrum of methyl ethyl ketone in the gas phase compared to the UV spectrum of acetone. The spectra represent the first absorption bands of the ketones due to their $S_0 \rightarrow S_1$ ($n\pi^*$) transitions and were recorded at 298 K in the gas phase at 18 mbar vapor pressure.

The absorption spectrum of MEK is very similar to that of acetone. The same unstructured and broad bands appear in the spectra. The maximum of the absorption band of MEK lies also around 280 nm. No vibrational structure could be detected, which again repeats the shape of the absorption band of acetone.

The photodecompositions of methyl ethyl ketone and methyl butyl ketone (MBK) were studied for the first time by Norrish and Appleyard in the light of a Hg lamp [173]. It was detected that about 80% of MEK decomposes and produces CO and a mixture of C_2H_6, C_3H_8 and C_4H_{10}, the remaining 20% forming C_2H_4, and CH_3CHO. The authors considered a mechanism by which the absorbed energy is transferred from the chromophoric group to the point of rupture. An inner sensitization, similar to a collision of the second kind, was suggested [173].

Ionization and dissociation of MEK was studied by electron impact spectroscopy by Kanomata [174]. In this work the first ionization potential and dissociation energy of the C_2H_5CO-CH_3 bond of MEK were determined to be 7.66 eV and 3.15 eV, respectively [174]. The latter agrees with previous measurements of 3.13 eV [175].

A lot of investigations were done on the dynamics of the MEK transition states in the femtosecond timeregime [176, 177, 128]. TOF mass spectra taken 50 fs after time-zero for two-photon excitation at 307 nm exhibit mass peaks of 72 Da, 57 Da, and 43 Da, which were assigned to the parent molecule, the propionyl and the acetyl radicals, respectively [177]. The parent transient decays monoexponentially on a timescale of 100 ± 30 fs. The decays of the transients with the mass of 57 Da and 43 Da exhibit biexponential behaviors with rise times of $\sim$ 100 fs, which correlates with the parent transient decay time [177]. However, these two intermediates decay with different time constants; the C_2H_5CO signal decays with $\tau_2 = 550 \pm 50$ fs, while the CH_3CO signal decays with $\tau_2 = 900 \pm 100$ fs. These results clearly show that two different α-C-C bonds of MEK are involved in a stepwise scission to produce either acetyl or propionyl as the transient intermediates. In the case of acetone dissociation, the decay time constant for the acetyl radical was measured to be 500 fs [34], which is for 1.8 times faster than in the case of MEK. These intermediates are internally excited and undergo a secondary decomposition forming CO and the CH_3 or the C_2H_5 radicals. Such an ultrashort time dynamics reflects a direct repulsion in the α-cleavage, without the involvement of the entire vibrational phase space [177]. The authors claim that no intermediates due to β-cleavage, such as CH_3COCH_2, were found [177]. However, the mass peak of 57 Da may correspond either to C_2H_5CO radicals or to CH_3COCH_2 radicals, which means that essentially different MEK photodissociation dynamics should be involved. This possibility was not regarded in Ref. [177], and it is impossible to make an unambiguous conclusion about the nature of the mass peak at 57 Da only from the TOF spectrum present. On the other hand, α-cleavage seems to be preferential, because the β-C-C bond is chemically more stable.

The dynamics of MEK excited to the S_2 state exhibit an essentially different, longer time scale. Baronavski *et al.* investigated the MEK photodissociation dynamics in the deep UV [127]. The S_2 excited state lifetime of MEK was measured to be 4 ps, for acetone it was 4.7 ps [127, 125]. The acetyl lifetime (after acetone excitation to the $3s$ Rydberg state) was about 3 ps. The excitation scheme, used in these experiments

(195 nm pump and 390/260 nm probe) excites MEK very close to the origin of the 3s Rydberg state and the available energy is not sufficient for the excited molecule to undergo either a direct surface crossing to the S_1 PES *via* a conical intersection I (see [128]) or a prompt first $\alpha-$C-C bond breakage on the S_2 PES *via* TS1. Therefore, the α-cleavage process takes place on the S_1 PES after a relatively slow $S_2 \rightarrow S_1$ internal conversion (IC), which proceeds in a few picoseconds.

A comprehensive review of the alkyl ketone photodissociation dynamics in the deep UV was written by Zewail and co-workers in [128, 131]. However, little is known about the MEK photolysis in the near UV.

In the present chapter, the results for the photodissociation dynamics of MEK studied by velocity map imaging are presented. The dynamics differ strongly from those observed in the case of acetone, even considering the methyl radical abstraction.

3.4.2 REMPI Spectra of CH_3 and C_2H_5 Radicals

The products of the MEK photolysis were detected *via* REMPI. MEK is known to have two main photodissociation channels resulting either in CH_3CO + C_2H_5 or in CH_3 + C_2H_5CO. In the present work, both channels were studied by probing the CH_3 and C_2H_5 radicals.

Figure 3.48 shows the REMPI spectrum of the CH_3 radicals, which were ionized *via* the $3p^2A_2''$ resonance state. The REMPI spectrum exhibits a well pronounced peak in the vicinity of 333.5 nm, which corresponds to the ionization of methyl radicals in their vibrational ground state ($v = 0$) *via* the $Q-$branch of the electronic transition.

The ethyl radical did not demonstrate any peaks in its ionization spectrum, rather just a constant ion signal. The ionization efficiency is independent of the probe wavelength, which was scanned over the range between 240 nm and 247 nm. Ionization of C_2H_5 was observed to be insensitive to its internal state. The same results were observed by Kandel *et al.* in [178]. They investigated the angular distribution for the Cl + C_2H_6 →HCl + C_2H_5 reaction by observing the C_2H_5 radical [178]. C_2H_5 is know to have a broad absorption spectrum at wavelengths shorter than 260 nm [179]. This unstructured absorption band was associated with a Rydberg state progression, in which little or no rotational structure is apparent [179]. By analogy with [178], the observed ionization of the ethyl radical in the region of $240 - 247$ nm proceeds, most probably, *via* (1+1) photon absorption mediated by the $3s$ Rydberg state. The absence of structure in the REMPI spectrum is a sign for a dissociative character of the C_2H_5 excited state. As was already assumed in [178], the MPI process is insensitive to the internal state of the C_2H_5 radical. Howerever, this assumption should not be extended for the highly internally excited C_2H_5 radicals, because the MPI process may proceed differently for the C_2H_5 fragments with significant internal energy.

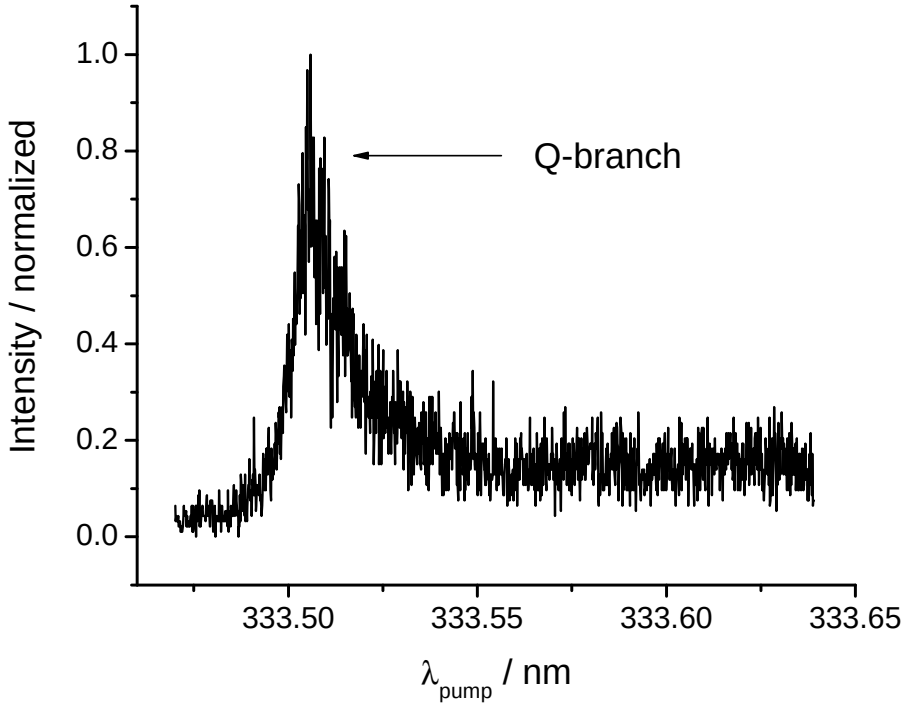

Figure 3.48: (2+1) REMPI spectrum of CH_3 ($v = 0$) excited *via* the $3p^2A_2''$ state generated by photolysis of MEK at 286 nm.

3.4.3 Velocity Map Imaging Experiments

The photodissociation dynamics of MEK excited to the first absorption band was studied by observing the CH_3 velocity images. The experiments were done in the same way as for acetone by using two laser beams, one to excite the parent molecule and the other one for probing the photofragments. The fragment distributions did not show any dependence on the pump wavelength. An example for the ion distributions after MEK photolysis at $\lambda_{pump} = 271$ nm is shown in Fig. 3.49.

The CH_3 distribution exhibits an isotropic, broad, unstructured and diffusive image with an intensive central spot. The corresponding TKER profile is shown in Fig. 3.50.

The dissociation energy of the asymmetric C-C bonds (CH_3CO-C_2H_5 and C_2H_5CO-CH_3) of MEK can be estimated *via* Hess' law [172] from the known enthalpies of formation of the parent molecule and the fragments at 0 K ($\Delta_f H_0^0$). The $\Delta_f H_0^0$ values were taken from the literature [180, 181, 182, 142, 141, 183] and are presented in the following list together with the calculated dissociation energies of two non-

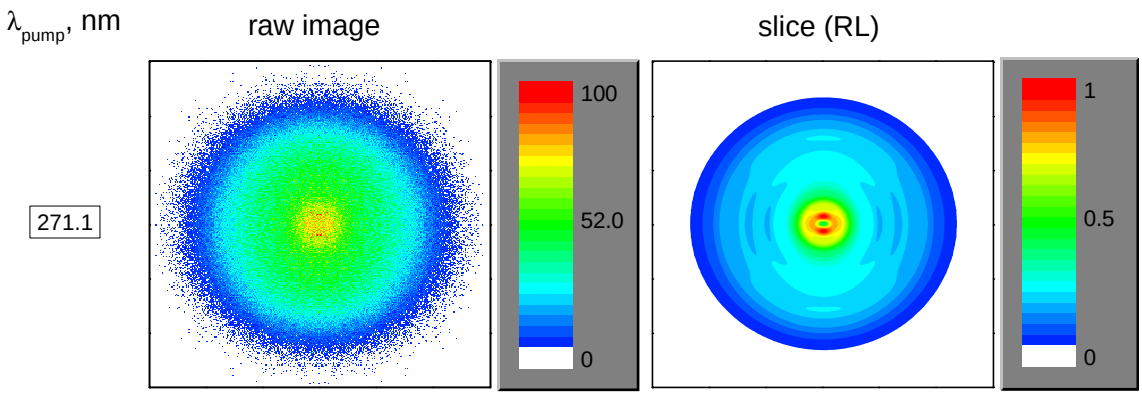

Figure 3.49: Two-color velocity map images of the methyl radical from the MEK photolysis at 271 nm. Notations and color code are the same as in Fig. 2.13. The methyl radicals were detected by a (2+1) REMPI *via* the 3*p* Rydberg state.

equivalent C-C bonds:

$$\begin{aligned}
\Delta_f H^o(CH_3C(O)C_2H_5) &= -217.1 \pm 0.6 \text{ kJ/mol};\\
\Delta_f H^o(CH_3CO) &= -3.6 \pm 1.8 \text{ kJ/mol};\\
\Delta_f H^o(CH_3) &= 150.3 \pm 0.4 \text{ kJ/mol};\\
\Delta_f H^o(C_2H_5) &= 129.3 \pm 0.7 \text{ kJ/mol};\\
\Delta_f H^o(C_2H_5CO) &= -18.0 \pm 3.4 \text{ kJ/mol};
\end{aligned}$$

From the Hess' law it follows:

$$D_0(CH_3CO - C_2H_5) = 342.8 \pm 3.1 \text{ kJ/mol} = 28\,656 \pm 259 \text{ cm}^{-1} \quad (3.17)$$

$$D_0(C_2H_5CO - CH_3) = 349.4 \pm 4.4 \text{ kJ/mol} = 29\,208 \pm 368 \text{ cm}^{-1} \quad (3.18)$$

The TKER curve exceeds the maximum available energy, which is governed by the energy conservation law (see Fig. 3.50). The same behavior was observed for acetone-*h*6 and -*d*6, and by analogy, this tail of the TKER curve is associated to the fast CH_3 fragments coming from the MEK photolysis by absorption of two successive photons. The first photon of the pump laser pulse excites MEK to the S_1 state, where it undergoes an IC back to the S_0 state. The second photon of the probe beam brings this highly internally excited MEK molecule to upper states followed by dissociation, which results in such a fast methyl fragments. The fact that this tail on the TKER distribution (see Fig. 3.50) originates from two-photon excitation from both the pump and the probe laser pulses, and not just from one of this lasers, is ensured by low laser powers, which were turned down, so that no ion signal was coming from either the pump or the probe laser pulses. Probing

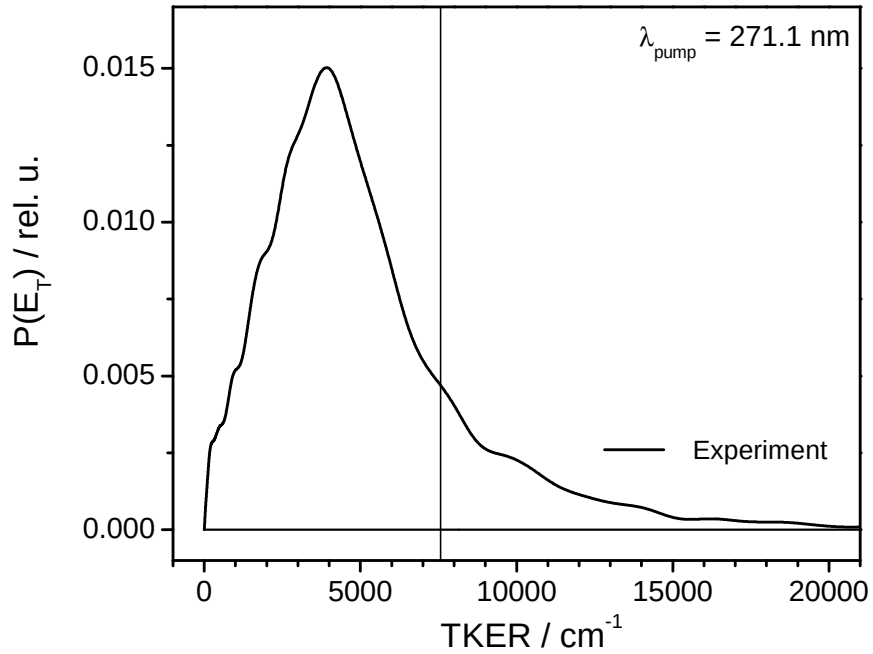

Figure 3.50: The TKER distribution by probing CH_3 fragments after the MEK photolysis at 271 nm. The available energy ($E_{avail.}$) for an one-photon dissociation process (vertical solid line) was calculated by assuming that $D_0(MEK) = 29\ 208\ cm^{-1}$.

at different photolysis energies (286, 271 and 265 nm) did not show any specific features in the ion distributions, but the velocity images were always isotropic and unstructured.

Another attempt, by probing the C_2H_5 fragments was to study the dynamics of the photodissociation of MEK *via* the channel $C_3HCO + C_2H_5$. The ethyl fragment was probed at 242 nm. The ion image is presented in Fig. 3.51 and the corresponding TKER profile is shown in Fig. 3.52. The total translation energy release was calculated for the C_2H_5 at a time-of-flight of 3.621 μs.

The C_2H_5 fragment distribution recorded after MEK photolysis at 241 nm also exhibits isotropic, broad and unstructured VMIs. This experiment also exhibits a high energy tail on the TKER distribution corresponding to the two-photon absorption followed by dissociation from higher states (see Fig. 3.52). The most intense central part of the distribution in Fig. 3.51 is narrower compared to that of the detected CH_3 fragments (see Fig. 3.52 and 3.50), even at the higher excitation energy (271 nm for CH_3 and 241 nm for C_2H_5). The narrower distribution of the C_2H_5 fragments follows from the lower kinetic energy, which they receive after dissociation of the parent molecule. This is due to the heavier mass of the ethyl radical (27 Da), compared to the mass of the methyl radical (15 Da) and more internal degrees of freedom. However, the overall shape of the total translation energy distribution

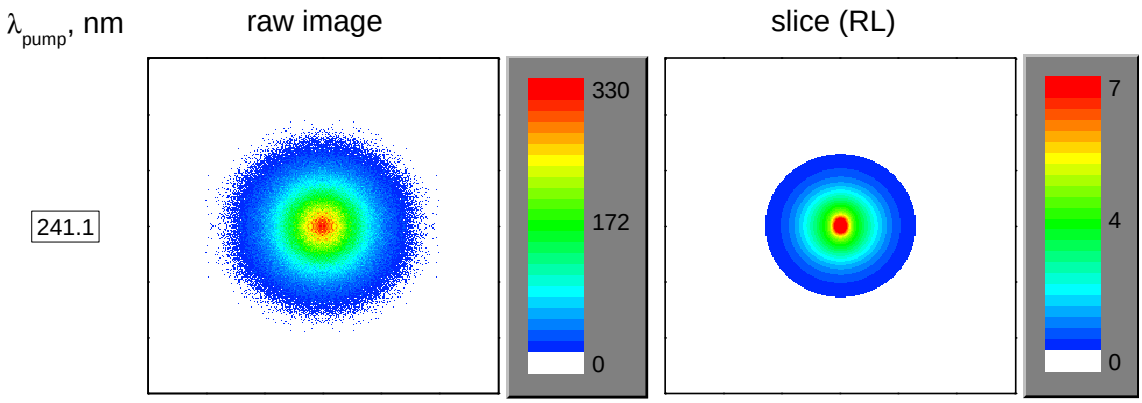

Figure 3.51: Two-color velocity map images of the ethyl radicals after MEK photolysis at 241 nm. Notations and color code are the same as in Fig. 2.13. The ethyl radical was detected by (1+1) REMPI *via* the 3*s* Rydberg state.

observed by the detecting of the C_2H_5 fragments is very similar to that one observed in the case of CH_3.

For both dissociation channels, the product distributions were observed to be insensitive to the photolysis wavelengths, *i.e.* the velocity map images were always isotropic, broad and unstrucutered. Varying of the excitation energy was only affecting the overall width of the ion distributions. The corresponding TKER distributions are characterized by smooth and monomodal curves. These results differ strongly from those after acetone photolysis at the same spectral region, suggesting that other processes are involved in the MEK photodissociation. The alternative possibilities will be discussed in Section 3.4.4.

The CH_3CO and C_2H_5CO internal energy distributions calculated from the corresponding TKER profiles are presented in Fig. 3.53 and 3.54.

The internal energy distributions of both photofragments exhibit broad profiles, peaking at 3 761 cm^{-1} for the acetyl radical and at 13 042 cm^{-1} for the propionyl radical (see Fig. 3.53 and Fig. 3.54). This is not surprising, if one takes into account the corresponding TKER distributions (Figure 3.52 and 3.50). Such high internal excitation of the nascent photofragments suggests a vibrational redistribution prior to dissociation. A relative large fraction of the photoproducts can experience secondary dissociation, if the internal energy received in the first step of the dissociation of the parent molecule exceeds the dissociation barrier of the acetyl and propionyl radicals. The height of the dissociation barrier for CH_3CO was measured to be 17 kcal/mol [140] and the height of the C_2H_5CO dissociation barrier is similar to that of the acetyl radical (16.3 ± 1.5 kcal/mol) [184]. These values truncate the fraction of the potentially hot acetyl and propionyl radicals, which can undergo secondary dissociation. These fractions are marked as shaded area under the internal energy

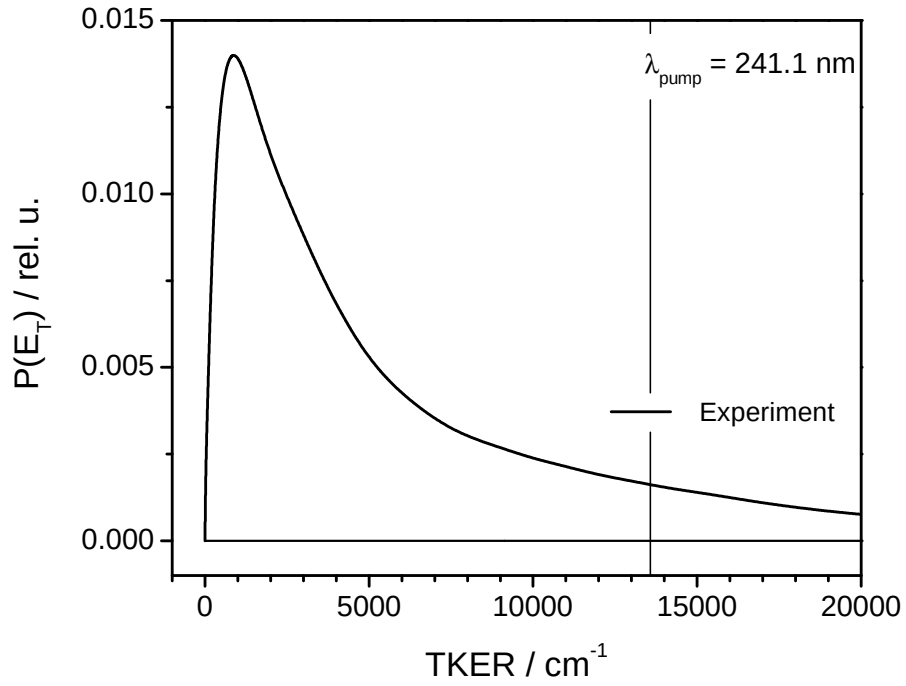

Figure 3.52: TKER distributions by probing C_2H_5 fragments after the MEK photolysis at 241.1 nm. The available energy ($E_{avail.}$) for an one-photon dissociation process (vertical solid line) was calculated by assuming that $D_0(MEK) = 28\,656$ cm^{-1};.

curves in Fig. 3.53 and 3.54. In the case of the MEK photolysis at 241 nm and detection of C_2H_5, about 80% of CH_3CO possess enough internal energy to overcome the dissociation barrier of 17 kcal/mol on the ground state surface. The photolysis of MEK at 271 nm and detection of the CH_3 radicals results in $\sim$ 10% of C_2H_5CO, which can undergo the secondary decomposition.

3.4.4 Discussion and Conclusions

The present results do not provide enough data to clearly understand the photodissociation dynamics of MEK. Nevertheless, the results are discussed in the following chapter.

The MEK molecule has two unequal α-bonds, thus the excitation to the first absorption band (see Fig. 3.47) results, unlike acetone, in two different dissociation channels:

1. $CH_3C(O)C_2H_5 \rightarrow C_2H_5CO + CH_3$
2. $\rightarrow CH_3CO + C_2H_5$

Both possibilities were tested in the present work and will be discussed separately.

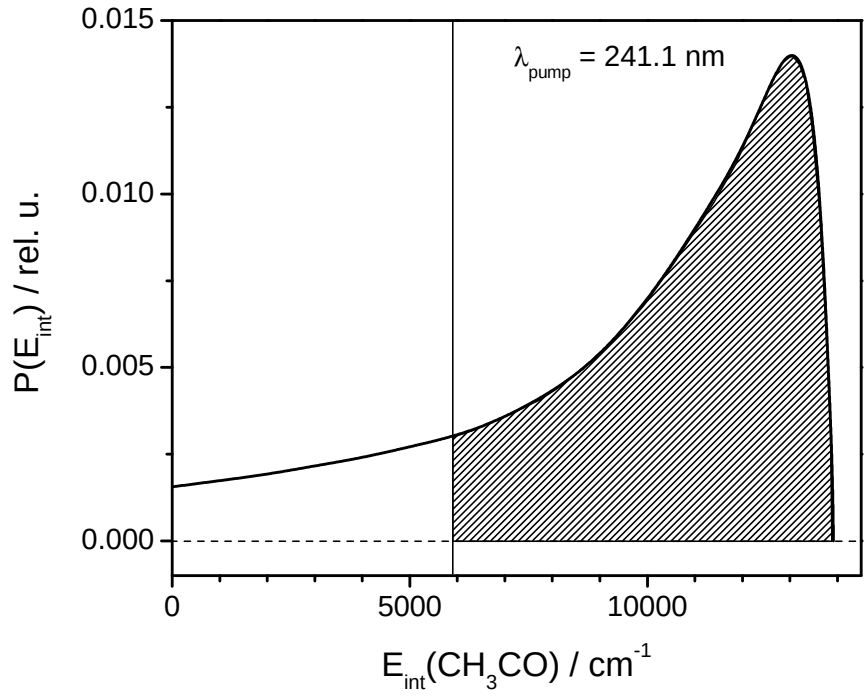

Figure 3.53: Internal energy distribution of CH_3CO following the MEK photolysis at 241.1 nm and probing C_2H_5 fragments. The shaded area demonstrates the amount of the CH_3CO radicals having enough internal energy to undergo the secondary dissociation. For further elucidations see the text.

(1) The first channel proceeds *via* cleavage of the α-C-C (α_1) bond between the carbon atoms in the carbonyl and in the methyl groups. The direct determination of the dissociation energy D_0^0 of the corresponding bond was not possible, therefore the value of D_0^0 was estimated from the known values of the standard enthalpy of formation of the photofragments and is equal to $D_0^0(C_2H_5C(O)\text{-}CH_3) = 349.4 \pm 4.4$ kJ/mol $= 29\,208 \pm 368$ cm^{-1}.

The first dissociation channel was tested by observing the vibrationalless ($v = 0$) CH_3 radicals in their ground electronic state *via* (2+1) MPI. The photolysis of $CH_3C(O)C_2H_5$ excited at 286, 271 and 265 nm within the first absorption band (Figure 3.47) did not demonstrate any specific ion distributions. Regardless of the photolysis wavelength, the velocity map images were isotropic, broad and unstructured, which points out that the complete redistribution and randomization of the available energy occurs prior to the dissociation of the MEK molecule.

To the best of our knowledge, there are no available data in the literature explaining which electronic states are involved in the photodissociation process of MEK, as well as their shape. However, MNDCO-CI calculations of Reinsch and Klessinger on the α-cleavage reaction of acetone and di-tert-butyl ketone have found essentially the same shapes of the potential energy surfaces (PESs) for both compounds [122]. Small differences were found in the position and the height of the dissociation barrier in

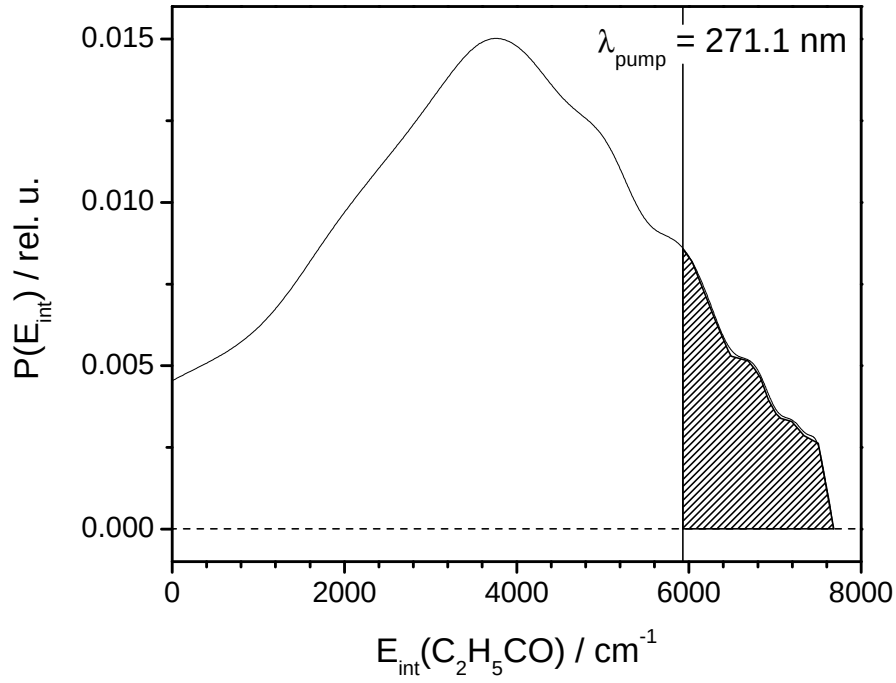

Figure 3.54: Internal energy distribution of C_2H_5CO following the MEK photolysis at 271.1 nm and probing CH_3 fragments. The shaded area demonstrate the amount of the C_2H_5CO radicals having enough internal energy to undergo the secondary dissociation.

the T_1 state. With increasing degree of branching at the α-carbon, the T_1 barrier occurs earlier along the reaction coordinate and the activation energy decreases by $\sim$25 kJ/mol for each alkyl substituent. The nature of the remaining alkyl substituent and branching at the β-position of the leaving alkyl group was shown to have no influence on the activation energy [122]. These results let one assume that the PESs of MEK do not differ much from those of acetone and the same mechanism should be involved in the photodissociation. However, the present results strongly differ from those, observed in the case of acetone. The calculations of Reinsch and Klessinger show that the $n\pi^*$ excited states of ketones (acetone and di-tert-butyl ketone) are planar, this does not agree with the calculations made in the present work and the other recently published theoretical papers (see Section 3.2.1 and Ref. [36]). The geometry of acetone in the S_1 state is strongly pyramidalized due to the oxygen atom (see Section 3.2.1).

There are several possible explanations for the observed ion distributions: (i) The methyl radical, detected in the present experiment did not come from the α-C-C bond cleavage, but from the β-C-C, which would imply different PESs and photodissociation dynamics. However, the β-C-C bond is chemically more stable ($\sim$421 kJ/mol) and this possibility does not seem to be plausible. (ii) The presence of the

ethyl group changes the vibrational degrees of freedom s by a factor of 1.4 ($s = 24$ for acetone and 33 for MEK). The consequence of the increased number of degrees of freedom is an increase of the density of states and a more efficient IC from the S_1 state to the S_0 state. This argument would mean that the ISC efficiency should also become higher, which is obviously not the case. (iii) The presence of the ethyl group changes the coupling constants in such a way that the coupling between the T_1 and S_1 states becomes less preferential and the $S_1 - S_0$ coupling becomes more efficient. (iv) The PESs of MEK differ from those of acetone so that the triplet dissociation barrier is higher than in the case of acetone. The dissociation of MEK would proceed in this case *via* IC ($S_1 \rightarrow S_0$) and ISC ($T_1 \rightarrow S_0$) followed by unimolecular decay from high vibrational levels of the S_0 state. The assumption of a lower barrier does not explain the absence of fast methyl fragments at lower excitation energy ($\lambda_{pump} = 286$ nm) as it was observed for the acetone photolysis (see Section 3.2.4). (v) The increased density of states made the IVR so efficient that complete randomization and redistribution occurs prior to the dissociation. The increased internal degrees of freedom make the trajectory of the excited wave packet to the bottleneck on the dissociative PES very curved and complicated, from the classical point of view. Such a motion is a superposition of vibrations with different amplitudes and phases, which can finally bring the molecule to the dissociative valley. This process takes place on the S_1 state before it is coupled to the S_0 or the T_1 state and on the latter ones before the dissociation. Additionally, such a traveling on the PES does not lead to an instantaneous dissociation, but the lifetime of the excited state becomes longer with increased vibrational degrees of freedom, and there is a higher chance for the absorption the second photon from the probe laser beam by MEK, followed by the dissociation of MEK excited to the upper states. The last possibility seems to be the most plausible.

Already, the photolysis of MEK at 271 nm results in $\sim 10\%$ of C_2H_5CO (see Fig. 3.54), which can undergo secondary decomposition. Such an internal energy distribution in the propionyl radical supports also the last hypothesis of an increased density of states and efficient energy redistribution among the vibrational degrees of freedom prior to the dissociation. On the other hand, this result can originate from the two-photon absorption followed by the dissociation from the higher states. Such dissociation pathway will produce highly internally excited nascent photoproduct, which can easily undergo secondary dissociation.

(2) The second channel proceeds *via* cleavage of the α-C-C (α_2) bond between the carbonyl atom and carbon in the ethyl group. The direct determination of the D_0^0 energy was not possible. The D_0^0 value was also estimated from the known values of the standard enthalpy of formation of the photofragments and is equal to $D_0^0(CH_3CO\text{-}C_2H_5) = 342.8 \pm 3.1$ kJ/mol $= 28\ 656 \pm 259 \text{cm}^{-1}$.

The second channel was tested by observing the C_2H_5 fragments. There was an additional problem caused by the insensitivity of the excitation of the ethyl radical

to its internal state. As was mentioned above in Section 3.4.2, the probing of the ethyl radical was not state specific, unlike the detection of the methyl radical. This fact makes the interpretation of the observed results difficult.

The MEK photolysis in this channel was only probed at 241 nm and gave also isotropic, broad and unstructured ion distributions. It is impossible to make any conclusion about the dissociation mechanism involved in the α_2 bond cleavage at the present time. The diffusive and isotropic character of the ion distribution suggests a long lifetime of the S_1 state of MEK and vibrational relaxation prior to dissociation. Assuming that similar PESs are involved in the second dissociation channel of MEK, the internal conversion and intersystem crossing are expected to be involved in the MEK photolysis. Further experimental and theoretical investigations are needed.

4 Summary

The photodissociation dynamics of several molecules, such as methyl nitrite, acetone and methyl ethyl ketone was investigated by velocity map imaging.

The photodissociation of the *trans*-methyl nitrite molecule following excitation into the S_1 state with 0 and 1 quanta of excitation in the NO-stretching mode has been investigated using the method of velocity map imaging. State selective probing of the nascent NO fragments with (1+1) REMPI was performed for NO in vibrational states with $v'' = 0$ and 1, and a rotational excitation of $j'' = 33.5$.

The resulting distribution of the TKER and internal energy distribution of the methoxy radical show both a vibrationally non-adiabatic predissociation with a loss of one quantum of the NO vibrational excitation in the course of the dissociation and an adiabatic channel, where the dissociation occurs by tunneling through a potential barrier on the S_1 potential energy surface. The overall intensity of the detected ion signal in both channels is comparable. The Tarte's assignment of the UV absorption spectrum was confirmed.

For the non-adiabatic channel, a highly asymmetric and bimodal ion distribution was found for a rotational excitation of $j'' = 33.5$. The ion distributions for the adiabatic channels were monomodal and less asymmetric. The results were interpreted in favour of a selective vibrational excitation in the CH_3O fragment *via* intramolecular vibrational relaxation preceding dissociation. The accepted assumption of the methoxy group being simply a spectator is therefore at least questionable in this specific case, and an overall dissociation mechanism with the methoxy group participating in the IVR has to be considered.

From the maximum of the kinetic energy release, an upper limit for the O-NO bond dissociation energy could be determined spectroscopically as $D_0^0 = 13\ 560 \pm 200\ \mathrm{cm}^{-1}$. The observed anisotropies of the photofragment angular distributions lead to a S_1 excited state lifetime of $\tau \approx 350$ fs.

The photodissociation dynamics of acetone-$h6$ excited within the first absorption band was studied in the present thesis by detecting the distributions of nascent methyl fragments in their ground state ($v = 0$) *via* REMPI, probing with $\lambda_{probe} = 333.5$ nm.

The experimental results on the photodissociation of acetone-$h6$ clearly demonstrate that three distinct dissociation pathways exist, corresponding to three different spectral regions of acetone excitation within the first absorption band ($340 - 230$ nm).

Photolysis of acetone-$h6$ excited in Region 1 (333.5 nm$>\lambda_{pump}>$ 305.3 nm) proceeds *via* internal conversion of the excited S_1 state to the ground state S_0, followed by unimolecular decomposition on the S_0 PES. The nascent photofragments are methyl and acetyl radicals.

Excitation of acetone-$h6$ in Region 2 (305.3 nm$>\lambda_{pump}>$ 261 nm) opens an additional dissociation channel. An efficient $S_1 \rightarrow T_1$ coupling (ISC) starts at wavelengths shorter than 320 nm, but the T_1 surface has a dissociation barrier above the $0-0$ $S_1 \leftarrow S_0$ transition. This barrier preserves acetone from direct decomposition. The barrier height of the T_1 state was measured in the present thesis to be 4 700 $\pm$ 40 cm^{-1}.

From the maximum of the kinetic energy release, the CH_3CO-CH_3 bond dissociation energy has been determined as $D_0^0 = 29\ 090 \pm 250$ cm^{-1}.

Photolysis of acetone-$h6$ excited in Region 3 (261 nm$>\lambda_{pump}>$ 220 nm) yields methyl and vibrationally "hot" acetyl fragments. The internal energy of the acetyl radical received by the parent molecule dissociation is high enough to overcome the dissociation barrier on the ground state PES and decay to carbon monoxide and secondary methyl fragments. CO fragments, resulting from the acetyl dissociation, exhibit high rotational excitation and probably some vibrational excitation is also presented in the fragment.

The angular distributions of the methyl fragments are essentially isotropic. An angular anisotropy parameter of $\beta < 0.3$ (but not zero) points out that the excited parent molecule survives for several rotational periods before dissociation.

The photodissociation dynamics of the deuterated acetone-$d6$ molecule was studied by excitation at the same λ_{pump} and the same detection procedure was used. Isotopic substitution of the methyl groups did not demonstrate any noticable influence on the dissociation dynamics and dissociation barrier height. The present results suggest that possibly molecular rotation and internal rotors affect the effective T_1 barrier height in the acetone molecule. As for acetone-$h6$, three dissociation pathways were determined for the same spectral regions of the excitation wavelength.

Secondary dissociation of acetyl-$d3$ occurs at slightly higher excitation energy, compared to acetyl-$h3$. The acetyl-$d3$ dissociation barrier height of 6 832 cm^{-1} $\pm$ 564 cm^{-1} has been estimated. The increase upon deuteration may partially reflect the longer lifetime of acetyl-$d3$ radical toward unimolecular dissociation. Carbon monoxide demonstrates high rotational excitation.

The angular anisotropy parameter of $\beta < 0.3$ points out again that the dissociation lifetime is long enough to let acetone-$d6$ have several rotational periods before dissociation.

The photolysis of methyl ethyl ketone can have two possible channels:

$$CH_3C(O)C_2H_5 + h\nu \longrightarrow CH_3 + C_2H_5CO^*$$
$$CH_3C(O)C_2H_5 + h\nu \longrightarrow C_2H_5 + CH_3CO^*$$

Both were studied in the present thesis by probing methyl and ethyl fragments by REMPI with $\lambda_{probe} = 333.5$ and 242 nm, respectively. The present results do not provide enough data to clearly understand the photodissociation dynamics of MEK. Theoretical calculations point out that longer excitation wavelengths have to be probed. Further experimental and theoretical investigations would be of great interest.

Bibliography

[1] J. S. Lewis, R. G. Prinn, *Planets and Their Atmospheres: Origins and Evolution*, Academic Press, Inc. (1984).

[2] J. R. Barker, *Progress and problems in atmospheric chemistry*, World Scientific Publishing Co. Pte. Ltd. (1995).

[3] R. P. Wayne, *Chemistry of atmospheres, 3 ed.*, Oxford University Press (2000).

[4] G. K. Moortgat, Important photochemical processes in the atmosphere, *Pure Appl. Chem.* 73, 487–490 (2001.).

[5] B. N. Buu N. Tran, J. C. Josepha, M. Force, R. G. Briggs, V. Vuitton, J. P. Ferris, Photochemical processes on Titan: Irradiation of mixtures of gases that simulate Titan's atmosphere, *Icarus* 177, 106–115 (2005).

[6] R. Koppman, *Volatile organic compounds in the atmosphere*, Blackwell Publishing (2007).

[7] C. Tanner, C. Manca, S. Leutwyler, Probing the Threshold to H Atom Transfer Along a Hydrogen-Bonded Ammonia Wire, *Science* 302, 1736–1739 (2003).

[8] W. Domcke, A. L. Sobolewski, Unraveling the Molecular Mechanisms of Photoacidity, *Science* 302, 1693–1694 (2003).

[9] A. T. J. B. Eppink, Photodissociation of CH_3I and O_2 studied by velocity map imaging, Dissertation, Katholieke Universiteit Nijmegen (1999).

[10] H. B. Singh, P. L. Kanakidou, P. J. Crutzen, D. J. Jacob, High concentrations and photochemical fate of oxygenated hydrocarbons in the global troposphere, *Nature* 378, 50–54 (1995).

[11] H. Singh, Y. Chen, A. Staudt, D. Jacob, D. Blake, B. Heikes, J. Snow, Evidence from the Pacific troposphere for large global sources of oxygenated organic compounds, *Nature* 410, 1078–1081 (2001).

[12] P. H. Turner, M. Corkill, P. Cox, Microwave Spectra and Structures of *cis*- and *trans*-Methyl Nitrite. Methyl Barrier in *trans*-Methyl Nitrite, *J. Phys. Chem.* 83, 1473–1482 (1979).

[13] J. A. Darsey, D. L. Thompson, Ab initio molecular orbital calculation of the methyl nitrite syn-anti isomeriztion potential, *Chem. Phys. Lett.* 145, 523–528 (1988).

[14] O. Benoist D'azy, F. Lahmani, C. Lardeux, D. Solgadi, State-selective photochemistry: energy distribution in the NO fragment after photodissociation of the CH_3ONO $n\pi^*$ state, *Chem. Phys.* 94, 247–256 (1985).

[15] F. Lahmani, C. Lardeux, D. Solgadi, Photofragmentation of CH_3ONO at 355 nm. Energy distribution in the NO fragment, *Chem. Phys. Lett.* 102, 523–528 (1983).

[16] F. Lahmani, C. Lardeux, D. Solgadi, Rotational and electronic anysotropy in NO $X^2\Pi$ from the photodissociation of CH_3ONO, *Chem. Phys. Lett.* 129, 24–30 (1986).

[17] M. N. R. Aschfold, J. R. Baggott, *Molecular photodissociation dynamics*, The royal society of chemistry (1987).

[18] H. Suter, B. U., J. R. Huber, Photodissociation of CH_3ONO by a direct and indirect mechanism, *Chem. Phys. Lett.* 171, 63–67 (1990).

[19] S. A. Reid, J. T. Brandon, H. Reisler, State-specific photofragment yield spectroscopy of jet-cooled methyl nitrite, *Chem. Phys. Lett.* 209, 22–28 (1993).

[20] R. Schinke, *Photodissociation dynamics*, Cambridge university press (1993).

[21] R. Schinke, S. Hennig, A. Untch, M. Nonella, J. R. Huber, Diffusive vibrational structures in photoabsorption spectra: A comparison of CH_3ONO and CH_3SNO using ab initio two-dimensional potential energy surfaces, *J. Chem. Phys.* 91, 2016–2029 (1989).

[22] P. Tarte, Rotational isomerizm as a genneral property of alkyl nitrites, *J. Chem. Phys.* 20, 1570–1575 (1952).

[23] M. Hippler, J. Pfab, Electronic Absorption Spectrum of Methyl Nitrite in the Near-ultraviolet, *J. Chem. Soc. Faraday Trans.* 88, 2109–2110 (1992).

[24] M. Hippler, F. A. H. Al-Janabi, J. Pfab, Photodissociation of jet-cooled methyl and t-butyl nitrite near 380 nm, *Chem. Phys. Lett.* 192, 173–178 (1992).

[25] A. Hennig, V. Engel, R. Schinke, M. Nonella, J. R. Huber, Photodissociation dynamics of methylnitrite (CH_3O-NO) in the 300-400 nm range: An ab initio quantum mechanical study, *J. Chem. Phys.* 87, 3522–3529 (1987).

[26] A. Kuczmann, Zustandaufgeloeste Untersuchung zur photoinduzierten Zerfalldynamik von Methylnitrit und Formyl-Radikalen mittels Photofragment-Geschwindigkeitskartographe, Dissertation, Christian-Albrechts-Universitaet zu Kiel (2002).

[27] H. B. Singh, Y. Chen, G. L. Gregory, G. W. Sachse, R. Talbot, D. R. Blake, Y. Kondo, J. D. Bradshaw, B. Heikes, D. Thornton, Trace Chemical Measurements from the Northern Midlatitude Lowermost Stratosphere in Early Spring: Distributions, Correlations, and Fate., *J. Geophys. Res.* 24, 127–130 (1997).

[28] P. O. Wennberg, T. F. Hanisco, L. Jaegle, D. J. Jacob, E. J. Hintsa, E. J. Lanzendorf, J. G. Anderson, R.-S. Gao, E. R. Keim, S. G. Donnelly, L. A. Del Negro, D. W. Fahey, S. A. McKeen, R. J. Salawitch, C. R. Webster, R. D. May, R. L. Herman, M. H. Proffitt, J. J. Margitan, E. L. Atlas, S. M. Schauffler, F. Flocke, C. T. McElroy, T. P. Bui, Hydrogen Radicals, Nitrogen Radicals, and the Production of O_3 in the Upper Troposphere., *Science* 279, 49–53 (1998).

[29] R. G. W. Norrish, H. G. Crone, O. D. Saltmarsh, Primary Photochemical Reactions. Part V . The Spectroscopy and Photochemical Decomposition of Acetone., *J. Chem. Soc.* 318, 1456–1464 (1934).

[30] W. A. Noyes, G. B. Porter, J. E. Jolley, The primary photochemical process in simple ketones, *Chem. Rev.* 56, 49 – 94 (1956).

[31] K. A. Trentelman, S. H. Kable, D. B. Moss, P. L. Houston, Photodissociation dynamics of acetone at 193 nm: Photofragment internal and translational energy distributions, *J. Chem. Phys.* 91, 7498–7513 (1989).

[32] L. D. Waits, R. J. Horwitz, J. A. Guest, Translational energy study of CH_3 photofragments following $^1(n,\pi^*)$ excitation of acetone, *Chem. Phys.* 155, 149–156 (1991).

[33] S. W. North, D. A. Blank, J. D. Gezelter, C. A. Longfellow, Y. T. Lee, Evidence for stepwise dissociation dynamics in acetone at 248 and 193 nm, *J. Chem. Phys.* 102, 4447–4460 (1995).

[34] S. K. Kim, S. Pedersen, A. H. Zewail, Direct femtosecond observation of the transient intermediate in the α-cleavage reaction of $(CH_3)_2CO$ to $2CH_3+CO$: Resolving the issue of concertedness, *J. Chem. Phys.* 103, 477–480 (1995).

[35] J. C. Owrutsky, A. P. Baranovski, Ultrafast photodissociation dynamics of the S_1 and S_2 states of acetone, *J. Chem. Phys.* 110, 11206–11213 (1999).

[36] D. W. Liao, A. M. Mebel, M. Hayashi, Y. J. Shiu, Y. T. Chen, S. H. Lin, Ab initiostudy of the $n - \pi^*$ electronic transition in acetone: Symmetry-forbidden vibronic spectra, *J. Chem. Phys.* 111, 205–215 (1999).

[37] D. Liu, W.-H. Fang, X.-Y. Fu, An ab initio study on photodissociation of acetone, *Chem. Phys. Lett.* 325, 86–92 (2000).

[38] R. Atkinson, J. Arey, Atmospheric Degradation of Volatile Organic Compounds, *Chem. Rev.* 103, 4605 – 4638 (2003).

[39] I. R. Slagle, Q. Feng, D. Gutman, Kinetics of the reaction of ethyl radicals with molecular oxygen from 294 to 1002 K, *J. Phys. Chem.* 88, 3648–3653 (1984).

[40] E. Grosjean, D. Grosjean, M. P. Fraser, G. R. Cass, Air Quality Model Evaluation Data for Organics. 3. Peroxyacetyl Nitrate and Peroxypropionyl Nitrate in Los Angeles Air, *Environ. Sci. Technol.* 30, 2704–2714 (1996).

[41] G. S. Tyndall, J. J. Orlando, T. J. Wallington, M. D. Hurley, Pressure Dependence of the Rate Coefficients and Product Yields for the Reaction of CH_3CO Radicals with O_2, *Int. J. Chem. Kinet.* 29, 655–663 (1997).

[42] M. A. Blitz, D. E. Heard, M. J. Pilling, OH formation from $CH_3CO + O_2$: a convenient experimental marker for the acetyl radical, *Chem. Phys. Lett.* 365, 374–379 (2002).

[43] L. Jaegle, D. J. Jacob, W. H. Brune, P. O. Wennberg, Chemistry of HO_x radicals in the upper troposphere, *Atmos. Environ.* 35, 469–489 (2001).

[44] R. B. Smalley, L. Wharton, D. H. Levy, Molecular optical spectroscopy with supersonic beams and jets, *Accounts of Chemical Research* 10, 139–145 (1977).

[45] D. H. Levy, Laser spectroscopy of cold gas-phase molecules, *Ann. Rev. Phys. Chem.* 31, 197–225 (1980).

[46] J. Riedel, Untersuchung photoinduzierte molecularer Zerfallsprozesse mittels Pfotofragment-Geschwindigkeitskartographie, Dissertation, Christian-Albrechts University (2006).

[47] W. E. Stephens, A Pulsed Mass Spectrometer with Time Dispersion, *Phys. Rev.* 69, 691 (1946).

[48] W. C. Wiley, I. H. McLaren, Time-of-Flight Mass Spectrometer with Improved Mass Resolution, *Rev. of Sci. Instruments* 26, 1150–1157 (1955).

[49] J. Solomon, Photodissociation as Studied by Photolysis Mapping, *J. Chem. Phys.* 47, 889–895 (1967).

[50] A. J. R. Heck, D. W. Chandler, Imaging techniques for the study of chemical reaction dynamics, *Ann. Rev. Phys. Chem.* 46, 335–372 (1995).

[51] R. N. Zare, D. R. Herschbach, Angular momentum, *Proc. IEEE* 51, 173 (1963).

[52] B.-Y. Chang, R. C. Hoetzlein, J. A. Mueller, J. D. Geiser, P. L. Houston, Improved two-dimensional product imaging: The real-time ion-counting method, *Rev. Sci. Instrum.* 69, 1665–1670 (1998).

[53] E. Wrede, S. Laubach, S. Schulenburg, A. Brown, J. Wouters, E. R. Orr-Ewing, M. N. R. Aschfold, Continuum state spectroscopy: A high resolution ion imaging study of IBr photolysis in the wavelength range 440-685 nm, *J. Chem. Phys.* 114, 2629–2646 (2001).

[54] F. Renth, J. Riedel, F. Temps, Inversion of velocity map ion images using iterative regularization and cross validation, *Rev. of Sci. Instruments* 77, 033103–1–033103–12 (2006).

[55] J. J. Vrakking, An iterative procedure for the inversion of two-dimensional ion-photoelectron imaging experiments, *Rev. Sci. Instrum.* 72, 4084–4089 (2001).

[56] V. Dribinski, O. Ossadtchi, V. A. Mandelshtam, H. Reisler, Reconstruction of Abel-transformable images: The Gaussian basis-set expansion Abel transform method, *Rev. Sci. Instrum.* 73, 2634–2642 (2002).

[57] L. Garcia, G. A. Nahon, I. Powis, Two-dimensional charged particle image inversion using a polar basis function expansion, *Rev. Sci. Instrum* 75, 4989–4996 (2004).

[58] A. D. Hammerich, U. Manthe, R. Kosloff, H. D. Meyer, L. S. Cederbaum, Time-dependent photodissociation of methyl iodide with five active modes, *J. Chem. Phys.* 101, 5623–5646 (1994).

[59] Y. Amamatsu, K. Morokuma, S. Yabushita, Ab initio potential energy surfaces and trajectory studies of A-band photodissociation dynamics: $CH_3I^* \rightarrow CH_3$+I and CH_3+I^*, *J. Chem. Phys.* 94, 4858–4876 (1991).

[60] H. Guo, G. C. Schatz, Time-dependent dynamics of methyl iodide photodissociation in the first continuum, *J. Chem. Phys.* 93, 393–402 (1990).

[61] B. R. Johnson, C. Kittrell, P. B. Kelly, J. L. Kinsey, Resonance Raman Spectroscopy of Dissociative Polyatomic Molecules., *J. Phys. Chem.* 100, 7743–7764 (1996).

[62] A. T. J. B. Eppink, D. H. Parker, Methyl iodide A-band decomposition study by photofragment velocity imaging., *J. Chem. Phys.* 109, 4758–4767 (1998).

[63] M. A. Eliashevich, *Atomic and molecular spectroscopy*, State publisher of physical and mathematical literature, Leningrad (1962).

[64] R. E. Continetti, B. A. Balko, Y. T. Lee, Symmetric stretch excitation of CH_3 in the 193.3 nm photolysis of CH_3I, *J. Chem. Phys.* 89, 3383–3384 (1988).

[65] M. Dzvonik, S. Yang, R. Bersohn, Photodissociation of molecular beams of aryl halides, *J. Chem. Phys.* 61, 4408–4421 (1974).

[66] Y. Amamatsu, S. Yabushita, K. Morokuma, Full nine-dimensional ab initio potential energy surfaces and trajectory studies of A-band photodissociation dynamics: $CH_3I^* \rightarrow CH_3$+I, CH_3+I^*, and $CD_3I^* \rightarrow CD_3$+I, CD_3+I^*, *J. Chem. Phys.* 104, 9783–9794 (1996).

[67] D. A. Dahl, *SimIon 3D version 6.0 User's maual*, Princenton Electronic Systems, Inc. (1995).

[68] J. Riedel, Untersuchung der Photodissocziation von CH_3ONO mittels Ion Imaging: Implementation eines Einzelionenzael-Verfahrens, Diplomarbeit, Christian-Albrechts-Universitaet zu Kiel (2002).

[69] J. M. Mestdagh, M. Berdah, I. Dimicoli, M. Mons, P. Meynadier, P. d'Oliveira, F. Piuzzi, J. P. Visticot, C. Jouvet, C. Lardeux-Dedonder, S. Martrenchard-Barra, B. Soep, D. Solgadi, Observation of an indirect pathway in the femtosecond study of alkyl nitrite photodissociation in the S_1 state, *J. Chem. Phys.* 103, 1013–1023 (1995).

[70] A. Untch, K. Weide, R. Schinke, 3D wavepacket study of the photodissociation of CH_3ONO (S_1), *Chem. Phys. Lett.* 180, 265–270 (1991).

[71] G. Herzberg, *Molecular Spectra and Molecular Structer I. Spectra of Diatomic Molecule*, D. Van Nostrand Reinhold Company (1951).

[72] P. Felder, H. H. Günthard, Conformational interconversions in supersonic jets: Matrix IR spectroscopy and model calculations, *Chem. Phys.* 71, 9–25 (1982).

[73] M. Bodenbinder, S. E. Ulic, H. Willner, A gas-phase and matrix isolation study of the equilibrium CH_3ONO (*cis*), *J. Phys. Chem.* 98, 6441–6444 (1994).

[74] J. Kappert, F. Temps, Rotationally resolved laser-induced fluorescence excitation studies of CH_3O, *Chem. Phys.* 132, 197–208 (1989).

[75] D. L. Osborn, D. J. Leahy, E. M. Ross, D. M. Neumark, Study of the predissociation of CH_30, $(^2A_1)$ by fast beam photofragment translational spectroscopy, *Chem. Phys. Lett.* 235, 484–489 (1995).

[76] D. E. Powers, M. B. Pushkarsky, T. A. Miller, Rovibronic analysis of the laser induced fluorescence excitation spectrum of the jet-cooled methoxy radical, *J. Chem. Phys.* 106, 6863–6877 (1997).

[77] T. A. Barckholtz, T. A. Miller, Quantitative insights about molecules exhibiting Jahn-Teller and related effects, *Int. ReV. Phys. Chem.* 17, 435–529 (1998).

[78] G. D. Bent, G. F. Adams, R. H. Bartram, G. D. Purvis, R. J. Bartlett, Many body pertrubation theory electronic structure calculations for the methoxy radical. I. Determination of Jahn-Teller surfaces, spin-orbit splitting and Zeeman effect., *J. Chem. Phys.* 76, 4144–4156 (1982).

[79] A. Geers, J. Kappert, F. Temps, T. J. Sears, Stimulated emission pumping spectroscopy of CH_30 (X^2E, ν_6): New observations on the Jahn-Teller effect, *J. Chem. Phys.* 98, 4297–4300 (1993).

[80] Z. Zhengyu Zhou, X. Cheng, X. Zhou, H. Fu, Vibrational mode analysis for the multi-channel reaction of $CH_3O + CO$, *Chem. Phys. Lett.* 353, 281–289 (2002).

[81] T. A. Barckholtz, T. A. Miller, The Calculation of Spectroscopic Jahn-Teller Parameters by ab Initio Methods, *J. Phys. Chem. A* 103, 2321–2336 (1999).

[82] W. Koch, M. C. Holthausen, *A Chemist's Guide to Density Functional Theory*, Wiley-VCH, Weinheim, ed. 2 (2002).

[83] A. D. Becke, Density-functional thermochemistry. III. The role of exact exchange, *J. Chem. Phys.* 98, 5648–5652 (1993).

[84] W. J. Hehre, R. F. Stewart, J. A. Pople, Self-consistent molecular orbital methods. I. Use of Gaussian expansions of Slater-type atomic orbitals, *J. Chem. Phys.* 51, 2657–2664 (1969).

[85] A. P. Scott, L. Radom, Harmonic Vibrational Frequencies: An Evaluation of Hartree-Fock, Moeller-Plesset, Quadratic Configuration Interaction, Density Functional Theory, and Semiempirical Scale Factors, *J. Phys. Chem.* 100, 16502–16513 (1996).

[86] M. Hippler, M. R. S. McCoustra, J. Pfab, Structured absorption spectrum and vibrational state-selectivity in the photodissociation of methyl nitrite in the near-UV, *Chem. Phys. Lett.* 198, 168–176 (1992).

[87] G. E. Busch, K. R. Wilson, Triatomic photofragment spectra. II. Angular distributions from NO_2 photodissociation, *J. Chem. Phys.* 56, 3638–3654 (1972).

[88] U. Bruehlmann, J. R. Huber, Fragment state distribution, energy partitioning and rotational alignment in the state-to-state photodissociation of methylnitrite, *Z. Phys. D - Atoms, Molecules and Clusters* 7, 1–8 (1987).

[89] A. Untch, R. Schinke, R. Cotting, J. R. Huber, The vibrational predissociation of cis-methyl nitrite in the S_1, state: A comparison of exact quantum mechanical wave packet calculations with classical trajectory calculations and detailed experimental results, *J. Chem. Phys.* 99, 9553–9566 (1993).

[90] J. D. Ray, A. A. Gershon, The heat of formation of gaseouse methyl nitrite, *J. Phys. Chem.* 66, 1750–1752 (1962).

[91] R. Silverwood, J. H. Thomas, Reaction Between Methanol and Nitrogen Dioxide Part 1 . Low-temperature Reaction and the Thermodynamic Constants of Methyl Nitrite, *Trans. Faraday Soc.* 63, 2476–2579 (1967).

[92] S. Dertinger, A. Geers, J. Kappert, J. Wiebrecht, F. Temps, Rotation-Vibration State-resolved Unimolecular Dynamics of Highly Excited CH_30 (2^E) Part 3.State-specific Dissociation Rates from Spectroscopic Line Profiles and Time-resolved Measurements, *Faraday discuss.* 102, 31–52 (1995).

[93] T. M. Ramond, R. L. Davico, G. E. Schwartz, W. C. Lineberger, Vibronic structure of alkoxy radicals via photoelectron spectroscopy, *J. Chem. Phys.* 112, 1158–1169 (2000).

[94] M. J. Chase, NIST-JANAF Themochemical Tables, Fourth Edition, J. Phys. Chem. Ref. Data, Monograph 9 (1998). Internet NIST.

[95] L. A. Curtiss, K. Raghavachari, G. W. Trucks, J. A. Pople, Gaussian-2 theory for molecular energies of first- and second-row compounds, *J. Chem. Phys.* 94, 7221–7230 (1991).

[96] H. T. Thuemmel, Theoretical Study on $X-H$, $-O$, $-OH$, $-NO$, $-ONO$, $and-NO_2$ $(X = CH_3,\ t-C_4H_9,\ C_{13}H_{21})$, *J. Phys. Chem. A* 102, 2002–2008 (1998).

[97] J. C. Cramer, *Essentials of Computational Chemistry*, John Wiley and Sons, Ltd. (2004).

[98] G. E. Busch, K. R. Wilson, Triatomic photofragment spectra. I. Energy partitioning in NO_2 photodissociation, *J. Chem. Phys.* 56, 3626–3638 (1972).

[99] A. F. Tuck, Molecular Beam Studies of Ethyl Nitrite Photodissociation, *J. Chem. Soc. Faraday Trans.* 73, 689–708 (1977).

[100] B. A. Keller, P. Felder, J. R. Huber, Molecular beam photodissociation study of methyl nitrite in the near-ultraviolet region, *J. Phys. Chem.* 91, 1114–1120 (1987).

[101] R. Vasudev, R. N. Zare, R. N. Dixon, State-selected photodissociation dynamics: Complete characterization of the OH fragment ejected by the HONO A state, *J. Chem. Phys.* 80, 4863–4878 (1984).

[102] M. Frisch, I. N. Ragazos, M. A. Robb, H. B. Schlegel, An evaluation of three direct MC-SCF procedures, *Chem. Phys. Lett.* 189, 524–528 (1992).

[103] S.-Y. Yu, C.-G. Zhang, M.-B. Huang, Electronic states of the cis- and trans-CH_3ONO molecules: a CASPT2 study, *Molecular Physics* 105, 2977–2986 (2007).

[104] M. Nonella, J. R. Huber, A. Untch, R. Schinke, Photodissociation of CH_3ONO in the first absorption band: A three-dimensional classical trajectory study, *J. Chem. Phys.* 91, 194–204 (1989).

[105] B. J. van der Veken, R. Maas, G. A. Guirgis, H. D. Stidham, T. G. Sheehan, J. R. Durig, Infrared Spectrum, ab Initio Calculations, Barriers to Internal Rotation, and Structural Parameters for Methyl Nitrite, *J. Phys. Chem.* 94, 4029–4039 (1990).

[106] R. H. Gilette, E. H. Eyster, The Fundamental Rotation-Vibration Band of Nitric Oxide, *Phys. Rev.* 56, 1113 (1939).

[107] D. J. Wallace, The gas-phase photochemical decomposition of the simple aliphatic ketones., *Chem. Rev.* 40, 201–250 (1947).

[108] H. Shaw, S. Toby, The Photochemistry of Gaseous Acetone, *J. Phys. Chem.* 72, 2337–2343 (1968).

[109] J. Solomon, C. Jonah, P. Chandra, R. Bersohn, Photolysis Mapping Studies of Aliphatic Carbonyl Compounds, *J. Chem. Phys.* 55, 1908 (1971).

[110] L. Salem, Surface Crossings and Surface Touchings in Photochemistry, *J. Am. Chem. Soc.* 96, 3486–3501 (1974).

[111] Y. Haas, Photochemical α-cleavage of ketones: revisiting acetone, *Photochem. Photobiol. Sci.* 3, 6–16 (2004).

[112] E. W.-G. Diau, C. Koetting, A. H. Zewail, Femtochemistry of Norrish Type-I Reactions: I. Experimental and Theoretical Studies of Acetone an Related Ketones on the S_1 Surface, *ChemPhysChem* 2, 273–293 (2001).

[113] R. F. Borkman, D. R. Kearns, Electronic-Relaxation Processes in Acetone, *J. Chem. Phys.* 44, 945–949 (1966).

[114] G. M. Breuer, E. K. C. Lee, Fluorescence decay times of cyclic ketones, acetone, and butanal in the gas phase, *J. Phys. Chem.* 75, 989–990 (1971).

[115] M. A. El-Sayed, Spin–orbit coupling and the radiationless processes in nitrogen heterocyclics, *J. Chem. Phys.* 38, 2834–2838 (1963).

[116] M. Baba, I. Hanazaki, The S_1,$^1A_2(n,\pi^*)$ state of acetone in a supersonic nozzle beam. Methyl internal rotation, *Chem. Phys. Lett.* 103, 93–97 (1983).

[117] A. Gandini, P. A. Hackett, Electronic Relaxation Processes in Acetone and 1, 1 , 1 -Trifluoroacetone Vapor and the Gas Phase Recombination of the Acetyl Radical at 22°C, *J. Am. Chem. Soc.* 99, 6195–6205 (1977).

[118] R. E. Rebbert, P. Ausloos, Triplet-state energy transfer from acetone to aliphatic aldehydes in the gas phase, *J. Am. Chem. Soc.* 86, 4803 (1964).

[119] O. Anner, H. Zuckermann, Y. Haas, Fluorescence Decay of Jet-Cooled Acetone, *J. Phys. Chem.* 89, 1336–1339 (1985).

[120] H. Zuckermann, B. Schmitz, Y. Haas, Dissociation Energy of an Isolated Triplet Acetone Molecule, *J. Phys. Chem.* 92, 4835–4837 (1988).

[121] H. Zuckermann, B. Schmitz, Y. Haas, Acetone Photophysics in Seeded Supersonic Molecular Beams, *J. Phys. Chem.* 93, 4083–4091 (1989).

[122] M. Reinsch, M. Klessinger, MNDCO-CI calculations for organic photoreactions. I. The α-cleavage reaction of carbonyl compounds, *J. Phys. Org. Chem.* 3, 81–88 (1990).

[123] S. A. Buzza, E. M. Snyder, D. E. Card, D. A. andFolmer, J. A. W. Castleman, Femtosecond excitation dynamics of acetone: Dissociation, ionization, and the evolution of multiply charged elemental species, *J. Chem. Phys.* 105, 7425–7431 (1996).

[124] S. A. Buzza, E. M. Snyder, J. A. W. Castleman, Further direct evidence for stepwise dissociation of acetone and acetone clusters, *J. Chem. Phys.* 104, 5040–5047 (1996).

[125] J. C. Owrutsky, A. P. Baronavski, Ultrafast studies of the photodissociation of the acetone 3s Rydberg state at 195 nm: Formation and unimolecular dissociation of the acetyl radical, *J. Chem. Phys.* 108, 6652–6659 (1998).

[126] Q. Zhong, L. Poth, J. A. W. Castleman, Ultrafast dissociation dynamics of acetone: A revisit to the S_1 state and 3s Rydberg state, *J. Chem. Phys.* 110, 192–196 (1999).

[127] A. P. Baronavski, J. C. Owrutsky, Ketone excited state lifetimes measured by deep UV ultrafast photoionization spectroscopy, *Chem. Phys. Lett.* 333, 36–40 (2001).

[128] T. I. Soelling, E. W. G. Diau, C. Koetting, S. D. Feyter, A. H. Zewail, Femtochemistry of Norrish Type-I Reactions: IV. Highly Excited Ketones - Experimental, *Chem. Phys. Chem.* 3, 79–97 (2002).

[129] N. Rusteika, K. B. Moeller, T. I. Soelling, New insights on the photodynamics of acetone excited with 253-288 nm femtosecond pulses, *Chemical Physics Letters* 461, 193–197 (2008).

[130] T. Shibata, T. Suzuki, Photofragment ion imaging with femtosecond laser pulses, *Chem. Phys. Lett.* 262, 115–119 (1996).

[131] E. W. G. Diau, C. Koetting, T. I. Solling, A. H. Zewail, Femtochemistry of Norrish Type-I Reactions: III. Highly Excited Ketones - Theoretical, *Chem. Phys. Chem.* 3, 57–78 (2002).

[132] G. Kovacs, J. Zador, E. Farkas, R. Nadasdi, I. Szilagyi, S. Dobe, T. Berces, F. Marta, G. Lendvay, Kinetics and mechanism of the reactions of CH_3CO and $CH_3C(O)CH_2$ radicals with O_2. Low-pressure discharge flow experiments and quantum chemical computations., *Phys. Chem. Chem. Phys.* 9, 4142–4154 (2007).

[133] V. Khamaganov, R. Karunanandan, A. Rodrigues, J. N. Crowley, Photolysis of $CH_3C(O)CH_3$ (248 nm, 266 nm), $CH_3C(O)C_2H_5$ (248 nm) and $CH_3C(O)Br$ (248 nm): pressure dependent quantum yields of CH_3 formation., *Phys. Chem. Chem. Phys.* 9, 4098–4113 (2007).

[134] T. Gierczak, J. B. Burkholder, S. Bauerle, A. R. Ravishankara, Photochemistry of acetone under tropospheric conditions, *Chem. Phys.* 231, 229–244 (1998).

[135] H. Somnitz, M. Fida, T. Ufer, R. Zellner, Pressure dependence for the CO quantum yield in the photolysis of acetone at 248 nm: A combined experimental and theoretical study, *Phys. Chem. Chem. Phys.* 7, 3342–3352 (2005).

[136] M. A. Blitz, D. E. Heard, M. J. Pilling, Study of Acetone Photodissociation over the Wavelength Range 248-330 nm: Evidence of a Mechanism Involving Both the Singlet and Triplet Excited States, *J. Phys. Chem. A* 110, 6742–6756 (2006).

[137] A. Maranzana, J. R. Barker, G. Tonachini, Master equation simulations of competing unimolecular and bimolecular res: applications to OH production in the reaction of acetyl radical with O_2., *Phys. Chem. Chem. Phys.* 9, 4129–4141 (2007).

[138] M. J. Frisch, G. W. Trucks, H. B. Schlegel, G. E. Scuseria, M. A. Robb, J. R. Cheeseman, J. A. Montgomery, J. T. Vreven, K. N. Kudin, J. C. Burant, W. Millam, S. S. Iyengar, J. Tomasi, V. Barone, B. Mennucci, M. Cossi, G. Scalmani, N. Rega, G. A. Petersson, H. Nakatsuji, M. Hada, M. Ehara, K. Toyota, R. Fukuda, J. Hasegawa, M. Ishida, T. Nakajima, Y. Honda, O. Kitao, H. Nakai, M. Klene, X. Li, J. E. Knox, H. P. Hratchian, J. B. Cross, V. Bakken, C. Adamo, J. Jaramillo, R. Gomperts, R. E. Stratmann, O. Yazyev, A. J. Austin, R. Cammi, C. Pomelli, J. W. Ochterski, P. Y. Ayala, K. Morokuma, G. A. Voth, P. Salvador, J. J. Dannenberg, V. G. Zakrzewski, S. Dapprich, A. D. Daniels, M. C. Strain, O. Farkas, D. K. Malick, A. D. Rabuck, K. Raghavachari, J. B. Foresman, J. V. Ortiz, Q. Cui, A. G. Baboul, S. Clifford, J. Cioslowski, B. B. Stefanov, G. Liu, A. Liashenko, P. Piskorz, I. Komaromi, R. L. Martin, D. J. Fox, T. Keith, M. A. Al-Laham, C. Y. Peng, A. Nanayakkara, M. Challacombe, M. M. Gill, B. Johnson, W. Chen, M. W. Wong, C. Gonzalez, J. A. Pople, Gaussian 03, Revision C.02 (2004). Gaussian, Inc., Wallingford CT.

[139] G. H. Damon, F. Daniels, The Photolysis of Gaseous Acetone and the Influence of Water, *J . Am. Chem. Soc.* 55, 2363–2375 (1933).

[140] S. North, D. A. Blank, Y. T. Lee, Determination of the barrier height to CH_3CO dissociation, *Chem. Phys. Lett.* 224, 38–42 (1994).

[141] E. A. Fogleman, H. Koizumi, J. P. Kercher, B. Sztaray, T. Baer, Heats of Formation of the Acetyl Radical and Ion Obtained by Threshold Photoelectron Photoion Coincidence, *J. Phys. Chem. A* 108, 5288–5294 (2004).

[142] CODATA Key Values for Thermodynamics Hemisphere, N.Y. (1989).

[143] J. F. Black, I. Powis, Rotational structure and predissociation dynamics of the methyl $4p_z(v = 0)$ Rydberg state investigated by resonance enhanced multiphoton ionization spectroscopy, *J. Chem. Phys.* 89, 3986–3992 (1988).

[144] J. W. Hudgens, T. G. DiGiuseppe, M. C. Lin, Two photon resonance enhanced multiphoton ionization spctroscopy and state assignments of the methyl radical, *J. Chem. Phys.* 79, 571–582 (1983).

[145] E. L. Knuth, Dimer-formation rate coefficients from measurements of terminal dimer concentrations in free-jet expansion, *J. Chem. Phys.* 66, 3515–3525 (1977).

[146] G. Herzberg, *Molecular Spectra and Molecular Structure III. Electronic Spectra and Electronic Structure of Polyatomic molecules*, Van Nostrand Reinhold Company (1966).

[147] T. Baer, W. L. Hase, *Unimolecular Reaction Dynamics. Theory and Experiments.*, Oxford University Press (1996).

[148] S. Deshmukh, J. D. Myers, S. S. Xantheas, W. P. Hess, Investigation of Acetyl Chloride Photodissociation by Photofragment Imaging, *J. Phys. Chem.* 98, 12535–2544 (1994).

[149] W. Mao, Q. Li, F. Kong, M. Huang, Ab initio calculations of the electronic states of acetyl radical, *Chem. Phys. Lett.* 283, 114–118 (1998).

[150] D. A. Hansen, E. K. C. Lee, Radiative and nonradiative transitions in the first excited singlet state of symmetrical methyl-substituted acetones, *J. Chem. Phys.* 62, 183–189 (1975).

[151] J. Mühlbach, J. R. Huber, Intramolecular dephasing and relaxation in the molecule butynal ($CH_3 - C \equiv CCHO$), *J. Chem. Phys.* 85, 4411–4421 (1986).

[152] G. Z. Whitten, B. S. Rabinovitch, Accurate and Facile Approximation for Vibrational Energy-Level Sums, *J. Chem. Phys.* 38, 2466–2473 (1963).

[153] M. Sun, J. H. Moon, M. S. Kim, Improved Whitten-Rabinovitch Approximation for the Rice-Ramsperger-Kassel-Marcus Calculation of Unimolecular Reaction Rate Constants for Proteins, *J. Phys. Chem. B* 111, 2747–2751 (2007).

[154] D. H. Mordaunt, D. L. Osborn, D. M. Neumark, Nonstatistical unimolecular dissociation over a barrier, *J. Chem. Phys.* 108, 2448–2457 (1998).

[155] G. E. Hall, D. V. Bout, T. J. Sears, Photodissociation of acetone at 193 nm: Rotational- and vibrational-state distributions of methyl fragments by diode laser absorption/gain spectroscopy, *J. Chem. Phys.* 94, 4182–4188 (1991).

[156] W.-K. Chen, J.-W. Ho, P.-Y. Cheng, Isotope effects in the ultrafast photodissociation of acetone 3s Rydberg state excited at 195 nm., *Chem. Phys. Lett.* 415, 291–295 (2005).

[157] E. L. Woodbridge, T. R. Fletcher, S. R. Leone, Photofragmentation of acetone at 193 nm: Rotational- and vibrational-state distributions of the CO fragment by time-resolved FTIR emission spectroscopy, *J. Chem. Phys.* 92, 5387–5393 (1988).

[158] W. Chen, J. W. Ho, P. Y. Cheng, Ultrafast photodissociation dynamics of the acetone 3s Rydberg state at 195 nm: a new mechanism, *Chem. Phys. Lett.* 380, 411–418 (2003).

[159] W. K. Chen, J. W. Ho, P. Y. Cheng, Ultrafast Photodissociation Dynamics of Acetone at 195 nm: I. Initial-state, Intermediate, and Product Temporal Evolutions by Femtosecond Mass-Selected Multiphoton Ionization Spectroscopy, *J. Phys. Chem. A* 109, 6805–6817 (2005).

[160] W. K. Chen, P. Y. Cheng, Ultrafast Photodissociation Dynamics of Acetone at 195 nm: II. Unraveling Complex Three-Body Dissociation Dynamics by Femtosecond Time-Resolved Photofragment Translational Spectroscopy, *J. Phys. Chem. A* 10, 6818–6829 (2005).

[161] M. Baba, I. Hanazaki, U. Nagashima, The $S_1(n, \pi^*)$ states of acetaldehyde and acetone in supersonic nozzle beam: Methyl internal rotation and C=O out-of-plane wagging, *J. Chem. Phys.* 82, 3938–3947 (1985).

[162] R. O. Loo, G. E. Haerri, H. P.and Hall, P. L. Houston, Methyl rotation, vibration, and alignment from a multiphoton ionization study of the 266 nm photodissociation of the methyl iodide, *J. Chem. Phys.* 90, 4222–4236 (1989).

[163] J. D. Swaley, C. C. Costain, Ketones IR spectroscopy, *J. Chem. Phys.* 31, 1562 (1959).

[164] P. Cadman, C. Dodwell, A. J. Trotman-Dickenson, A. F.and White, The kinetics of hydrogen abstraction by difluoroamino-radicals, from propionaldehyde, and n- and iso-butylaldehyde, and their acyl radical decompositions, *J. Chem. Soc. A* -, 2371–2376 (1970).

[165] H. M. Frey, I. C. Vinall, The photolysis of 3,3-dimethylbutan-2-one (methyl t-butyl ketone) and the decomposition of the acetyl radical, *Intern. J. Chem. Kinetics* 5, 523–538 (1973).

[166] A. Szirovicza, R. Walsh, Gas phase addition of HI to Ketene and the kinetics of decomposition of the acetyl radical, *Farad. Trans. I* 70, 33–42 (1974).

[167] K. W. Watkins, W. W. Word, Addition of methyl radicals to carbon monoxide: Chemically and thermally activated decomposition of acetyl radicals, *Intern. J. Chem. Kinetics* 6, 855–873 (1974).

[168] M. T. B. Romero, M. A. Blitz, D. E. Heard, M. J. Pilling, B. Price, P. W. Seakins, L. Wang, Photolysis of methylethyl, diethyl and methylvinyl ketones and their role in the atmospheric HO_x budget, *Farad. Discuss.* 130, 73 – 88 (2005).

[169] T. Shimanouchi, M. Abe, M. Mikami, Skeletal deformation vibrations and rotational isomerism of some ketones and olefins, *Spectrochimica Acta* 24A, 1037–1053 (1968).

[170] M. Abe, K. Kuchitsu, T. Shimanouchi, Electron-diffraction study of rotational isomerizm of methy ethyl ketone, *J. Mol. Structure* 4, 245–253 (1969).

[171] C. Moeller, M. S. Plesset, Note on an approximation treatment for many-electron system, *Phys. Rev.* 46, 618–622 (1934).

[172] J. Foresman, A. Frish, *Exploring chemistry with electronic structure methods: A guide to using Gaussian*, Gaussian, Inc. (1993).

[173] R. G. W. Norrish, M. S. Appleyard, Primary Photochemical Reactions. Part IV. Decomposition of Methyl Ethyl Ketone and Methyl Butyl Ketone, *J. Chem. Soc.* -, 874–880 (1934).

[174] I. Kanomata, Mass-spectrometric study on ionization and dissociation of formaldehyde, acetaldehyde, acetone and ethyl methy ketone by electron impact, *Bulletin of the Chem. Soc. of Japan* 34, 1864–1871 (1961).

[175] J. S. Roberts, H. A. Skinner, Dissociation energies of carbon bonds, carbon radicals and resonance energies in hydrocarbons radicals, *Trans. Faraday Soc.* 45, 339–357 (1949).

[176] S. K. Kim, J. Guo, J. S. Baskin, A. H. Zewail, Femtosecond Chemically Activated Reactions: Concept of Nonstatistical Activation at High Thermal Energies, *J. Phys. Chem.* 100, 9202–9205 (1996).

[177] S. K. Kim, A. H. Zewail, Femtosecond elementary dynamics of transition states and asymmetric α-cleavage in Norrish reactions, *Chem. Phys. Lett.* 250, 279–286 (1996).

[178] S. A. Kandel, T. P. Rakitizis, T. Lev-On, R. N. Zare, Angular distribution for the $Cl + C_2H_6 \rightarrow HCl + C_2H_5$ reaction observed via multiphoton ionization of the C_2H_5 radical., *J. Phys. Chem. A* 102, 2270–2273 (1998).

[179] H. R. Wendt, H. E. Hunziker, The UV spectra of primary, secondary, and tertiary alkyl radicals, *J. Chem. Phys.* 81, 717–723 (1984).

[180] K. W. Watkins, W. W. Thompson, Addition of ethyl monoxide. Kinetic properties of the radicals to carbon and thermochemical propionyl radical, *Intern. J. Chem. Kinetics* 5, 791–803 (1973).

[181] L. V. Gurvich, I. V. Veyts, C. B. Alcock, *Thermodynamic Properties of Individual Substances*, Hemisphere Publishing Co.: New York (1989).

[182] M. Frenkel, K. N. Marsh, R. C. Wilhoit, G. J. Kabo, G. N. Roganov, *Thermodynamics of Organic Compounds in the Gas State*, Thermodynamics Research Center, College Station, TX (1994).

[183] J. P. Kercher, E. A. Fogleman, H. Koizumi, B. Sztaray, T. Baer, Heats of Formation of the Propionyl Ion and Radical and 2,3-Pentanedione by Threshold Photoelectron Photoion Coincidence Spectroscopy, *J. Phys. Chem. A* 109, 939–946 (2005).

[184] L. R. McCunn, M. J. Krisch, K. Takematsu, L. J. Butler, J. Shu, Competing Pathways in the 248 nm Photodissociation of Propionyl Chloride and the Barrier to Dissociation of the Propionyl Radical, *J. Phys. Chem. A* 108, 7889–7894 (2004).

Acknowledgment

It would be impossible to make this dissertation without help, support, inspiration and encouragement which I have been receiving from many persons for the last five years and whom I sincerely grateful.

First of all, I would like to thank my doctoral advisor Prof. Dr. Friedrich E. E. Temps, for the given oportunities and interesting research topics. I appreciate very much his invaluable discussions, which helped me to understand more deeper the research field and motivated me for further work during the whole time of my work on this thesis.

I thank Dr. Jens Ridel for the introduction to me the velocity map imaging technique and for a support in the laboratory, especially in the beginning of this work.

I thank my best friend Dr. Harald Studzinski very much for his inestimable help during the whole time of my work on the dissertation, fruitful discussions and corrections of the thesis and for his support in my life in Germany.

I am very grateful to Dr. Falk Renth, who developed and programmed indispensable algorithms for data analysis, for useful discussions of some theoretical aspects and for his grateful help by corrections and improvements of this thesis.

Very special thanks go to Dipl.-Chem. Nina Schwalb and Dipl.-Chem. Ron Siewertsen for a wonderful collaboration during the whole time, their help with explaining me Mathematica software and solving problems with German language and not only with the language. Additionally, I thank Nina Schwalb for her translation of the Abstract part of this thesis to German language.

I am also very grateful to Dr. Joachim Gripp, who was always on-the-fly helping me to fix plentiful technical problems with excimer lasers and vacuum equipment and for the supply with UV absorption spectra and synthesis of necessary chemicals.

I appreciate Dipl.-Chem. Thomas Michalak, for his great collaboration in the laboratory and for his help with corrections of this thesis.

I thank Mr. Klaus Warns and Mr. Michael Karstens as well as the whole workshop crew for the permanent cooperativeness even with short-term special requirements.

Mr. Uwe Eggers and Dipl.-Chem. Carsten Grun, I thank for the help with solving different PC problems.

I thank the whole workgroup for the friendly atmosphere and the strong company.

Also I appreciate our secretary Ms. Ursula von der Heydt, for the help with such a complicated bureaucracy.

At last I would like to thank my parents for their great encouragement and support during the whole time of my work on this thesis.

Eidesstattliche Erklärung

Hiermit erkläre ich an Eides Statt, dass die vorliegende Abhandlung - abgesehen von der Beratung durch meinen Betreuer Herrn Prof. Dr. F. Temps - nach Inhalt und Form meine eigene Arbeit ist.

Diese Arbeit hat weder in Auszügen noch in ganzer Form einer anderen Stelle im Rahmen eines Prüfungsverfahrens vorgelegen. Sie wurde nicht veröffentlicht und auch nicht zur Veröffentlichung eingereicht.

_____

Siarhei Dziarzhytski